MICROSTRUCTURAL CHARACTERIZATION AND MECHANICAL PROPERTY ASSESSMENT OF A NEUTRON IRRADIATED URANIUM-ZIRCONIUM NUCLEAR FUEL AND HT9 CLADDING

by

Jonova Thomas

A Dissertation

Submitted to the Faculty of Purdue University

In Partial Fulfillment of the Requirements for the degree of

Doctor of Philosophy

School of Materials Engineering

West Lafayette, Indiana

August 2020

THE PURDUE UNIVERSITY GRADUATE SCHOOL
STATEMENT OF COMMITTEE APPROVAL

Dr. Maria Okuniewski, Chair

School of Materials Engineering

Dr. David Bahr

School of Materials Engineering

Dr. David Johnson

School of Materials Engineering

Dr. Vikas Tomar

School of Aeronautics and Astronautics

Approved by:

Dr. David Bahr

Dedicated to those who pursue knowledge and truth despite setbacks and failures.

ACKNOWLEDGMENTS

fruitful discussions and assisting me with my research in some form or capacity. I am deeply grateful to Nesredin Kedir, Cody Kirk, Shikar Misra, Mohammed Naziru, Dr. Alejandro Alcaraz, Dr. Angel Monroy, Dr. Lorena Alzate, Michael Giacomazza, Jaehun Cho, Dr. Jorge Ramirez and many other who helped me immensely at every stage of my graduate student life at Purdue University.

I would like to thank Dr. David Bahr for his valuable insights on nano-indentation and Dr. David Johnson for agreeing to be my committee member and providing brilliant suggestions to improve the quality of my research. I would also like to extend my thanks to Dr. Vikas Tomar for agreeing to be my committee member and allowing me to collaborate with Dr. Hao Wang's research. Finally, I would like to thank Dr. Janelle Wharry for permitting me to use various software available at Purdue University for analyzing my TEM data.

I also extend my gratitude to the staff and technicians at the School of Materials Engineering at Purdue University for letting me use various pieces of equipment available for research. Additionally, I would also like to thank all the faculty at Purdue University for letting me attend various classes to expand my intellect and research skills.

Finally, I would like to thank God, my parents, siblings, and niece for their endless support throughout my life without whom, I would not have been where I am today.

TABLE OF CONTENTS

LIST OF TABLES

LIST OF FIGURES

Figure 4.6: (a) STEM-HAADF micrograph of FIB lamella-4 from region B, and (b-j) elemental maps of U, Zr, C, O, Ce, Fe, La, Pd, and Nd, respectively. The STEM-EDS maps were produced at localities from where SAED pattern labeled 2 in Fig. 4.5 (a, k, and l) were produced. Markers labeled 1 (matrix) and 2 (Zr-rich precipitate) in (a) shows localities from where multiple EDS point

edge, HT9+fission products, and FCCI) of the neutron irradiated HT9 cladding. The linear relationship between the calculated yield stresses (Milot's and Busby's method) as a function of nano-hardness in the HT9 edge locality of the neutron irradiated HT9 cladding is shown in (b). An overlay of calculated yield stress (Milot's and Busby's method) as a function of nano-hardness for several neutron irradiated steels reported by Krumwiede et al. [105] is also presented in (b)... 114

LIST OF SYMBOLS

α-U	Alpha uranium phase
at.%.	Atomic percent
μ	Attenuation
β-U	Beta uranium phase
C	Carbon
˚C	Celsius
cm	Centimeter
Ce	Cerium
ΔHV	Change in Vickers micro-hardness
$\Delta\sigma_y$	Change in yield stress
h^*	Characteristic depth
H_0	Characteristic hardness
X	Chi phase
R	Coefficient of correlation
Cr	Chromium
z/L	Column height
˚	Degree
δ-UZr$_2$	Delta UZr$_2$ phase
ρ	Density
h	Depth
E_d	Displacement energy
eV	Electron volt
F	Force
T_0	Fuel centerline temperature
R_f	Fuel radius
T_s	Fuel surface temperature
G	G phase
γ	Gamma uranium phase
GPa	Giga Pascal

hr	Hour
I_0	Incident intensity
V_0	Initial volume Percent
Fe	Iron
K/min	Kelvin/minute
Kg	Kilogram
keV	Kilo electron volt
La	Lanthanum
α'	Martensitic phase
μ	Measured attenuation
SA	Measured surface area
V	Measured volume
MeV	Mega electron volt
MPa	Mega Pascal
$M_6C_{(n)}$	Metal carbide phase
m	Meter
μ	Micro (10^{-6})
μm	Micrometer
mm	Millimeter
mR	MilliRem
Mo	Molybdenum
H_n	Nano-hardness
nm	Nanometer
Nd	Neodymium
Φ	Neutron fluence
Ni	Nickel
O	Oxygen
Pd	Palladium
%	Percent
Pu	Plutonium
Pr	Praseodymium

E_i	Projected neutron energy
r	Radial position
T_r	Radial position temperature
R	Rem
σs	Scattering cross-section
s	Second
Ψ	Sphericity
α'	Supersaturated alpha uranium phase
SA_S	Surface area of an ideal sphere
V_{Swell}	Swelled volume percent
x	Thickness
Sn	Tin
T_v	Total volume of voxels
I	Transmitted intensity
W	Tungsten
U	Uranium
γ_1	U-rich, gamma uranium phase
V	Vanadium
HV	Vickers micro-hardness
$V_{fraction}$	Volume fraction
P_v	Volume of voxels in a threshold range
w_i..	Weight fraction of ith constituent
wt.%	Weight percent
Xe	Xenon
σ_y	Yield stress
Zr	Zirconium
ZrO_2	Zirconium oxide
γ_2	Zr-rich, gamma uranium phase

LIST OF ABBREVIATIONS

APS   Advanced Photon Source

ANL   Argonne National Laboratory

BSE   Back scatter electron

BCC   Body-centered cubic

dpa   Displacements per atom

DBTT   Ductile to brittle transition temperature

EDS   Energy dispersive spectroscopy

Eq   Equation

EBR-II   Experimental Breeder Reactor – II

FCC   Face-centered cubic

FFTF   Fast Flux Test Facility

F/M   Ferritic-Martensitic

FP   Fission product

FIB   Focused ion beam

FCCI   Fuel cladding chemical interaction

HCP   Hexagonally closed packed

HFEF   Hot Fuel Examination Facility

INL   Idaho National Laboratory

ISE   Indentation size effects

IMCL   Irradiated Materials Characterization Laboratory

LD   Load displacement

MFF-3   Mechanistic Fuel Failure -3

μ-CT	Micro-computed tomography
OM	Optical microscopy
PIE	Post irradiation examination
RIS	Radiation-induced segregation
SEM	Scanning electron microscope
STEM-BF	Scanning transmission electron microscope-bright field
STEM-EDS	Scanning transmission electron microscope-energy dispersive spectroscopy
STEM-HAADF	Scanning transmission electron microscope-high angle annular dark field
SE	Secondary electron
SAED	Selected area electron diffraction
SFR	Sodium Cooled Fast Reactor
3D	Three dimensions
TEM	Transmission electron microscope
2D	Two dimensions

ABSTRACT

Metallic uranium-10 weight percent zirconium (U-10wt.%Zr) nuclear fuels are classified as potential fuels for fast breeder reactors as they possess a high fissile density and have increased compatibility with sodium, a frequently used reactor coolant. Despite their advantages when exposed to neutron irradiation in reactors, the fuels are subject to damage cascades and microstructural alterations. Fuel constituent re-distribution, phase transformation, fuel swelling, and fuel cladding chemical interactions (FCCI) are a few of the major interdependent microstructural alterations that occur in these fuels at the onset of neutron irradiation. The primary objective of this research is to understand the above-mentioned microstructural alterations in different regions of a neutron irradiated U-10wt.%Zr fuel and HT9 cladding that has achieved a cross-sectional burnup of 5.7 atomic percent (at%.). Additionally, this study also aims to provide a relationship between the microstructural alterations and local mechanical property changes exhibited at different regions of the HT9 cladding as a consequence of neutron irradiation, FCCI, and fission product migration.

To achieve this goal, a coordinated group of experiments was performed on the neutron irradiated U-10wt.%Zr/HT9 (fuel/cladding) at the nanoscale, microscale, and mesoscale, respectively. The experimental techniques used for microstructural analysis included the following: (1) transmission electron microscopy of focused ion beam (FIB) lamellas for nanoscale assessments, (2) serial sectioning of FIB cuboids for microscale assessments, and (3) synchrotron micro-computed tomography of FIB obelisks for mesoscale assessment. Following the microstructural assessments, nano-indentation experiments were performed on the neutron irradiated HT9 cladding to determine the changes in mechanical properties as a function of distance from cladding edge to FCCI locality, and the changes in mechanical properties as a consequence of several microstructural alterations. Furthermore, the results produced from the various experiments in this study were compared and correlated to existing literature (both in-reactor and out-of-reactor experiments), and new theories to explain the reason for the observed changes were established. This research also revealed several novel observations such as probable radiation induced segregation in fuels, localized fuel swelling and porosity distribution at different regions in the fuel, crystal structure of phases present at different regions in the fuel and their influence on pore morphologies, and nano mechanical properties of a neutron irradiated HT9 cladding.

CHAPTER 1.   INTRODUCTION

1.1   Background and Motivation

Metallic fuels were classified as candidate fuels for fast breeder reactors as a consequence of their high fissile density and compatibility with sodium, a frequently used reactor coolant [1,2]. Fast breeder reactors constructed in the 1940s to 1960s utilized metallic fuels comprising of uranium (U) and plutonium (Pu) [2]. Even though U-Pu fuels possessed a high fissile density, they also possessed a low melting temperature, and consequently, it was imperative to alloy them with other materials so that they can be operable at higher temperatures in reactors. Chromium, molybdenum, titanium, and zirconium (Zr) were few of the candidate materials that were selected to be used as an alloying element to raise the liquidus temperature of metallic fuels used in reactors. From the four candidate materials, alloying with Zr proved to be more beneficial as a consequence of its inherent ability to form a Zr-rich barrier between the fuel and cladding interface [2–4]. The formation of a Zr-rich barrier was believed to impede interdiffusion and hence mitigate fuel cladding chemical interaction (FCCI) which is a major fuel performance inhibitor [3,5]. Evidence of a Zr-rich barrier potentially impeding the interdiffusion between fuel and cladding at the FCCI locality of a neutron irradiated U-10wt.%Zr/HT9 (fuel/cladding) was also observed in the scanning electron microscope-energy dispersive spectroscopy (SEM-EDS) maps produced by Harp et al. [6]. Additionally, several other studies have also reported on: (1) the effectiveness of a Zr-rich barrier impeding FCCI, and (2) various theories detailing the mechanisms that facilitate the formation of a Zr-rich barrier at the fuel-cladding interface [4,5,7–11]. In summary, the advantages of being operable at higher temperatures and forming a Zr-rich barrier to impede FCCI made U-10wt.%Zr fuels ideal candidate test fuels for reactor applications.

Neutron irradiation experiments on metallic fuels at the Experimental Breeder Reactor–II (EBR-II) began in early 1985 with three sets of polycrystalline U-xPu-10Zr (0<x<19) (wt%) fuels (i.e. U-10Zr, U-9Pu-10Zr, and U-19Pu-10Zr) [2]. The U-xPu-10Zr fuels were encased in austenitic D9 and ferritic-martensitic HT9 stainless steel claddings and were reported to have achieved an overall burnup of 18.4 at.% and 17.5 at.%, respectively [12]. Burnup is the measure of energy extracted from nuclear fuel and is dependent on the fraction of heavy metal atoms that has undergone fission. Hence, if a fuel achieves a burnup of 18.4 at.%, it is indicative that 18.4% of

the initial heavy metal atoms have undergone fission. Although fuel burnup can be expressed as Megawatt-day per metric ton and effective full power days, it will be expressed as burnup at.% throughout this dissertation. Furthermore, in this dissertation, the terms "in-pile" and "out-of-pile" experiments correspond to neutron irradiated (in-reactor) and un-irradiated (out-of-reactor) experiments, respectively.
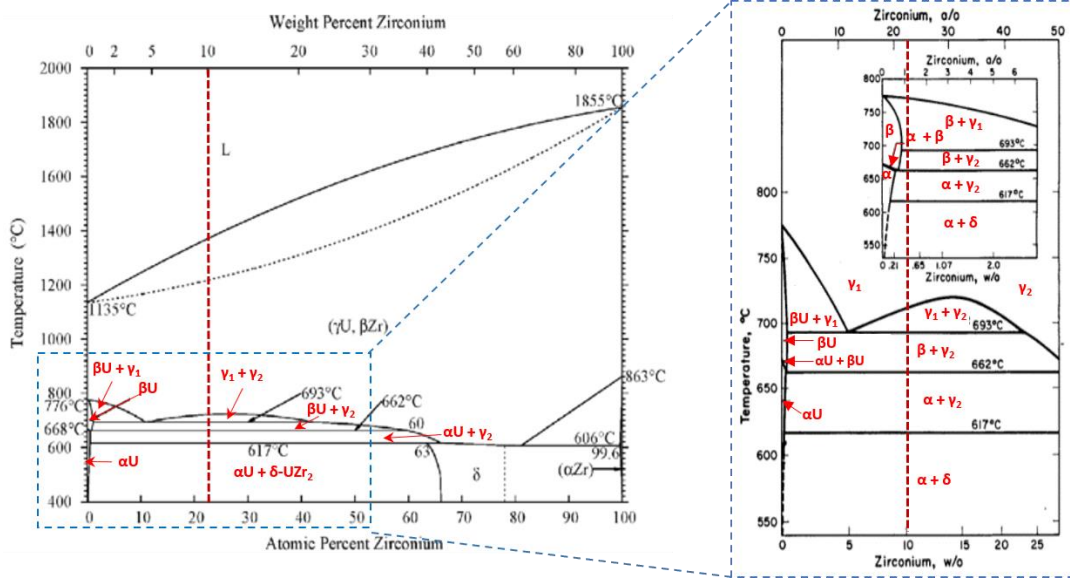
Figure 1.1: Binary phase diagram of the U-Zr alloy system constructed by Sheldon et al. [13] and modified by Hofman et al. [35]. Red dashed line indicates the U-10wt.%Zr composition.

Since the U-10wt.%Zr fuel cross-section assessed in this study was subjected to a temperature gradient when neutron irradiated in the reactor, it is imperative to identify the various phases that are stable at different temperature ranges. As presented in the U-Zr equilibrium phase diagram (constructed by Sheldon et al. [13]) in Fig. 1.1, a composition of U-10wt%Zr possesses γ_1 (U-rich)+γ_2 (Zr rich) phases stable within a temperature range of 737-692°C, β-U+γ_2 phases stable within 692-656°C, α-U+γ_2 phases stable between 656-617°C, and α-U+δ-UZr$_2$ phases stable between 617-435°C, respectively [13]. Even though the U-Zr phase diagram published by Sheldon et al. [13] is more widely used, a comparison with the U-Zr phase diagrams published by Rough and Bauer [14,15] revealed several inconsistencies. The major distinction between the two phase diagrams is the phase transformation path followed by the β-U phase. Sheldon et al. [13] reported a eutectoid decomposition of β-U $\rightarrow$ α-U+γ_2, while Rough and Bauer [14,15] reported a peritectoid formation of α-U from β-U and γ_2. Differential scanning calorimetry experiments by Rai et al. [16]

on out-of-pile U-10wt.%Zr alloys (homogenized at 1000ºC for 10 hours and furnace cooled) showed the phase transformations of α-U+α'+δ-UZr$_2$ → α-U+γ$_2$ → β-U+γ$_2$ → γ$_1$+γ$_2$ → γ when heated at 3 K/min from a baseline temperature of 200ºC. Whereas in-situ neutron diffraction assessment by Williams et al. [17] on out-of-pile U-10wt.%Zr that were annealed at 900˚C for 2 hours showed the phase transformations of γ → α-U+γ$_2$ → α-U+δ-UZr$_2$ (i.e. they did not observe the presence of a β-U+γ$_2$ dual phase region). More importantly, even though out-of-pile experiments on U-Zr alloys provides us an understanding on phase transformations and their effect on mechanical properties, they do not take into consideration the effects of several uncertainties [such as radiation damage, temperature gradient, burnup gradient, fuel constituent re-distribution, generation of fission product (FP), and fuel swelling] that emerge as a consequence of neutron irradiation. Table. 1.1 details the key phenomena that have been observed to occur during neutron irradiation of nuclear fuels, and their consequences to fuel performance [12].

Table 1.1: Key phenomena that control fuel performance. (Reported by Pahl et al. [12]).

Phenomena	Experimental Observations	Consequences
Fuel Swelling	Irradiation growth and grain boundary tearing; Xe/Kr bubble growth; fission product generation; fuel alloy type; and burnup at.% effects	Reactivity loss; gas release; fuel and cladding chemical interaction; fuel and cladding mechanical interaction; and thermal conductivity loss
Fuel Constituent Re-distribution	U and Zr interdiffusion	Lowered solidus temperature; complexities in properties modeling; and formation of intermetallic precipitates
Fuel and Cladding Chemical Interaction	Penetration of U or Pu into the cladding; migration of fission products (from the lanthanide series) from fuel to cladding; and loss of nickel in austenitic steel cladding	Thinning of cladding walls; formation of brittle fuel cladding chemical interaction layers; eutectic composition approach in fuel; and formation of low temperature melting phases
Cladding Deformation	Irradiation/thermal creep by fission gas pressure; fuel and cladding contact pressure (a consequence of radial and axial fuel swelling); and swelling in austenitic steel cladding	Stress and rupture lifetime of cladding determines ultimate burnup at.% achieved by fuel; high cladding strains can lead to elemental and stress interactions between fuel and cladding

The changes in microstructure, mechanical properties, and performances of neutron irradiated U-10wt.%Zr fuels are interdependent on various factors such as temperature gradient, burnup gradient, fuel constituent re-distribution, the formation of FP, swelling, and FCCI. Consequently, they follow a non-equilibrium phase transformation route, and this warrants a more comprehensive assessment of the phase transformations in neutron irradiated U-10wt.%Zr fuels.

Numerous neutron irradiation experiments at the EBR-I and EBR-II, and the Fast Flux Test Facility (FFTF) involved the utilization of U-10wt.%Zr metallic fuels that were clad to HT9 steels. Ferritic-martensitic (F/M) HT9 steels were used as an alternative to austenitic stainless steel for core material application due to their enhanced resistance to neutron irradiation-based swelling and creep, high thermal conductivity, low thermal expansion coefficient, and usability at high temperatures [18–24]. Despite the existing advantages, F/M steels with compositions >12wt.%Cr were reported to exhibit embrittlement when subjected to neutron irradiation at low temperatures [25,26]. Since F/M HT9 steels possess a body-centered cubic (BCC) structure, they exhibit a ductile to brittle transition fracture with decreasing temperature. Furthermore, it has been reported that the ductile to brittle transition temperature (DBTT) of F/M HT9 steels increases rapidly with neutron irradiation at temperatures below 0.3 times the melting temperature [27,28]. Phase instability in neutron irradiated F/M HT9 steels are known to influence the mechanical properties exhibited by the structural material. Several studies have reported on the formation of different kinds of second phase precipitates (such as α', G-phase, χ, $M_6C_{(n)}$, etc.) as a consequence of thermal and irradiation effects [29–33]. Although several studies have been performed on HT9 steels to determine the effects of irradiation (neutron, proton, and ion), they have been assessed from a structural material point of view. Consequently, this warrants a comprehensive assessment of neutron irradiated F/M HT9 steel claddings.

Currently available knowledge on microstructural alterations in neutron irradiated U-10wt.%Zr/HT9 (fuel/cladding) include the following: (1) fuel constituent re-distribution and FCCI (determined via SEM-EDS assessments), (2) assumption of phases at different regions of the fuel cross-section (determined via SEM micrographs, estimated fuel temperatures, and the equilibrium phase diagram), (3) macroscopic view of fuel cross-sections at different burnup at.% (produced via optical microscopy (OM) and SEM imaging), and (4) macroscopic fuel swelling estimates (determined via neutron radiography) [1,6,34,35]. In summary, the lack of detailed investigations

and proofs correlating various microstructural alterations and mechanical property changes in neutron irradiated U-10wt.%Zr/HT9 necessitates a more comprehensive study to be conducted.

With the advent of new specimen preparation tools for irradiated materials, as well as advances in characterization techniques, researchers can now obtain previously inaccessible microstructural insight into irradiated fuels [36]. This possibility naturally lends itself to improved fuel performance models for the nuclear community. Hence, the objective of the study presented in this dissertation is to provide the first detailed insight on the: (1) microstructural alterations in different regions of a neutron irradiated U-10wt.%Zr fuel at various length scales, and (2) variation in the nano mechanical properties at different regions of a neutron irradiated HT9 steel cladding.

1.2   Objectives

The primary objective of this research is to understand the microstructural alterations in different regions of a neutron irradiated U-10wt.%Zr fuel and HT9 cladding that has achieved a cross-sectional burnup of 5.7 at.%. Additionally, this study also aims to provide a relationship between the microstructural alterations and local mechanical property changes exhibited at different localities of the HT9 cladding as a consequence of neutron irradiation, FCCI, and FP migration.

To achieve this goal, a coordinated group of experiments was performed on the neutron irradiated U-10wt.%Zr/HT9 cross-section at a nanoscale, microscale, and mesoscale, respectively. In this study, the experimental techniques used for the microstructural analysis included the following: (1) transmission electron microscope (TEM) investigations of focused ion beam (FIB) lamellas for nanoscale assessments, (2) serial sectioning experiments of FIB cuboids for microscale assessments, and (3) synchrotron micro-computed tomography (μ-CT) experiments of FIB obelisks for mesoscale assessments. Furthermore, nano-indentation experiments were performed on the neutron irradiated HT9 cladding to determine the changes in mechanical properties as a function of distance from cladding edge to FCCI locality. The results produced from the various experiments were compared and correlated to existing literature, and new theories/hypotheses to explain the reasoning for the observed changes were established.

CHAPTER 2.   LITERATURE REVIEW

The broad range of fundamental knowledge and historical literature required to comprehend this study is presented in Section 2 of the dissertation. Firstly, a brief discussion on sodium cooled fast reactors and metallic fuels is presented in Section 2.1 and Section 2.2. Section 2.2 also details background on: (1) U-Pu-Zr fuels, (2) U-Zr fuels, and (3) historical literature of U-10wt.%Zr fuels that were neutron irradiated in the EBR-II and the FFTF reactor. Finally, Section 2.3 details a comprehensive assessment of various interdependent phenomena (such as fuel swelling, phase transformations, fuel constituent re-distribution, etc.) that occur in U-10wt.%Zr fuels exposed to neutron irradiation. Comprehending the effect of various interdependent phenomena in neutron irradiated U-10wt.%Zr fuels is crucial since they dictate how the fuel behaves and fails, and consequently, are the focal point of the research presented in this dissertation. To achieve a clear understanding of the various interdependent phenomena, in this study, a neutron irradiated U-10wt.%Zr fuel and HT9 cladding cross-section (irradiated at the FFTF reactor), was assessed at a nanoscale, microscale, and mesoscale, respectively. Furthermore, the research presented in this dissertation is the first comprehensive study that assesses: (1) various microstructural alterations in a neutron irradiated U-10wt.%Zr fuel at various size scales, and (2) nano mechanical properties in various regions of a neutron irradiated HT9 cladding.

2.1   Sodium Cooled Fast Reactor

Sodium cooled fast reactors (SFRs) were one of the advanced fast reactors concepts suggested by the Generation-IV International Forum [37]. The proposed aims of the forum were as follows: (1) have Generation-IV reactors developed for commercial deployment by 2030, and (2) achieve short term goals of having these reactors developed by the industry in 15 years (i.e. approximately by 2024) [37]. This initiative was further reinforced by the US-led proposal for a global nuclear energy partnership which aimed specifically on improving research required to deliver a sustainable fuel cycle [37].

SFRs typically use U-Zr based metallic fuels as the core fuel material and sodium as the reactor coolant. Sodium was selected as a reactor coolant as a consequence of several desirable material characteristics, such as neutron transparency, high thermal conductivity, high boiling

temperature, low melting temperature, and high compatibility with metals [38–40]. U-Zr based metallic fuels were selected as core fuel material as a consequence of high stability at elevated temperatures, good neutron economy, high thermal conductivity, and compatibility with sodium coolant [2]. Hence utilization of sodium coolant and metallic fuels in fast reactors facilitates reactor operations with fast neutron spectrums, ambient pressure, and high temperatures [38–40]. Furthermore, a typical SFR design possesses a three-loop system (i.e. primary and secondary sodium loops and a water/steam loop), which is essential for minimizing radioactive environmental contamination in case of an accident scenario. A comprehensive explanation of how the three-loop system minimized radioactive environmental contamination at the incident in MONJU SFR facility in Japan is detailed elsewhere [41,42]. Hence, the capability of providing a high energy yield output, operating safely at high temperatures, and reduced environmental contamination in the case of a potential accident scenario provided the necessary reasons to facilitate increased research on metallic fuels and Generation-IV SFRs.

2.2   Metallic Fuels

EBR-I was among one of the first reactors that used metallic fuels as core fuel material [43]. As specified in Section 1, metallic fuels were widely used in fast breeder reactors as a consequence of their enhanced breeding performance when compared to oxide and other types of ceramic fuels. Furthermore, metallic fuels are also known for possessing a high fissile density, high thermal conductivity, and a high burnup at.%. Additionally, metallic fuels were also suggested to undergo reprocessing when used in a closed fuel cycle [44–46]. In contrast, oxide fuels require chemical reduction before reprocessing. Since the study presented in this dissertation discusses the effects of neutron irradiation on a U-10wt.%Zr metallic fuel that was irradiated at the FFTF reactor, Section 2.2 is aimed at discussing the different types of U-Zr based metallic fuels, and early post irradiation examination (PIE) of U-10wt.%Zr metallic fuels which were neutron irradiated at the EBR-II and the FFTF reactor.

2.2.1   U-Pu-Zr Fuels

Ternary uranium-plutonium-zirconium (U-Pu-Zr) fuels were selected for use in EBR-II reactors as a consequence of their enhanced performance [47]. Since U-Pu fuels are not operable

at high temperatures, they were alloyed with Zr to raise the solidus temperature of the fuels to ensure its safe operation in reactors at high temperatures [35]. Like the U-Zr fuels (see Section 1), Zr addition to U-Pu fuels was preferred over Cr and Mo due to its superior compatibility with austenitic stainless-steel claddings.

U-Pu-Zr fuels were also reported to have formed Zr nitride and Zr oxide layers (a consequence of minor interstitial elements such as nitrogen and oxygen in the cladding) at the periphery of the fuel pin, and these layers are known for hindering the diffusion of major cladding elements such as iron and nickel into the fuel. More importantly, the Zr-rich layers at the periphery of the fuel pin assists in preventing the formation of low melting temperature U-Fe and U-Ni intermetallic phases that limits fuel performance [9,48–54]. Although alloying U-Pu fuels with Zr seemed beneficial, these fuels were still prone to anisotropic fuel swelling [55]. However, this issue was resolved by lowering the smear density of the fuel down to 75%. Smear density is the cross-sectional area fraction occupied by the as-fabricated fuel inside the as fabricated inner wall of the cladding. Lowering the smear density facilitated the fuel to accommodate nearly 30% of the volumetric fuel swelling [56–58]. To acclimate the changes made to the fuel design, the cladding dimension was changed accordingly (such as larger diameter and plenum to accommodate an increase in fission gas without a significant increase in internal pressure). The design modifications facilitated U-Pu-Zr fuels to achieve burnups of 18.4 at.% and 19.9 at.% when clad to D9 and HT9 claddings, respectively. Hence, U-Pu-Zr fuels were considered as promising metallic fuels for fast breeder reactor application.

2.2.2   U-Zr Fuels

Like the U-Pu-Zr fuels, U-Zr metallic fuels have been extensively used as driver fuels in the EBR-II and the FFTF reactor. Depending on the reactor type, fuel dimensions, cladding material, and irradiation conditions, U-10wt.%Zr fuels were reported to have achieved a maximum burnup of 20 at.% [59]. Furthermore, U-Zr fuels are considered as excellent representatives for U-Pu-Zr fuel (especially for low Pu content fuels), and consequently, the binary U-Zr phase diagram has often been referred for phase analysis of U-Pu-Zr fuels. Hence, it is extremely important to understand the various phase transformations that occur in out-of-pile and in-pile U-Zr fuels so that the information attained can be used to construct ternary U-Pu-Zr phase diagrams.

Furthermore, like U-Pu-Zr fuels, U-Zr fuels also show the presence of Zr-rich barriers at the fuel and cladding interfaces, and consequently, these barriers mitigate the progression of FCCI [2–4].

Several out-of-pile experiments have been performed on U-Zr alloys to identify phase transformations, thermal properties, mechanical properties, and FCCI [4,5,7–9,11,16,17]. The purpose of conducting the various out-of-pile experiments was for comparing/correlating the microstructural alterations observed in out-of-pile U-Zr fuels to those of in-pile U-Zr fuels. However, the method of comparing/correlating the microstructural alterations observed in out-of-pile and in-pile experiments should be approached with caution since out-of-pile experiments do not exhibit the effects of neutron irradiation, and hence cannot provide a one to one comparison/correlation with in-pile experiments. Currently, most of the existing microstructural investigation on in-pile U-Zr fuels include SEM, OM, SEM-EDS, and neutron radiography [1,6,12,35]. Consequently, Section 2.2.3 and Section 2.2.4 of this dissertation provide a comprehensive description of the available PIE information of U-10wt.%Zr fuels that were neutron irradiated in the EBR-II and the FFTF reactor. Based on the PIE of U-10wt.%Zr fuels that were neutron irradiated at the EBR-II and the FFTF reactor, several assumptions (such as major phases that exist at different regions, FCCI layers, fuel swelling threshold of 30-32%, pore morphologies, etc.) were proposed; and were used to make several theories over the past five decades. Even though the proposed assumptions and theories facilitated the development of several fuel models, there exists a lack of detailed experimental proof to validate the proposed theories. Hence, the research presented in this dissertation provides a comprehensive assessment of several interdependent phenomena (see Section 2.3) that occur as a consequence of neutron irradiation in a U-10wt.%Zr fuel that was irradiated at the FFTF reactor at a nanoscale, microscale, and mesoscale. Consequently, the findings from this research will assist in developing new theories, and these theories will be compared to what was historically assumed.

2.2.3   Post Irradiation Examination of X447 Series U-10wt.%Zr Fuels

The X447 series U-10wt.%Zr fuels were clad with HT9 stainless steel and were irradiated at the EBR-II to assess FCCI and the stress rupture properties of the cladding. The assembly containing the X447 series U-10wt.%Zr fuels were removed from the reactor after achieving a burnup of 4.87 at.%. From the assembly, a few of the U-10wt.%Zr fuel pins were removed for analysis, and the remaining were retitled as the X447A series and re-inserted into the reactor for

further irradiation [1]. Post re-insertion, the X447A series irradiation experiments achieved a burnup of 10 at.% [1]. Since the purpose of the neutron irradiation experiments at the EBR-II was to assess FCCI and the stress rupture properties of the cladding, the X447 series U-10wt.%Zr fuels were designed to operate at high temperatures ranging between 630˚C-660˚C [1]. Furthermore, the neutron irradiated X447 series U-10wt.%Zr fuels showed fuel failure at a burnup of 10 at.% [1]. Fuel failure was detected via identification of Xe gas in the plenum [1].

From the X447 series U-10wt.%Zr fuels that achieved a burnup of 4.87 at.%, four fuel pins (DP-03, -06, -69, and -81) were analyzed by Carmack [1]. The initial PIE performed on these fuel pins include neutron radiography, pin profilometry, and gamma scan analysis. From the four fuel pins, DP-69 and DP-81 fuel pins were subjected to radiography, profilometry, and gamma scanning experiments, while DP-03 and DP-06 fuel pins received only profilometry [1]. Furthermore, the DP-69 and DP-81 fuel pins were destructively examined to receive OM and electron probe microanalysis (EPMA). Carlson [60], performed the first known OM evaluation on the DP-69 irradiated fuel pin, and Carmack [1] reported the formation of three zoned regions comprising of various phases and chemical compositions. Carmack [1] also reported on the formation of FCCI layers at the periphery of the DP-69 fuel pin. Sanecki et al. [61] performed the first known EPMA experiments on the DP-81 fuel pin that achieved a burn up of 4.8 at.%, and Carmack [1] reported on the fuel constituent re-distribution and FCCI layers. Carmack [1] assessed the same fuel pin and reported on the formation of three distinct radial zones known as zone A, zone B, and zone C, respectively. His assessment indicated that zone A and zone B possessed ~26wt.%Zr, and <1wt.%Zr, respectively, while zone C possessed two types of low Zr wt.% phases and δ-UZr$_2$. Additionally, Carmack [1] also reported that the lanthanides present in the fuel penetrated the cladding as a consequence of FCCI.

From the X447A series U-10wt.%Zr fuels that achieved a burnup of 10 at.%, four fuel pins (DP-04, -11, -70, and -75) were analyzed by Carmack [1]. Even though initial inspection of the fuel pins revealed that DP-70 and DP-75 were breached, the DP-04 and DP-11 remained intact despite being subjected to the same burnup at.%. A more comprehensive PIE revealed that both DP-04 and DP-11 fuel pins showed the presence of lanthanide phases, FCCI layers at the fuel edge, and thinning of the cladding. EPMA examinations of the DP-11 fuel pins also revealed that certain fuel cladding contact regions possessed minimal FCCI, while others possessed severe FCCI. Furthermore, Carmack [1] also identified the presence of three distinct zones (zone A:~14-

34wt.%Zr, zone B:~0-3wt.%Zr, and zone C:~9wt.%Zr) in the DP-11 fuel pin. He concluded that the large variations in the chemical compositions at different zones of the fuel cross-section are a consequence of various microstructural alterations and porosity [1]. More importantly, Carmack [1] also reported the following: (1) a large quantity of Zr-rich phases, (2) interdiffusion of Cr in comparison to Fe at the FCCI is negligible, (3) several types of FP precipitates (such as Ce, Pr, Nd, and Pd based precipitates), and (4) buildup and reaction of Nd, Pr, Ce, and La elements at the fuel-cladding interface.

2.2.4 Post Irradiation Examination of MFF Series U-10wt.%Zr Fuels

The Mechanistic Fuel Failure (MFF) series of metallic fuels was established as a comparison between the data generated from the EBR-II experiments, and that expected in a larger scale fast reactor [62]. The MFF series fuels that were irradiated in the FFTF reactor were reported to have peak burnup at.% near the centerline of the core and peak fuel temperature at the top of the fuel column [1]. Furthermore, from the MFF series, the MFF-3 and MFF-5 series U-10wt.%Zr fuel pins operated to a peak burnup of 13.8 at.% and 10.1 at.%, respectively. The MFF-3 and MFF-5 series also achieved a peak inner cladding temperature of 643˚C and 651˚C, respectively. Carmack [1] suggested that the data obtained from the MFF series fuel pins can be compared with data obtained from the X447 series fuel pins as a consequence of the X447 fuel pins experiencing a burnup of 10 at.% with peak cladding temperatures of 648˚C and 638˚C. The PIE of the MFF-3 and MFF-5 series U-10wt.%Zr fuel pins included neutron radiography, profilometry, gamma scans, metallography, micro-hardness measurements, and isotopic chemical analyses [1]. Carmack [1] provided a detailed correlative metallographic assessment at various axial locations of the fuel pins from the MFF series experiments. Akin to the assessments reported by Hofman et al. [35] and Rest [63], the metallographic assessments reported by Carmack [1] revealed the presence of distinct phase regions at different fuel cross-sections. A more detailed assessment of the various microstructural alterations on the MFF-3 series U-10wt.%Zr fuel cross-section that achieved a burnup of 5.7 at.% was performed by Harp et al. [6] via SEM-EDS. Harp et al. [6] reported the following: (1) presence of three distinct phase regions which were classified on basis of average chemical compositions, and (2) FCCI at select fuel and cladding interfaces.

The study presented in this dissertation assesses the same fuel cross-section assessed by Harp et al. [6], and consequently, provides a more comprehensive assessment on the various

microstructural alterations observed on the MFF-3 series U-10wt.%Zr fuel cross-section that achieved a burnup of 5.7 at.% at a nanoscale, microscale, and mesoscale. Furthermore, the main aim of the study presented in this dissertation is to determine the effects of several interdependent phenomena that occur in U-10wt.%Zr fuels.

2.3   Neutron Irradiation Based Interdependent Phenomena

Several interdependent phenomena (such as fuel constituent re-distribution, phase transformations, fuel swelling, and FCCI) occur as a consequence of neutron irradiation, and these phenomena have an adverse effect on the fuel performance. Section 2.3 of the dissertation serves as a platform to discuss the effects of fuel constituent re-distribution, phase transformations, fuel swelling, and FCCI in a binary U-Zr fuel system. Furthermore, the study presented in this dissertation seeks to analyze each of the above mentioned interdependent phenomena in a neutron irradiated U-10wt.%Zr fuel that achieved a cross-sectional burnup of 5.7 at.%.

2.3.1   Fuel Constituent Re-distribution in U-Zr Fuels

Fuel constituent re-distribution is defined as the de-mixing and diffusion of primary fuel constituents (i.e. U and Zr in U-Zr fuels) and occurs as a consequence of neutron irradiation [64,65]. Fuel constituent re-distribution occurs along the temperature gradient in the fuel system and may affect fuel performance by facilitating the segregation of fuel constituents into localized regions with unique chemical compositions [64,65]. For instance, fuel constituent re-distribution in a neutron irradiated U-10wt.%Zr fuel facilitated the segregation of primary fuel constituents into localized regions consisting of nearly pure U and U~30-40wt.%Zr, respectively [6]. Furthermore, the segregation of fuel constituents into localized regions affects the local power and material properties which are critical for reactor safety.

Some of the first PIE on fuel constituent re-distribution was performed by Murphy et al. [66] who assessed U-Pu-Zr fuels that achieved a burnup of 4.5 at.%. Murphy et al. [66] reported the following: (1) formation of three distinct regions (i.e. central region, inner region, and periphery region) with varying Zr concentrations, and (2) the Pu concentration remained consistent throughout the entirety of the neutron irradiated fuel [66]. Their study also revealed that the central, inner, and periphery regions of the neutron irradiated U-Pu-Zr fuel had a depletion of Zr, an

increase in Zr, and Zr enrichment, respectively [66]. Early works by Hofman et al. [35,65], suggested that fuel constituent re-distribution in U-Zr fuels was complete at ~5 at.% burnup. Hofman et al. [35,65] also reported that neutron irradiated U-10wt.%Zr fuels that achieved a cross-sectional burnup of 0.9 and 6 at.%, possessed two and three distinct regions, respectively. Yacout et al. [34] examined a U-10wt.%Zr fuel that achieved a burnup of 5 at.% and reported on the formation of three distinct regions. Harp et al. [6] performed a detailed fuel constituent re-distribution assessment on the MFF-3 series U-10wt.%Zr fuel that was clad to an HT9 F/M steel, and neutron irradiated at the FFTF reactor to a peak burnup of 13.8 at.%. The PIE of the fuel cross-section that achieved a burnup of 5.7 at.% revealed the presence of three concentric regions with distinct chemical compositions [6]. Harp et al. [6] reported that the Zr migration from the intermediate region to the fuel center facilitated the formation of the three concentric regions in the fuel (i.e. central zone or region A, intermediate zone or region B, and periphery zone or region C, respectively) [6]. Regions A, B, and C from their study were determined to possess an average chemical composition of U~30-35wt.%Zr, U~4wt.% Zr, and U~10wt.% Zr, respectively [6].

In summary, the variations in the average chemical compositions at different regions of a neutron irradiated metallic fuel provide evidence of fuel constituent re-distribution, and consequently, suggest the potential evolution of different phases within the concentric regions. Hence, the current study is aimed at providing an understanding of the variation in local chemical composition in different regions of the U-10wt.%Zr fuel cross-section that achieved a burnup of 5.7 at.%. Furthermore, knowledge and understanding of the variation in local chemical composition at different regions of the neutron irradiated U-10wt%Zr fuel will assist in determining the phases that have evolved due to fuel constituent re-distribution.

2.3.2 Phase Transformations in U-Zr Fuels

Phase transformations and fuel constituent re-distribution are interdependent phenomena that occur as a consequence of neutron irradiation. Fuel constituent re-distribution facilitates the formation of distinct regions with unique chemical compositions, and consequently, each distinct region possesses unique phase transformations [2,34,35,65]. Hofman et al. [35,65] postulated that neutron irradiated U-10wt.%Zr fuels that achieved a cross-sectional burnup of 6 at.% (with a fuel centerline temperature above 662˚C) possessed a central, an intermediate, and a periphery region with $\gamma+\beta$-U, α-U+γ_2, and α-U+δ-UZr$_2$ phases, respectively, while U-10wt.%Zr fuels that achieved

a burnup of 0.8 at.% (with a fuel centerline temperature below 662˚C) possessed two concentric regions (i.e. α-U+δ-UZr$_2$ at the fuel exterior and α-U+γ$_2$ at the fuel center). The postulations reported by Hofman et al. [35,65] were based on the evaluation of multiple SEM micrographs from EBR-II irradiated U-10wt.%Zr fuels that merely took into account the estimated irradiation temperatures at beginning of life and phases from the equilibrium U-Zr phase diagram. Yacout et al. [34] examined a U-10wt.%Zr fuel that achieved a burnup of 5 at.% and postulated that γ$_2$ was present at the central region (with a fuel temperature ~693-699˚C), γ$_2$+β-U was present at the intermediate region (with a fuel temperature ~663-693˚C), and γ$_2$+α-U was present at the fuel periphery region (with a fuel temperature ~636-663˚C), respectively [34]. The postulations reported by Yacout et al. [34] were based on the following: (1) micro-chemical assessment of fuel constituent re-distribution via EPMA, (2) estimation of fuel irradiation temperature at different regions of the fuel, and (3) correlation of the estimated fuel irradiation temperatures to the equilibrium U-Zr phase diagram [34]. Furthermore, several studies have attributed fuel swelling, pore morphology, and temperature gradient experienced at different regions of a neutron irradiated U-Zr fuel to be dependent on the crystal structure of phases present at the locality [35,63,67,68]. For instance: (1) the presence of α-U, γ, and δ-UZr$_2$ have been suggested to facilitate the formation of irregular/aspherical pores, globular pores, and small pores, respectively [35,63,67], and (2) finite element analysis simulations by Yun et al. [68] revealed the influence of porosity distribution and phases on the temperature gradient along the fuel surface. Table. 2.1 details the crystal structure and lattice parameter of various phases determined in the binary U-Zr system [69–72].

Table 2.1: Crystal structure and lattice parameters of phases in the U-Zr system [69–72]

Phase	Crystal Structure	Lattice Parameters		
		a [Å]	b [Å]	c [Å]
α-U [72]	Orthorhombic [Cmcm]	2.91	5.84	5.04
δ-UZr$_2$ [70,71]	Hexagonal [P6/mmm]	5.05	a=b	3.09
β-U [72]	Tetragonal [P42/mnm]	10.78	a=b	5.66
γ [69]	Body Centered Cubic [Im-3m]	3.55	a=b	a=c

*The lattice parameters detailed in Table 2.1 are not absolute values. They are approximated values, and the alloy systems from which they were determined were not subjected to irradiation experiments.

In summary, the lack of crystallographic assessments on phase transformations in a neutron irradiated U-10wt.%Zr fuel warrants a comprehensive study to be conducted, and consequently, one of the main goals of this study is to determine the various major phases present in different regions of the neutron irradiated U-10wt.%Zr fuel cross-section that achieved a burnup of 5.7 at.%.

2.3.3 Swelling in U-Zr Fuels

Fuel swelling is a consequence of the generation and accumulation of gaseous and solid FP in nuclear fuels. At low burnups (<1 at.%), fuel swelling proceeds rapidly and results in the direct contact between the fuel and cladding [2]. After contact continued fuel swelling leads to reduced thermal conductivity, increased stresses in cladding, and eventual cladding failure [12,73]. Hence, fuel swelling was determined to be detrimental to fuel performance.

Metallic fuels, such as U-Zr and U-Pu-Zr alloys, are known to swell as a consequence of FP generation (including both gaseous and solid products) and cavitation from the anisotropic growth of the α-U phase [2,12,67,74,75]. Hofman et al. [2], Ogata et al. [76], and Pahl et al. [75] reported that solid FP contributed to a linear increase in the fuel swelling of 1.2%, 1.5%, and 1.6% per at.% burnup, respectively. Ogata et al. [76] and Karahan et al. [77] also reported that fuel swelling from fission gases was dependent on gas bubbles and open pores, and open pores in a neutron irradiated fuel system are interconnected and act as a release conduit for the fission gases to escape to the plenum. Neutron irradiated metallic fuels also possess certain gas bubbles that retain insoluble fission gases such as krypton and xenon [78]. Furthermore, the fuel swelling contributions from the gas bubbles and open pores change as a non-linear function with respect to the burnup [76,77]. Currently-used metallic fuel swelling models assume that at ~30-36.5% fuel swelling, a bubble interconnection threshold is reached, beyond which further gaseous swelling is eliminated as a consequence of release of fission gas from the interconnected bubble into the plenum [79]. Furthermore, a recent study by Thomas et al. [36], revealed the effect of pores with varying morphology and sizes on the localized fuel swelling of a neutron irradiated U-10wt.%Zr fuel.

PIE of U-10wt.%Zr fuels irradiated in the EBR-II to burnups of 0.8 at.% and 3 at.% showed the presence of irregularly shaped pores, spherical pores, and interconnected globular pores, respectively [35]. The irregularly shaped pores were postulated to be a consequence of grain boundary tearing and anisotropic growth of the α-U phase, the smaller pores were believed to be

associated with either the δ-UZr$_2$ phase or the γ_2 phase, and the interconnected globular pores were associated to the γ phase [35]. Hofman et al. [35] postulated that the swelling at the fuel center where the temperature was the highest was characterized by isotropic growth of large fission gas bubbles due to the presence of a BCC structured γ phase; while, at lower irradiation temperatures near the fuel periphery where α-U and δ-UZr$_2$ were the probable phases, the swelling was characterized by grain boundary tearing due to anisotropic swelling. PIE of a U-10wt.%Zr fuel irradiated in the FFTF reactor to a burnup of 5.7 at.% showed the presence of three concentric regions with each region possessing different phases and pore morphologies (i.e. region A possessed spherical pores, while region B possessed a large number of aspherical pores) [6].

In summary, fuel swelling significantly affects the fuel performance and is dependent on several factors (such as FP generation, temperature gradient, fuel constituent re-distribution, the crystal structure of phases at the locality, etc.). Hence, a comprehensive understanding of fuel swelling, as a consequence of pore volume and pore distribution at different regions of the neutron irradiated fuel is essential for enhancing the currently used fuel swelling models. One of the goals of the study presented in this dissertation is to determine the variation in pore distribution, pore volume, and localized swelling in different regions of a neutron irradiated U-10wt.%Zr fuel cross-section that achieved a burnup of 5.7 at.%.

2.3.4   Fuel Cladding Chemical Interaction in U-Zr Fuels

FCCI is one of the major problems faced when using metallic fuels that are cladded to F/M HT9 steels in liquid cooled fast reactors [5,80]. During neutron irradiation, the fuel experiences a temperature and burnup gradient along with the formation of FP that causes the fuel to swell and come in direct contact with the cladding. Upon contact, varying diffusion rates between the irradiated fuel and cladding elements lead to the formation of multiple FCCI layers which inherently affects the integrity of the cladding [4,7]. FCCI layers are also known for thinning the cladding material, forming cracks within the fuel and cladding, and creating low melting eutectic phases leading to localized melted regions within the fuel [5].

Historically, several out-of-pile experiments were performed to understand the diffusion kinetics for the formation of various FCCI layers between fuel and cladding [4,7,81–83]. Although the out-of-pile experiments provided valuable insight on the effect of temperature on FCCI, they do not take into consideration the effects of several other uncertainties (such as radiation damage,

temperature gradient, FP migration, fuel swelling, and irradiation based stresses in cladding and fuel) that emerge as a consequence of neutron irradiation. Fission products are usually observed in large quantities at the fuel edge as a consequence of slow solid-state diffusion between the fuel and cladding [5,84]. It has been proposed that FPs in the fuel migrate to the fuel edge via a liquid-like diffusion [5,84]. Matthews et al. [5] reported on the potential capability of bubbles and pores in neutron irradiated fuels being filled with a mixture of noble fission gases and liquid cesium, while Mariani et al. [84] reported that FPs in the fuel migrated to the fuel edge via a liquid-like diffusion through the pores and bubbles that formed during neutron irradiation. In addition to liquid-like diffusion through pores and bubbles, it has been reported that the temperature gradient present in nuclear fuels also provides a driving force for FP migration to the fuel edge. In conclusion, several studies have attempted to prove that liquid-like diffusion was responsible for FP migration in fuels; however, the true mechanism is yet to be determined (both experimentally and computationally) [5,84–86].

Several studies have reported the presence of a Zr-rich barrier at the fuel edge impeding FCCI [4,5,7]. Since ZrO_2 mold powder was used on quartz to protect the mold during injection casting of metallic fuels, the formation of a Zr-rich barrier at the fuel edge was initially assumed to be a byproduct from fuel fabrication [8]. Even though ZrO_2 mold powder residues may assist in the formation of a Zr-rich barrier at the fuel edge, the assumption came under scrutiny when out-of-pile diffusion couple experiments on sectioned regions of the injection cast fuels that were not in contact with the mold also showed the formation of a Zr-rich barrier [5]. Keiser et al. [4] performed out-of-pile diffusion couple experiments on U-10wt.%Zr/HT9 and suggested that the Cr in the HT9 steel may have affected the activity of Zr in the δ-UZr_2 precipitates, and consequently, facilitated the dissolution of the δ-UZr_2 precipitates into U-rich and Zr-rich regions. Even though Cr may affect the activity of Zr, out-of-pile diffusion couple experiments by Keiser et al. [4,7] on U-10wt.%Zr/Fe (a system that has 0wt.% Cr) also showed the formation of a Zr-rich barrier at the fuel/cladding interface. Hence, it can be inferred that Cr need not be the main contributor that facilitates the formation of a Zr-rich barrier. Hofman et al. [9] suggested that the dissolution of δ-UZr_2 in injection cast U-10Zr fuels into U-rich and Zr-rich layers may arise as a reaction to nitrogen impurities present during fabrication, and corroborations to the suggestion that were provided by Akabori et al [11,87]. Akabori et al. [11,87] reported that the dissolution of δ-UZr_2 into U-rich and Zr-rich layers occur when the metallic alloys were exposed to 0.19kPa and

20kPa of nitrogen at elevated temperatures. Lee et al. [3] performed numerous out-of-pile diffusion couple experiments between U-10wt.%Zr/HT9 to assess the various stages of FCCI. They hypothesized that dissolution of δ-UZr$_2$ into U-rich and Zr-rich layers occur at the interface of the U-10wt.%Zr/HT-9 diffusion couple, and was followed by: (1) the diffusion of U at the interface to form a (U, Zr) (Fe, Cr)$_2$ phase, and (2) the supersaturation of a Zr-rich barrier [3]. Their study also revealed the eventual cracking of the Zr-rich barrier occurs as a consequence of increased annealing time, thermal stresses, and an increase in driving forces between the diffusion couple constituents [3]. The SEM-EDS maps produced by Harp et al. [6] at the FCCI locality of a neutron irradiated U-10wt.%Zr fuel that achieved a cross-sectional burnup of 5.7 at.% revealed the following: (1) Depletion of Fe along the grain boundaries of the cladding and interdiffusion of Fe into the fuel. (2) Presence of a Zr-rich layer acting as a barrier and impeding the interdiffusion of U into the cladding. (3) Presence of Ce-Nd solid FP precipitates, mixing of Ce-Nd with the Zr-rich barrier at the FCCI locality, and migration of FPs along the grain boundaries of the cladding. (4) A Ce-Nd-Fe FCCI layer between the fuel and cladding sides. From their SEM-EDS maps, it is evident that even though the Zr-rich barrier may have assisted in preventing the initial gross interdiffusion between fuel and cladding, formation of cracks on the Zr-rich barrier (a consequence of fuel swelling and irradiation stresses) led to accelerated FCCI and formation of multiple binary/ternary phases [6].

In summary, even though several mechanisms on: (1) diffusion of FPs from fuel to cladding and (2) formation of a Zr-rich barrier between fuel and cladding interface have been proposed, confirmed mechanisms are yet to be established. Furthermore, the formation of Zr-rich barriers, FCCI layers, and FP migration along the grain boundaries of the neutron irradiated cladding significantly alters the local mechanical properties exhibited by the cladding material, and consequently, it is imperative to understand how these alterations affect the cladding integrity. Hence, some of the goals presented in this dissertation are to: (1) identifying the microstructural alterations at the FCCI locality of a neutron irradiated U-10wt.%Zr fuel and HT9 cladding, and (2) establish a relationship between the alterations in microstructure and their mechanical properties at different localities of a neutron irradiated HT9 cladding (i.e. from HT9 edge locality to HT9+fission products locality to FCCI locality). Consequently, the data produced from this study can be used to enhance the currently used fuel cladding mechanical interaction models.

CHAPTER 3.   MATERIALS AND METHODS

3.1   Specimen History

The MFF series metallic fuels were irradiated in the FFTF reactor in Hanford, Washington to provide a potential comparison to the metallic fuels irradiated in the EBR-II and that of a larger scale fast reactor [1]. The FFTF reactor core housed fuels in fuel columns that were 91.4 cm tall and had a chopped cosine neutron flux profile [1]. Consequently, the peak cladding temperature was at the top of the fuel column, and peak burnup was at the core centerline [1]. The MFF-3 series U-10wt.%Zr metallic fuel assessed in this study composed of a U-10wt.%Zr fuel sodium bonded to an F/M HT9 steel cladding and was enriched to ~32.4 wt.% U^{235} [1]. Furthermore, the MFF-3 series metallic fuel has undergone neutron irradiation for 726.2 effective full power days in the FFTF reactor and achieved a peak burnup of 13.8 at.% and inner cladding temperature 643˚C [62,88]. Table 3.1 details the nominal design features of the MFF-3 series fuel pin assembly. Further specifications on the irradiation conditions, fuel cell assembly, and removal of the irradiated alloy from the reactor are provided in detail by Carmack et al. [88].

Table 3.1: Nominal design features of the MFF-3 series fuel pin assembly irradiated at the FFTF reactor (Reported by Carmack [1])

Fuel alloy composition	U-10wt.%Zr
Fuel slug diameter	4.98 mm
Fuel slug length	91.44 cm
Fuel plenum volume	28.9 cm^3 at 25˚C
Cladding material	HT9
Cladding outer diameter	6.86 mm
Cladding wall thickness	0.56 mm
Fuel pin length	238.1 cm
Maximum pin linear power	613 W/cm
Maximum cladding temperature	640 – 650 ˚C
Maximum fuel temperature	860˚C

In this study, a cross-section from an MFF-3 fuel pin that was neutron irradiated at the FFTF reactor was extracted from an axial fuel column length of z/L = 0.98 and was subjected to several experiments for subsequent nanoscale, microscale, and mesoscale assessments. Furthermore, the fuel cross-section analyzed in this study is the same cross-section examined by Carmack et al. [88] and Harp et al. [6]. Fig. 3.1 shows the secondary electron SEM image of the cross-section of the MFF-3 series U-10wt.%Zr fuel pin used for this study. The fuel cross-section presented in Fig. 3.1 was reported to have achieved a burnup of 5.7 at.% and a fission density of 2.01 x 10^{21} fissions/cm^3 [1,6]. The superimposed fuel heat map shown in Fig. 3.1 reveals a drop in temperature from fuel centerline to fuel surface. The heat map was estimated by inputting the fuel centerline temperature and fuel surface temperature reported by Carmack et al. [1,88] into Eq. (3.1).

$$\frac{T_r - T_s}{T_0 - T_s} = 1 - \left(\frac{r^2}{R_f^2}\right) \tag{3.1}$$

In Eq. (3.1), T_r is the temperature at a radial position measured from the center of the fuel pin , T_s is the fuel surface temperature, T_0 is the fuel centerline temperature, r is the radial position within the fuel, and R_f is the fuel radius. As shown in Fig. 3.1, the temperature gradient for region-A, -B, and -C ranges between ~682-671˚C, ~671-655˚C, and ~655-623˚C, respectively.

Fig. 3.1 also serves as a data map revealing locations from where specimens of various sizes were lifted out for nanoscale, microscale, and mesoscale assessments (i.e. for TEM assessment of FIB lamellas 1-9, serial sectioning of FIB cuboids 10-13, and synchrotron µ-CT of FIB obelisks 14-16, respectively). The presence of three concentric phase regions formed after neutron irradiation provides evidence of fuel constituent re-distribution in U-10wt.%Zr fuels, and the classification of the U-10wt.%Zr fuel cross-section into regions A, B, and C in this study was based on the fuel constituent re-distribution of the same fuel cross-section assessed by Harp et al. [6]. Harp et al. [6] reported that regions A, B, and C possessed an average chemical composition of U~30-35wt.%Zr, U~4wt.%Zr, and U~10wt.%Zr, respectively. Additionally, the variations in the average chemical compositions in regions A, B, and C also suggested the potential evolution of different phases at the three concentric phase regions.
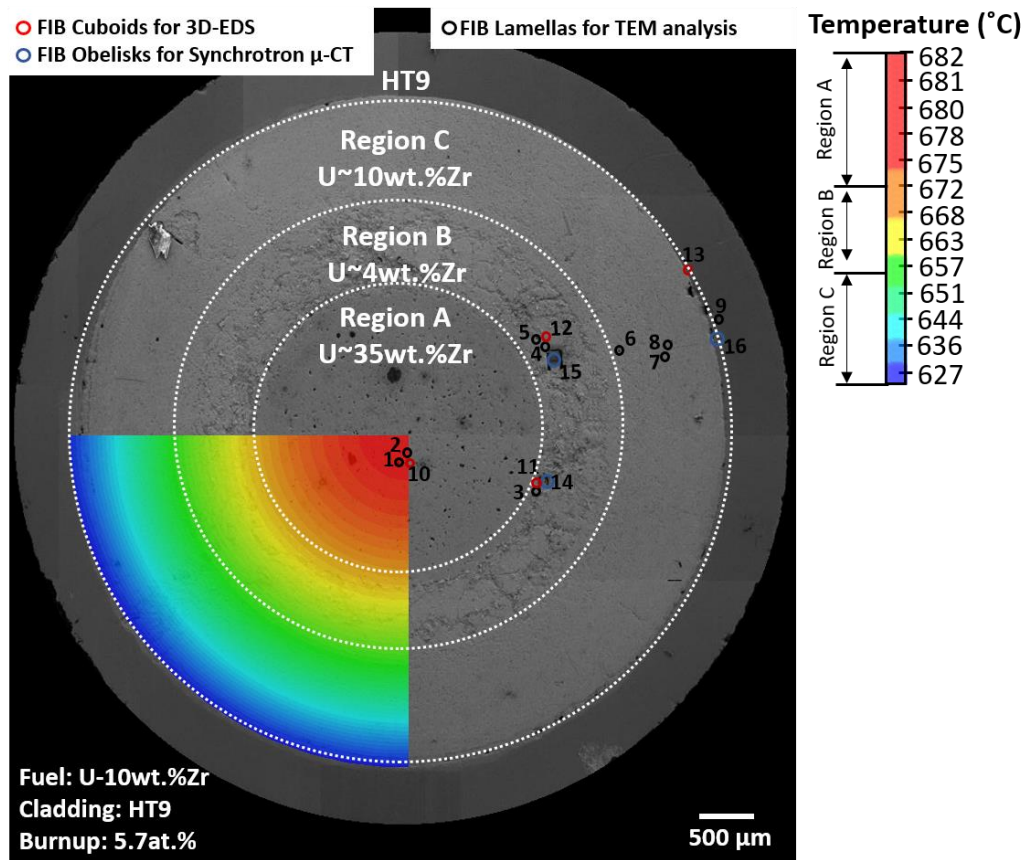
Figure 3.1: SE micrograph of cross-section of U-10wt.%Zr/HT9 specimen irradiated to a burnup of 5.7 at.% at a column height of z/L=0.98. Circular markings labeled 1-9, 10-13, and 14-16 indicate localities from where the FIB lift-outs were produced for TEM investigations, serial sectioning experiments, and synchrotron µ-CT experiments, respectively. The heat map overlaid on the SE micrograph reveals the estimated temperature gradient from the fuel centerline (682˚C) to the inner fuel surface (623˚C). The localities labeled as Region-A, -B, and -C was based on the classification of the same fuel cross-section assessed by Harp et al. [6]. Harp et al. [6] reported the regions to possess an average chemical composition of U~35wt.%Zr, U~4wt.%Zr, and U~10wt.%Zr, respectively [6].

The neutron irradiated U-10wt.%Zr/HT9 cross-section presented in Fig. 3.1 was re-polished at the Hot Fuel Examination Facility (HFEF) to remove oxide layers that had built up on the surface due to specimen storage. Post initial re-polishing at the HFEF, the neutron irradiated U-10wt.%Zr/HT9 specimen was transferred to the Electron Microscopy Laboratory glovebox for additional hand polishing with a 1µm diamond suspension to achieve a fine surface polish [6]. The neutron irradiated U-10wt.%Zr/HT9 specimen was then decontaminated and coated with a thin layer of Au for conductivity during SEM investigations and production of FIB lamellas for TEM investigations. The Au coating was then removed via polishing prior to the lift-out of FIB cuboid

and FIB obelisk specimens for serial sectioning and synchrotron μ-CT experiments. Post SEM investigations and production of FIB lift-outs (i.e. FIB lamellas, FIB cuboids, and FIB obelisks), the neutron irradiated U-10wt.%Zr/HT9 cross-section was re-polished to ensure that a smooth surface finish was obtained for performing nano-indentation experiments.

3.2   Electron Microscopy

Various electron microscopes available at the Irradiated Materials Characterization Laboratory (IMCL) at Idaho National Laboratory (INL), were used for the preparation of FIB-lamella, -cuboid, and -obelisk lift-outs for TEM investigations, serial sectioning experiments, and synchrotron μ-CT experiments, respectively.

3.2.1   Scanning Electron Microscopy

Scanning electron microscopy (SEM) is a technique that has been used extensively to characterize the microstructure of various materials. In this study, a Shielded FEI QUANTA 3D FEG and a Shielded FEI Helios dual-beam SEM-plasma FIB available at the IMCL at INL was used to produce secondary electron (SE) micrographs, back scatter electron (BSE) micrographs, and FIB lift-outs (i.e. FIB lamellas, FIB cuboids, and FIB obelisks). The FIB-SEMs available at the IMCL at INL were specifically designed to be capable of handling irradiated materials, and for safety reasons, the FIB-SEM chambers were coupled to glove boxes that consisted of two loading/unloading ports. One of the ports in the glove boxes was coupled to the FIB-SEM chambers, while the other was used for loading/unloading specimens into the glove boxes. This was done to provide personnel safety and prevent any radioactive contamination because of specimen transfer. The glove boxes were also fitted with robotic manipulators to ensure minimal contact between the personnel and irradiated specimen that is to be analyzed. Additionally, the entire set-up was enclosed with a 21 cm thick shield steel wall. Fig. 3.2 presents a schematic and actual image of the FIB-SEMs instrumentation set-up at the IMCL at INL.

In summary, a total of 9 FIB lamellas (see markers labeled 1—9 in Fig. 3.1), 4 FIB cuboids (see markers labeled 10—13 in Fig. 3.1), and 3 FIB obelisks (see markers labeled 14—16 in Fig. 3.1) were produced from the neutron irradiated U-10wt.%Zr fuel and HT9 cladding via utilization of the FIB-SEMs available at the IMCL at INL.
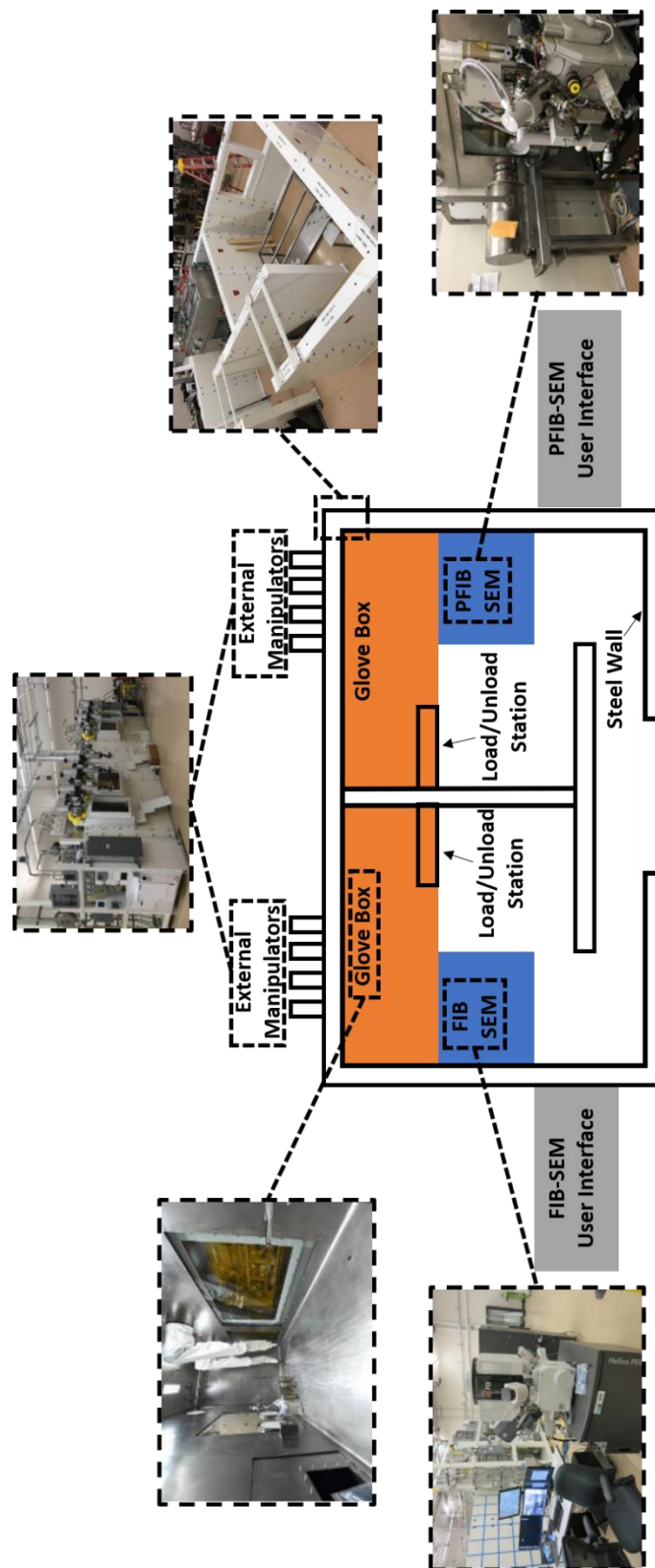
Figure 3.2: Schematic representation of the FIB-SEM set-up at the IMCL at INL. The outset images (courtesy of INL) in dashed black boxes show actual experimental set-up of several pieces of FIB-SEM equipment, glove boxes, robotic manipulators, and a 21 cm thick steel wall at the IMCL at INL.

3.2.2   Transmission Electron Microscopy

Transmission electron microscopy (TEM) is a technique that has been widely used for the nanoscopic characterization of radiation induced alterations in the microstructure of various materials. In this study, the nanoscopic characterization of a neutron irradiated U-10wt.%Zr/HT9 specimen cross-section that achieved a burnup of 5.7 at.% was performed via TEM assessment of 9 FIB lamellas (from regions A, A/B, B, C, and HT9). An FEI Titan ChemiSTEM FEG-STEM, and an FEI Talos F200X G2 TEM available at the IMCL at INL was used for the determining the crystal structure of various phases and local chemical compositions at different regions of the fuel cross-section. The TEMs available at the IMCL are state of the art equipment altered specifically to handle irradiated materials. The TEMs functions within an energy range of 80-200 kV and have a TEM and scanning TEM resolution of 0.24 nm and 0.16 nm, respectively. Furthermore, they are also equipped with a super-X energy dispersive X-ray spectroscopy system to perform fast speed EDS points and map analysis. Additionally, the FEI Titan ChemiSTEM FEG-STEM was placed in a specifically made TEM room to prevent any external influence from affecting the data that was produced. Fig. 3.3 presents a schematic and actual experimental set-up of the TEM instruments at the IMCL at INL.

The FIB lamellas analyzed via the TEMs were prepared in the FIB-SEMs available at the IMCL at INL. The following are the procedural steps taken for preparing electron transparent FIB lamellas for subsequent TEM investigations: (1) Deposition of a Pt layer on the region of interest pre-milling. Since Pt acts as a protective coating, it mitigates the effects of ion beam milling/damage unto the volume of the specimen to be analyzed. (2) Milling trenches of rectangular shapes to required depth across the volume required to be analyzed. (3) Providing undercut milling patterns to ensure that the resultant FIB lamella block specimens to be analyzed were supported by two beams connected to the bulk of the sample. (4) Utilization of the Omniprobe needle to remove the FIB lamella block from the bulk sample. (5) Mounting of the FIB lamella blocks was on separate copper posts via Pt deposition. (6) Thinning the mounted FIB lamellas to electron transparency via ion milling at various voltages and currents. The TEM data produced from the electron transparent FIB lamellas include scanning transmission electron microscope-high angle annular dark field (STEM-HAADF) micrographs, STEM-bright field (STEM-BF) micrographs, STEM-energy dispersive spectroscopy (STEM-EDS) hyper maps, and selected area electron diffraction (SAED) patterns.
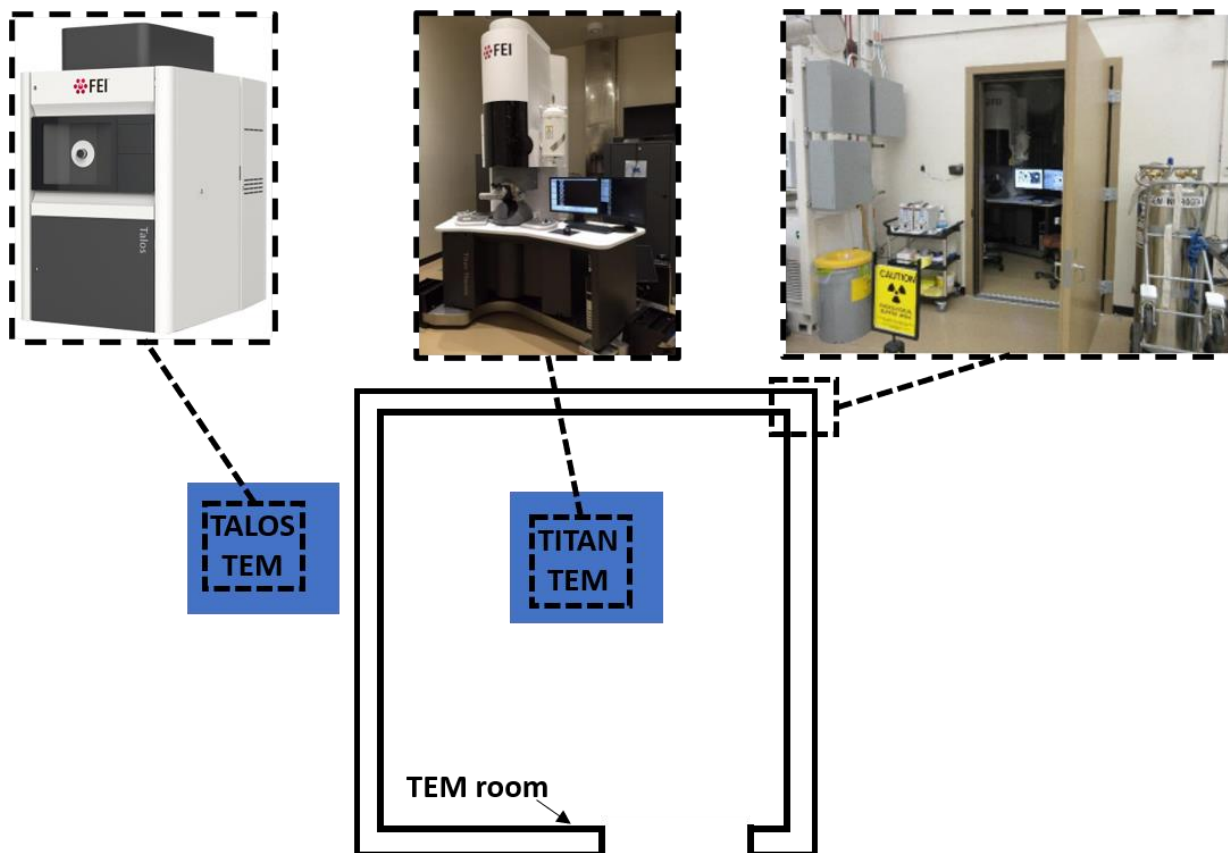
Figure 3.3: Schematic representation of the TEM set-up at the IMCL at INL. The outset images in dashed black boxes (courtesy of FEI and INL) show the actual experimental set-up of several pieces of equipment and the TEM room at the IMCL at INL.

3.3   Serial Sectioning

The microscale characterization of the neutron irradiated U-10wt.%Zr/HT9 specimen cross-section that achieved a burnup of 5.7 at.% was performed via production and sequential serial sectioning of 4 FIB cuboids of ~(30 µm x 30 µm x 30 µm) in size. The FIB cuboids (from regions A, A/B, B, and FCCI) were produced and serial sectioned via a Xe plasma beam produced from the Shielded FEI Helios dual-beam SEM-plasma FIB available at the IMCL at INL. The following are the procedural steps taken for the preparation of the FIB cuboids for subsequent serial sectioning experiments: (1) Deposition of a Pt layer on region ~(30 µm x 30 µm). (2) Milling rectangular trenches ~30 µm deep (at a high voltage and current) around the region of interest. (3) Cleaning the surfaces of the region of interest with the Xe plasma beam at a low voltage and current.

(4) Performing side and undercut milling to ensure that the specimen is in contact with the bulk sample at a single point of contact. (5) Utilization of the Omniprobe needle to remove the FIB cuboid block which was then mounted onto a copper post via Pt deposition. (6) Cleaning the surfaces of the mounted FIB cuboid via plasma beam milling at a low voltage and current. Post the final cleaning, the mounted FIB cuboids were moved to the adequate height required in the FIB-SEM for performing the subsequent serial sectioning experiments. The FIB cuboids were serial sectioned with a pre-programmed slice thickness of 100 nm per slice. Post serial sectioning a 100 nm slice, a BSE micrograph, and an EDS map of the serially sectioned surface was produced. The serially sectioned surfaces of the FIB cuboids were then re-sectioned another 100 nm to produce new surfaces for the collection of sequential BSE micrographs and EDS maps. The process was repeated until minimal or no remnant material was available for further serial sectioning. Serial sectioning in such a manner provided a depth perspective to the data produced and consequently facilitated in the characterizing the material from a three dimension (3D) point of view.

3.4   Synchrotron Micro-Computed Tomography

3.4.1   Synchrotron Generated X-rays

An equivalent of bremsstrahlung X-rays are generated in a synchrotron facility due to the acceleration of electrons in a magnetic field [89]. Fig. 3.4 depicts a schematic of the synchrotron facility at the Advanced Photon Source (APS) located at Argonne National Laboratory (ANL). The electrons produced from an electron gun are accelerated in a linear accelerator and a circular accelerator or booster ring to reach the pre-determined final energy. These high-energy electrons are then transported to a storage ring where they circulate without gaining any further energy. The storage ring possesses straight and curved sections and is equipped with magnets that bend the path of the electrons. The circulating electrons are either accelerated or decelerated to produce X-rays, and this occurs at localities where the bending magnets are placed in the storage ring. In all cases, the X-ray is emitted in a direction which is tangential to the electron storage ring and is consequently used for various experiments which are aligned with the direction of the incoming X-ray beam. Several tangential exit point locations exist in a synchrotron facility, and these locations have several pieces of equipment arranged in the direction of the X-ray beam. These

locations are commonly referred to as beamlines, and the type of magnets, undulators, monochromator, and several pieces of equipment used at a specific beamline depends on the type of experiment being performed. Hence the instrumentation used and experimental configuration at each beamline is unique and non-repetitive.
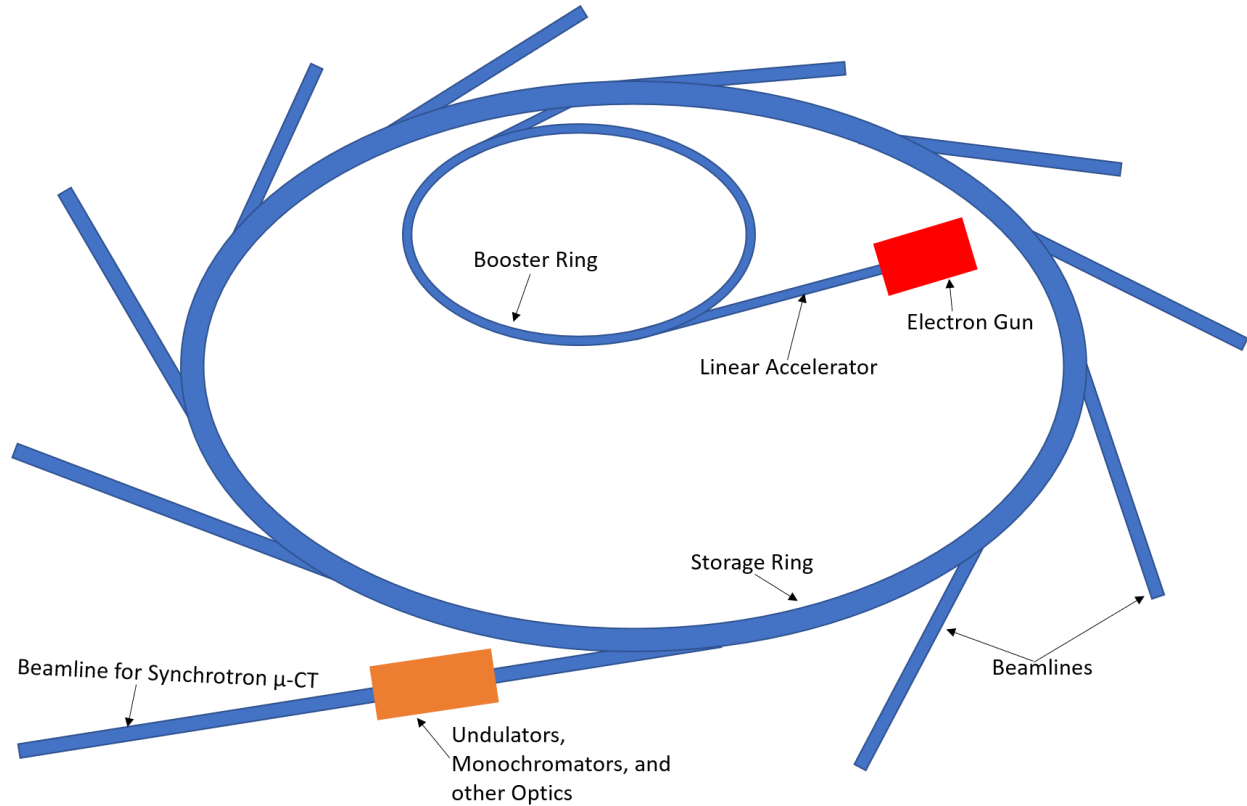
Figure 3.4: Schematic showing the assembly and functional principle of a synchrotron facility. Electrons emitted from the electron gun are accelerated in the linear accelerator and are sent to the booster ring where they accelerated to higher energy levels. These high energy electrons are then circulated in the storage ring at constant energy and sent various beamlines for various experiments. (The schematic presented is an adapted and modified version of the schematic reported by Betz et al. [89])

3.4.2 Absorption Contrast and Propagation-based Phase Contrast Enhanced Micro Tomography

The most commonly used method of X-ray imaging is absorption contrast μ-CT [89]. As X-rays pass through a material, they are attenuated and results in a lower intensity beam. As stated in the Beer-Lambert law given by:

$$\frac{I}{I_0} = exp^{[-\left(\frac{\mu}{\rho}\right)x]} \tag{3.2}$$

Where I_0 is the incident intensity of the beam, x is the thickness of the material, ρ is the density of the material, μ is the attenuation coefficient of the material, and I is the transmitted beam intensity which is determined by the exponential attenuation law. Hence for a given wavelength or energy of the X-rays, the attenuation of the X-rays is dependent on the electron density and the atomic number of constituent elements in the material being analyzed. This implies that a high atomic number, high atomic weight, and a large difference in the atomic number of the elements in a material analyzed will facilitate in producing images with stronger absorption and contrast. For example, absorption contrast imaging has been widely used in medicinal research for imaging bones (high density materials) and tissues (low density materials) [89]. Despite the advantages, absorption contrast μ-CT is not a satisfactory method of assessing materials that have a low absorption coefficient and possess only small differences in atomic number. Although specific issues exist when assessing absorption contrast μ-CT images, these images can be used to estimate the average chemical composition of the specimen material being analyzed in a non-destructive manner.
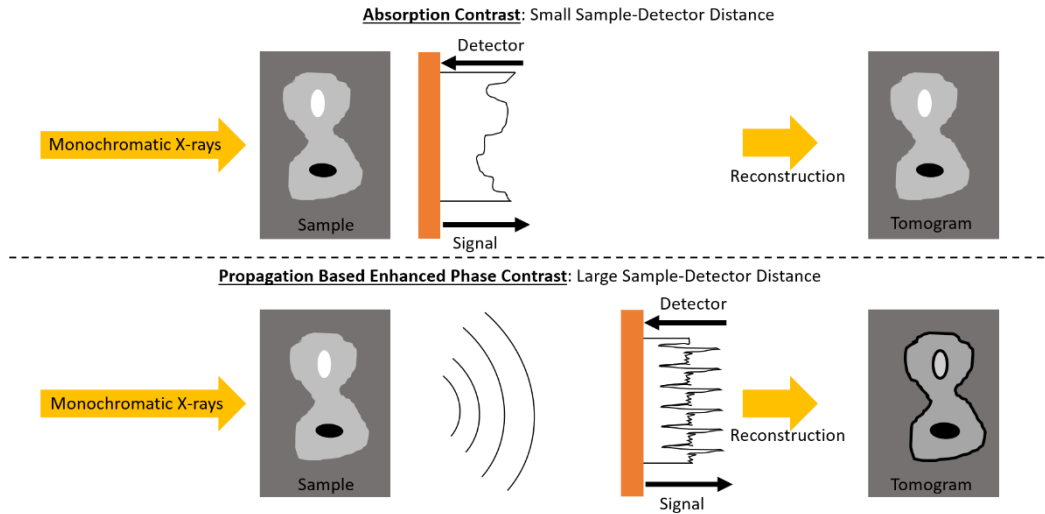
Figure 3.5: Schematic showing the two types of synchrotron X-ray μ-CT techniques. The portion above the dashed black line shows absorption contrast μ-CT, while the portion below the dashed black line shows propagation-based enhanced phase contrast μ-CT. (The schematics presented are adapted and modified versions of the schematics reported by Betz et al. [89]).

Propagation-based enhance phase contrast μ-CT exploits the difference in the refractive indices of materials and voids, which leads to phase shifts in the beam following interaction with

the material. Unlike absorption contrast μ-CT, propagation-based phase contrast enhanced μ-CT is not solely dependent on amplitude changes of the diffracted beam, but rather utilizes the changes in the phase of X-rays that are inherently dependent on the changes in the refractive index of the material [89]. Since the changes in the refractive index of a material are contingent on the interfaces of electron density changes of the region analyzed, this enables propagation-based enhanced phase contrast μ-CT technique to produce images with greater edge-enhancement and improved contrast for small features which would otherwise remain unidentifiable and blended into the matrix of the adjacent material [89]. Hence, the sharper edge enhancement facilitates propagation-based enhanced phase contrast μ-CT provide a quantitative 3D assessment of various microstructural features in neutron irradiated fuels. Fig. 3.5 details a schematic showing the two types of synchrotron μ-CT imaging.

Acquiring μ-CT information by both propagation-based phase contrast enhanced, and absorption contrast methods were important since both techniques are complementary. The information determined post analysis of the absorption contrast μ-CT images included local chemical composition estimates. While the propagation-based phase contrast enhanced μ-CT images provided volume fraction estimates. For convenience, hereafter, propagation-based phase contrast enhanced μ-CT experiments will be referred to as phase contrast μ-CT experiments.

3.4.3   Synchrotron μ-CT Experiments at ANL

Mesoscale characterization of the neutron irradiated U-10wt.%Zr/HT9 cross-section that achieved a burn up of 5.7 at.% was conducted by performing high energy X-ray synchrotron μ-CT experiments on 3 FIB obelisks (from regions A/B, B, and HT9). The procedural steps followed for the production of the 3 FIB obelisks for synchrotron μ-CT experiments are similar to the steps followed for the production of 4 FIB cuboids for the serial sectioning experiments (see Section 3.3). Post-production of the FIB obelisks at INL, they were sealed in a double-walled Kapton enclosure for performing X-ray synchrotron μ-CT experiments at the beamline 1-ID-E at the APS located at ANL. Fig. 3.6 presents a schematic of the experimental setup for the beamline and an enlarged schematic of the specimen holder. Fig. 3.7 shows an image of the overall experimental configuration at the APS. X-ray energy of 71.68 keV, selected by a cryogenically cooled, fixed-vertical-offset, bent double-Laue monochromator, was used to image the FIB obelisks. The absence of a focusing lens for the μ-CT experiments enabled the use of parallel beam illumination

on the entire FIB obelisks. The FIB obelisks were imaged using a QImaging Retiga 4000DC camera which was focused on a 25 µm thin LuAG:Ce single crystal scintillation screen and a similar set-up were described in detail by Hunter et al. [90] and Thomas et al. [36]. The pixel pitch was 0.746 µm from the images collected by the scintillator, and the rotation of the FIB obelisks ranged from -180° to +180° with successive 0.2° angular steps in the ω rotation axis with a 0.125 s exposure. Consequently, the setup led to the generation of several individual projection images for tomographic reconstruction. Additionally, the FIB obelisks radiographs were obtained at separation distances of 6 mm and 40 mm between the sample and detector for absorption contrast and propagation-based phase contrast enhanced µ-CT experiments, respectively.
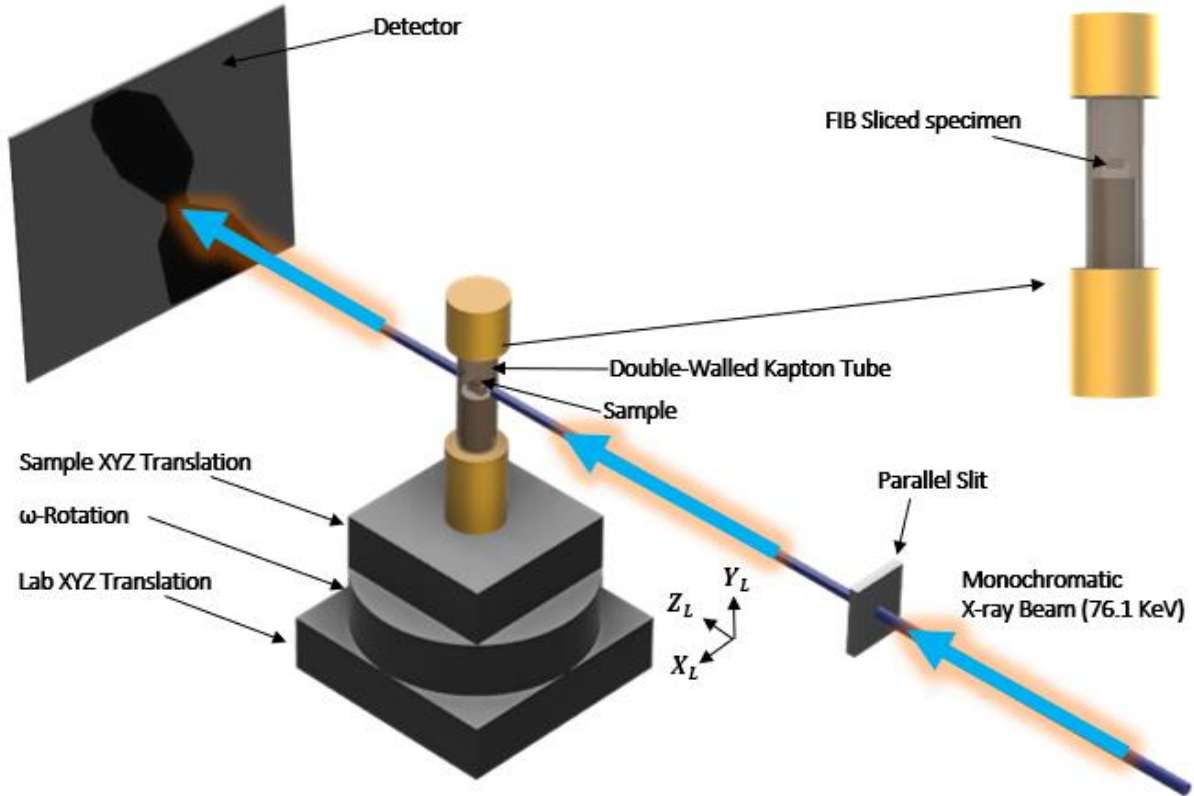
Figure 3.6: Schematic showing the X-ray synchrotron µ-CT experimental setup for irradiated materials at APS beamline 1-ID-E [36].
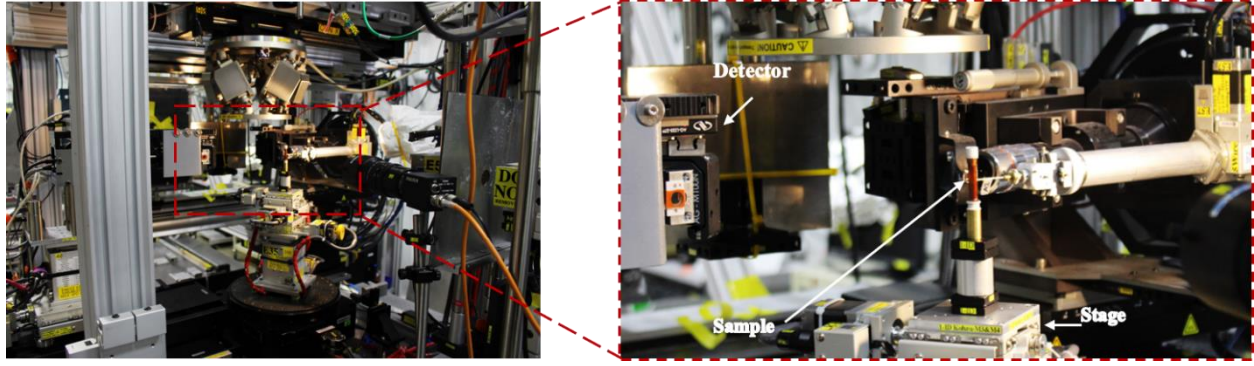
Figure 3.7: Images showing the experimental setup for X-ray synchrotron μ-CT experiments at APS beamline 1-ID-E [36].

The radiographs produced from the X-ray synchrotron μ-CT experiments were then calibrated and converted to projected attenuation images via the utilization of white-field and the dark-field images. A 3D map of the specimen attenuation was created via utilization of the several individual projection images and pixel pitch in the RECON software [91]. The resulting 3D map was comprised of a set of voxels with values corresponding to the attenuation of each voxel in units of mm^{-1}, where one voxel has a volume of 0.41 μm^3. Median and low bandpass filters were applied during the reconstruction to remove imaging artifacts, such as rings and bright spots.

3.4.4   Tomography Image Processing

The tomography data were reconstructed into 32-bit float images which were sequentially arranged to form image stacks. Utilization of 32-bit float images as image stacks allowed for the highest fidelity data to be used for subsequent image analysis. The image stacks were analyzed in both two dimension (2D) and 3D to determine the volume fraction of the phase regions and porosity at different regions of the neutron irradiated fuel cross-section. The image analysis was performed using various image analysis software (such as ImageJ [92] and its plugins, Fiji and BoneJ [93]). The term "phase regions" used throughout the synchrotron μ-CT sections in Chapters 3-7 refer to self-similar composition regions determined via X-ray phase and absorption interactions.

The reconstructed tomographs of the FIB obelisks from region A/B and region B possess attenuation-based voxel values ranging from $0 - 7$ mm^{-1} and $0 - 8$ mm^{-1}, respectively. A voxel value of 0 corresponds to the absence of material and 7 or 8 corresponds to a more attenuating

53

material. By establishing multiple threshold limits within the ranges of 0 - 7 mm^{-1} [for the FIB obelisk from region A/B] and 0 – 8 mm^{-1} [for the FIB obelisk from region A/B], phase regions and porosity can be isolated and analyzed individually. The summation of all voxels that were located within a designated threshold limit assigned to an image stack resulted in the determination of the volume fraction for specific phase regions and porosity [94]. For this study, individual voxels were analyzed as a whole voxel; the analysis via subdivision of voxels into smaller subsections is beyond the scope of this study.

The analyses of volume fractions of the phase regions and pores were conducted using BoneJ [93]. The volume fraction tool calculated the volume by utilizing the area of each threshold limit and the number of images in a stack. The volume fractions of phases and pores were calculated using Eq. (3.3), where T_v represents the total volume of voxels in the fuel specimen from the stacked images; and P_v is the volume of voxels for a designated threshold range in the images, representing a phase region or pore. All voxels in the tomographs external to the fuel were assigned an intensity value of 0.

$$V_{fraction} = \frac{P_v}{T_v}$$ (3.3)

Following the pore volume fraction determination, an ImageJ plugin (3D Objects Counter) was utilized to further segment and rank individual pores within the FIB obelisks on the basis of pore volume ranges. The 3D Object Counter plugin segments and ranks individual pores by assessing the entire porosity image stack and providing unique tags to the pixels present in each pore identified. When the first objects pixel is found on an image from the porosity image stack, the plugin assigns a tag to the pixel. The tag is a unique number and will be assigned to all the pixels in the porosity image stack that is constitutive of the same object. Hence, each time a new object is identified, a new tag is provided to all the pixels constituting the new object in the porosity image stack. Furthermore, the plugin also facilitates each voxel tagged in an object to be connected to its neighboring voxel via one of 26 possibilities (i.e. the voxels are connected if either one of the: 6 faces, 8 corners, or 12 edges are in contact with each other). Further specifications regarding the 3D Objects Counter plugin functions are provided in detail elsewhere [95]. Furthermore, the UCSF Chimera package was used for 3D visualization of the segmented phase regions and

porosity assessed in this study. The UCSF Chimera package was developed by the Resource for Biocomputing, Visualization, and Informatics at the University of California, San Francisco.

Sphericity values were determined for all of the pores within the FIB obelisks from region A/B and B. Sphericity is defined as the estimation of similarity in shape that a 3D object resembles that of a perfect sphere [96]. Sphericity values range on a scale between 0 to 1 [96,97]. A value of 1 corresponds to a perfectly spherical 3D object (in this case a pore) [96,97]. Similarly, a value of 0 corresponds to an object that has no resemblance to a sphere (e.g. aspherical in shape) [96,97]. The sphericity values for the pores segmented from the phase contrast μ-CT images were estimated using Eq. (3.4), where SA_S represents the surface area of an ideal sphere of a 3D object of volume V, and SA is the measured surface area of the 3D object [39].

$$\Psi \ (Sphericity) = \frac{SA_s}{SA} = \frac{(36\pi V^2)^{1/3}}{SA} \tag{3.4}$$

The V and SA parameters for all of the pores within the specimen were determined via 3D Objects Counter and was used in Eq. (3.4) to determine the sphericity values [95]. The voxels analyzed in this study were considered as whole voxels, and analysis via subdivision of voxels into smaller subsections was not performed and was beyond the scope of this study. Consequently, no smoothing factor was used for determining the SA of individual pores. Further procedural details for the determination of the SA values of pores via 3D Objects Counter are provided elsewhere [95]. Sphericity has been previously used by Chuang et al. [97] to quantitatively assess particle size distributions in high-strength cast iron specimens characterized using synchrotron μ-CT.

Furthermore, in this study, the average chemical composition of the phase regions that were identified via thresholding the tomography image stacks of the FIB obelisks from regions A/B and B were estimated via utilization of average attenuation voxel values determined from the absorption contrast tomography μ-CT experiments and Eq. (3.5).

$$\frac{\mu}{\rho} = \Sigma_i \, w_i \left(\frac{\mu}{\rho}\right)_i \tag{3.5}$$

In Eq. (3.5), μ is the measured attenuation of the system and ρ is the density of the major elements in the U-Zr fuel. This ratio is equivalent to the weighted sum of the ratio of the attenuation

coefficient (μ_i) and density (ρ_i) of the individual atomic constituents, i. In Eq. (3.5), w_i is the weight fraction of the ith constituent.

$$V_{Swell} = \frac{V - V_0}{V_0} \tag{3.6}$$

Eq. (3.6) was then used to determine the localized microscopic fuel swelling in the FIB obelisks from regions A/B and B. The three assumptions that were taken into consideration for the determination of localized microscopic fuel swelling in the FIB obelisks analyzed in this study were: (1) the total expanded volume percent, V, of the FIB obelisks post-irradiation was taken to be equal to 100%; (2) the initial fuel was considered to be fully dense; and (3) the initial volume percent, V_0, before irradiation was determined by subtracting the total porosity volume fraction determined from the total expanded volume percent (i.e. the sum of volume fraction of all phase regions excluding the pores).

3.5   Nano-Indentation

Nano-indentation experiments conducted on the neutron irradiated HT9 steel cladding were performed from the HT9 edge to FCCI locality via a Hysitron PI-88 nano-indenter that was housed in a shielded FEI QUANTA 3D FEG at the IMCL at INL. The Hysitron PI-88 nano-indenter available at the IMCL at INL is a state-of-the-art in-situ nano-mechanical testing instrument that is capable of performing nano-indentation, tensile testing, beam bending, and pillar compression tests inside an SEM chamber [98,99]. Furthermore, the Hysitron PI-88 nano-indenter available at the IMCL at INL is also capable of performing the above-mentioned test modes at high temperatures. In this study, a set of 5 nano-indentation tests were performed with a Berkovich indenter tip at a depth of 400 nm at 12 distinct localities of the neutron irradiated HT9 cladding. The localities were pre-determined to be ~55 µm apart from each other so that the change in mechanical properties from HT9 edge to FCCI locality in the neutron irradiated HT9 cladding can be evaluated as a function of distance and interaction of the cladding with the fuel. Fig. 3.8 presents a schematic that details the nano-indentation experiments performed on the neutron irradiated HT9 cladding (i.e. from HT9 edge to FCCI locality).
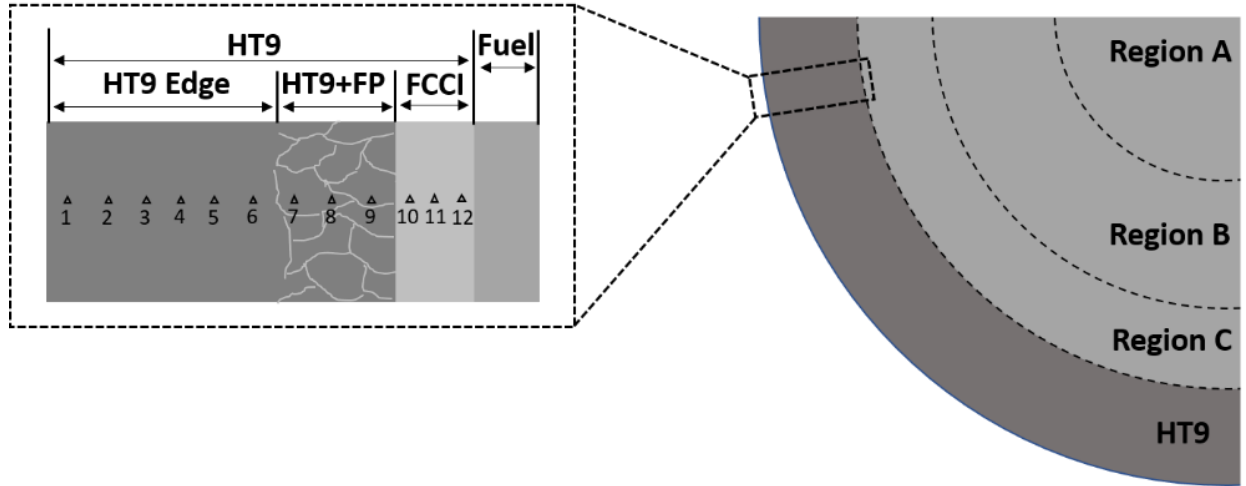
Figure 3.8: Schematic of the cross-section of U-10wt.%Zr/HT9 specimen irradiated to a burnup of 5.7 at.% at a column height of z/L=0.98. Outset schematic enclosed in a black dotted box reveals localities on the neutron irradiated HT9 cladding along which in-situ nano-indentation experiments were performed. Indents marked 1-6, 7-9, and 10-12 were performed along the HT9 edge, HT9+fission products, and FCCI localities, of the neutron irradiated HT9 cladding, respectively.

During nano-indentation testing, a load-displacement (LD) curve is produced, and consequently, each nano-indentation test generates a unique LD curve. The nano-indentation tests were performed at several depths for the following reasons: (1) to generate a nano-hardness versus depth profile, and (2) performing the tests at several depths facilitates in determining the depth at which indentation size effects (ISE) does not influence the nano hardness measurements. Following the nano-indentation experiments, the nano-hardness (H_n) was calculated using the Oliver-Pharr method [100]. Eq. (3.7) determined by Nix and Gao [101] was used to further analyze the ISE on the nano-hardness measurements produced from this study. Nix and Gao [101] modeled ISE based on geometrically necessary dislocations, and consequently, correlated the depth dependence of hardness of crystalline materials.

$$\frac{H_n}{H_0} = \sqrt{1 + \frac{h^*}{h}} \tag{3.7}$$

Plotting the nano-hardness squared (H_n^2) versus the reciprocal of the indentation depth (1/h), facilitates the extraction of a characteristic hardness and characteristic depth. The characteristic hardness (H_0) represents the hardness exhibited by the material in case of an infinitely deep indent

(i.e. ISE does not contribute to additional hardening), while the characteristic depth (h^*) represents the length that characterizes the dependence of increased hardness on depth (i.e. a large h^* value indicates that ISE plays a role for deep indents) [101]. Linear fitting was performed on the H_n^2 vs $1/h$ plot for extraction of H_0 and h^* values, and the calculated values are presented in Section 4.4, respectively. The ISE model by Nix and Gao [101] also possesses an indentation limitation depth of 0.1 µm. This is a consequence of the shape of the indenter not being self-similar at small indentation depths and uncertainties that arise in the contact area at small indentation depths [101]. The ISE modeled by Nix and Gao [101] was also used by several other researchers to assesses the mechanical properties of the irradiated materials [102–105].

Milot's [106] and Busby's [107] empirical relations were then used to calculate the tensile properties of the neutron irradiated HT9 cladding at each nano-indentation locality. Since Milot's [106] and Busby's [107] empirical relations were determined using Vickers micro-hardness measurements and measured tensile stresses, a conversion factor must be established to convert nano-hardness (H_n) to Vickers micro-hardness (HV). Eq. (3.8) was determined by Fisher-Cripps [108], and was extensively used by Krumwiede et al. [109] who reported on a direct comparison between calculated tensile properties (determined via nano-indentation) and actual tensile properties (determined by tensile testing) of reactor-irradiated structural materials. Vickers micro-hardness (HV) is typically expressed in Kgf/mm^2 or 9.8N/mm^2.

$$HV = 94.5H_n \qquad (3.8)$$

Eq. (3.9) presents the empirical relation developed by Milot [106] to determine yield stress via micro-indentation. The relation was determined by comparing standard diamond pyramid hardness test data and tensile test data produced from a large number of reactor steels with varying properties [106]. Krumwiede et al. [109] validated Eq. (3.9) by calculating the Milot's yield stresses via nano-indentation and comparing them to the yield stresses obtained via tensile testing experiments. In Eq. (3.9), σ_y denotes the tensile yield stress, while HV denotes the Vickers micro-hardness measurement. The Milot's yield stress presented in Eq. (3.9) is expressed in MPa.

$$\sigma_y = 2.82HV - 114 \qquad (3.9)$$

Eq. (3.10) presents the empirical relation developed by Busby et al. [107] who assessed austenitic and F/M steels. In. Eq. (8), $\Delta\sigma_y$ and ΔHV denote the change in yield stresses and Vickers micro-hardness measurement, respectively. The Busby's yield stresses presented in Eq. (3.10) is expressed in MPa.

$$\Delta\sigma_y = 3.06 \Delta HV \tag{3.10}$$

Even though Eqs. (3.9) and (3.10) can be used to determine the absolute and change in yield stresses of the neutron irradiated HT9 cladding via nano-indentation, Hosemann et al. [104] and Krumwiede et al. [109] also used Eq. (3.10) to determine the absolute yield stresses in irradiated (ion, proton, and neutron) and control steels. Milot [106] assessed the mechanical properties of pressure vessel alloys via performing extensive shear punch and Vickers micro-indentation tests. Furthermore, Milot [106] formulated Eq. (3.9) to correlate the tensile properties observed from the two testing methods. In comparison, Busby et al. [107] formulated Eq. (3.10) by correlating the yield stresses and micro-hardness estimates of several austenitic and ferritic steels which were reported by numerous researchers. Furthermore, Krumwiede et al. [109] assessed several types of neutron irradiated steels and performed an error analysis on the calculated yield stresses determined via Milot's method (Eq. (3.9)) and Busby's method (Eq. (3.10)). The error analysis revealed that the yield stresses determined via Milot's method had fewer deviations and were statistically more precise than the yield stresses determined via Busby's method [109].

3.6   Challenges Associated with Research on Neutron Irradiated Nuclear Fuels

The MFF-3 series U-10wt.%Zr fuels were neutron irradiated at the FFTF reactor for 726.2 effective full power days. Following the neutron irradiation experiments, they were placed in storage at INL for nearly two decades due to high levels of radioactivity and dose being emitted by the fuel. Hence, to perform any research on the neutron irradiated U-10wt.%Zr fuel required the acceptance of several proposals and completion of multiple safety training courses at INL. Furthermore, specialized equipment available only at certain national laboratories was required for handling the neutron irradiated fuel. The fuel cross-section assessed in this study achieved a burnup of 5.7 at.% and possess a current radiation rate of ~1.2 R/hr on contact and ~100 mR/hr at a distance of a foot. Even though the safety measures mentioned in Section 3.2.1 and Section 3.2.2 provide

more than the required safety, there is always a risk of contamination and dose absorption during specimen polishing and transfer for SEM, TEM, and nano-indentation experiments. Additionally, the high levels of radiation being emitted by the specimen reduces the life of the detectors used in the electron microscopes.

To address the radiological safety at APS, several precautions and measurements were taken [36]. Following the preparation of the FIB obelisks from the fuel cross-section, they were mounted and sealed in a double-walled Kapton enclosure for synchrotron µ-CT experiments [36]. A double layered, independently enclosed containment was required for radiological materials at the APS [36]. The high penetration length of the high-energy X-rays ensured that the Kapton tubes caused negligible effects on the tomography data produced [36]. Furthermore, APS had an additional requirement that a radiological specimen must be less than 5 mR/hr $\beta+\gamma$ at 30 cm [36]. The FIB obelisks measured 40.2 mR/hr $\beta+\gamma$ on contact and 0.6 mR/hr γ on contact, 1.8 mR/hr $\beta+\gamma$ at 30 cm, <0.5mR/hr γ at 30 cm. Moreover, the specimen was required to be smearably clean for all types of radiation (α, β, and γ) [36].

CHAPTER 4.   RESULTS

4.1   Nanoscale Characterization

Nanoscale characterization of the neutron irradiated U-10wt.%Zr fuel cross-section that achieved a burnup of 5.7 at.% was performed via TEM investigation of 9 FIB lamellas. Markers labeled in 1-9 in Fig. 2.1 shows localities from where the FIB lamellas were produced for localized phase and chemical composition analysis. BSE micrographs presented in Figs. 4.1 (a-e) show higher magnification micrographs of various regions next to the localities from where the FIB lamellas were produced. Visual assessment of Figs. 4.1 (a-e) revealed that regions A, B, and C possessed heterogenous microstructural alterations (i.e. the microstructural features observed at different regions of the neutron irradiated fuel cross-section are not homogenous). The heterogeneous microstructural alterations also indicate that each region (i.e. regions A, B, and C) possessed unique major phases with varying chemical compositions. Furthermore, the microstructural alterations observed at the different regions of the neutron irradiated U-10wt.%Zr fuel is also a consequence of several interdependent effects such as temperature gradient, burnup gradient, fuel constituent re-distribution, and FP generation.
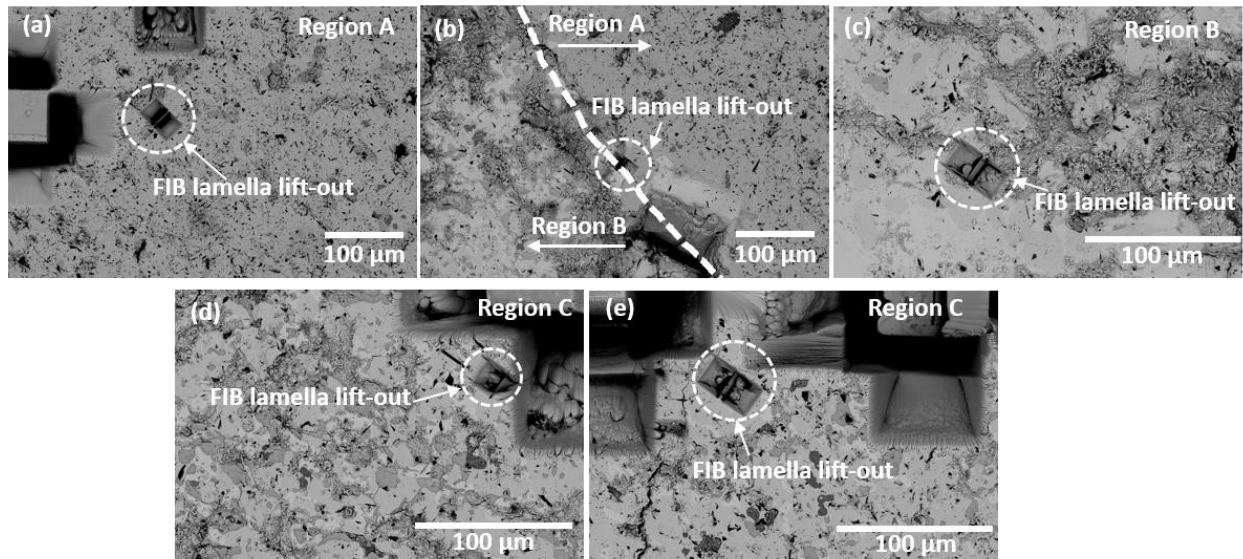
Figure 4.1: BSE micrographs showing localities from where the FIB lamella lift-outs from regions (a) A, (b) A/B, (c) B, and (d, e) C of the neutron irradiated U-10wt.%Zr fuel cross-section that achieved a burnup of 5.7 at.% were produced.

4.1.1 Transmission Electron Microscopy of Region A and Region A/B

A STEM-BF micrograph and STEM-EDS maps of FIB lamella-1 produced from region A at low and high magnifications are presented in Figs. 4.2 (a-j). Various STEM-EDS point scans (see markers labeled 1, 2, and 3 in Fig. 4.2 (a)) confirmed the presence of U-rich, U-intermediate, and U-lean localities. The chemical compositions of the localities identified in Fig. 4.2 (a) are detailed in Table. 4.1. The STEM-EDS assessments presented in Fig. 4.2 (a) and Table. 4.1 revealed that the U-rich, U-intermediate, and U-lean localities in FIB lamella-1 from region A possessed chemical compositions of U~7wt.%Zr, U~46wt.%Zr, and U~62wt.%Zr, respectively.

A STEM-BF micrograph of FIB lamella-2 produced from region A at low magnification is shown in Fig. 4.3 (a), while Figs. 4.3 (b-h) present STEM-EDS maps of the STEM-BF micrograph presented in Fig. 4.3 (a). The STEM-EDS maps from Figs. 4.3 (b-h) also confirmed the presence of U-rich, U-intermediate, and U-lean localities. Figs. 4.3 (i-l) present SAED patterns produced from the lamella presented in Fig. 4.3 (a). Markers labeled (1-4) in Fig. 4.3 (a) shows localities from where the SAED patterns presented in Figs. 4.3 (i-l) were produced. Correlative STEM-EDS and SAED pattern assessment revealed that the U-rich regions are α-U precipitates (indexed at the [110] and [111] zone axes), and the U-intermediate regions are δ-UZr$_2$ matrix phase (indexed at the [001] zone axis), respectively. More interestingly, the U-lean localities appear to be enriched in Zr and reveal potential pathways along which Zr migrated from the region B to region A. The JEMs simulated SAED pattern overlay of the experimental SAED patterns presented in Fig. 4.3 (i-k) is shown in Figs. 4.3 (m-o). Although the STEM-EDS assessments provided in Figs. 4.2 and 4.3 revealed U-intermediate regions to have chemical compositions similar to off-stoichiometry δ-UZr$_2$ phase compositions, these off-stoichiometry compositions are justifiable. As per the U-Zr phase diagram determined by Sheldon et al. [13], a dashed composition line at U~57wt.%Zr indicating the chemical composition of the δ-UZr$_2$ phase implies that there is no ideal stoichiometric composition for the δ-UZr$_2$ phase [110,111]. Furthermore, several out-of-pile experiments on annealed U-Zr specimens also revealed that the chemical composition of Zr in the δ-UZr$_2$ phase ranges between 44-62wt.%Zr [70,112].

The STEM-EDS maps presented in Figs. 4.2 (b) and 4.3 (b) also revealed the presence of Zr-enrichment (see U-lean localities marked with white arrows in Figs. 4.2 (b) and 4.3 (b)). Zr-enrichment was observed along the grain boundaries of the U-intermediate grains, and show pathways along which Zr migrated from region B (average chemical composition of U~4wt%Zr

[6]) to region A (average chemical composition of U~30-35wt.%Zr [6]) of the fuel cross-section. Fig. 4.3 (a) also shows the presence of coarse and acicular structured α-U precipitates (see red and yellow arrows in Fig. 4.3 (a)) in a δ-UZr$_2$ matrix phase. Furthermore, the presence of acicular structured precipitates in U-rich U-Zr alloys was also reported by Moore et al. [113].
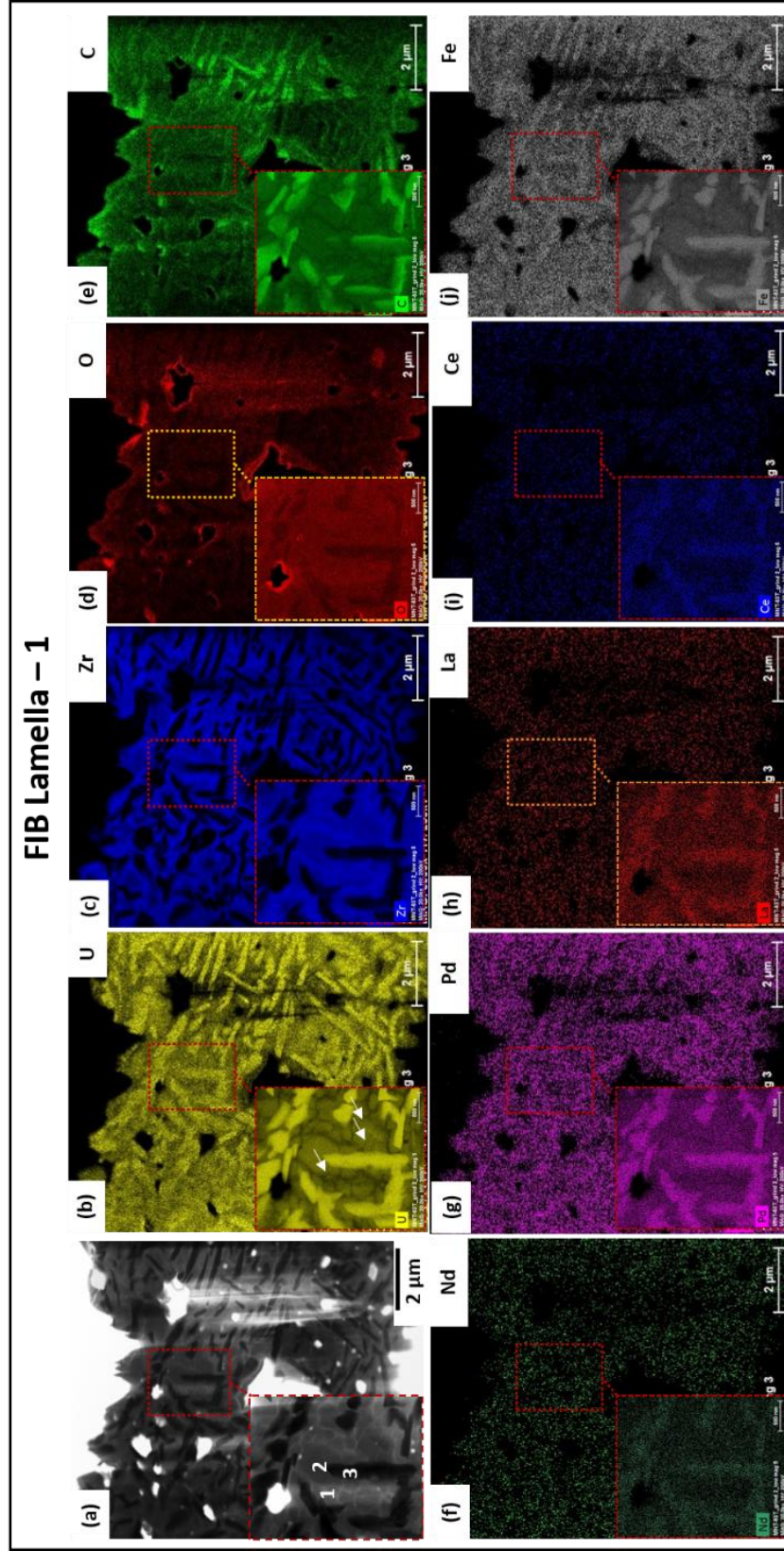
Figure 4.2: (a) STEM-BF micrograph of FIB lamella-1 from region A, and (b-j) elemental maps of U, Zr, O, C, Nd, Pd, La, Ce, and Fe, respectively. Inset micrographs in (a-j) present higher magnification STEM-BF micrograph and elemental maps from FIB lamella-1, respectively. Markers labeled (1-3) in the inset image of (a) shows localities from where STEM-EDS point scans were produced. The chemical compositions determined via averaging multiple point scans are detailed in Table 4.1. White arrows in the U map (see inset image in (b)) showing U-lean localities with Zr-enrichment reveal pathways along which Zr migrated from region B to region A of the fuel cross-section
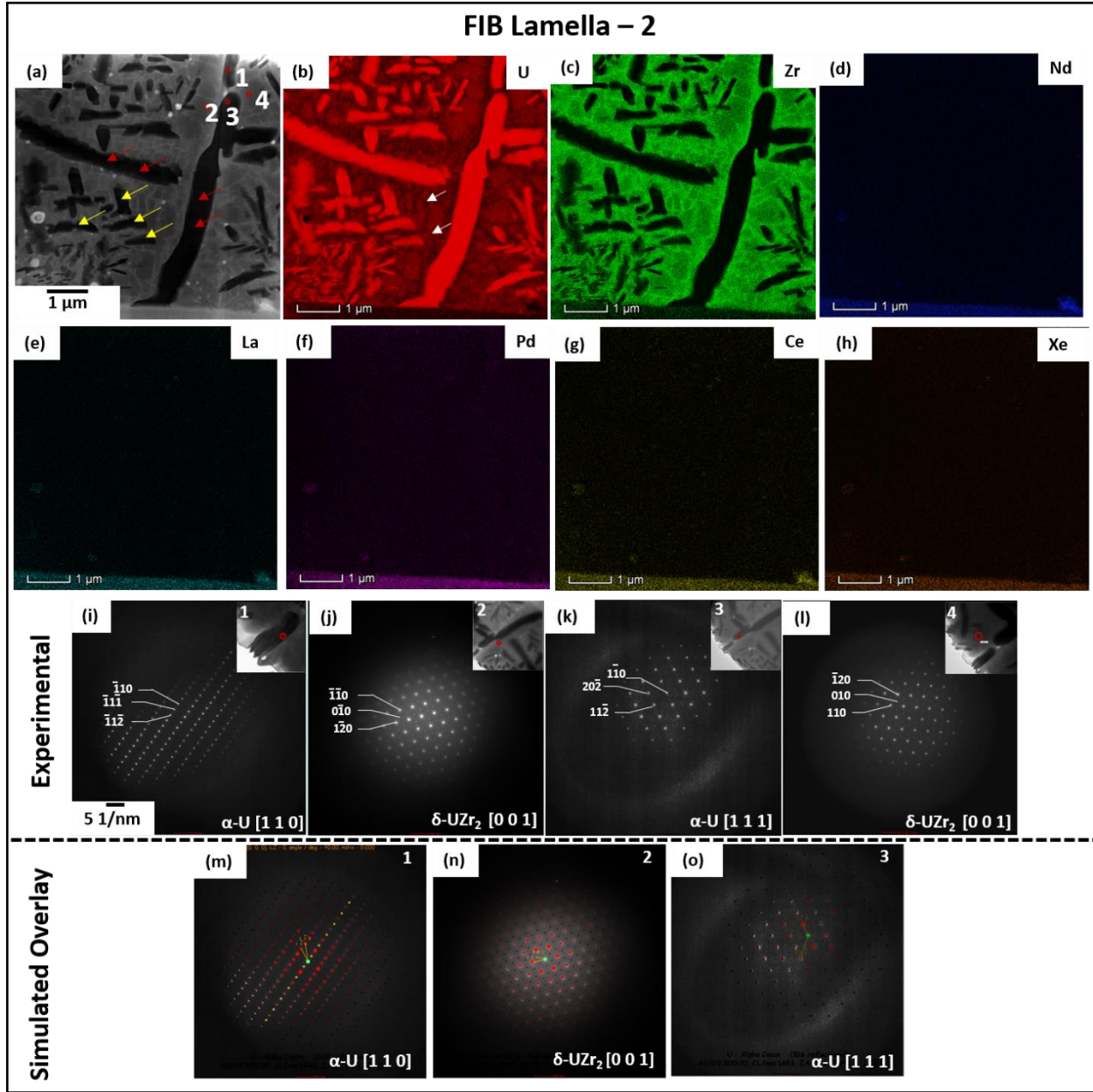
Figure 4.3: (a) STEM-BF micrograph of FIB lamella-2 from region A, and (b-h) elemental maps of U, Zr, Nd, Pd, Ce, and Xe, respectively. Red and yellow arrows in (a) show coarse and acicular structured α-U precipitates, respectively. White arrows in (b) show U-lean localities with Zr-enrichment. SAED patterns presented in (i-l) were produced from localities labeled (1-4) in (a). SAED patterns shown in (i and k) reveal that the U-rich precipitates are α-U at the [110] and [111] zone axes, and the matrix (see (j and l)) is δ-UZr$_2$ at the [001] zone axis. Simulated SAED pattern overlays presented in (m-o) were produced from the experimental SAED patterns presented in (i-k) with α-U at the [110] and the [111] zone axes, and δ-UZr$_2$ at [001] zone axes, respectively. Red spots in simulated diffraction patterns show indexed spots, while, yellow spots show forbidden zone reflections.
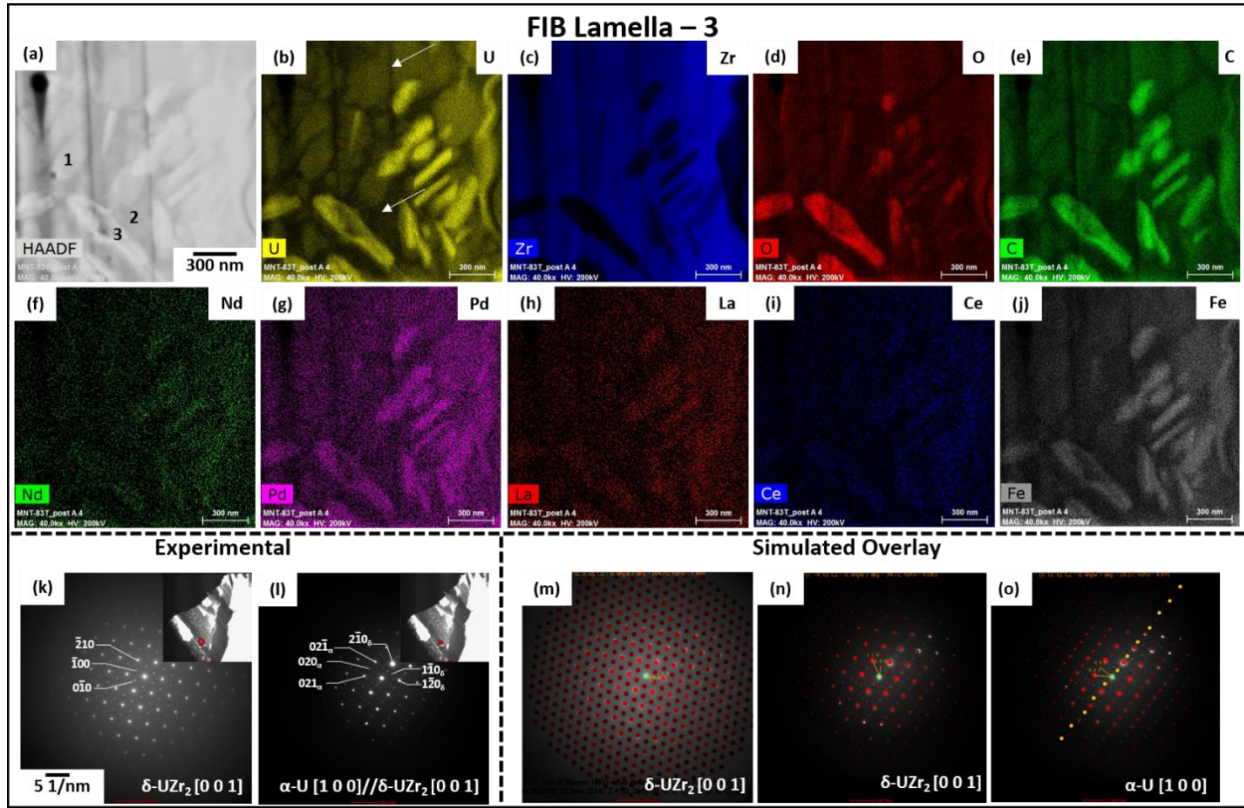
Figure 4.4: (a) STEM-HAADF micrograph of FIB lamella-3 from region A/B, and (b-j) representative elemental maps of U, Zr, O, C, Nd, Pd, La, Ce, and Fe, respectively. Markers labeled (1-3) in (a) shows localities from where several STEM-EDS point scans were produced. The chemical compositions determined via averaging several STEM-EDS point scans are detailed in Table 4.1. SAED patterns presented in (k and l) revealed that the U-intermediate matrix phase is δ-UZr$_2$ indexed at the [001] zone axis, and the U-rich precipitates are α-U at the [100] zone axis, respectively. Simulated SAED pattern overlay presented in (m) was produced from the experimental SAED pattern presented in (k) with δ-UZr$_2$ indexed at the [001] zone axis. Similarly, (n and o) shows simulated SAED pattern overlays of (l) with δ-UZr$_2$ and α-U indexed at the [001] and the [100] zone axes, respectively. Red spots in simulated diffraction patterns show indexed spots, while, yellow spots show forbidden zone reflections.

The STEM-HAADF micrograph and STEM-EDS maps of FIB lamella-3 from region A/B are presented in Figs. 4.4 (a-j). Various STEM-EDS point scans (markers labeled 1, 2, and 3 in Fig.4.4 (a)) confirmed the presence of U-rich, U-intermediate, and U-lean localities. Furthermore, the chemical compositions of the localities identified in Fig. 4.4 (a) are detailed in Table. 4.1. The STEM-EDS assessments on FIB lamella-3 from region A/B revealed that the U-rich, U-intermediate, and U-lean localities possessed chemical compositions of U~8wt.%Zr, U~41wt,%Zr, and U~63wt.%Zr, respectively. The SAED patterns produced from FIB lamella-3 are presented in

Figs. 4.4 (k and l). The SAED patterns indicate that the U-rich and U-intermediate localities are α-U (indexed at the [100] zone axis), and δ-UZr$_2$ (indexed at the [001] zone axis), respectively. The JEMs simulated SAED pattern overlay of the experimental SAED patterns presented in Figs. 4.4 (k and l) is as shown in Figs. 4.4 (m-o). The observation of similar SAED patterns of δ-UZr$_2$ and α-U+ δ-UZr$_2$ phases was previously reported by Basak et al. [112] and McKeown et al. [114]. Even though Basak et al. [112] and McKeown et al. [114] performed out-of-pile experiments to study the phase transformations of γ-U in U-Zr alloys and the co-existence of α-U and δ-UZr$_2$ phases, it is interesting to note that certain features such as the δ-UZr$_2$ phase and α-U+δ-UZr$_2$ phases identified from the out-of-pile experiments were similar to the in-pile observations seen in this study.

4.1.2   Transmission Electron Microscopy of Region B

The STEM-HAADF micrograph and STEM-EDS maps of FIB lamella-4 from region B at low and high magnifications are presented in Figs. 4.5 (a-h). The STEM-EDS maps presented in Figs. 4.5 (b-h) revealed the following: (1) presence of two different types of U-rich grains, (2) presence of Nd-Ce-Pd, Nd-Ce-Pd-La, and Nd-Ce-La FP precipitates, and (3) presence of Zr-rich precipitates on one of the U-rich grains. Markers labeled 1-7 in Fig. 4.5 (a) represent localities from where the SAED patterns shown in Figs. 4.5 (i-p) were produced. SAED patterns presented in Figs. 4.5 (i-p) revealed the following: (1) presence of α-U at the [001] zone axis, (2) presence of β-U (at the [-110] zone axis) and δ-UZr$_2$ (at the [001] zone axis) phases, (3) presence of polycrystalline Nd-Ce-Pd and Nd-Ce-Pd-La FP precipitates, and (4) presence of amorphous Nd-Ce-La FP precipitates.

Furthermore, Fig. 4.5 also revealed that the α-U grain was more affected by radiation, thus possessed a greater concentration of inhomogeneities (such as cavities and FP precipitates) than the U-rich (β-U) grain with Zr-rich precipitates. The SAED patterns also revealed the presence of polycrystalline and amorphous FP precipitates (see Figs. 4.5 (l–p)), and the diffraction spots seen in Fig. 4.5 (p) is a consequence of diffraction pattern overlap from neighboring grains in the FIB lamella-4. A high magnification STEM-BF micrograph and STEM-EDS maps of a specific locality of FIB lamella-4 from region B are presented in Figs. 4.6 (a-j). The STEM-EDS maps in Fig. 4.6 were produced at localities from where SAED patterns presented Figs. 4.5 (j and k) were produced.
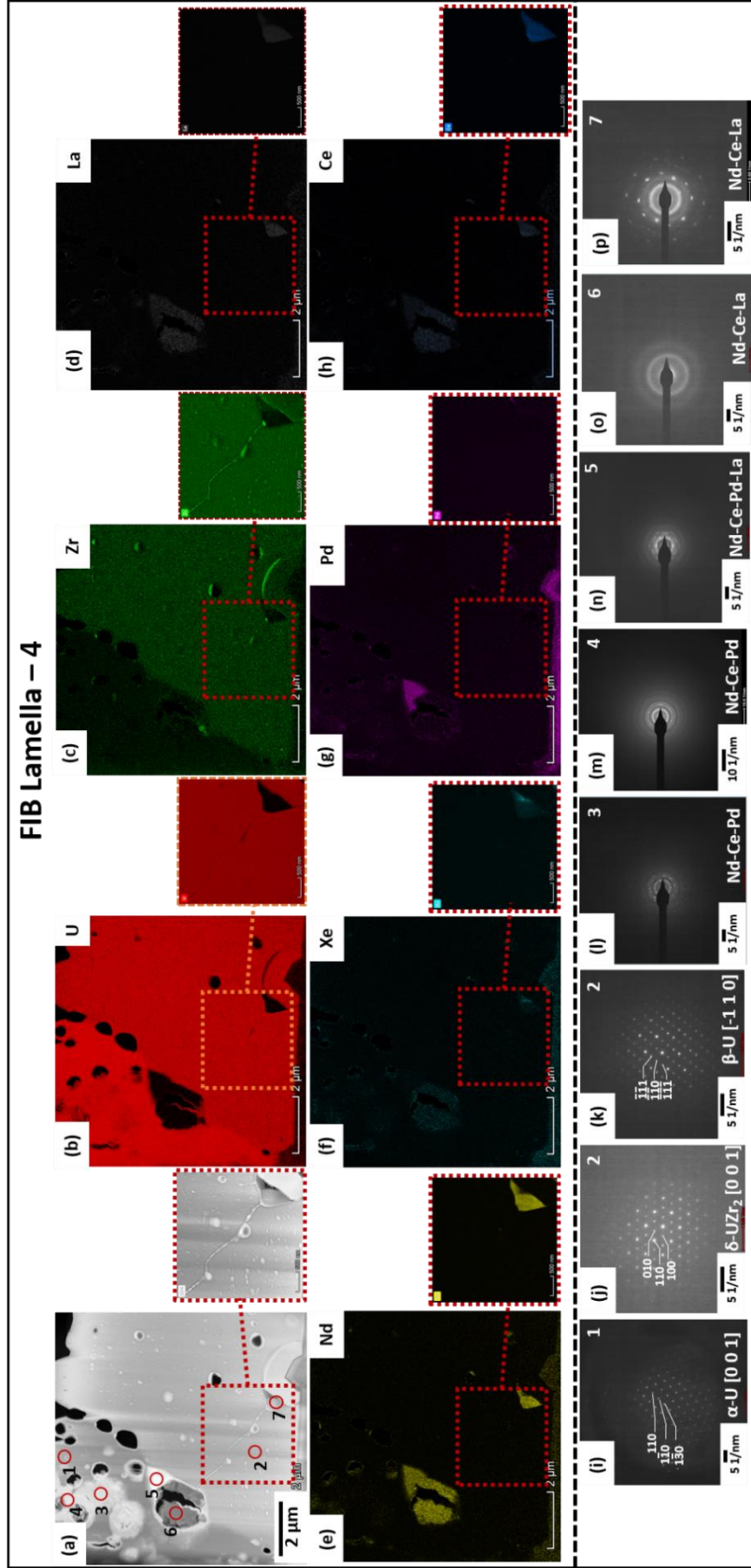
Figure 4.5: STEM-HAADF micrograph of FIB lamella–4 from region B, and (b-h) elemental maps of U, Zr, La, Nd, Xe, Pd, and Ce, respectively. Outset micrographs in (a-h) present higher magnification elemental maps from the FIB lamella. SAED patterns presented in (i- p) were produced at localities labeled (1-7) in (a). SAED patterns shown in (i-k) reveal the presence of α-U, δ-UZr$_2$, and β-U at the [001], [001], and [-110] zone axes, respectively. SAED patterns presented in (l-p) reveal that Nd-Ce-Pd/Nd-Ce-Pd-La solid FP precipitates are poly-crystalline, while, Nd-Ce-La solid FP precipitates are amorphous.
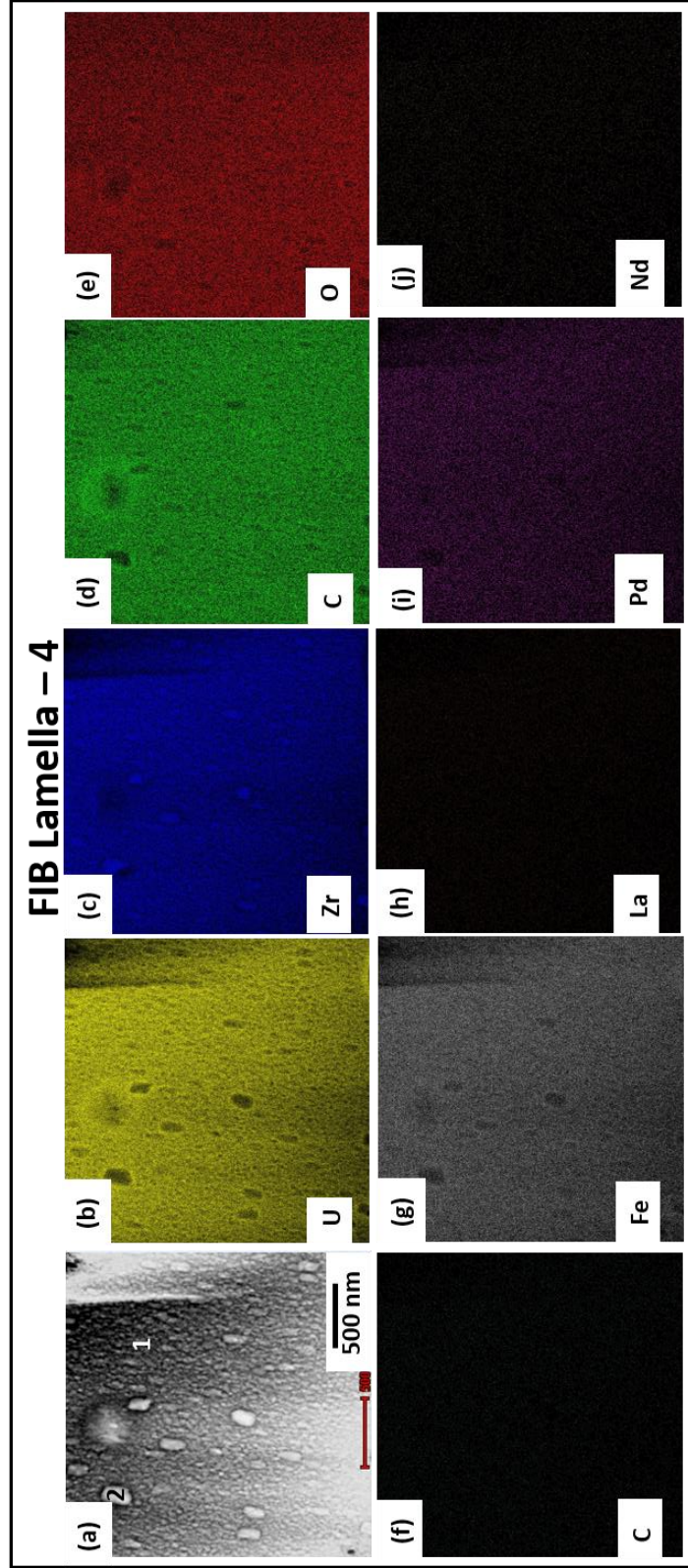
Figure 4.6: (a) STEM-HAADF micrograph of FIB lamella-4 from region B, and (b-j) elemental maps of U, Zr, C, O, Ce, Fe, La, Pd, and Nd, respectively. The STEM-EDS maps were produced at localities from where SAED pattern labeled 2 in Fig. 4.5 (a, k, and l) were produced. Markers labeled 1 (matrix) and 2 (Zr-rich precipitate) in (a) shows localities from where multiple EDS point scans were produced for assessment of the local chemical compositions that are detailed in Table 4.1.
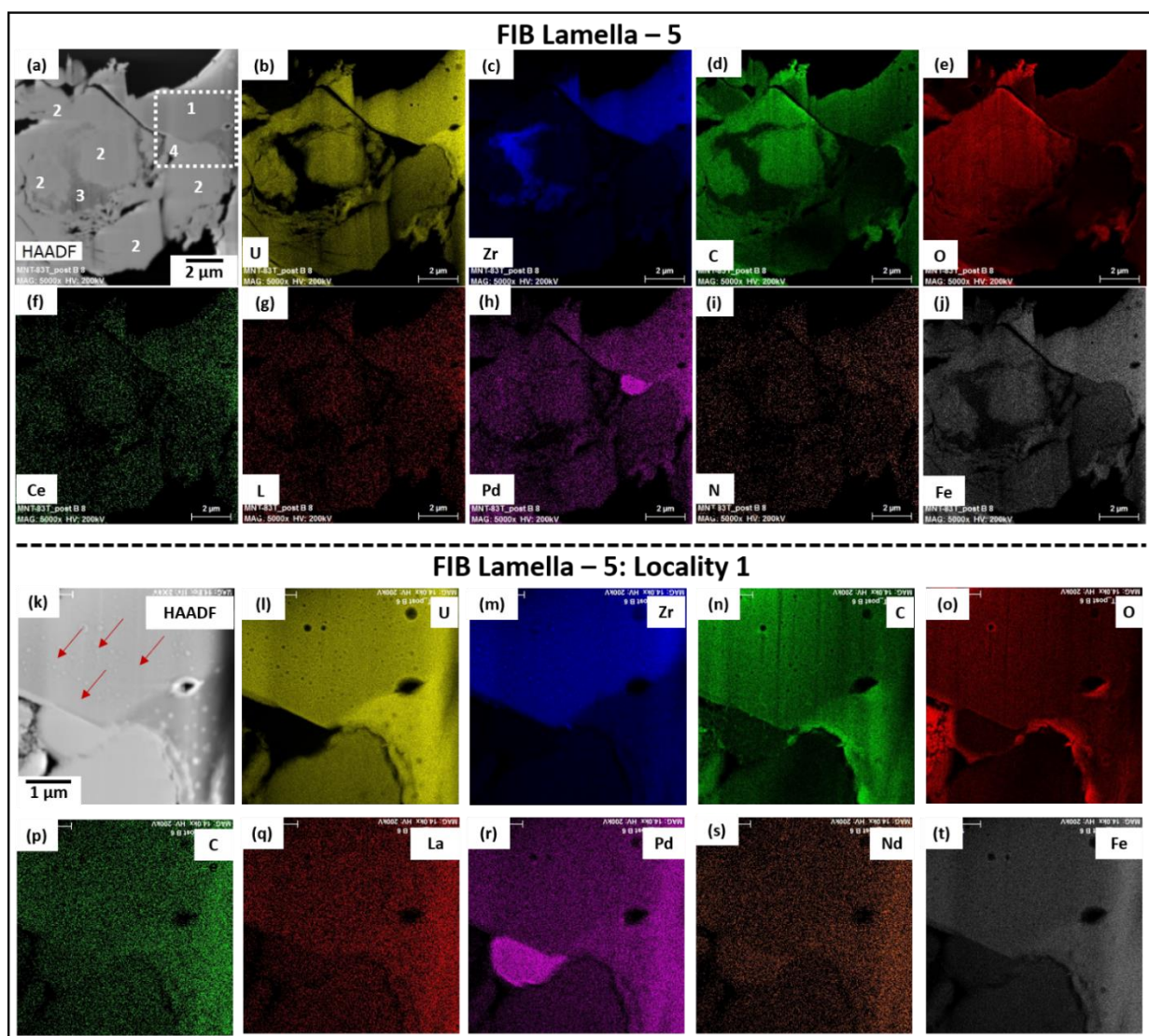
Figure 4.7: (a, k) STEM-HAADF micrographs of FIB lamella-5 from region B, and (b-j, and l-t) presents elemental maps of U, Zr, C, O, Ce, La, Pd, Nd, and Fe at low and high magnifications, respectively. White dashed box in (a) reveals the locality from where STEM-EDS maps presented in (l-t) were produced, and markers labeled (1-4) in (a) shows localities from where multiple EDS point scans were produced for determining the local chemical compositions that are detailed in Table 4.1. Red arrows in (k) indicate U-rich grains with Zr-rich precipitates in FIB lamella-5. (Note: Marker 2 in Fig. 4.7 (a) is labeled multiple times to show that the U-rich grain spanned over a large area of the FIB lamella-5).

Assessment of the STEM-EDS maps (see markers labeled 1 and 2 in Fig. 4.6 (a)) revealed the presence of a U-rich matrix phase (U~15wt.%Zr) with Zr-rich precipitates (U~24wt.%Zr), and the chemical compositions of two localities determined via averaging multiple STEM-EDS point scans are detailed in Table 4.1. A STEM-HAADF micrograph and STEM-EDS maps of FIB

lamella-5 from region B are presented in Figs. 4.7 (a-t). The chemical compositions of the various localities determined via STEM-EDS point scans (see markers labeled 1-4 in Fig. 4.7 (a)) are detailed in Table 4.1. The STEM-EDS assessments revealed the presence of two types of U-rich grains (i.e. U~14wt.%Zr and U~2wt.%Zr), a Zr-rich grain (~70wt.%Zr), and an Nd-Pd-La FP precipitate. Figs. 4.8 (a and b) present STEM-BF micrographs of FIB lamella-5 produced from region B. Markers labeled 1-4 in Figs. 4.8 (a and b) indicate localities from where SAED patterns presented in Fig. 4.8 (c-f) were produced. It should also be noted that the face-centered crystal (FCC) structured U-rich phases observed in Figs. 4.8 (c and d) share similar d-spacing to FCC structured UO_2 phase and is most likely a consequence of oxidation (see oxide rings in Figs. 4.8 (c and d)) of the U-rich grains during specimen storage. Figs. 4.8 (e and f) present SAED patterns produced from a Zr-rich grain. Fig. 4.8 (e) revealed that the Zr-rich grain is FCC structured, while Fig. 4.8 (f) revealed that the Zr-rich grain possesses nano-crystalline precipitates. Furthermore, the STEM-EDS assessment also revealed that the Zr-rich grain possessed concentrations of FPs (see marker labeled 3 in Fig. 4.7 (a) and corresponding chemical composition in Table. 4.1).
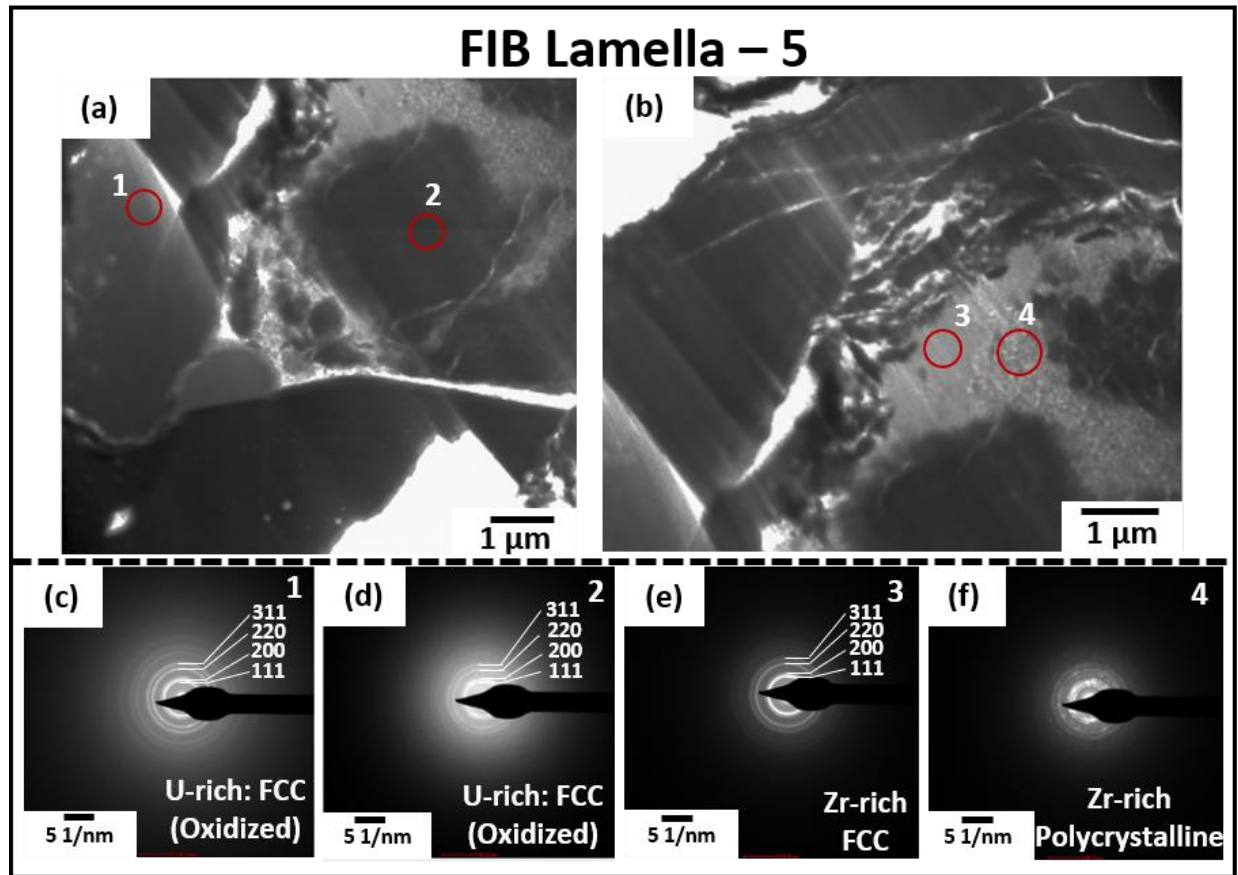
Figure 4.8: (a, b) low magnification STEM-BF micrograph of FIB lamella-5 from region B. Labels marked (1-4) in (a and b) show locations from where SAED patterns presented in (c-f) were produced. The SAED patterns presented in (c-f) revealed FCC structured U-rich phases and FCC structured Zr-rich grain, respectively. The presence of FCC structured U-rich phases is a consequence of lamella oxidation during specimen storage.

4.1.3 Transmission Electron Microscopy of Region C

STEM-HAADF micrographs and STEM-EDS maps of FIB lamella-6 and -7 from region C are presented in Figs. 4.9 (a-t), while Figs. 4.10 (a-t) present high magnification STEM-EDS maps of specific localities from FIB lamella-6 (i.e. localities that possess U-rich grains with Zr-rich precipitates). Interestingly, several microstructural alterations such as Zr-enrichment at grain boundaries of U-rich grains, and the presence of U-rich grains with Zr-rich precipitates observed in Fig. 4.10 at region C were also identified in region B (see Figs. 4.5 (a-h) and Figs. 4.6 (a-j)) of the neutron irradiated fuel. A detailed assessment of the STEM-EDS maps (see inset micrographs in Figs. 4.9 (a-j)) of FIB lamella-6 from region C also revealed the presence of U-rich precipitates

and U-lean localities along grain boundaries of a U-intermediate matrix phase. The microstructural features observed in the inset micrographs presented in Figs. 4.9 (a-j) share resemblance to the structure and composition of the features observed in the FIB lamellas-1, -2, and -3 from regions A and A/B. The compositions of various localities in FIB lamella-6 identified via STEM-EDS point scans [i.e. localities labeled 1-5 in Fig. 4.9 (a), and 1-2 in Figs. 4.10 (a and k)] are detailed in Table 4.1. The STEM-EDS assessments of FIB lamellas-6 and 7 in Fig. 4.9 revealed the following: (1) U-rich, U-intermediate, and U-lean localities seen at region C (similar to the microstructural alterations seen at regions A and A/B) possess chemical compositions of U~8wt.%Zr, U~34wt.%Zr, and U~61wt.%Zr, respectively. (2) two types of U-rich grains (i.e. U~15wt.%Zr and U~3wt.%Zr). (3) A Zr-rich particle/grain (~84wt.%Zr) and a U-rich grain (U~16wt.%Zr). High magnification STEM-EDS assessments of FIB lamella-6 indicated that the U-rich grain (U~15wt.%Zr) possess Zr-rich precipitates at cavities and grain boundaries with a chemical composition of U~64wt.%Zr and U~45wt.%Zr, respectively. The STEM-BF micrographs of FIB lamella-6 and -8 are presented in Figs. 4.11 (a-c), and markers labeled (1-4) in Figs. 4.11 (a-c) indicate localities from where SAED patterns presented in Figs. 4.11 (d-g) were produced. Fig. 4.11 (d) revealed that the U-rich matrix phase has oxidized as a consequence of specimen storage, while Figs. 4.11 (e-g) revealed the presence of the δ-UZr_2 phase (indexed at the [111] and [110] zone axes).

STEM-BF micrographs of FIB lamella-7 produced from region C at low and high magnifications are as shown in Figs. 4.12 (a-d). In Fig. 4.12 (a), the dashed white boxes labeled 1'-3' show localities from where high magnification micrographs presented in Figs. 4.12 (b-d) were produced. The SAED patterns produced at different localities of the Zr-rich particle/grain are presented in Figs. 4.12 (e-h), and the SAED patterns revealed that the Zr-rich particle/grain is FCC structured. A STEM-BF micrograph and STEM-EDS maps of the Zr-rich particle/grain from FIB lamella-7 at high magnification is presented in Figs. 4.12 (i-p). The STEM-EDS maps of the Zr-rich particle/grain were produced at a locality labeled 4' in Fig. 4.12 (a). From the STEM-EDS maps presented in Figs. 4.12 (j-p), it is evident that the Zr-rich particle/grain possessed: (1) nano-sized U-rich precipitates (see white arrows in Fig. 4.12 (j)), and (2) FPs (see dashed white circles with red arrows in Figs. 4.12 (l-p)),.
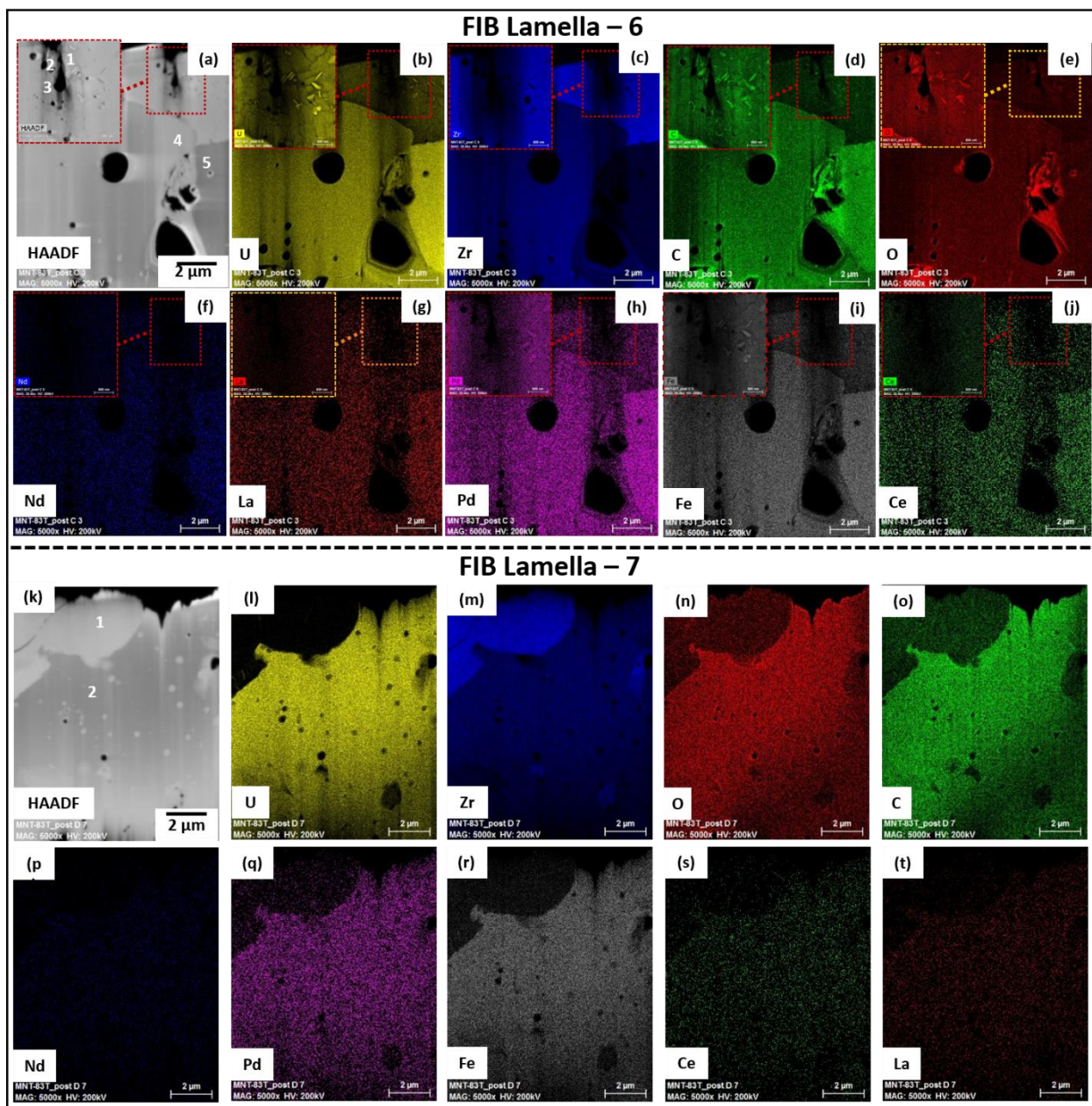
Figure 4.9: (a, k) STEM-HAADF micrograph of FIB lamella-6 and lamella-7 from region C, and (b-j, and l-t) presents elemental maps of U, Zr, O, C, Nd, Pd, La, Ce, and Fe, respectively. Inset micrographs in (a-j) present higher magnification elemental maps from FIB lamella-6, and labels (1-5) in (a) and (1-2) in (k) shows localities from where STEM-EDS point scans were produced for determining the local chemical compositions detailed in Table 4.1.
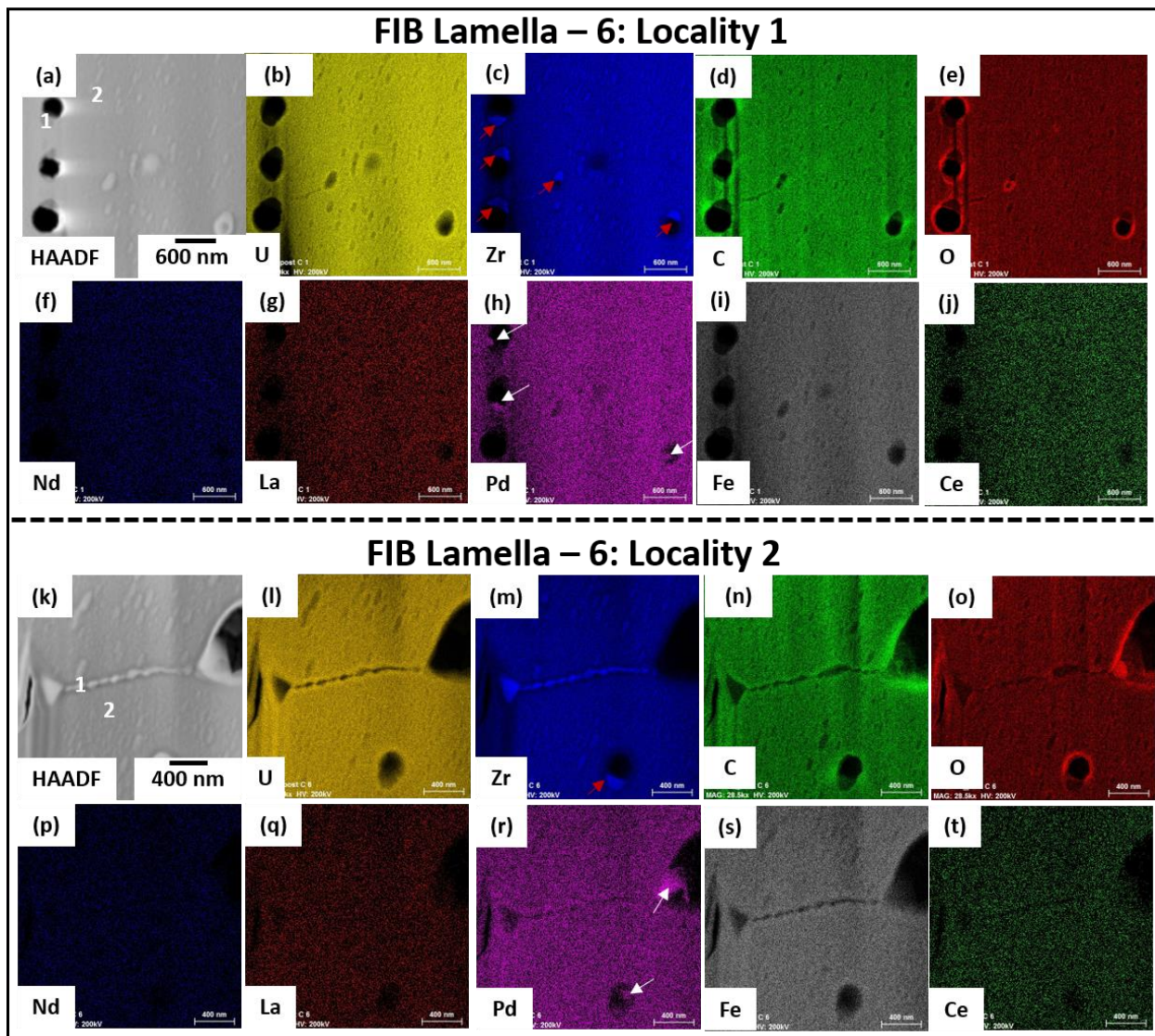
Figure 4.10: (a and k) STEM-HAADF high magnification micrographs of FIB lamella-6 from region C, and (b-j and k-t) show elemental maps of U, Zr, O, C, Nd, Pd, La, Ce, and Fe, respectively. Markers labeled marked 1 and 2 in Fig. 4.10 (a and k) shows localities from where STEM-EDS point scans were produced for determining the local chemical compositions detailed in Table 4.1. White arrows in the Pd maps indicate the presence of solid FPs in cavities; whereas, red arrows in the Zr maps show regions with Zr enrichment at cavities.
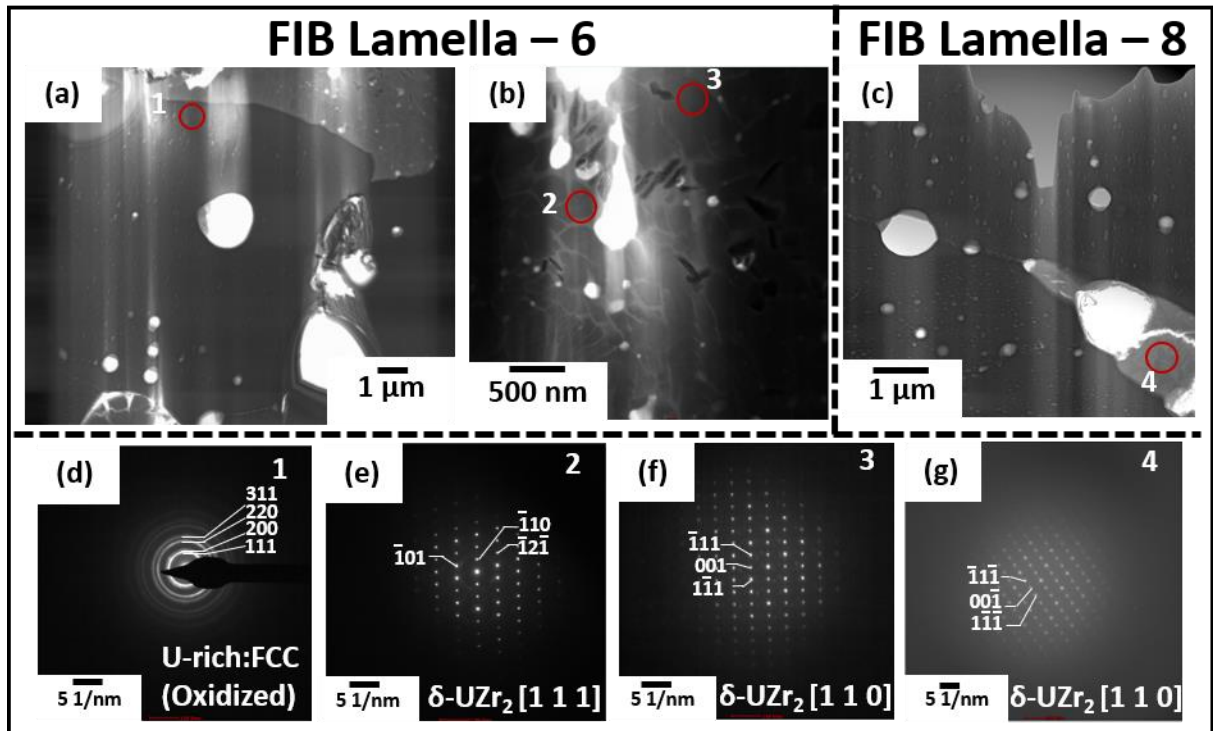
Figure 4.11: (a-c) STEM-BF micrographs of FIB lamella -6 and -8 from region C at low magnifications with labels 1-4 showing localities from where SAED patterns presented in (d-g) were produced. SAED pattern shown in (d) reveal that the U-rich phase has oxidized during storage and consequently possesses an FCC structure, while (e-g) shows the presence of δ-UZ$_2$ at the [111] and [110] zone axes, respectively.
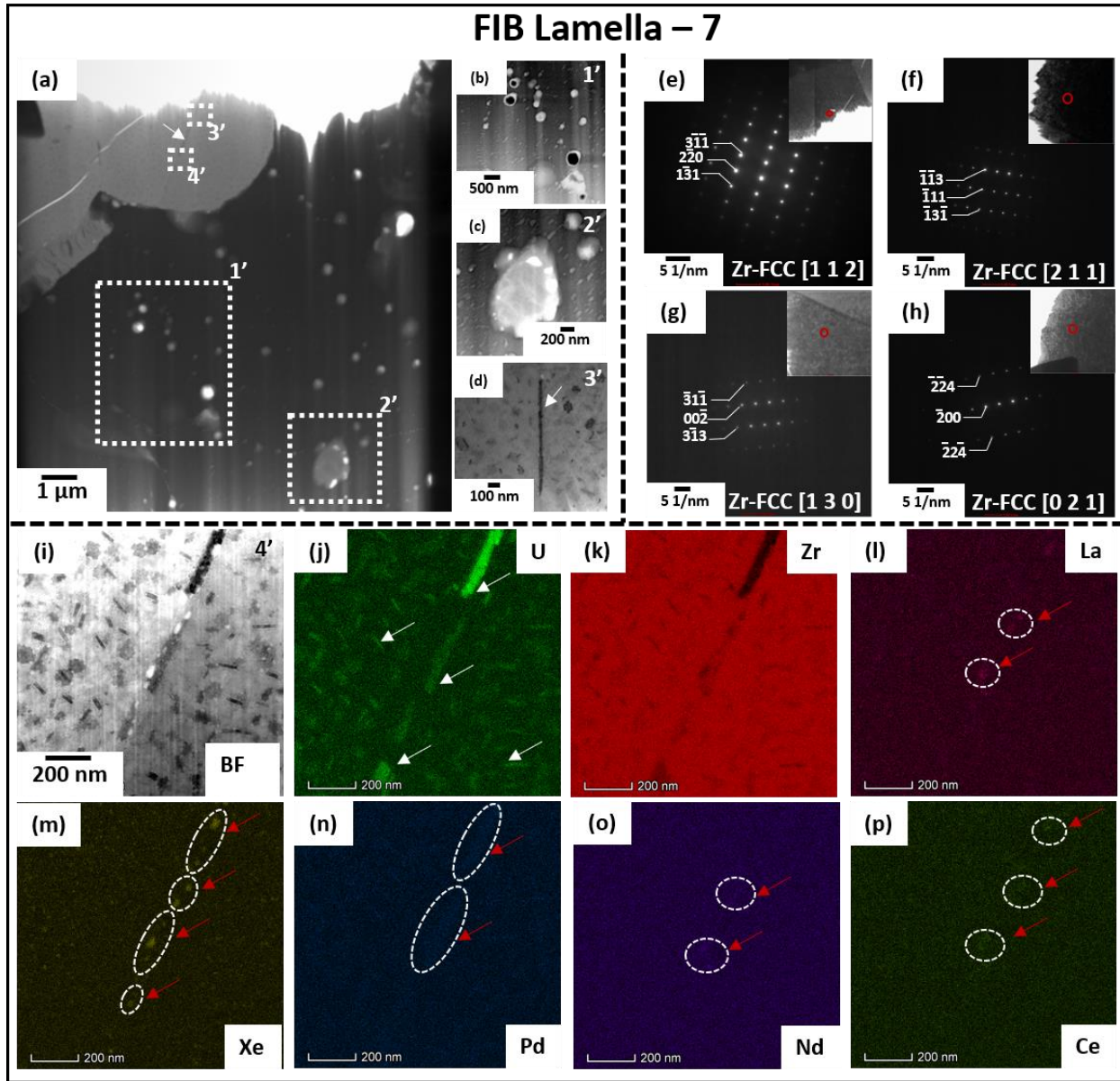
Figure 4.12: (a) presents a low magnification STEM-BF micrograph of FIB lamella-7 produced from region C, and (b-d) present higher magnification micrographs of certain locations (enclosed by a white box labeled 1'-3') of the micrograph presented in (a). SAED patterns shown in (e-h) were produced from the Zr-rich grain (marked with a white arrow) in (a). SAED indexing of (e-h) indicate that the Zr-rich particle/grain possesses an FCC crystal structure at the [112], [211], [130], [021] zone axes, respectively. STEM-BF micrograph shown in (i) was produced at locality marked 4' in (a), and elemental maps of U, Zr, La, Xe, Pd, Nd, and Ce showed in (i-p) revealed the presence of a large quantity of U-rich precipitates (see white arrows in (j)) and FPs (see the white dashed circles with red arrows in (l-p)) in the Zr-rich grain.

Table 4.1: STEM-EDS point scan assessment of various localities in the 8 FIB lamellas produced from regions A, A/B, B, and C of the neutron irradiated U-10wt.%Zr fuel that achieved a cross-section burnup of 5.7 at.%..

Region	*Point Scan Locality	Major Elements (wt%)		Other Elements (wt%)							Fig. No
		U	Zr	Nd	Pd	La	Ce	Fe	O	C	
A	1	27.0 ±2.68	62.59 ±5.13	0	0.19 ±0.43	4.54 ±3.51	4.93 ±5.28	0.61 ±0.20	0.11 ±0.25	0	
	2	47.13 ±1.53	46.61 ±2.07	2.77 ±1.32	0.04 ±0.06	0.09 ±0.21	2.29 ±2.73	0.77 ±0.03	0.04 ±0.1	0.03 ±0.08	4.2 (a)
	3	86.12 ±5.06	7.25 ±3.04	1.76 ±3.26	0.24 ±0.38	1.46 ±2.79	1.40 ±2.22	1.53 ±0.07	0	0.2 ±0.32	
A/B	1	42.34 ±6.47	41.41 ±3.82	6.78 ±7.45	0.22 ±0.39	3.63 ±3.49	3.61 ±4.15	0.68 ±0.23	1.37 ±1.23	0	
	2	27.35 ±1.56	63.31 ±2.73	3.28 ±4.22	0	2.02 ±3.11	2.50 ±2.71	0.48 ±0.16	1.03 ±0.31	0	4.4 (a)
	3	78.90 ±5.69	8.02 ±3.11	2.02 ±3.18	0.28 ±0.46	5.23 ±5.7	2.02 ±3.39	1.03 ±0.13	2.46 ±1.98	0	
B	1	78.28 ±4.28	15.64 ±0.96	1.91 ±3.64	0	1.17 ±1.43	2.14 ±1.99	0.99 ±0.08	0.06 ±0.06	0	4.6 (a)
	2	60.95 ±3.66	23.90 ±4.38	4.34 ±3.67	0.04 ±0.09	0.60 ±0.79	4.34 ±3.67	0.75 ±0.20	0.12 ±0.15	0.05 ±0.1	
	1	75.75 ±4.50	14.82 ±0.81	5.25 ±4.92	0.04 ±0.06	1.07 ±1.55	1.86 ±3.15	0.82 ±0.19	0.002 ±0.006	0.36 ±0.39	
B	2	81.79 ±10.99	2.17 ±0.66	7.95 ±7.80	0.36 ±0.75	3.99 ±6.45	1.59 ±3.42	0.62 ±0.28	1.24 ±1.05	0.24 ±0.59	4.7 (a)
	3	4.77 ±5.62	70.67 ±12.25	0.53 ±1.42	8.45 ±4.01	6.39 ±6.63	4.68 ±5.36	0.22 ±0.25	4.19 ±2.24	0.06 ±0.13	
	4	0.67 ±0.30	2.90 ±0.68	45.76 ±8.17	28.69 ±4.76	9.97 ±7.33	10.63 ±7.48	0.99 ±0.40	0.13 ±0.17	0.22 ±0.28	
	1	49.51 ±4.29	34.75 ±4.24	4.04 ±6.67	0.07 ±0.18	4.43 ±6.30	5.28 ±4.84	0.58 ±0.16	0.85 ±0.60	0.45 ±0.62	
	2	77.49 ±10.60	8.15 ±3.37	5.22 ±5.54	0.13 ±0.20	4.45 ±7.83	1.43 ±7.56	0.72 ±0.31	2.37 ±1.54	0	
	3	33.57 ±3.30	51.68 ±7.64	4.66 ±4.93	0.94 ±1.02	5.93 ±7.43	2.04 ±5.01	0.45 ±0.20	0.68 ±0.93	0	4.9 (a)
	4	69.47 ±6.31	15.18 ±1.35	4.13 ±5.28	0.86 ±0.79	2.39 ±3.35	6.38 ±6.13	0.82 ±0.21	0.51 ±0.28	0.20 ±0.20	
	5	88.32 ±4.68	3.71 ±0.57	1.56 ±2.49	0.03 ±0.06	2.53 ±2.99	2.72 ±5.44	0.92 ±0.08	0.18 ±0.11	0	
C	1	0.91 ±0.72	84.73 ±6.02	8.55 ±5.36	0.07 ±0.14	1.99 ±2.46	3.02 ±2.80	0.19 ±0.12	0.51 ±0.16	0	4.9 (k)
	2	73.45 ±6.16	16.57 ±2.14	2.64 ±5.29	0.40 ±0.63	1.43 ±2.17	3.77 ±5.23	1.23 ±0.18	0.17 ±0.21	0.30 ±0.60	
	1	24.11 ±1.35	64.18 ±5.66	4.33 ±4.47	0.08 ±0.11	0	6.05 ±6.90	0..40 ±0.09	0.76 ±0.49	0.06 ±0.09	4.10 (a)
	2	69.82 ±0.78	15.27 ±1.04	11.35 ±3.34	0.57 ±0.77	1.25 ±2.50	0	0.96 ±0.13	0.31 ±0.19	0.43 ±0.38	
	1	42.83 ±4.08	44.81 ±5.54	2.39 ±2.93	0.13 ±0.26	7.97 ±4.42	1.22 ±2.45	0.38 ±0.13	0.18 ±0.09	0.04 ±0.09	4.10 (k)
	2	75.76 ±1.48	16.14 ±0.50	2.44 ±2.75	0.21 ±0.29	1.25 ±1.75	2.28 ±2.41	1.06 ±0.13	0	0.82 ±0.16	

*Point Scan Locality - STEM-EDS assessment at each locality labeled with a numerical figure was determined by averaging nearly 120-150 local point scans at the region of interest.

4.1.4 Transmission Electron Microscopy of the Neutron Irradiated HT9 Cladding

The STEM-BF and STEM-EDS maps of a FIB lamella-9 produced from the neutron irradiated HT9 cladding are presented in Figs. 4.13 (a-h). Markers labeled 1-3 in Fig. 4.13 (a) presents localities from where SAED patterns presented in Figs. 4.13 (m-p) were produced. The black dashed boxes labeled 1'-3' in Fig. 4.13 (a) presents localities from where high magnification STEM-EDS maps presented in Figs 4.14-4.16 were produced. Figs. 4.13 (m-p) revealed that the matrix phase of the neutron irradiated HT9 cladding was BCC structured Fe indexed at the [011] and [113] zone axes. The local chemical composition of the matrix phase detailed in Table. 4.2 was determined via assessment of multiple EDS point scans acquired at the localities labeled 1-3 in Fig. 4.13 (a). The STEM-EDS assessments revealed that the matrix phase of the neutron irradiated HT9 cladding possessed a local chemical composition of Fe~12wt.%Cr. More interestingly, the STEM-EDS maps also revealed the presence of Xe fission gas in a small pocket/cavity (see dashed white circle with a red arrow in Fig. 4.13 (i)).

The high magnification STEM-BF micrographs presented in Figs. 4.14 (a), 4.15 (a) and 4.16 (a) were produced at localities labeled 1'-3' in Fig. 4.13 (a). Consequently, Figs. 4.14 (b-h), 4.15 (b-h), and 4.16 (b-h) present high magnification STEM-EDS maps of the STEM-BF micrographs presented in Figs. 4.14 (a), 4.15 (a) and 4.16 (a). The high magnification STEM-EDS maps revealed the presence of various types of precipitates, and markers labeled 4-6 in Fig. 4.14 (a) and 4.15 (b) show localities from where multiple EDS point scans were produced for estimating the chemical compositions of the precipitates identified in this study. The high magnification STEM-EDS assessments revealed the presence of two types of precipitates rich in Fe (~48wt.%Fe and ~60wt.%Fe), and an FP precipitate rich in Nd (~31wt.%Nd). A more detailed estimation on the chemical compositions of the precipitates is presented in Table. 4.2.

Currently, there is no available database or study that categorizes the crystal structure of complex FP precipitate phases that migrate into steel claddings as a consequence of neutron irradiation. Hence, a detailed assessment of the crystal structure of the complex FP precipitate phases presented in Figs. 4.14-4.16 was not performed in the current study and requires further investigation. Furthermore, a comprehensive investigation of different types of FP precipitates is of precedence since the crystal structure of a phase contributes severely to the mechanical properties exhibited by the material. A detailed assessment of the effects of FP precipitates and

migration of FP on the localized mechanical properties of the neutron irradiated HT9 cladding is provided in Section 4.4 of the dissertation.
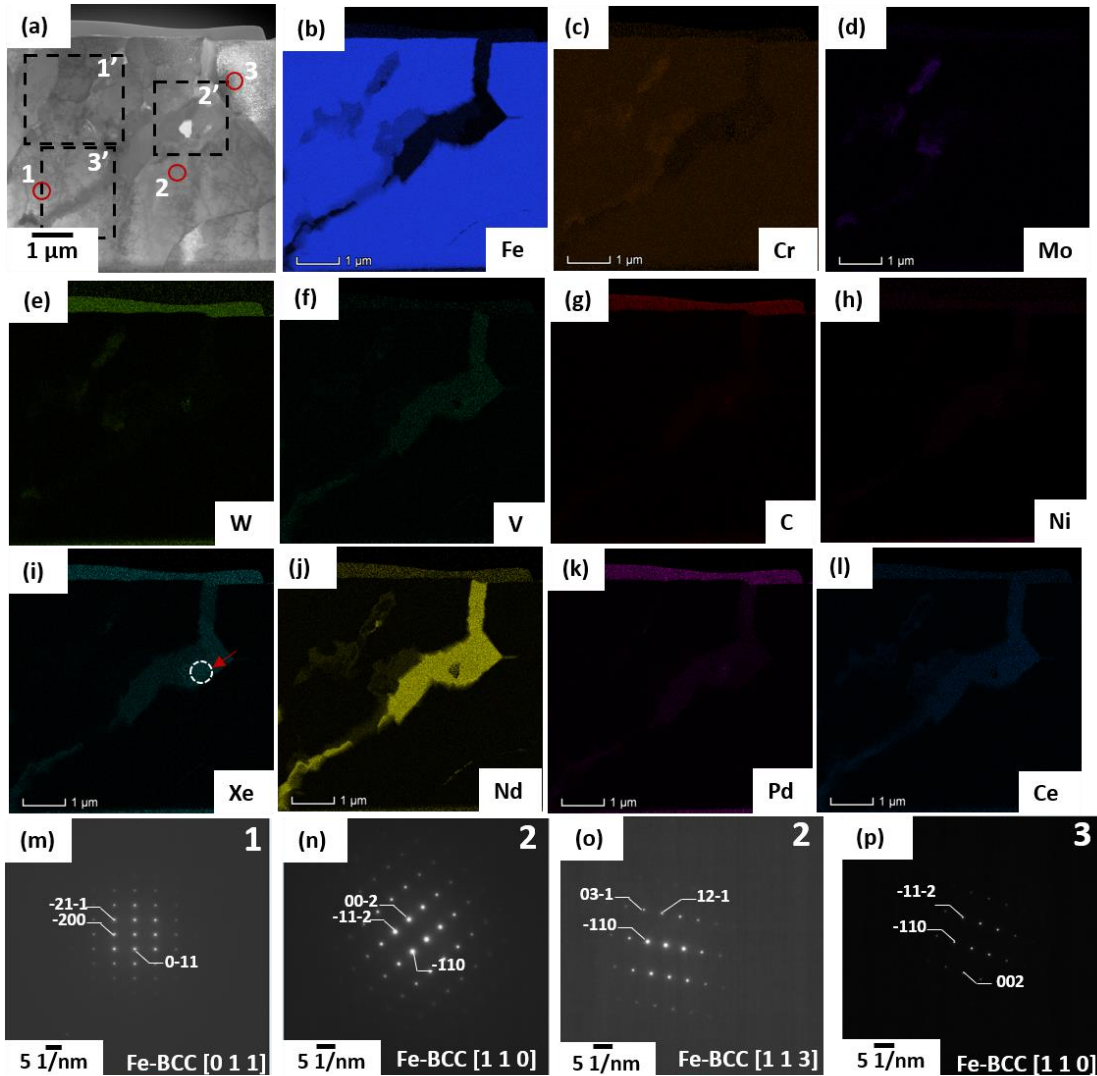
Figure 4.13: (a) STEM-BF micrograph of FIB lamella-9 from the neutron irradiated HT9 cladding. STEM-EDS maps in (b-l) show elemental maps of Fe, Cr, Mo, W, V, C, Ni, Xe, Nd, Pd, and Ce, respectively. Dashed white circles with a red arrow in (i) revealed a locality with Xe gas trapped in the lamella. The SAED patterns presented in (m-p) were produced at localities labeled 1-3 in (a). The SAED patterns presented in (m-p) indicate that the matrix of the neutron irradiated HT9 cladding is Fe-BCC at the [011], [110], [113], and [110] zone axes, respectively. Dashed black box labeled 1'-3' show localities from where high magnification STEM-EDS maps presented in Figs. 4.14-4.16 were produced.
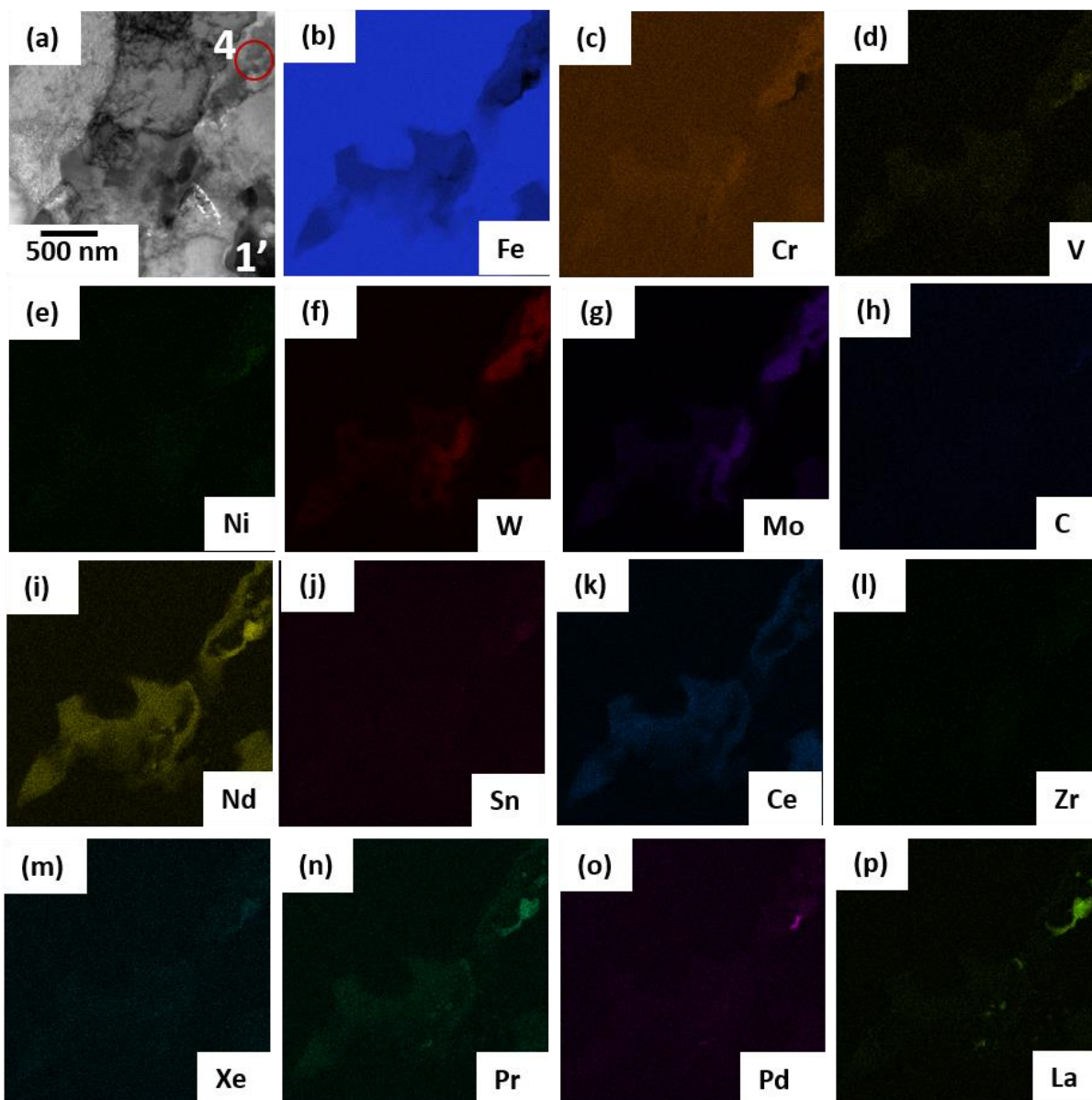
Figure 4.14: (a) STEM-BF micrograph of the dashed black box labeled 1' in FIB lamella-9 (see Fig. 4.13 (a)). STEM-EDS maps in (b-p) show elemental maps of Fe, Cr, V, Ni, W, Mo, C, Nd, Sn, Ce, Zr, Xe, Pr, Pd, and La respectively. The STEM-EDS maps presented in (b-p) revealed the presence of various types of precipitates. The red circle labeled 4 in (a) shows the locality from where multiple point scans were produced for determining the local chemical composition of the FP precipitate detailed in table 4.2.
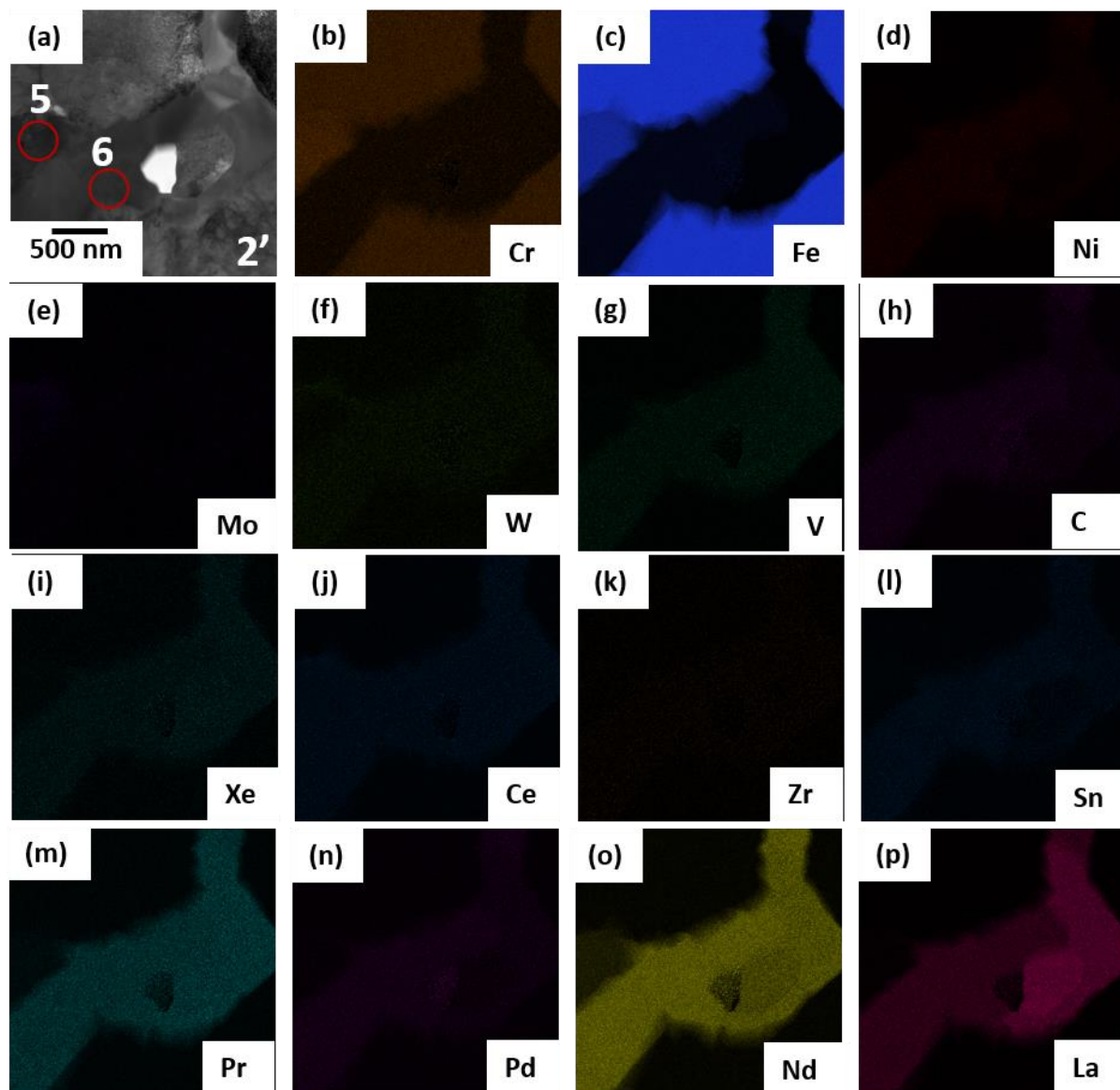
Figure 4.15: (a) STEM-BF micrograph of the dashed black box labeled 2' in FIB lamella-9 (see Fig. 4.13 (a)). STEM-EDS maps in (b-p) show elemental maps of Cr, Fe, Ni, Mo, W, V, C, Xe, Ce, Zr, Sn, Pr, Pd, Nd, and La respectively. The STEM-EDS maps presented in (b-p) revealed the presence of various types of FP precipitates. The red circles labeled 5 and 6 in (a) show locality from where multiple point scans were produced for determining the local chemical composition of the FP precipitates detailed in table 4.2.
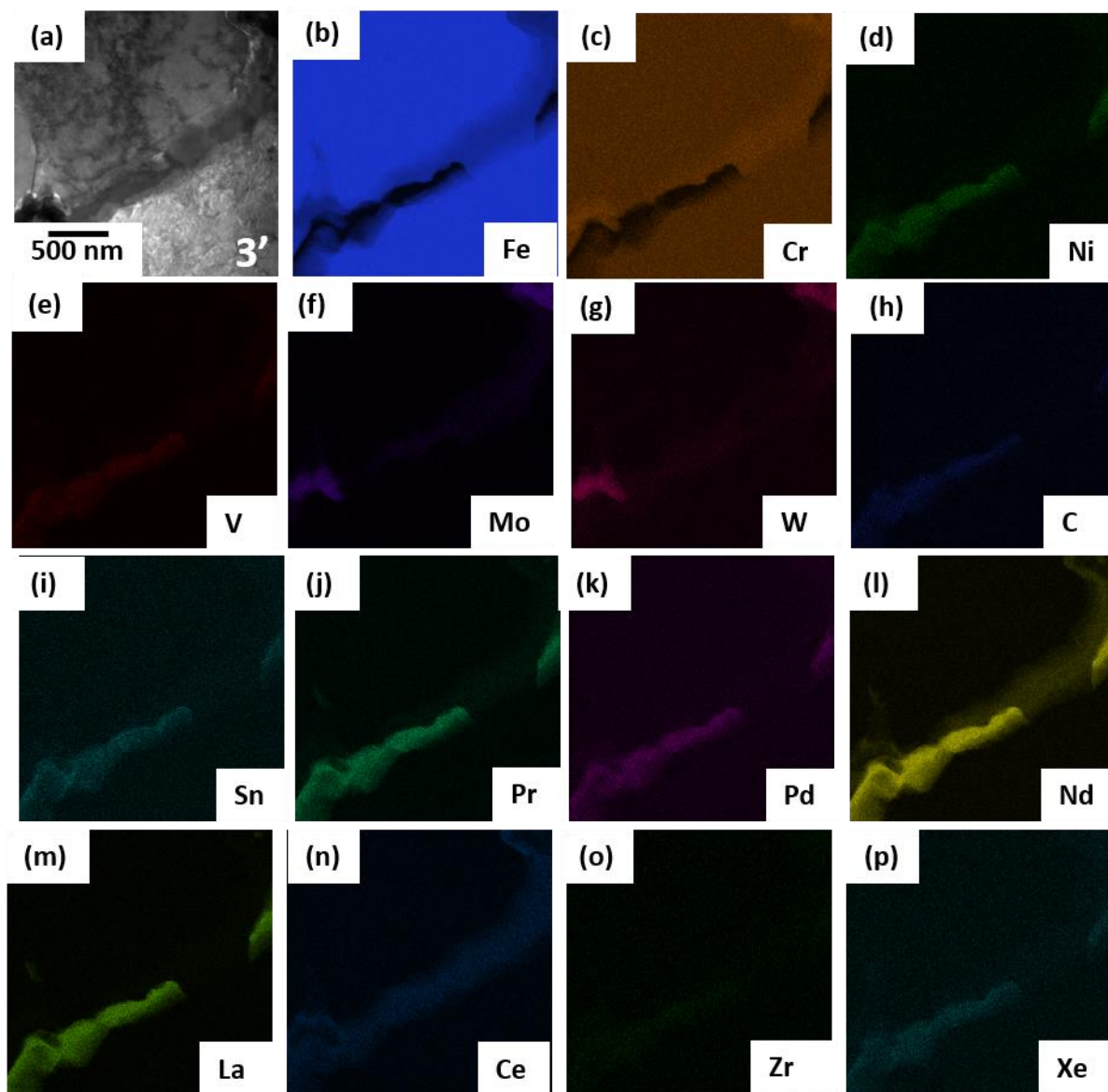
Figure 4.16: (a) STEM-BF micrograph of the dashed black box labeled 3' in FIB lamella-9 (see Fig. 4.13 (a)). STEM-EDS maps in (b-p) show elemental maps of Fe, Cr, Ni, V, Mo, W, C, Sn, Pr, Pd, Nd, La, Ce, Zr, and Xe respectively. The STEM-EDS maps presented in (b-p) revealed the presence of various types of precipitates.

Table 4.2: STEM-EDS point scan assessment of various localities in the neutron irradiated HT9 cladding

Scan No (#)	Major Elements (wt.%)							Other Elements (wt.%)								Fig. No
	Fe	Cr	Mo	W	Ni	V	C	Nd	Zr	Pd	Pr	Sn	Ce	La	Xe	
1	83.1 ± 1.71	12.7 ± 0.89	0.37 ± 0.07	1.89 ± 0.68	0.31 ± 0.06	0.86 ± 0.17	0.74 ± 0.36	-	-	-	-	-	-	-	-	4.13 (a)
2	85.1 ± 0.81	11.3 ± 0.59	0.24 ± 0.18	1.2 ± 0.08	0.56 ± 0.18	0.84 ± 0.13	0.83 ± 0.17	-	-	-	-	-	-	-	-	4.13 (a)
3	84.5 ± 0.66	12.1 ± 0.38	0.36 ± 0.3	1.49 ± 0.29	0.34 ± 0.01	0.64 ± 0.18	0.56 ± 0.24	-	-	-	-	-	-	-	-	4.13 (a)
4	48.6 ± 1.0	12.5 ± 0.38	10.2 ± 0.43	6.82 ± 0.58	0.7 ± 0.14	0.64 ± 0.05	0.71 ± 0.05	6.37 ± 0.36	1.2 ± 0.34	1.60 ± 0.14	2.72 ± 0.26	1.49 ± 0.05	2.93 ± 0.28	1.82 ± 0.52	1.58 ± 0.03	4.14 (a)
5	60.8 ± 0.69	12.7 ± 0.59	2.27 ± 0.34	1.32 ± 2.84	0.46 ± 0.20	0.81 ± 0.07	1.09 ± 0.12	9.53 ± 0.32	-	-	3.54 ± 0.2	-	4.39 ± 0.43	1.72 ± 0.27	1.26 ± 0.13	4.15 (a)
6	9.35 ± 1.32	3.61 ± 0.43	0.85 ± 0.28	2.06 ± 0.11	2.35 ± 0.42	2.40 ± 0.39	2.35 ± 0.28	31.2 ± 0.19	1.49 ± 0.05	4.19 ± 0.18	12.2 ± 1.30	4.30 ± 0.2	4.5 ± 0.25	15.0 ± 0.52	3.03 ± 0.47	4.15 (a)

*Point Scan Localities (#) labeled 1-6 were determined by averaging nearly 120-150 local point scans at the region of interest.

4.2 Microscale Characterization

Microscale characterization of the neutron irradiated U-10wt.%Zr fuel cross-section that achieved a burnup of 5.7 at.% was performed via serial sectioning of 4 FIB cuboids of ~(30µm x 30µm x 30µm) in size. Markers labeled 10-13 in Fig. 2.1 shows localities from where the FIB cuboids were produced for the serial sectioning experiments. High magnification BSE micrographs presented Figs. 4.17 (a-d) show that the FIB cuboids produced for the serial sectioning experiments were obtained near localities from where FIB lamellas and FIB obelisks were obtained for TEM investigations and synchrotron µ-CT experiments, respectively. As specified in Section 3.3 and presented in Fig. 4.17 (a-d), a total of 4 FIB cuboids (from regions A, A/B, B, and FCCI) were produced and serially sectioned with a pre-programmed slice thickness of 100 nm per slice. Post sectioning of a 100nm slice, a BSE micrograph, and an EDS map of the sectioned surfaces were produced, and this process was performed until minimal or no material was available for further serial sectioning. Furthermore, performing the microstructural assessment in such a manner provided a depth perspective to the data produced.
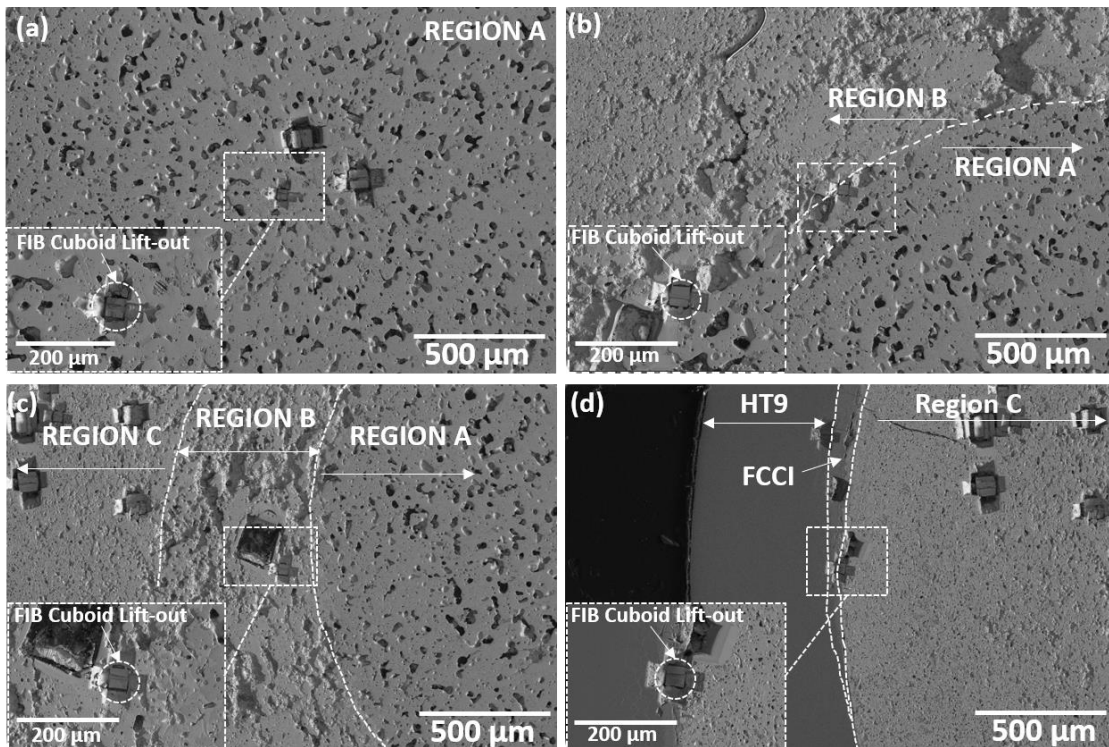
Figure 4.17: BSE images of localities from where the FIB cuboids from regions (a) A, (b) A/B, (c) B, and (d) FCCI of the fuel cross-section that achieved a burnup of 5.7 at.% were produced.

4.2.1 Serial Sectioning of Region A, Region A/B, and Region B

The BSE micrograph of the FIB cuboid-1 from region A of the neutron irradiated U-10wt.%Zr fuel cross-section that achieved a burnup of 5.7 at.%, is presented in Fig. 4.18 (a), while Fig. 4.18 (b-h) show the serial sectioned BSE and EDS map overlays at a depth of 0 µm (the first layer or surface of the FIB cuboid-1), 2.2 µm, 4.4 µm, 6.6 µm, 8.8 µm, 11.0 µm, and 13.2 µm, respectively. As shown in the elemental map color scheme box presented in Fig. 4.18, green, red, blue, yellow, and dark blue shades in the BSE and EDS map overlays represent U, Zr, Palladium (Pd), Neodymium (Nd), and Cerium (Ce), respectively. The serial sectioning experiment of the FIB cuboid-1 from region A revealed the following: (1) a U-Zr matrix phase, (2) U-rich precipitates in the U-Zr matrix phase and along the grain boundaries, (3) large spherical pores, and (4) Nd-Pd-Ce based FP precipitates in pores. Furthermore, correlating the TEM investigations (see Section 4.1.2) and the serial sectioning experiments (see Fig. 4.18 (b-h)) at region A, indicate that the U-Zr matrix phase is δ-UZr$_2$, and the U-rich precipitates are α-U. A comprehensive assessment of the phases and probable phase transformation routes involved in region A of the fuel cross-section is provided in Section 5 of the dissertation.
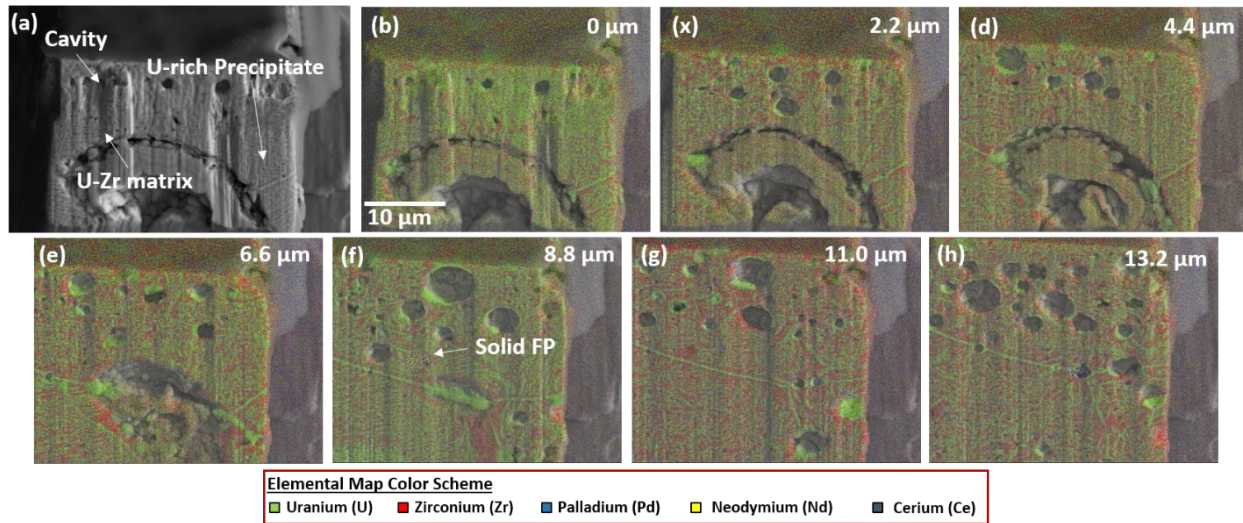
Figure 4.18: (a) BSE micrograph of the FIB cuboid-1 from region A, and (b-h) BSE and EDS map overlay of the FIB cuboid serial sectioned at a depth of 0 µm, 2.2 µm, 4.4 µm, 6.6 µm, 8.8 µm, 11.0 µm, and 13.2 µm, respectively.

The BSE micrograph of the FIB cuboid-2 from region A/B of the neutron irradiated U-10Zr fuel cross-section that achieved a burnup of 5.7 at.% is presented in Fig. 4.19 (a), while Figs.

4.19 (b-h) show the serial sectioned BSE and EDS map overlays at a depth of 0 µm (the first layer or surface of the FIB cuboid-2), 1.7 µm, 3.1 µm, 4.5 µm, 5.9 µm, 7.1 µm, and 8.5 µm, respectively. As shown in the elemental map color scheme box presented in Fig. 4.19, green, red, blue, yellow, and dark blue shades in the BSE and EDS map overlays represent U, Zr, Pd, Nd, and Ce, respectively. The serial sectioning experiment of the FIB cuboid-2 from region A/B revealed the following: (1) a U-Zr grain with U-rich precipitates, (2) U-rich grains, (3) small spherical pores in U-rich grains, and (4) large spherical pores in a U-Zr grain with U-rich precipitates. Furthermore, correlating the TEM investigations (see Section 4.1.2) and the serial sectioning experiments (see Fig. 4.19 (b-h)) at region A/B, indicate that the U-Zr grain with U-rich precipitates are δ-UZr$_2$ and α-U phases, respectively.

Additionally, the FIB cuboids from both region A and region A/B possess: (1) a U-Zr grain with U-rich precipitates, and (2) large spherical pores in the δ-UZr$_2$ phase. The presence of similar features in the FIB cuboids produced from regions A and A/B is most likely a consequence of the FIB cuboid-2 being produced at the intersection of the regions A and B. More interestingly, both the serial sectioning and synchrotron µ-CT experiments (detailed in Section 4.3.1) revealed the presence of spherical and aspherical pores with varying sizes at region A/B. A detailed assessment of the various microstructural alterations observed via serial sectioning of FIB-cuboid 2 from region A/B of the neutron irradiated U-10wt.%Zr fuel cross-section is provided in Section 5.2.1 of the dissertation.
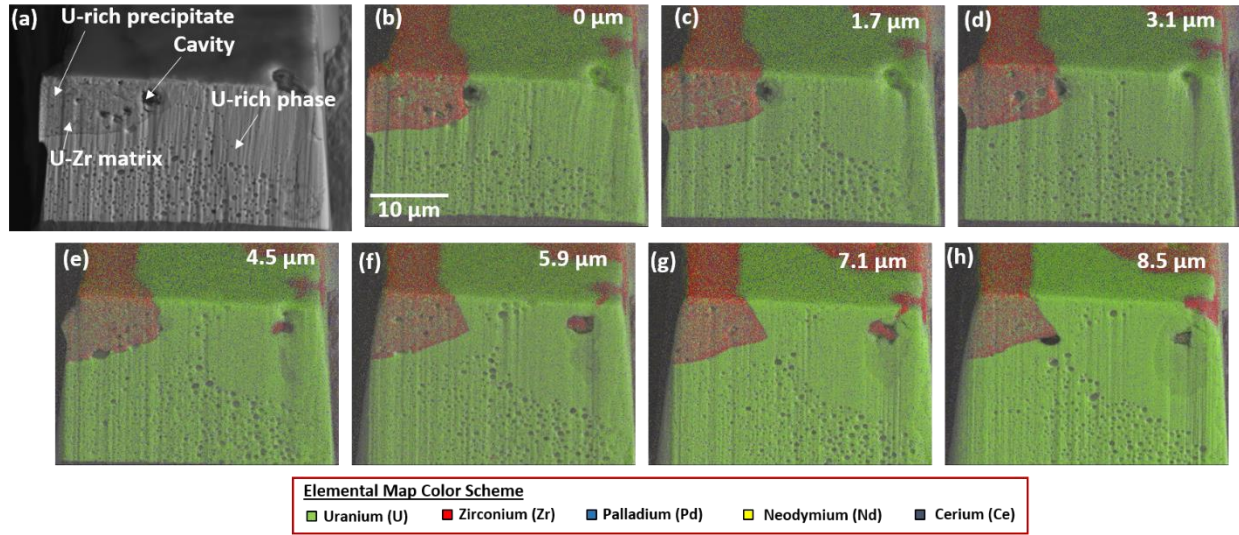
Figure 4.19: (a) BSE micrograph of the FIB cuboid-2 from region A/B, and (b-h) BSE and EDS map overlay of the FIB cuboid serial sectioned at a depth of 0 µm, 1.7 µm, 3.1 µm, 4.5 µm, 5.9 µm, 7.1 µm, and 8.5 µm, respectively.

The BSE micrograph of the FIB cuboid-3 from region B of the neutron irradiated U-10wt.%Zr fuel cross-section that achieved a burnup of 5.7 at.% is presented in Fig. 4.20 (a), while Figs. 4.20 (b-h) show the serial sectioned BSE and EDS map overlays at a depth of 0 µm (the first layer or surface of the FIB cuboid-3), 2.8 µm, 5.6 µm, 8.4 µm, 11.2 µm, 14.0 µm, and 16.8 µm, respectively. As shown in the elemental map color scheme box in Fig. 4.20, green, red, blue, yellow, and dark blue shades in the overlaid BSE and EDS maps represent U, Zr, Pd, Nd, and Ce, respectively. The serial sectioning experiment of the FIB cuboid-3 from region B revealed the following: (1) U-Zr grains with spherical pores, (2) U-rich grains with spherical and/or aspherical pores, (3) extended and interconnected pores, and (4) Nd-Ce-Zr FP precipitates in various types of pores (i.e. both spherical and aspherical). The presence of spherical and aspherical porosities in region B of the neutron irradiated fuel cross-section was also identified via synchrotron µ-CT experiments (see Section 4.3.1). Furthermore, in region B, both the serial sectioning experiments and the TEM investigations (see Section 4.1.3) revealed the following: (1) the presence of different types of U-rich grains with varying levels of inhomogeneities (i.e. certain U-rich grains appear to be more affected by radiation), and (2) a high concentration of FP precipitates. A more comprehensive explanation on the various microstructural alterations observed via serial sectioning of FIB-cuboid 3 from region B of the neutron irradiated U-10wt.%Zr fuel cross-section is detailed in Section 5.2.1 of the dissertation.
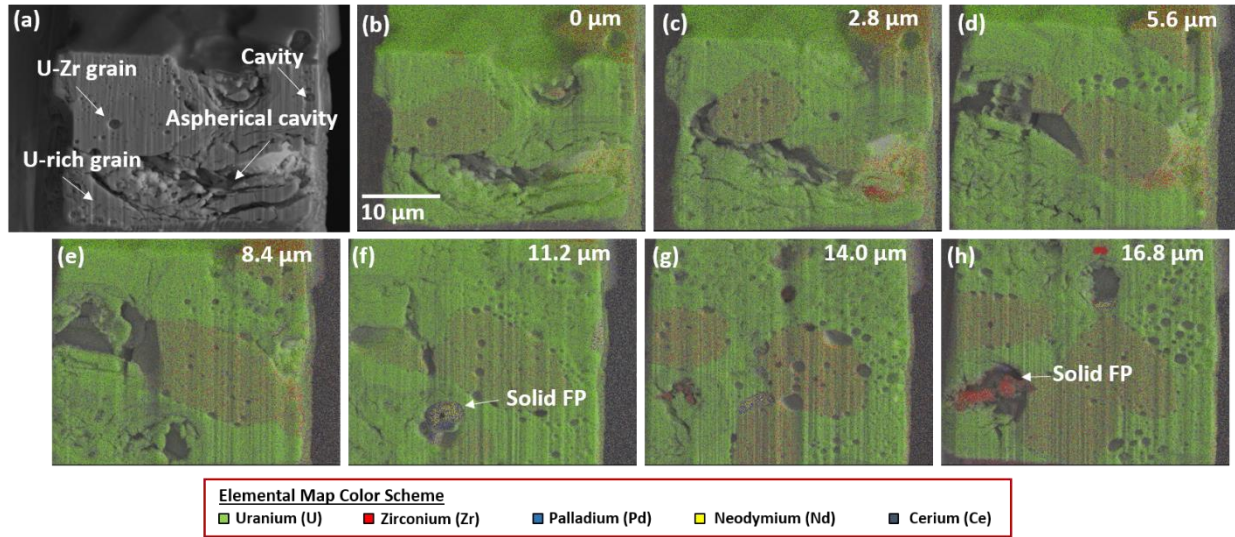
Figure 4.20: (a) BSE micrograph of the FIB cuboid-3 from region B, and (b-h) BSE and EDS map overlay of the FIB cuboid serial sectioned at a depth of 0 µm, 2.8 µm, 5.6 µm, 8.4 µm, 11.2 µm, 14.0 µm, and 16.8 µm, respectively.

4.2.2   Serial Sectioning of the FCCI Locality

Fig. 4.21 (a) presents the BSE micrograph of the FIB cuboid-4 from the FCCI locality of the neutron irradiated U-10wt.%Zr fuel cross-section that achieved a burnup of 5.7 at.%, while Figs. 4.21 (b-h) show the serial sectioned BSE and EDS map overlays at a depth of 0 µm (the first layer or surface of the FIB cuboid-4), 3.6 µm, 7.2 µm, 10.8 µm, 14.4 µm, 18.0 µm, and 21.6 µm, respectively. As shown in the elemental map color scheme box in Fig. 4.21, green, red, blue, yellow, dark blue, cyan, and orange colors in the overlaid BSE and EDS maps represent U, Zr, Pd, Nd, Ce, Cr, and Fe, respectively. The serial sectioning of the FIB cuboid-4 from the FCCI locality revealed the following: (1) U-rich grains on the fuel side, (2) U-Zr intermetallic grains on the fuel side, (3) spherical and aspherical cavities on the fuel side, (4) Zr-rich layer acting as a barrier and mitigating the interdiffusion of U into the cladding, (5) Ce-Pd-Nd FCCI layer between the fuel and cladding sides, (6) Cr-rich precipitate clusters on the cladding side, and (7) HT9 cladding side (rich in Fe).

Although FCCI is a complex phenomenon to assess, it occurs at the onset of point of contact between the neutron irradiated fuel and cladding surfaces and is consequently detrimental to the integrity of the fuel system. A comprehensive assessment on the probable phenomena

89

occurring at the FCCI locality of the neutron irradiated U-10wt.%Zr fuel and HT9 cladding are detailed in Section 5.2.2 of the dissertation, and the effects of FCCI on the local mechanical properties of the neutron irradiated HT9 cladding is presented in Section 4.4 and Section 5.4 of the dissertation.
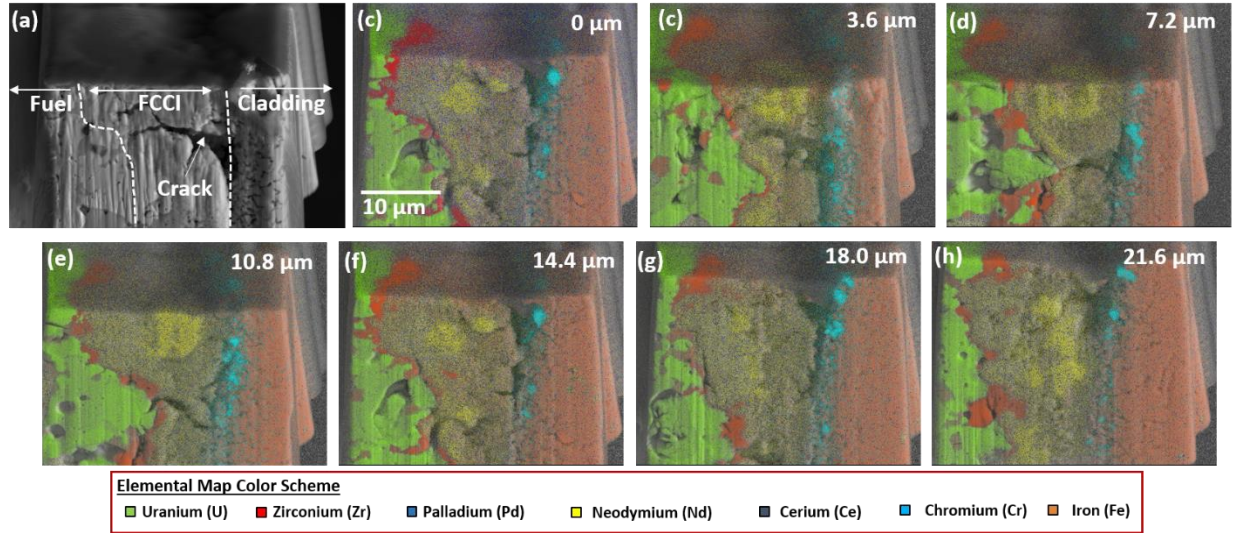
Figure 4.21: (a) BSE micrograph of the FIB cuboid-4 from the FCCI locality, and (b-h) BSE and EDS map overlay of the FIB cuboid serial sectioned at a depth of 0 µm, 3.6 µm, 7.2 µm, 10.8 µm, 14.4 µm, 18.0 µm, and 21.6 µm, respectively.

4.3   Mesoscale Characterization[1]

Mesoscale characterization of the neutron irradiated U-10wt.%Zr fuel cross-section that achieved a burnup of 5.7 at.% was performed via high energy X-ray synchrotron µ-CT experiments on FIB obelisks that were produced from region A/B, region B, and HT9 locality. As presented in Fig. 3.1, markers labeled 14-16 show localities from where the FIB obelisks were produced for the synchrotron µ-CT experiments. BSE micrographs presented Figs. 4.22 (a-c) show high magnification images of localities from where the FIB obelisks were produced. As specified in Section 3.3, both absorption and phase contrast µ-CT experiments were performed with a pixel

---

[1] Portions of Section 4.3 was recently published as an article: Thomas, J., Figueroa, A., Nori, S.T., Ren, R., Kenesei, P., Almer, J., Hunter, J., Harp, J. and Okuniewski, M.A., The application of synchrotron micro-computed tomography to characterize the three-dimensional microstructure in irradiated nuclear fuel. Journal of Nuclear Materials, p.152161, 2020. Permissions and copyrights to re-print the article into the dissertation has been attained from all the authors and the journal.

pitch of 0.746 µm at a distance of 6 mm and 40 mm from the detector, respectively. The mesoscale characterization of the neutron irradiated fuel cross-section presented in this dissertation involves the 3D segmentation and assessment of various phase regions and porosity in the FIB obelisks produced from region A/B, region B, and HT9, respectively. Furthermore, as specified in section 3.3, the term "phase regions" used throughout the synchrotron µ-CT sections of the dissertation refers to the specimen's microstructure that corresponds to self-similar compositional regions determined via the X-ray phase and absorption interactions. Although the crystal structure and chemical composition of the phases will require additional complementary techniques for determination, such as diffraction and spectroscopy methods, they are correlated to the TEM investigations presented in Section 4.1. Furthermore, the FIB lamella lift-outs used for the TEM investigations were produced near localities from where FIB obelisks were produced for the mesoscale assessments.
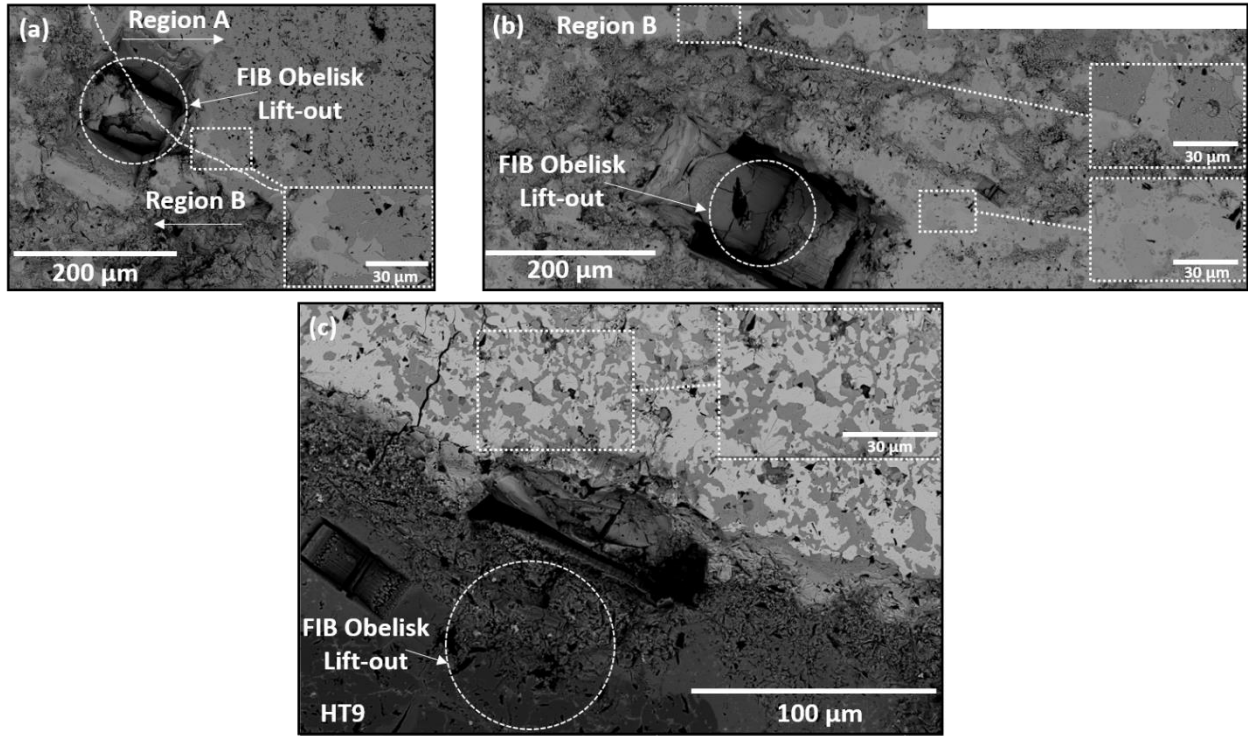
Figure 4.22: BSE micrographs at localities from where FIB obelisks from the region (a) A/B, (b) B, and (c) HT9 of the fuel cross-section that achieved a burn up of 5.7 at.% were produced for synchrotron µ-CT experiments.

4.3.1 Synchrotron μ-CT Experiments of Region A/B and Region B

As specified in Section 3.3, the μ-CT data produced from the FIB obelisks attained from regions A/B and B were reconstructed into 32-bit float images which were sequentially arranged to form image stacks. Reconstructing the images as a 32-bit float image stacks facilitated the attainment of the highest fidelity data for subsequent image processing and image analysis. The absorption and phase contrast μ-CT image stacks from regions A/B and B was then analyzed in both 2D and 3D to determine the following: (1) volume fraction of various phase regions and porosity, (2) the chemical composition of various phase regions, (3) categorization of different porosity classes, and (4) localized microscopic fuel swelling.
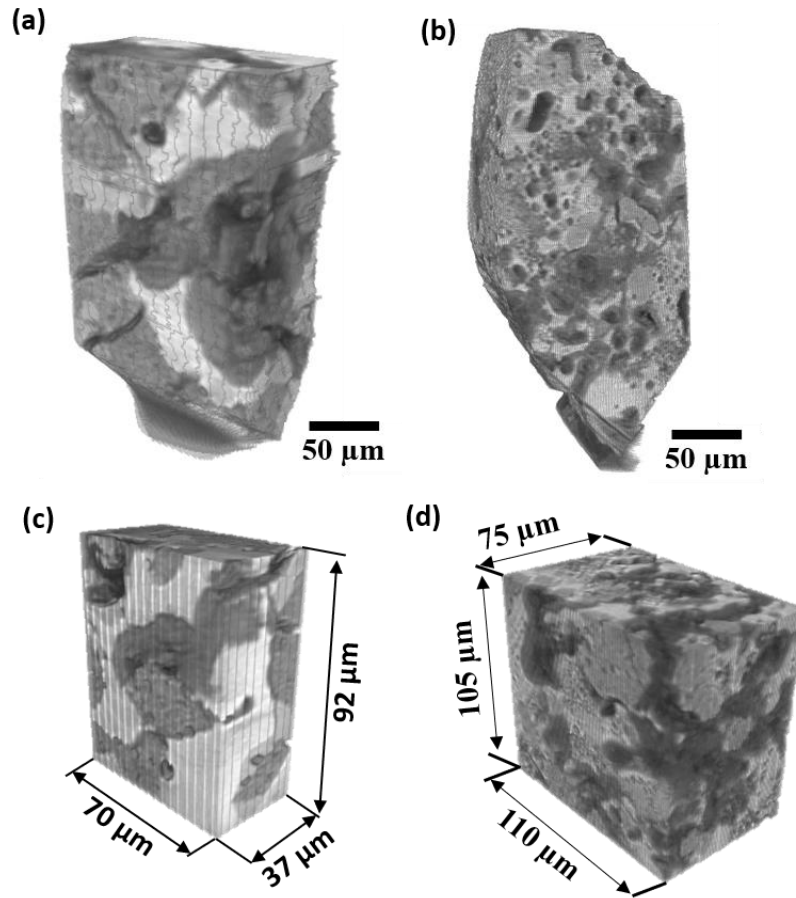
Figure 4.23: 3D reconstruction of the synchrotron X-ray generated phase contrast μ-CT image stacks of the FIB obelisks from regions (a) A/B, and (b) B of the neutron irradiated U-10Zr fuel. The sectioned 3D phase contrast μ-CT view of the FIB obelisks from regions A/B and B used for subsequent image analysis is presented in (c) and (d), respectively [36].

92

Figs. 4.23 (a and b) show the reconstructed FIB obelisks from regions A/B and B, while Figs. 4.23 (c and d) show reduced sections of the FIB obelisks that were used for subsequent image analysis. The μ-CT image of FIB obelisks from regions A/B and B had a thickness of 0.746 μm, defined by the voxel size of the detector used at beamline 1-ID-E, and each voxel in the synchrotron X-ray absorption and phase contrast μ-CT image stack was 0.41 μm^3 in volume. In this study, a two-voxel resolution limit was determined from an assessment of individual μ-CT images. Hence, features with a size smaller than two voxels were not resolvable and therefore categorized as noise in the data. Furthermore, the two-voxel resolution limit was also based on the Nyquist theorem which states that the sampling interval should be greater than or equal to twice the highest spatial resolution [115].

As shown in Fig. 4.23, the FIB obelisks from regions A/B and B were sectioned into smaller portions for subsequent image analysis. Sectioning of the FIB obelisks was a necessity for following reasons: (1) to remove external artifacts (such as oxidation layers or Ga ion beam damaged regions) that were present on the specimen surface, (2) to reduce the computational time, and (3) to establish a predefined cuboidal specimen volume for analysis. The sectioned FIB obelisks from regions A/B and B were then segmented into distinct phase regions, and each phase region is interdependent on the mass attenuation coefficient. An example of the different phase regions identified in the sectioned FIB obelisk from region B is as shown in Fig. 4.24. Absorption contrast μ-CT images in Fig. 4.24 (a-c) illustrates the observation of three distinct phase regions with varying levels of attenuation-based voxel values and porosity with low attenuation values. The darker phase regions were indicative of lower mass density (i.e. U-poor regions), while the converse was true for the phase regions which appeared brighter (i.e. U-rich regions).

The phase contrast μ-CT images in Fig. 4.24 (d-f) rely on the variation of the refraction of X-rays that are incident on various interfaces within the specimen [116]. When X-rays penetrate a specimen surface, they are absorbed and result in a subsequent change in phase of the wave, and unlike absorption contrast μ-CT, phase contrast μ-CT is not solely dependent on amplitude changes of the diffracted beam, but rather utilizes the changes in the phase of X-rays that are inherently dependent on the changes in the refractive index of the material [117,118]. Furthermore, as shown in Figs. 4.24, 4.25 and 4.26, both absorption contrast and phase contrast methods were used to assess the FIB obelisks produced from regions A/B and B. Assessment of the absorption contrast μ-CT images facilitated the determination of the localized chemical compositions of

different phase regions, while assessment of the phase contrast μ-CT images facilitated the determination of the volume fractions occupied by various phase regions and pores. A visual comparison between the phase and absorption contrast μ-CT images presented in Figs. 4.24 (a-f) confirms that the spatial resolution of pores, U-rich, U-intermediate, and U-poor regions (see regions labeled IV, III, II, and I in Fig. 4.24, respectively) were enhanced with sharper interfacial boundaries for the phase contrast μ-CT images. Consequently, phase contrast μ-CT images were used for segmentation and volume fraction estimation of phase regions and pores.
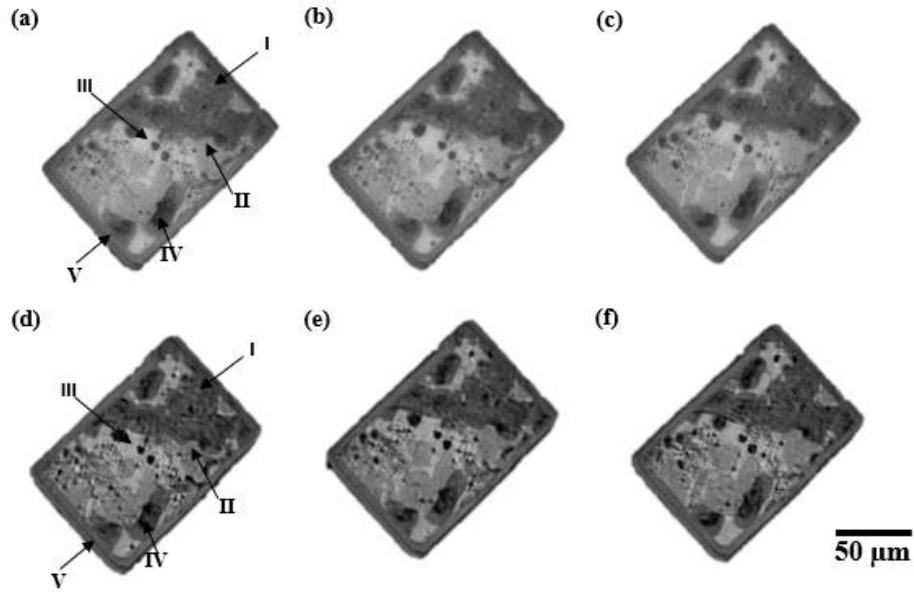
Figure 4.24: Sequential synchrotron X-ray generated tomography slices produced from (a-c) absorption contrast imaging, (d-f) phase contrast imaging of a FIB obelisk extracted from region B of the neutron irradiated U-10wt.%Zr. In (a, d), region I (dark gray) indicates a U-poor area, region II (light gray) indicates a U-intermediate area, region III (white) indicates a U-rich area, region IV (black) indicates pores, and region V indicates a surface damaged and/or oxidation area on the outer periphery of the FIB obelisk [36].

The phase regions identified in the sectioned FIB obelisks from regions A/B and B in this study were categorized as U-rich, U-intermediate, and U-poor regions for the following reasons: (1) Harp et al. [6] reported that the average chemical composition at regions A and B were U~30-35wt.%Zr and U~4wt.%Zr, respectively, and other transuranic elements were not reported. (2) From the neutronic calculations of this irradiated fuel, U comprises >97% by weight of the transuranic material, and consequently, U will dominate the attenuation coefficients for the transuranic elements. (3) The attenuation coefficients for pure U and Zr at an X-ray energy of 71.68 keV are 9.373 mm^{-1} and 1.662 mm^{-1}, respectively [119]. Furthermore, the attenuation and

the average chemical composition of U, which was greater than that of Zr (and transuranic elements) at both regions A/B and B, justified the categorization of the segmented phase regions in this study as U-rich, U-intermediate, and U-poor regions.
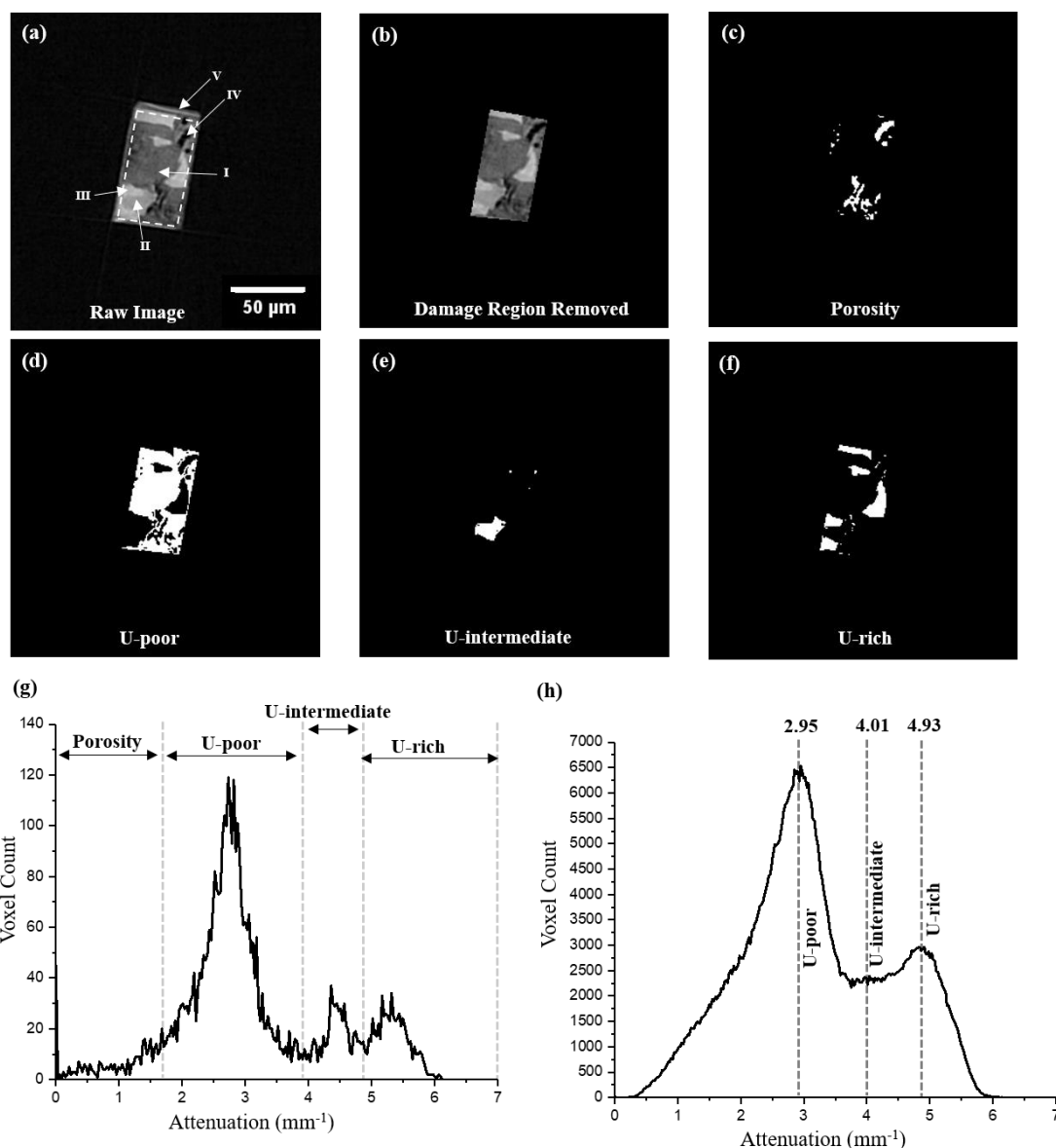
Figure 4.25: Synchrotron X-ray generated tomography slice produced from phase contrast imaging of a sectioned FIB obelisk extracted from region A/B of the neutron irradiated U-10wt.%Zr showing the (a) raw phase contrast image. In (a), region I (dark gray) indicates a U-poor area, region II (light gray) indicates a U-intermediate area, region III (white) indicates a U-rich area, region IV (black) indicates pores, and region V indicates a surface damaged/oxidation area on the outer periphery of the sectioned FIB obelisk. (b) Phase contrast image of the identical slice with the damaged outer region removed. Thresholded images obtained from the phase contrast enhanced image shown in (b) indicate (c) porosity (black), (d) U-poor (dark gray), (e) U-intermediate, (light gray), and (f) U-rich regions (white). (g) Attenuation-based histogram from a phase μCT image. Dashed black lines in (g) correspond to threshold ranges used for segmentation of porosity, U-poor, U-intermediate, and U-rich regions. (h) Attenuation-based histogram from the absorption contrast tomography image stack. Dashed black lines in (h) correspond to average attenuation values estimated for the U-poor, U-intermediate, and U-rich regions.

The phase contrast μ-CT images of sectioned FIB obelisks from regions A/B and B presented in Figs. 4.25 (a) and 4.26 (a) show images before any image processing. As seen in Figs. 4.25 (a) and 4.26 (a), the outer region of the specimens (the region outside the dotted white box) was observed to have an inconsistent morphology (i.e. an area of ~1052 μm^2 for region A/B and ~2447 μm^2 for region B). The observed varied outer region morphology of the sectioned FIB obelisks was presumed to have resulted from either gallium ion damage during FIB specimen preparation and/or oxidation of the fuel specimens. This inconsistent outer morphology was present in all of the μ-CT images and was therefore excluded in the subsequent analyses to prevent any spurious results in the estimation of U-rich, U-intermediate, and U-poor regions, as well as the porosity (see Figs. 4.25 (b) and 4.26 (b)). After removal of this inconsistent outer region, the dimensions of the sectioned FIB obelisks from regions A/B and B were reduced from ~(79 μm x 43 μm x 92 μm) to ~(70 μm x 37 μm x 92 μm), and ~(125 μm x 89 μm x 105 μm) to ~(110 μm x 75 μm x 105 μm), respectively.

The effect of varying mass attenuations leading to the formation of distinct phase regions is illustrated in further detail in Figs. 4.25 (h) and 4.26 (h). The average attenuation of each phase region (i.e. U-rich, U-intermediate, and U-poor) determined from the stacked histogram (see dashed black lines in Figs. 4.25 (h) and 4.26 (h) indicating the average attenuation) was used in Eq. (3.5) to estimate approximate U-Zr compositions of the phase regions segmented in this study. As shown in Fig. 4.25 (h), the U-rich, U-intermediate, and U-poor regions were estimated to possess average attenuations of 4.93 mm^{-1}, 4.01 mm^{-1}, and 2.95 mm^{-1} at region A/B. While Fig. 4.26 (h) revealed that the U-rich, U-intermediate, and U-poor regions possessed an average attenuation of 5.09 mm^{-1}, 4.11 mm^{-1}, and 2.88 mm^{-1} at region B. Using Eq. (3.5), the average chemical compositions of the U-rich, U-intermediate, and U-poor regions were determined to be ~51.9wt.%U, ~40.1wt.%U, and ~29.5wt.%U at region A/B, and ~54.0wt.%U, ~41.0wt.%U, and ~28.8wt.%U at region B, respectively. Furthermore, Table 4.3 details the average chemical compositions and volume fractions of the different phase regions identified in this study. Even though Eq. (3.5) revealed the average chemical compositions of the phase regions, identified in the sectioned FIB obelisks from regions A/B and B, the chemical compositions can be affected by the presence of various microstructural alterations such as FP, small voids, and other features that are smaller than the resolution of the μ-CT images.
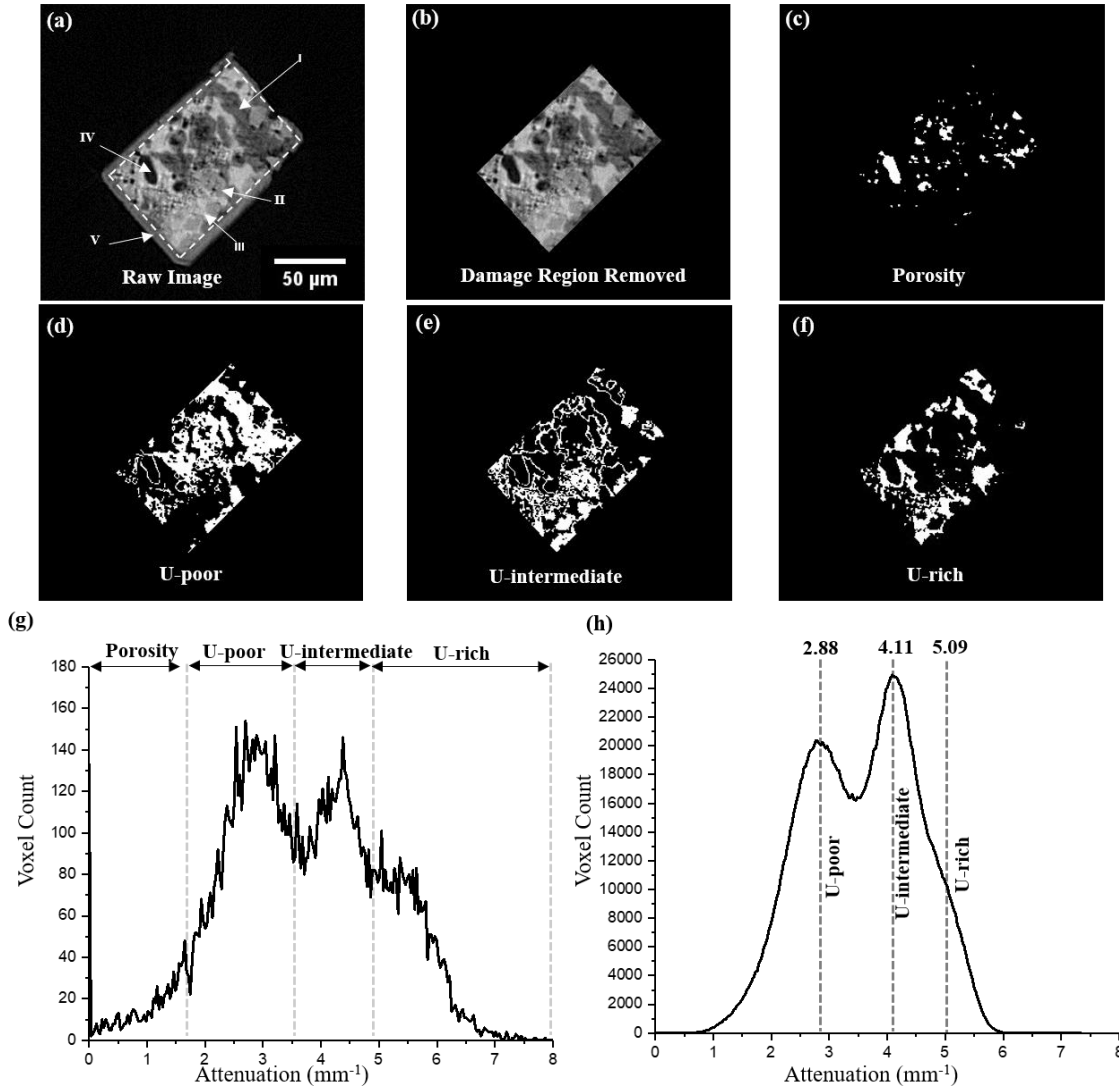
Figure 4.26: Synchrotron X-ray generated tomography slice produced from phase contrast imaging of a section FIB obelisk extracted from region B of the neutron irradiated U-10wt.%Zr showing the (a) raw phase contrast image. In (a), region I (dark gray) indicates a U-poor area, region II (light gray) indicates a U-intermediate area, region III (white) indicates a U-rich area, region IV (black) indicates pores, and region V indicates a surface damaged/oxidation area on the outer periphery of the sectioned FIB obelisk. (b) Phase contrast image of the identical slice with the damaged outer region removed. Thresholded images obtained from the phase contrast enhanced image shown in (b) indicate (c) porosity (black), (d) U-poor (dark gray), (e) U-intermediate, (light gray), and (f) U-rich regions (white). (g) Attenuation-based histogram from a phase µCT image. Dashed black lines in (g) correspond to threshold ranges used for segmentation of porosity, U-poor, U-intermediate, and U-rich regions. (h) Attenuation-based histogram from the absorption contrast tomography image stack. Dashed black lines in (h) correspond to average attenuation values estimated for the U-poor, U-intermediate, and U-rich regions [36].

Figs. 4.25 (c-f) and 4.26 (c-f) show thresholding of porosity and U-rich, U-intermediate, and U-poor regions for the stacked phase contrast μ-CT images from regions A/B and B. Figs. 4.25 (g) and 4.26 (g) show attenuation-based histograms from the representative phase contrast μ-CT image stacks. Dashed black lines in Figs. 4.25 (g) and 4.26 (g) indicate the thresholding ranges used for the segmentation of porosity and U-rich, U-intermediate, and U-poor regions. The attenuation-based voxel values ranging from (0-7) mm^{-1} and (0-8) mm^{-1} encompassed all of the voxels in the phase contrast μ-CT images of the sectioned FIB obelisks from regions A/B and B, respectively, and a value of 0 was assigned as the background (i.e. voxels that are not a part of the sectioned FIB obelisks were assigned a value of 0). Thresholding of attenuation-based voxel values within the sectioned FIB obelisk from region A/B was as follows: 0-1.85 mm^{-1} for porosity, 1.85-3.91 mm^{-1} for the U-poor (dark gray) region, 3.91-4.76 mm^{-1} for the U-intermediate (light gray) region, and 4.76-7.0 mm^{-1} for the U-rich (white) region. Similarly, the thresholding of attenuation-based voxel values within the sectioned FIB obelisk from region B was as follows: 0-1.64 mm^{-1} for porosity, 1.64-3.53 mm^{-1} for the U-poor (dark gray) region, 3.53-4.90 mm^{-1} for the U-intermediate (light gray) region, and 4.90-8.0 mm^{-1} for the U-rich (white) region. The above-mentioned threshold ranges for porosity and U-rich, U-intermediate, and U-poor regions were selected based on a visual assessment of the attenuation-based histogram from the phase contrast μ-CT images. Furthermore, Maire et al. [120] also detailed similar methods of thresholding histograms produced from X-ray tomography images for 3D quantification of phase fractions.

Figs. 4.27 (a-j) shows the 3D volume rendering of the phase contrast μ-CT images obtained from the segmentation technique described in Section 3.1, indicating pores and three separate phase regions of the sectioned FIB obelisks from regions A/B and B of the U-10wt.%Zr fuel as U-poor, U-intermediate, and U-rich regions. Observations of Figs. 4.27 (d and i), indicate that pores with varying morphologies and sizes evolved during the neutron irradiation of the fuel. Figs. 4.27 (a, d, f, and i) reveal that most of the pores were surrounded by a U-poor region (see Figs. 4.25 (c, d) and 4.26 (c, d) for 2D visualization). The volume fractions of pores and three regions identified from the analysis of phase contrast μ-CT experiments of the sectioned FIB obelisks from regions A/B and B are detailed in Table 4.3. This 3D volume fraction assessment indicated the following: (1) the U-poor region occupied the largest volume fraction in both regions A/B and B. (2) In the sectioned FIB obelisk from region A/B, the U-rich and U-intermediate phase regions occupied the second and third highest volume fractions, respectively. (3) In the sectioned FIB obelisk from

region B, the U-intermediate and U-rich phase regions occupied the second and third highest volume fractions, respectively. (4) The porosity volume fraction was greater in the sectioned FIB obelisk from region A/B than region B.

Table 4.3: Manual segmentation of volume fractions of regions determined from phase contrast μ-CT experiments of the sectioned FIB obelisks from regions A/B and B.

Segmented Phase Regions	Region A/B		Region B [36]	
	U Composition (wt%)	Volume Fraction (%)	U Composition (wt%)	Volume Fraction (%)
U-poor	~29.5	52.6	~28.8	39.2
U-intermediate	~40.1	6.90	~41.0	33.4
U-rich	~51.9	26.1	~54.0	20.2
Pores	-	14.4	-	7.20

Note: The term "phase regions" refers to the specimen's microstructure that corresponds to self-similar compositional regions determined via the X-ray phase and absorption interactions.
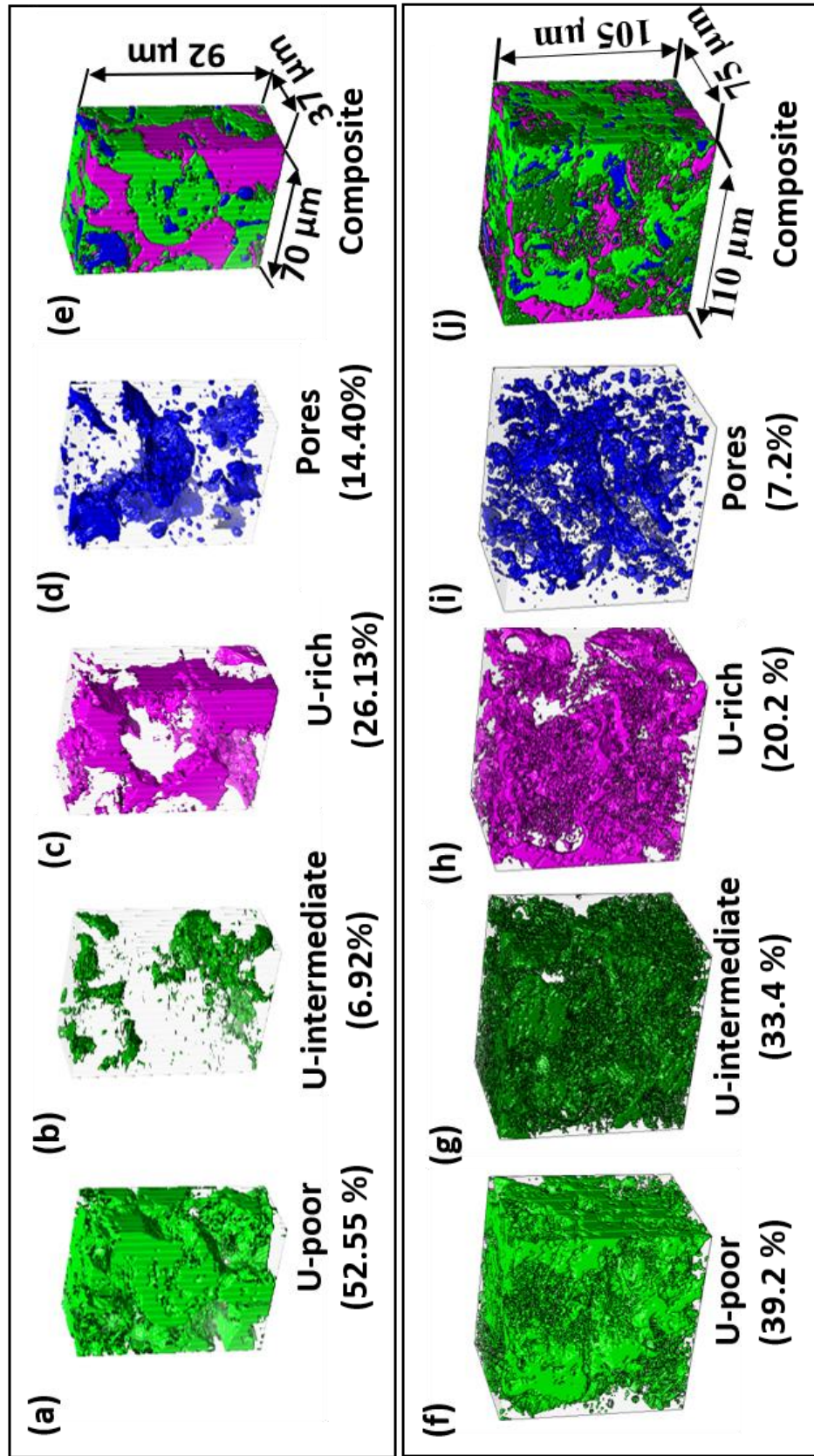
Figure 4.27: (a-d and f-i) show 3D segmentation of phase regions identified in the sectioned FIB obelisks from regions A/B and B, respectively. (e and j) show 3D composites of the segmented phase regions from regions A/B and B, respectively [36].

101

Figs. 4.28 (a-f) and (g-l) shows the 3D segmentation of the pores identified in the sectioned FIB obelisks from regions A/B and B on the basis of pore volume ranges. As shown in Figs. 4.28 (a-k), the segmented 3D pores from the sectioned FIB obelisks from regions A/B and B classified into volume ranges of >8401 μm^3, 1261-8400 μm^3, 379-1260 μm^3, 43-378 μm^3, and 0.84-42 μm^3, respectively. Since the smallest resolvable pore in 2D was identified to be ~2 pixels (1.5 μm) in size, pores occupying a volume less than 2 voxels (0.84 μm^3) are not resolvable in this study, and therefore they are excluded from pore segmentation. Composite images of all of the segmented pores from Figs. 4.28 (a-e) and 4.28 (g-k) are presented in Figs. 4.28 (f) and 4.28 (l), respectively. The pores are shown in each of the partitioned regions all exhibit different morphologies, which can also correspond to various pore growth stages. The morphologies shown in Figs. 4.28 (d, e) and Figs. 4.28 (j, k) are more spherical, whereas Figs. 4.28 (a, b, and c) and Figs. 4.28 (g, h, and i) have an aspherical appearance. In summary, Figs. 4.28 (a-e) and Figs. 4.28 (g-k) revealed the existence of pores in their extended/interconnected stage, interconnected stage, coalescence stage, growth stage, and nucleation stage. More interestingly, the porosity segmentation revealed the following: (1) A greater quantity of pores in their nucleation state at region B than region A/B. (2) A substantially larger extended/interconnected pore at region A/B than region B. Furthermore, the 3D porosity assessment presented in the current study revealed that the sectioned FIB obelisks from regions A/B and B possessed a total of 505 and 2272 resolvable pores, respectively.
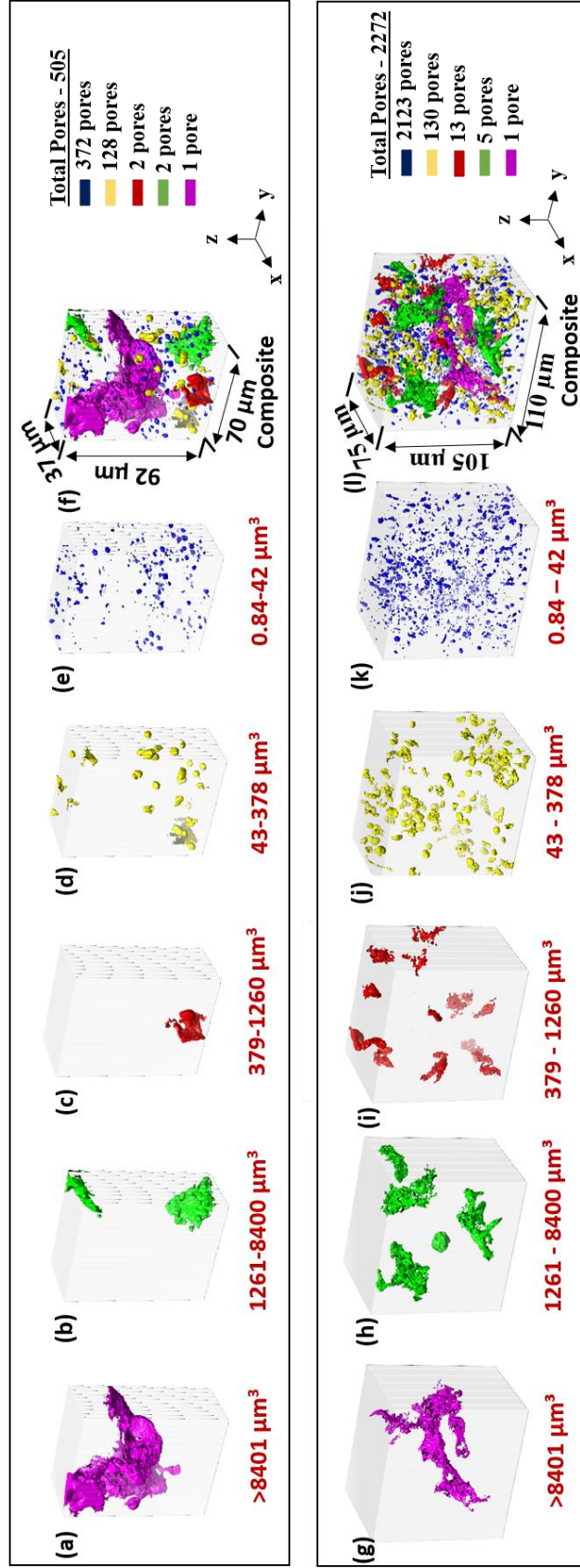
Figure 4.28: Pore segmentation of the 3D phase contrast μ-CT images with volumes of (a and g) >8401 μm³, (b and h) 1261-8400 μm³, (c and i) 379-1260 μm³, (d and j) 43-378 μm³, (e and k) 0.84-42 μm³, and (f and l) composite image of all pores segmented from the sectioned FIB obelisks from regions A/B and B, respectively [36].

103

The distribution of the number of pores as a function of the volume occupied in regions A/B and B are shown in Figs. 4.29 (a and d) indicating volumes of 0.84-26,000 μm^3 and 0.84-14,000 μm^3, respectively. Figs. 4.29 (b and e) provides a more resolved volumetric distribution of the quantity of pores ranging from 0.84-2000 μm^3 (region A/B) and 0.84-1000 μm^3 (region B), respectively. A notable observation from Figs. 4.29 (a, b, d, and e) is the existence of a large distribution in the volume occupied by pores, which is directly related to the varied morphologies observed in Fig. 4.28. Figs. 4.29 (c and f) show the distribution of pores (grey histograms) and noise (black histogram) ranging from 0.84-10 μm^3 and 0.0-0.83 μm^3 in sectioned FIB obelisks from regions A/B and B, respectively. The 3D porosity assessment revealed that for region A/B, a total of 114 pores occupied a volume less than 2 voxels (0.84 μm^3), while in region B, a total of 991 pores occupied a volume of less than 2 voxels (0.84 μm^3). Consequently, these pores were considered as noise and excluded from the subsequent porosity analysis.
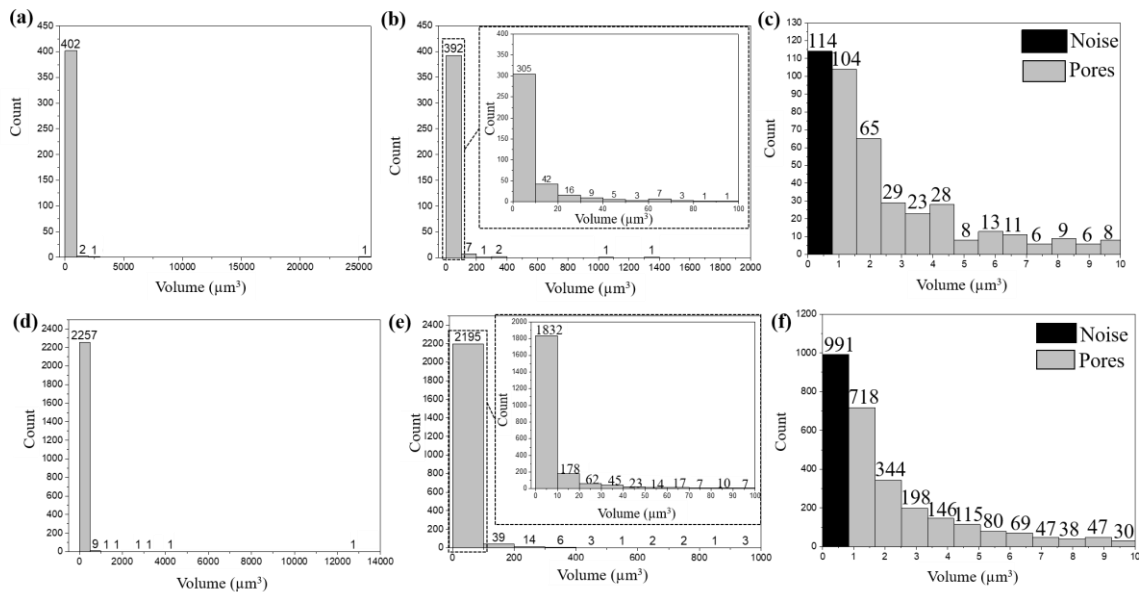
Figure 4.29: (a, d) Volume distribution of all segmented pores with histograms showing the pore distributions ranging from 0.84-26,000 μm^3 (from sectioned FIB obelisk-Region A/B) and 0.84-14,000 μm^3 (from sectioned FIB obelisk-Region B), respectively. Volume distribution of pores ranging from 0.84-2000 μm^3 (from sectioned FIB obelisk-Region A/B) and 0.84-1000 (from sectioned FIB obelisk-Region B) in (b and e) also show inset histograms showing the pore distribution from 0.84-100 μm^3. The noise (i.e. voxels excluded from porosity analysis) ranging from 0.0-0.83μm^3 in FIB cuboids produced from Region A/B and B is presented in (c and f), respectively [36].

The histograms in Figs. 4.30 (a and b) show sphericity values of all the pores identified from different pore volume ranges segmented in Fig. 4.28 (a-l). As shown in Fig. 4.30, pores from smaller volumes ranges of 0.84-42 μm^3 have sphericity values closer to 1; while those from larger volume ranges such as 1261-8400 μm^3 and > 8401 μm^3 have sphericity values closer to 0. It can be seen that the number majority of the pores (372 pores from region A/B and 2123 pores from region B) present have volumes ranging from 0.84-42 μm^3, indicative of the nucleation stage. These pores (0.84 - 42 μm^3 in size) occupy 6.19% and 17.8% of the total porosity volume fraction determined from regions A/B and B, respectively. In region A/B, most of the pores ranging from 0.84-42 μm^3 have sphericity values ranging between 0.38-0.77 (see Fig. 4.30 (a)), while at region B, most of the pores ranging from 0.84-42 μm^3 have sphericity values ranging between 0.33-0.80 (see Fig. 4.30 (b)). In comparison, for both regions' A/B and B, pores from larger volume ranges (1261-8400 μm^3 in size) appear to be aspherical with sphericity values ranging from 0.21-0.22 and 0.12-0.43, respectively. Furthermore, both regions A/B and region B possess one large centrally located pore (aspherical) with a sphericity value of 0.1.

Table 4.4 details the variation in the pore volume fractions and sphericity ranges of the different pore volume categories identified in the sectioned FIB obelisks from regions A/B and B. From Table 4.4, it can be seen that the largest volume fraction contribution to porosity in: (1) region A/B is the largest pore that occupies a volume of 25,047.1 μm^3, and (2) region B is the pores that occupy the volume ranging from 43–378 μm^3. Hence, it can be inferred that the majority of fuel swelling in regions A/B and B is a consequence of extended/interconnected pores and pores in their growth phase, respectively. Furthermore, correlating Figs. 4.28 (a-l), Fig. 4.30 (a and b), and Table 4.4 revealed the following: At region A/B, (1) One extended/interconnected pore occupies 71.77% of the total porosity fraction and is aspherical with a sphericity value of 0.12. (2) Interconnected pores occupy 9.7% of the total porosity fraction with a sphericity range of 0.21-0.22. (3) Pores in the coalescence stage occupy 4.23% of the total porosity fraction with a sphericity range of 0.28-0.60. (4) Pores in the growth stage occupy 7.97% of the total porosity fraction with a sphericity range of 0.26-0.68. (5) Pores in the nucleation stage occupy 6.19% of the total porosity fraction with a sphericity range of 0.38-0.77. Similarly, in region B, (1) One extended/interconnected pore occupies 21.2% of the total porosity fraction and is aspherical with a sphericity value of 0.1. (2) Interconnected pores occupy 21.0% of the total porosity fraction with a sphericity range of 0.12-0.43. (3) Pores in the coalescence stage occupy 14.4% of the total

porosity fraction with a sphericity range of 0.16-0.47. (4) Pores in the growth stage occupy 24.8% of the total porosity fraction with a sphericity range of 0.21-0.65. (5) Pores in the nucleation stage occupy 17.8% of the total porosity fraction with a sphericity range of 0.33-0.80.
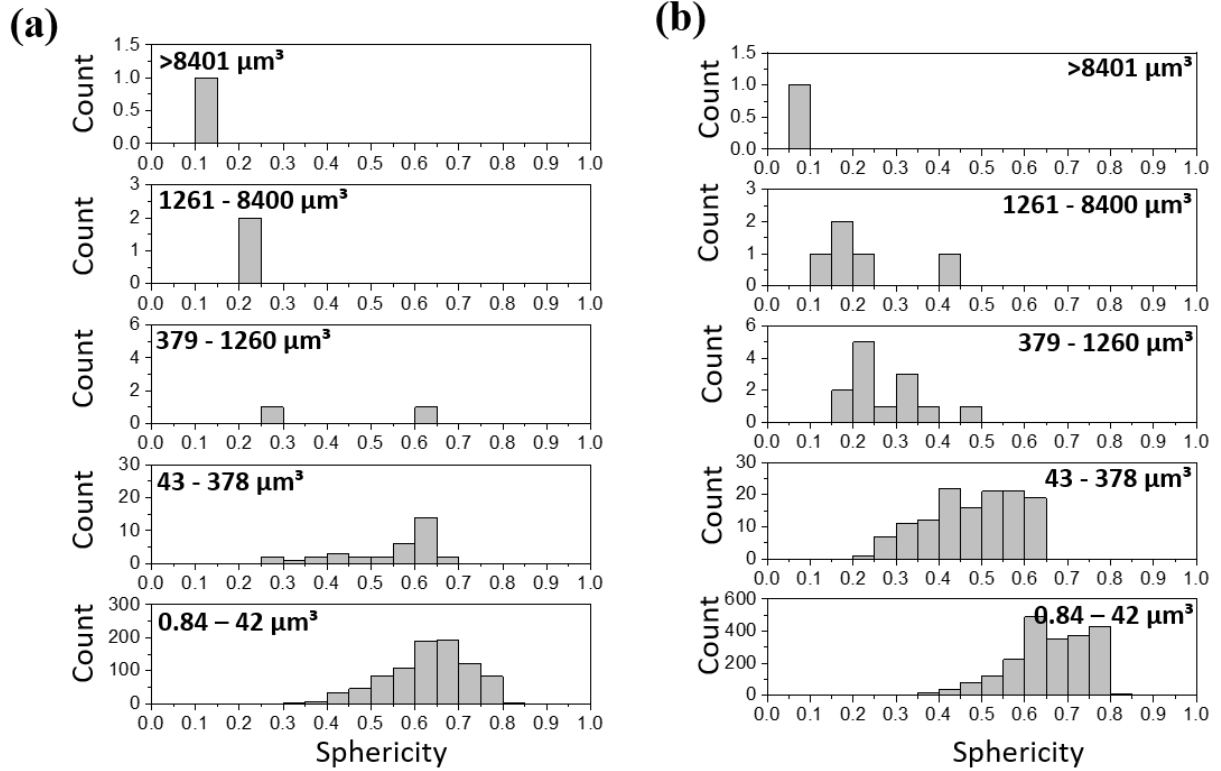
Figure 4.30: (a and b) Sphericity values of all pores segmented from the 3D phase contrast μ-CT images of sectioned FIB obelisks from regions A/B and B categorized into volumes ranging from >8401 μm³, 1261-8400 μm³, 379-1260 μm³, 43-378 μm³, and 0.84-42 μm³, respectively. Sphericity values in (a) correspond to values estimated from the sectioned FIB obelisk from regions A/B, while (b) correspond to values estimated from the sectioned FIB obelisk from regions B [36].

Table 4.4: Segmentation of porosity volume fractions at regions A/B and B on basis of pore volume and sphericity distribution.

FIB Cuboid	Porosity Volume Range (μm³)	Porosity Volume Fraction (%)	Pore Count	Sphericity
Region A/B	0.84 – 42	6.19	372	0.38-0.77
	43 - 378	7.97	128	0.26-0.68
	379 – 1260	4.23	2	0.28-0.60
	1261 - 8400	9.70	2	0.21-0.22
	> 8401	71.77	1	0.12
Region B [36]	0.84 – 42	17.8	2123	0.33-0.80
	43 - 378	24.8	130	0.21-0.65
	379 – 1260	14.4	13	0.16-0.47
	1261 - 8400	21.0	5	0.12-0.43
	> 8401	21.2	1	0.1
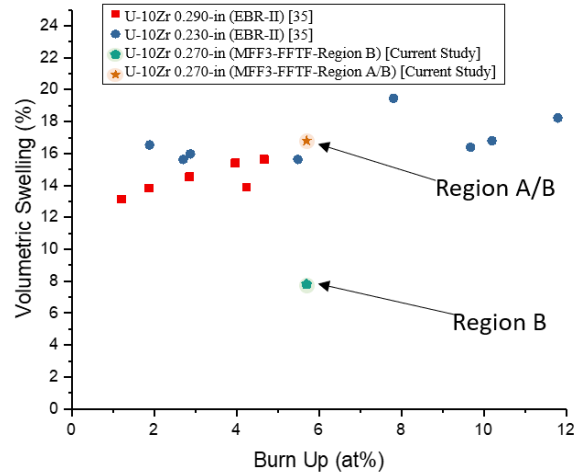
Figure 4.31: Comparison between the localized microscopic fuel swelling of the sectioned FIB obelisks from regions A/B and B, and the historical macroscopic fuel swelling data from various U-10wt.%Zr fuels irradiated in EBR-II with varied fuel slug and cladding diameters (0.171 in. and 0.223 in. diameter fuel slugs clad in 0.230 in. and 0.290 in. diameter stainless steel tubes, respectively [35]) [36].

A comparison between the localized microscopic and macroscopic fuel swelling (i.e. swelling in the sectioned FIB obelisks from regions A/B and B, and the U-10wt.%Zr fuels irradiated at EBR-II, respectively) is presented in Fig. 4.31. As specified in Section 3.4.1, three assumptions were taken into consideration for the determination of the localized microscopic fuel swelling in the sectioned FIB obelisks analyzed in this study. Furthermore, the effect of solid FP on the localized microscopic swelling is not considered in this study due to the lack of historical FP information and the difficulty of individually identifying FP from the μ-CT images. Using Eq. (3.6), the localized microscopic swelling, V_{Swell} of the sectioned FIB obelisks from regions A/B and B were estimated to be 16.8% and 7.70%, respectively. In summary, the synchrotron μ-CT assessments revealed that the localized microscopic swelling and type of pores (i.e. extended/interconnected pores, interconnected pore, coalescence pores, pores in the growth phase, and pores in nucleation phase) present at the locality are co-dependent factors and vary from region to region.

4.3.2 Synchrotron μ-CT Experiments of the Neutron Irradiated HT9 Cladding

The reconstructed 3D view of the absorption contrast μ-CT images of the FIB obelisk from the neutron irradiated HT9 cladding and the corresponding BSE micrographs produced near the localities from where the FIB obelisk was produced is presented in Fig. 4.32 (a). As shown in Fig. 4.32 (a), the FP migration was observed along the grain boundaries of the neutron irradiated HT9 cladding (see white arrows in the BSE micrographs in Fig. 4.32 (a)). Figs. 4.32 (b-d) present correlative absorption and phase contrast μ-CT images labeled as view-1, -2, and -3, respectively. The black and red boxes on the absorption and phase contrast μ-CT images (see view 1-3 in Figs. 4.32 (b-d)) enclose the approximate locality from where an average of 16 line scans was performed for the production of attenuation-based voxel and gray value line scan plots. The line scans plots presented in Figs. 4.32 (b-d) show FP (seen from absorption contrast μ-CT images) and grain boundary (seen from phase contrast μ-CT images) as crests and troughs, respectively. From these observations, it is evident that FP either migrates and/or accumulate at the grain boundaries of the neutron irradiated HT9 cladding. The accumulation of FP at grain boundaries may lead to localized swelling that can facilitate cracking at grain boundaries and consequently affect the local mechanical properties exhibited by the neutron irradiated HT9 cladding. A comprehensive

assessment of the effects of FP migration along the grain boundaries of the neutron irradiated HT9 cladding is detailed in Section 4.4.
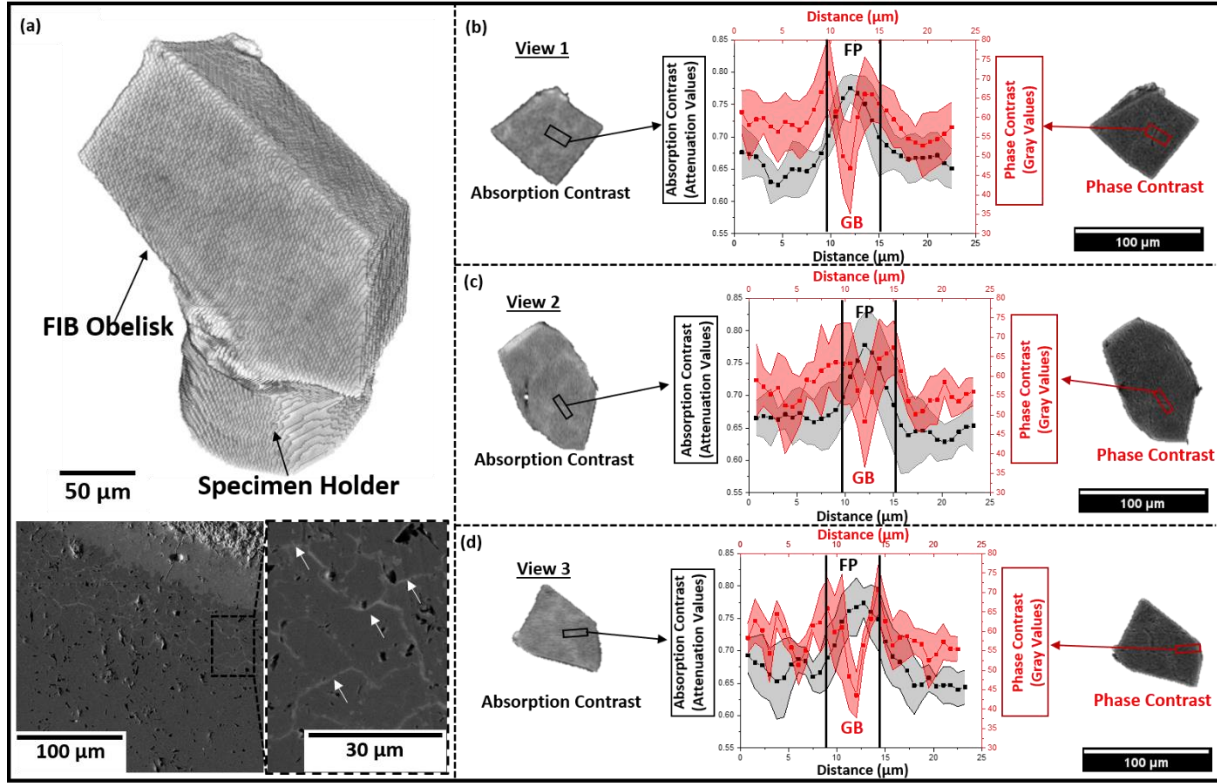
Figure 4.32: (a) 3D absorption contrast μ-CT image of a FIB obelisk produced from the neutron irradiated HT9 cladding. BSE micrographs in (a) were produced near the localities from where the FIB obelisk was produced. The white arrows in the BSE micrographs show the migration of FP along grain boundaries of the neutron irradiated HT9 cladding. The correlated absorption and phase contrast μ-CT images of (b) View 1, (c) View 2, and (d) View 3 show the accumulation of FP along the grain boundaries of the neutron irradiated HT9 FIB obelisk. The attenuation-based voxel line scans presented in (b-d) show a decrease in attenuation as a consequence of grain boundaries (seen via phase contrast μ-CT) and a rise in attenuation as a consequence of FP (seen via absorption contrast μ-CT).

4.4   Nano-Mechanical Property Assessment

Nano-indentation experiments were performed at various localities of the neutron irradiated HT9 cladding that was irradiated at the FFTF reactor as a part of the MFF-3 series experiments. The nano-indentation experiments were performed to comprehend the effects of microstructural alterations (i.e. changes that arise from neutron irradiation, FP precipitation, intermetallic formations. FCCI, etc.) on the localized mechanical properties at various localities of

the neutron irradiated HT9 cladding. Fig. 4.33 (a) presents a montage of SE micrographs of the neutron irradiated HT9 cladding at low magnification, while Figs. 4.33 (b-d) present BSE micrographs of various localities (such as fuel, FCCI, HT9+fission products, and HT9 edge) of the neutron irradiated HT9 cladding produced at higher magnifications. Figs. 4.33 (b-d) were produced at the locality marked by a black dashed box in Fig. 4.33 (a). The presence of FP migration (indicated by white arrows) along the grain boundaries of the neutron irradiated HT9 cladding is seen in Figs. 4.33 (c and d).
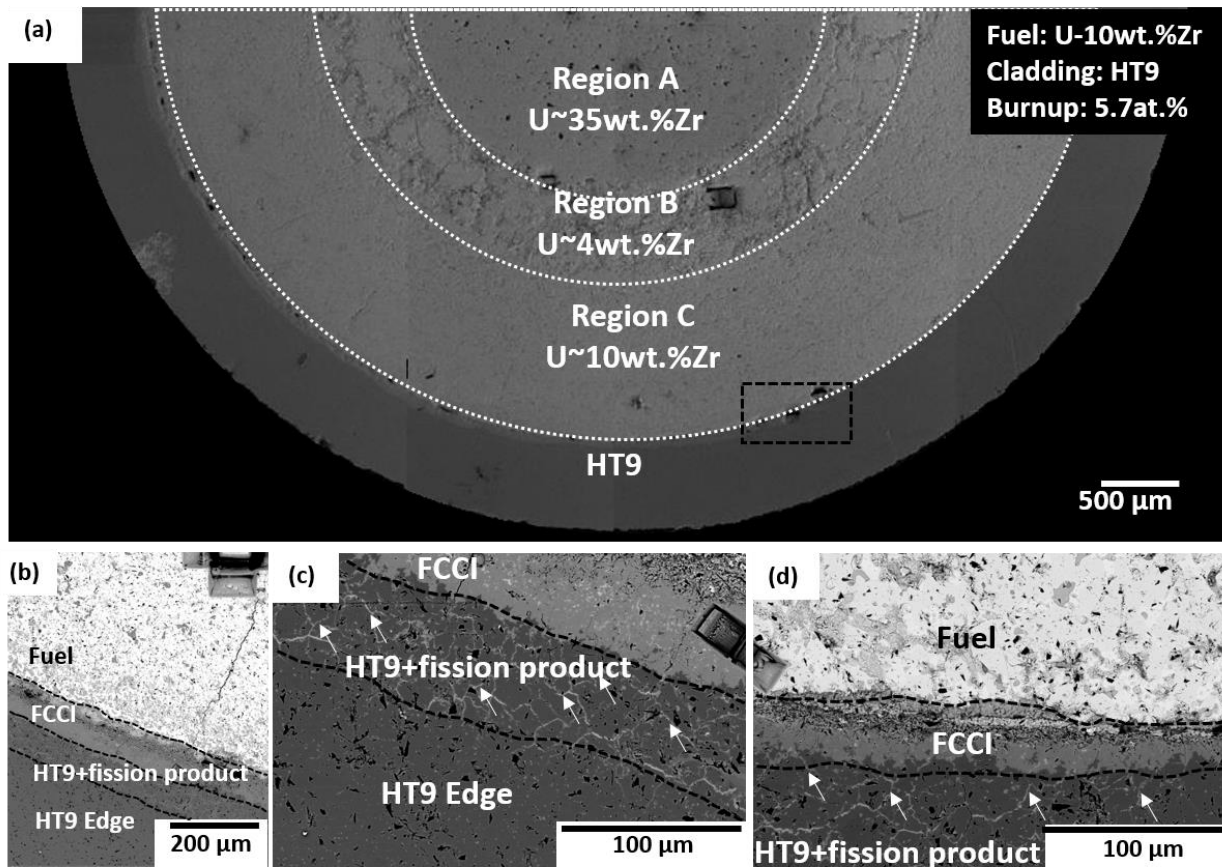
Figure 4.33: (a) SEM montage of the neutron irradiated U-10wt.%Zr fuel and HT9 cross-section that achieved a cross-sectional burnup of 5.7 at.%. BSE micrographs presented in (b-d) show distinct localities (i.e. fuel, FCCI, HT9+fission products, and HT9 edge) of the neutron irradiated HT9 cladding. White arrows in (c and d) show FP migration along the grain boundaries of the neutron irradiated HT9 cladding.

The nano-indentation experiments were performed with a Hysitron PI-88 nano-indenter that was housed in an SEM. The experiments were aimed at determining the effects of neutron

irradiation and FCCI on the localized mechanical properties of the neutron irradiated HT9 cladding and the fuel-cladding interaction region. Fig. 4.34 (a, b, and c) presents LD curves produced at various nano-indentation depths, H_n versus nano-indentation depths, and H_n^2 versus 1/h, respectively. As specified in Section 3.5, the H_0 and h^* values were determined using Eq. 3.7, and the linear fitting of the data is presented in Fig. 4.34 (c). The linear fitting revealed that the H_0 (i.e. square root of the y intercept or $\sqrt{b}$) and h* (i.e. slope over y-intercept or m/b) values determined at the HT9 edge locality of the neutron irradiated HT9 cladding was 4.77 GPa and -35.35 nm, respectively. Interestingly, in this study, a negative h^* value and a low R^2 value was observed. Similar observations of negative h^* values and low R^2 values were also reported for neutron irradiated T91 and HT9 steels assessed by Krumwiede et al. [105,109].
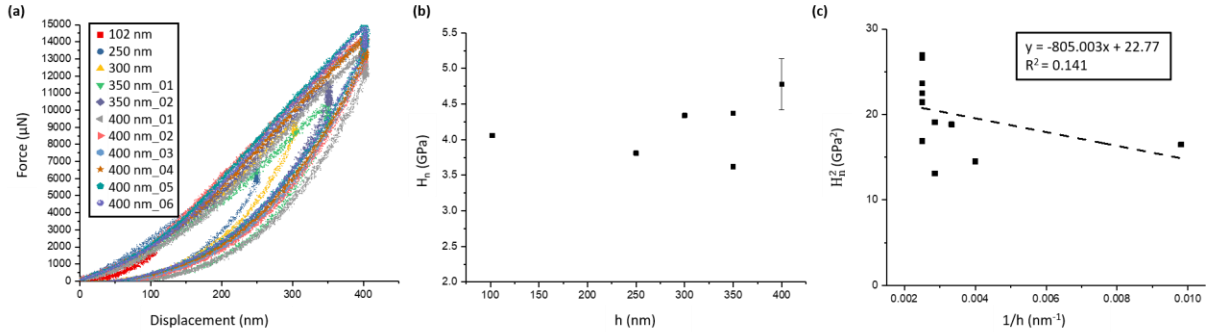
Figure 4.34: (a) LD curves performed at various nano-indentation depths, (b) nano-hardness determined at various nano-indentation depths, and (c) ISE analysis performed on H_n^2 vs 1/h plot for determining H_0 and h^* values.

Fig. 4.35 (a) presents the changes in H_n of the neutron irradiated HT9 cladding as a function of distance from the HT9 edge to the FCCI locality. As specified in Section 3.5, 12 distinct localities on the neutron irradiated HT9 cladding were assessed with each locality possessing 5 individual nano-indentation experiments at a depth of 400 nm. A spacing of ~55 µm was provided between each distinct locality so that the variation in the nano-mechanical properties can be assessed as a function of distance from cladding edge to the FCCI locality. As shown in Fig. 4.35 (a) the H_n versus cladding distance has been separated on basis of locality of the nano-indentation experiments. The HT9 edge, HT9+fission products, and FCCI localities of the neutron irradiated HT9 cladding possess a nano-hardness of ~4.4-5.6 GPa (locality shaded in green), ~4.7-5.2 GPa (locality shaded orange), and ~5.7-8.7 GPa (locality shaded blue), respectively. Figs. 4.35 (b-e)

presents SEM micrographs of the nano-indentation experiments being performed at different localities of the neutron irradiated HT9 cladding. Figs. 4.35 (b and c) show nano-indentation experiments being performed at positions of ~111 µm and ~332 µm of the HT9 edge locality, while Figs. 4.35 (d and e) show nano-indentation experiments being performed at positions of ~600 µm and ~695 µm of the HT9+fission products and FCCI localities, respectively. Furthermore, from Fig. 4.35 (a), it is evident that the variations in the nano-hardness measurements increased as the indentation experiments progressed from the HT9 edge to the FCCI locality, with the largest variations being present at the FCCI locality. The large variations in the nano-hardness measurements at the HT9+fission products and FCCI localities was a consequence of the indentations being performed on the matrix phase regions and on regions which possessed several neutron irradiation induced effects (such as FP along the grain boundaries, FP precipitates, localities near pores, intermetallics, and FCCI layers). The experiments were performed in such a manner so that the changes in local mechanical properties can be assessed as a function of: (1) distance from cladding edge to fuel edge, and (2) several neutron irradiation induced effects (such as FP migration, FCCI layers, and FP precipitates).
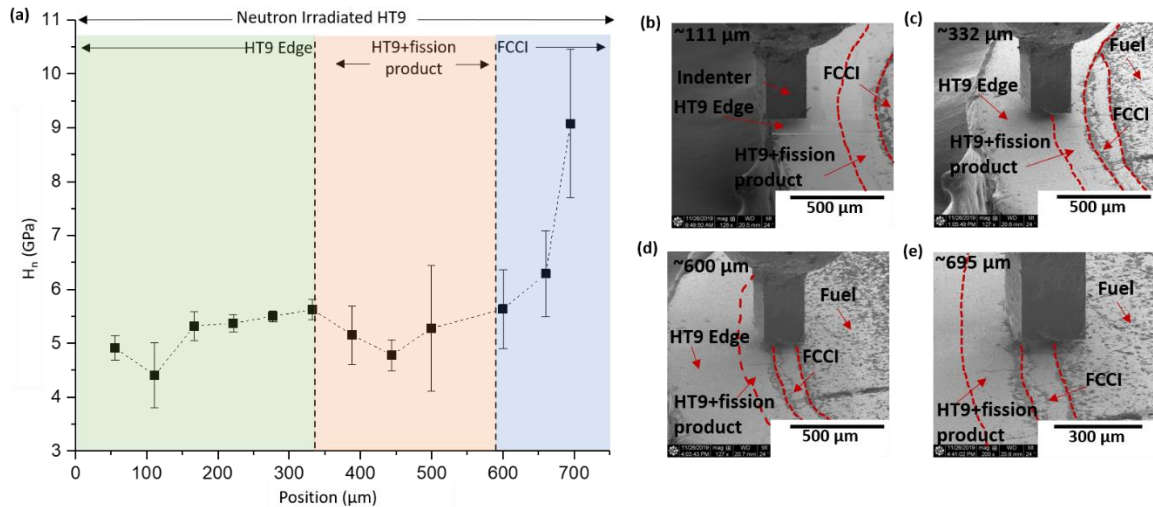
Figure 4.35: (a) Nano-hardness versus position plot of the neutron irradiated HT9 cladding from the HT9 edge to the FCCI locality. The SEM micrographs presented in (b-e) show in-situ nano-indentation experiments being performed at various localities (i.e. HT9 edge, HT9+fission products, and FCCI) of the neutron irradiated HT9 cladding. Furthermore, the HT9 edge, HT9+fission products, and FCCI locality in (b-e) correspond to the green, orange, and blue shaded regions in (a).

The calculated micro-hardness (determined via utilization of Eq. (3.8)) and calculated yield stresses (determined via utilization of Eq. (3.9) and (3.10)) at different localities of the neutron irradiated HT9 cladding is presented in Fig. 4.36 (a), while Fig. 4.36 (b) presents a comparison between the calculated yield stresses (determined via Milot's and Busby's method) versus nano-hardness measurements at the HT9 edge locality (green shaded region in Fig. 4.36 (a)) of the neutron irradiated HT9 cladding, and the calculated yield stresses versus nano-hardness measurements of various neutron irradiated steels reported by Krumwiede et al. [109]. Krumwiede et al. [109] performed nano-indentation experiments on several neutron irradiated steels and used Eqs. (3.8-3.10) to determine the calculated micro-hardness and calculated yield stresses. The steel specimens assessed by Krumwiede et al. [109] were irradiated at the Advanced Test Reactor to a dose and temperature of 6.49 dpa and 320˚C, respectively. More interestingly, the comparison presented in Fig. 4.36 (b) revealed that the few of nano-hardness measurements and calculated Milot's yield stresses (colored red boxes) form the HT9 edge locality of the neutron irradiated HT9 cladding from the current study matched the nano-hardness measurement and calculated Milot's yield stresses (colored red triangle) of the neutron irradiated HT9 steel assessed by Krumwiede et al. [109]. The comparison presented in Fig. 4.36 (b) was limited to the HT9 edge locality of the neutron irradiated HT9 cladding due to the following reasons: (1) Nano-hardness measurements at the other localities were affected by the presence of FP, intermetallics, and FCCI layers, and (2) the neutron irradiated steels assessed by Krumwiede et al. [109] were considered as structural materials and were not in contact with any fuel. Consequently, they are not affected by several neutron irradiation induced effects (such as FP migration, FCCI layers, FP precipitates, etc.) which are caused by fuel contact.
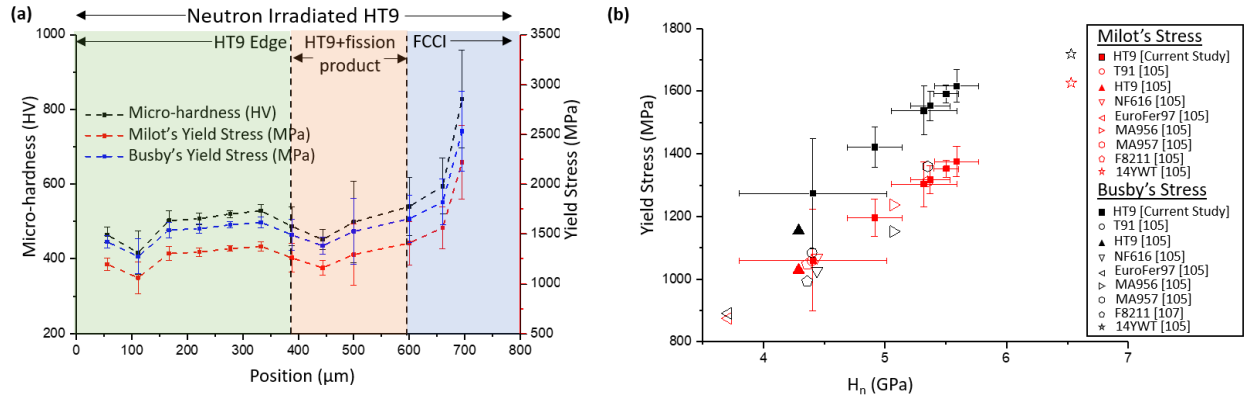
Figure 4.36: (a) Comparison between the calculated micro-hardness (in black), Milot's yield stress (in red), and Busby's yield stress (in blue) as a function of position at different localities (HT9 edge, HT9+fission products, and FCCI) of the neutron irradiated HT9 cladding. The linear relationship between the calculated yield stresses (Milot's and Busby's method) as a function of nano-hardness in the HT9 edge locality of the neutron irradiated HT9 cladding is shown in (b). An overlay of calculated yield stress (Milot's and Busby's method) as a function of nano-hardness for several neutron irradiated steels reported by Krumwiede et al. [105] is also presented in (b).

The comparison of yield stresses reported for several HT9 steels that were neutron irradiated at various doses and irradiation temperatures, and the calculated average yield stress (determined via Milot's and Busby's method) at the HT9 edge locality of the neutron irradiated HT9 cladding from the current study is presented in Fig. 4.37. The calculated average yield stress of the HT9 edge locality presented in Fig. 4.37 was determined by averaging the calculated yield stress values enclosed by the green shaded region in Fig. 4.36 (a).

In this study, the dose experienced by the neutron irradiated HT9 cladding from the MFF-3 series experiment was estimated to be 19.42 dpa. The MFF-3 series metallic fuel assembly in the FFTF reactor was reported to have a peak neutron fluence (φ) of $19.2*10^{22}$ n/cm^2 and a peak neutron energy (E_i) of 0.5 MeV when run for 726.2 effective full power days at a core power of 291 MW [1,121,122]. Different axial fuel column length positions of the MFF-3 series fuel pin experience different fluences, and consequently, the dose calculation presented in the current study was estimated via utilizing the fluence experienced at an axial fuel column length of z/L = 0.98. The neutron fluence (φ) at an axial fuel column length of z/L = 0.98 was determined to be $9.28*10^{22}$ n/cm^2, and was used along with the other known irradiation parameters (i.e. E_i, E_d, σ_s, and γ) in Eq. (4.1) to determine the dose experienced by the neutron irradiated HT9 cladding [123].

$$\text{Dose (dpa)} = \sigma_s * \frac{\gamma E_i}{4E_d} * \varphi \qquad (4.1)$$

In Eq. (4.1), σ_s is the neutron scattering cross-section of targeted material, γ is the interaction constant between the incoming neutron and the targeted material for collision, E_i is the neutron energy, E_d is the displacement energy of the targeted material for collision, and φ is the neutron fluence. Since Fe was the major/balance element in the neutron irradiated HT9 cladding, in this study, the dose was estimated by using the σ_s, γ, and E_d of Fe at an E_i of 0.5 MeV in Eq. (4.1). The σ_s of Fe at an E_i of 0.5 MeV was estimated to be 0.971×10^{-24} cm^2, γ was calculated to be 0.069, and E_d of Fe is 40 eV. Additionally, the irradiation temperature of MFF-3 series HT9 cladding was assumed to be ~615˚C due to the following reasons: (1) The inner cladding surface temperature of the neutron irradiated U-10wt.%Zr/HT9 cross-section that achieved a burnup of 5.7 at.% was reported to be 615˚C [88], and (2) lack of historical information detailing the outer cladding surface temperatures at different fuel burnups.

A detailed comparison between the data produced from the nano-indentation experiments in this study and several historical tensile testing experiments performed on neutron irradiated HT9 steels at various reactors, irradiation temperatures, and doses is presented in Table 4.5 [24,109,124–127]. Even though Table 4.5 details several historical yield stress assessments made on neutron irradiated HT9 steels (not in contact with any fuel), they cannot be used as a true point of comparison for the calculated yield stresses estimated from neutron irradiated HT9 cladding (in contact with fuel) assessed in this study. This is because the neutron irradiated HT9 cladding assessed in this study was used as core material and was consequently influenced by several phenomena that occur due to contact between fuel and cladding. In Table 4.5, the experiments performed by a group of researchers with different parameters are separated with a "/" symbol. For example, Klueh et al. [125] performed tensile tests on neutron irradiated HT9 steels to determine yield stresses (1135 MPa, 1025 MPa, and 920 MPa) at several doses (6 dpa, 12 dpa, and 15 dpa) and irradiation temperatures (300˚C, 400˚C, 393˚C). Consequently, to separate or show distinction to the test conditions and results listed above, "/" symbol was used in Table 4.5. The calculated average yield stresses from the HT9+fission product and FCCI localities of the neutron irradiated HT9 cladding are also listed in Table 4.5. Like the HT9 edge locality, the calculated average yield stresses from the HT9+fission product and FCCI localities were determined by

averaging the calculated yield stress values enclosed by the orange and blue shaded regions in Fig. 4.36 (a). A more comprehensive assessment of Table 4.5 is provided in Section 5.4.

In summary, the nano-indentation experiments revealed that each locality of the neutron irradiated HT9 cladding possessed unique mechanical properties. A comprehensive explanation of the relevance, necessity, and revelations determined from the nano-indentation experiments is detailed in Section 5.4 of the dissertation.
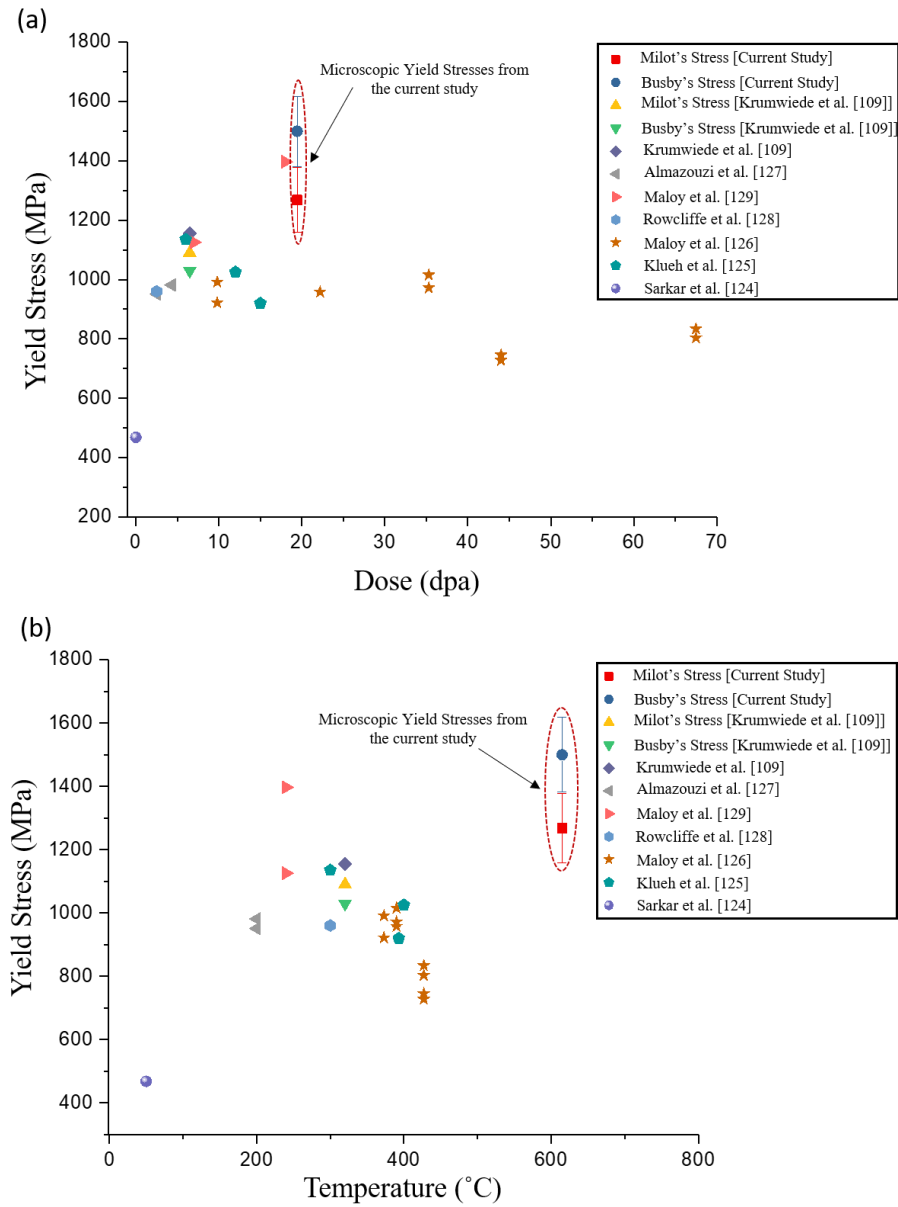
Figure 4.37: Comparision between (a) the calculated yield stresses (Milot's and Busby's) at the HT9 edge locality of the neutron irradiated HT9 cladding and historical literature of yield stresses determined for neutron irradiated HT9 steels that were irradiated at various doses, and (b) the calculated yield stresses (Milot's and Busby's) at the HT9 edge locality of the neutron irradiated HT9 cladding and historical literature of yield stresses determined for neutron irradiated HT9 steels that were irradiated at various irradiation temperatures [109,124–129].

Table 4.5: Comparison of the calculated yield stresses at various localities of the neutron irradiated HT9 cladding and yield stresses of neutron irradiated HT9 steels measured via various tensile testing methods and irradiated at various reactors, doses, and temperatures.

Study	Experiment	Dose (dpa)	Irradiation Temperature (°C)	Testing Temperature (°C)	Yield Stress (MPa)			Reactor
					σ_y	$\sigma_{y\,(Mlot)}$	$\sigma_{y\,(Busby)}$	
Sarkar et al. [124]	Tensile Test	0.0012	~50	RT	468	-	-	PULSTAR
Klueh et al. [125]	Tensile Test	6/12/15	300/400/393	**	1135/1025/920	-	-	HFIR/FFTF
Maloy et al. [126]	Tensile Test	9.8/22.2/35.3/44/67.5	373/390/390/427/427	25	921.6,991.18/957.46/971.79,1015.27/727.73,745.12/803.29/833.60	-	-	FFTF
Rowcliffe et al. [128]	Tensile Test	2.5	300	RT	960	-	-	HFIR
Maloy et al. [129]	Tensile Test	7/18	140-340	25	1125.42/1396.61	-	-	STIP II
Almazouzi et al. [127]	Tensile Test	2.55/4.33	200	**	951/981	-	-	BR2
Krumwiede et al. [109]	Tensile Test	6.49	320±10	**	1090	-	-	ATR
Krumwiede et al. [109]	Nanoindentation	6.49	320±10	**	-	1029.28	-	ATR
Krumwiede et al. [109]	Nanoindentation	6.49	320±10	**	-	-	1154.71	ATR
Neutron Irradiated HT9 Cladding MFF-3 Series (5.7 at.% burnup) — HT9 Edge	Nanoindentation	19.42	~615	RT	-	1267.71	-	FFTF
HT9+fission products	Nanoindentation	19.42	~615	RT	-	1292.94	-	FFTF
FCCI	Nanoindentation	19.42	~615	RT	-	1483.84	-	FFTF
HT9 Edge	Nanoindentation	19.42	~615	RT	-	-	1499.25	FFTF
HT9+fission products	Nanoindentation	19.42	~615	RT	-	-	1526.62	FFTF
FCCI	Nanoindentation	19.42	~615	RT	-	-	1733.77	FFTF

Note: RT indicates room temperature (°C) and ** indicates that the temperature (°C) was not specified. The symbols "/" and "," is used to separate test conditions for an irradiation parameter. For example, in the dose column, "/" is used to differentiate the various dpa at which the experiments were performed by the same author, while in the σ_y column, "," is used to show the yield stresses attained for different experiments with same irradiation parameters.

118

CHAPTER 5.   DISCUSSION

The research presented in this study involves performing a coordinated group of experiments from a nanoscale, microscale, and mesoscale perspective. The experiments were performed to better understand the effects of various neutron irradiation phenomenon (such as fuel constituent re-distribution, phase transformations, fuel swelling, and FCCI) on the microstructure and mechanical property of a neutron irradiated U-10wt.%Zr/HT9 (fuel/cladding) cross-section that achieved a burnup of 5.7 at.%. As specified in Section 3 of the dissertation, the experimental techniques used in this study involves TEM investigations of FIB lamellas, 3D-EDS serial sectioning of FIB cuboids, synchrotron μ-CT of FIB obelisks, and nano-indentation of the neutron irradiated HT9 cladding. Furthermore, through these coordinated groups of experiments, a better understanding of the microstructural alterations in a neutron irradiated U-10wt.%Zr/HT9 that was previously unknown have been attained, and several hypotheses describing various phenomena have been established.

5.1   Nanoscale Characterization

5.1.1   Transmission Electron Microscopy of Region A and Region A/B

SEM-EDS experiments by Harp et al. [6] confirmed that the Zr migration from region B to region A led to an increase in the average Zr composition (~30-35wt.%Zr) in region A. Although the large area SEM-EDS experiments by Harp et al. [6] provided an average estimate of U and Zr compositions in region A, the STEM-EDS assessment of lamellas from Region A and A/B in the current study revealed the presence of three distinct U-rich, U-intermediate and U-lean localities with varying chemical compositions (see Figs. 4.2-4.4). The U-rich, U-intermediate, and U-lean localities from FIB lamella-1 from region A possessed a chemical composition of U~7wt.%Zr, U~46wt.%Zr, and U~62wt.%Zr, respectively. The STEM-EDS assessments also revealed that the FIB lamella-3 from region A/B possessed U-rich, U-intermediate, and U-lean localities with chemical compositions of U~8wt.%Zr, U~41wt,%Zr, and U~63wt.%Zr, respectively. In conclusion, the STEM-EDS maps (see Figs. 4.2-4.4) revealed the following: (1) the U-intermediate localities are the matrix phase, (2) the U-rich localities possessing coarse and acicular

structures (see red and yellow arrows in Fig. 4.3 (a)) are precipitates, and (3) the U-lean localities are Zr-enriched grain boundaries (see white arrows in Fig. 4.2 (b), Fig. 4.3 (b), and Fig. 4.4 (b)). Furthermore, correlating the quantitative STEM-EDS assessment provided in Table. 4.1 and SAED assessments presented in Figs. 4.3 (i-o), revealed that the U-rich and U-intermediate localities were α-U (precipitate) and δ-UZr$_2$ (matrix) phases, and the U-lean localities were Zr-enrichments along the grain boundaries of the matrix phase. The presence of U-lean localities also revealed pathways along which Zr migrated from region B to region A of the fuel cross-section (i.e. evidence for fuel constituent re-distribution).

Since region A possessed a fuel centerline temperature of 682˚C and an average composition of U~35wt.%Zr, the observance of two-phase regions can be correlated to phase transformations occurring at a composition of U-35wt.%Zr [6,88]. As per the equilibrium phase diagram, at a composition of U-35wt.%Zr and temperature of 682˚C, the γ phase is the stable phase [13]. If the fuel is assumed to be cooled slowly from the elevated temperature post reactor shutdown, then the plausible phase transformation route is γ→α-U+γ$_2$→α-U+δ-UZr$_2$. The suggested phase transformation route was determined via examining the U-Zr equilibrium phase diagram reported by Sheldon et al. [13] for the stable phases at different temperatures ranges for an alloy composition of U-35wt.%Zr and is further corroborated by the observance of acicular structured and coarse α-U precipitates. The coarse precipitates are indicative of the primary phase transformation of γ→α-U+γ$_2$, whereas, the finer acicular structured α-U precipitates are indicative of the secondary phase transformation of α-U+γ$_2$→α-U+δ-UZr$_2$. Even though a plausible phase transformation route was determined via assessing the equilibrium U-Zr phase diagram at a nominal alloy composition of U-35wt.%Zr, the system was subjected to neutron irradiation and was consequently in a non-equilibrium condition. Hence, further investigations with appropriate in-pile experiments are essential to determine the true phase transformation route followed by a U-Zr fuel that possessed an average chemical composition of U-35wt.%Zr at the fuel center (i.e. region A). Furthermore, Basak [111] performed out-of-pile experiments on homogenized U-35wt.%Zr and revealed the presence of α-U precipitates with platelet/acicular structured morphologies in a δ-UZr$_2$ matrix phase.

Like region A, the SAED patterns produced from the FIB lamella from region A/B also showed the presence of α-U and δ-UZr$_2$ phases (see Figs. 4.2, 4.3, and 4.4). Fig. 4.4 (k) presents the SAED pattern of the δ-UZr$_2$ matrix phase at the [001] zone axis, while Fig. 4.4 (l) presents the

SAED pattern produced at the interface of the δ-UZr$_2$ matrix phase (U-intermediate locality) at the [001] zone axis and the α-U precipitate phase (U-rich locality) at the [100] zone axis, respectively. Even though the TEM investigations of the FIB lamellas from regions A and A/B will not be statistically sufficient to describe all the phases present at the central region of the fuel, the current study provided the first detailed nanoscale insights on a neutron irradiated U-10wt.%Zr fuel at regions where the average local composition is U~35wt.%Zr.

In conclusion, the TEM investigations at regions A and A/B revealed the following: (1) the presence of two major phases: α-U (U-rich precipitates) and δ-UZr$_2$ (U-intermediate matrix), and (2) Zr-enriched grain boundaries that revealed pathways along which Zr migrated from region B to A, providing evidence to fuel constituent re-distribution.

5.1.2   Transmission Electron Microscopy of Region B

SEM-EDS experiments by Harp et al. [6] confirmed the migration of Zr from region B to A. Furthermore, they reported that the average chemical composition at region B was U~4wt.%Zr [6]. The FIB lamellas assessed in this study were produced near the locality from where a FIB obelisk was previously produced and assessed by Thomas et al. [36]. Even though the phases determined from the current investigation will not capture all the phases present in the FIB obelisk analyzed Thomas et al. [36], correlations between the two investigations can be provided. The inability to capture all the phases present in the FIB obelisk is due to the following reasons: (1) The FIB obelisk possessed a substantially larger volume than the FIB lamellas. (2) High levels of heterogeneity in the chemical compositions and microstructural features seen in region B.

FIB lamella–4 from region B possessed: (1) a U-rich grain that is α-U with large quantities of solid FP precipitates (see Figs. 4.5 (a-h)), (2) Nd-Ce-Pd/Nd-Ce-Pd-La/Nd-Ce-La based solid FP precipitates (see Figs. 4.5 (a-h)), and (3) U-rich (β-U) grain with Zr-rich precipitates (see Figs. 4.5 (a and h) and Figs. 4.6 (a-j)), while FIB lamella-5 from region B possessed: (1) a U-rich grain that possessed several inhomogeneities and was more affected by radiation (see markers labeled 2 in Fig. 4.7 (a)), (2) U-rich grains with Zr rich precipitates (see grain with red arrows in Fig. 4.7 (k)), (3) a Zr-rich grain with diffused FPs (see marker labeled 3 in Fig. 4.7 (a)), and (4) an Nd-Ce-Pd based FP precipitate (see marker labeled 4 in Fig. 4.7 (a)), respectively. The TEM investigations from FIB lamella-4 revealed that the α-U grain (see Fig. 4.5 (a, b, and i)) was more affected by radiation and possessed microstructural inhomogeneities (such as cavities and multiple solid FP

precipitates) than the U-rich (β-U) grains with the Zr-rich precipitates. This may be a consequence of the Zr-rich precipitates in the U-rich (β-U) grains acting as defect sinks that absorb both vacancies and interstitials and inherently suppress the growth of voids and dislocations. Furthermore, historical literature suggests that during neutron irradiation, the orthorhombic crystal structure of the α-U phase facilitates anisotropic swelling of the crystal structure, and as a consequence, the α-U phase undergoes grain boundary tearing [35,63]. By correlating the historical literature to the observations from the current study, it can be inferred that the α-U grain observed in FIB lamella-4 is more affected by radiation, and consequently appears to possess greater quantities of microstructural inhomogeneities than the β-U grain which possesses Zr-rich precipitates. Furthermore, FIB lamella-4 and -5 from region B also revealed the presence of Pd based FP precipitates (see Figs. 4.5 and 4.7). Similar Pd based FP precipitates were also observed by Harp et al. [6]. Mariani et al. [84] hypothesized that Pd based FP precipitates in neutron irradiated metallic fuels at high temperatures act as sinks for lanthanides, and prevent their migration to the cladding, and consequently mitigate FCCI.

The STEM-EDS assessments also revealed that U-rich (β-U) grains with the Zr-rich precipitates from FIB lamella-4 were ~78wt.%U (see marker labeled 1 in Fig. 4.6 (a)) in composition, and a similar composition of ~75wt.%U was determined for the U-rich grain with Zr-rich precipitates in FIB lamella–5 ((see marker labeled 1 in Fig. 4.7 (a) and grain marked with red arrows in Fig. 4.7 (k)). Interestingly, similar microstructural alterations were also identified on the FIB lamellas with U-rich grains from region C (detailed in Section 4.4). Basak [111] assessed homogenized out-of-pile U-7wt.%Zr specimens and reported the presence of Zr-rich precipitates in an α-U matrix. Even though the Zr-rich precipitates observed by Basak [111] share morphologies similar to Zr-rich precipitates seen in this study, he assessed out-of-pile U-7wt.%Zr alloys, and reported the presence of an α-U matrix phase. In the current study, the U-rich grain with Zr-rich precipitates was identified to be β-U (see Fig. 4.5 (k)), and it should be noted that crystallographic proof of retained β-U has not been previously reported at room temperature. Hence, the current study also warrants a necessity for attaining a more detailed assessment of the cause for retention of the β-U phase at room temperature.

Another interesting observation is the presence of an FCC structured Zr-rich grain in FIB lamella-5 (see marker labeled 3 in Fig. 4.8 (b and e)). The presence of an FCC structured Zr-rich grain could be classified as a consequence of the following possibilities: (1) oxidation of a Zr-rich

grain, (2) mechanical deformation of an α-Zr rich grain, (3) formation of Zr-rich solid FP, or (4) impurity stabilized Zr particles (often observed as a byproduct in injection casted fuels). Even though oxidation of the FIB lamella during specimen storage may have facilitated the formation of an FCC structured Zr-rich grain, mechanical deformation of a hexagonally closed packed (HCP) α-Zr grain to an FCC structured Zr grain may also be a plausible cause. Manna et al. [130] utilized X-ray diffraction and TEM to reveal the polymorphic transformation of HCP structured α-Zr with an elemental purity >99.5 wt% to an FCC structured Zr when subjected to mechanical deformation. Hence, by correlating the findings by Manna et al. [130] to the current study, it can be assumed that the FCC structured Zr-rich grain observed in the current study may be a consequence of mechanical deformation of a Zr-rich grain via microscopic stresses (produced by cavities and formation of solid/gaseous FP precipitates) and macroscopic stresses (produced by fuel swelling and fuel constituent re-distribution) during neutron irradiation. Additionally, Zr is also known to be a high yield FP in U-Zr fuel systems, and the quantitative STEM-EDS assessments revealed that the Zr-rich grain possessed minor concentrations of other FPs (see marker labeled 3 in Fig. 4.7 and average chemical composition detailed in Table 4.1). Furthermore, Janney et al. [131] and Aitkaliyeva et al. [132] also reported the presence of impurity stabilized FCC structured Zr particles in injection cast metallic fuels prior to neutron irradiation. In conclusion, various factors may have resulted in the formation of an FCC structured Zr-rich grain and a confirmed mechanism cannot be provided from this study alone.

Correlating the TEM investigations produced from this study and the synchrotron μ-CT assessments of a FIB obelisk from region B by Thomas et al. [36], revealed the following: (1) the presence of Zr-rich grains and solid FP precipitates (observed via TEM investigations) at region B may increase the localized hardness, and as a consequence may be partially responsible for the formation of aspherical porosities and cracks (observed via synchrotron μ-CT assessments [Thomas et al. [36]]), (2) the presence of Zr-rich precipitates in an U-rich matrix phase and solid FP precipitates (observed via TEM investigations) may have affected the compositional estimates determined for the U-rich, U-intermediate, and U-poor phase regions of the FIB obelisk (determined via synchrotron μ-CT assessments [Thomas et al. [36]]), and (3) α-U grain being more affected by radiation (observed via TEM investigations) may have swelled in an anisotropic fashion and facilitated the formation of aspherical porosities (observed via synchrotron μ-CT assessments [Thomas et al. [36]]).

In conclusion, the TEM investigations at region B revealed: (1) the presence of two major phases: α-U and U-rich (β-U) grains with Zr-rich precipitates, (2) the presence of a Zr-rich grain which is FCC structured, (3) α-U grain is more affected by radiation and possess a greater concentration of microstructural inhomogeneities than the U-rich (β-U) grain with Zr-rich precipitates, and (4) the presence of solid FP precipitates with varying compositions and levels of crystallinity.

5.1.3 Transmission Electron Microscopy of Region C

SEM-EDS experiments by Harp et al. [6] found that the average Zr content in region C is the same as the cast material, i.e. U~10wt.%Zr. As shown in Figs. 4.9 (a-j), the FIB lamella-6 from region C possess U-rich grains with Zr-rich precipitates and grains with U-rich, U-intermediate, and U-lean localities (see dashed red box in Figs. 4.9 (a-j)). The STEM-EDS point scans detailed in Table. 4.1 revealed that the U-rich, U-intermediate, and U-lean localities (see labels (1-3) in Fig. 4.9 (a)) observed in region C share chemical compositions similar to the microstructural alterations observed in regions A and A/B (see labels (1-3) in Fig. 4.2 (a) and Fig. 4.4 (a)). Furthermore, like region B, region C also showed similar microstructural alterations such as U-rich grains with Zr-rich precipitates (see Fig. 4.6 (c), and Figs. 4.10 (c and m)).

Basak [111] conducted thermodynamic assessments on homogenized out-of-pile U-7wt%Zr alloys and reported that if the α-U phase is retained as a metastable phase with supersaturation of Zr, then the excess amount of Zr can be ejected as δ-UZr$_2$ precipitates. Furthermore, he also suggested that the reduced amount of Zr in the surrounding α-U matrix phase prevents the growth of these precipitates [111]. Although these analogies may hold for experiments on out-of-pile U-Zr alloys, various other factors such as the formation of Zr as an FP and retention of the β-U phase should also be considered when comparing the observations to neutron irradiated U-Zr fuels. In the current study, microstructural features similar to that observed by Basak [111] were identified at regions B and C; however, the SAED patterns from region B revealed that the U-rich grains with Zr-rich precipitates were β-U. Since both regions B and C share similar microstructural alterations (i.e. U-rich grains with Zr-rich precipitates), it is highly likely that the β-U phase identified for the U-rich grain at region B is the same phase for the U-rich grain at region C. However, a more detailed assessment which is beyond the scope of the current study is essential for determining: (1) the crystal structure of the U-rich matrix and Zr-rich precipitate phases at

region C, and (2) the cause for potential retention of β-U phase of the U-rich grains at room temperature.

Another unique observation from the STEM-EDS assessments presented in Fig. 4.10 are the varying concentrations of Zr-enrichment (see red arrows in Fig. 4.10 (c, m)) near cavities and in precipitates. The U-rich matrix phase (labeled 1 and 2 in Fig. 4.10 (a and k)) has a local Zr composition of ~15wt.%Zr, while the Zr-enriched locality near cavities (labeled 2 in Fig. 4.10 (a)) and Zr-rich precipitates (labeled 1 in Fig. 4.10 (k)) has a local Zr composition of ~64wt.%Zr and ~45wt.%Zr, respectively. Hence, it can be concluded that localities near cavities possess a greater quantity of Zr than the Zr-rich precipitates in the matrix phase. Although various factors such as temperature, stresses inside cavities, Zr-FP, and Zr-rich phase precipitation could be responsible for Zr-enrichment at cavities, radiation induced segregation (RIS) can also be a hypothesized as a probable cause. Neutron irradiation facilitates the production of point defects and defect clusters throughout the irradiated material. Mobile defects tend to escape recombination and migrate to sinks such as dislocations, grain boundaries, cavities, and other microstructural features [123]. In a binary alloy, the flux of defects such as vacancies to a sink is balanced by flux of atoms in the opposite direction [123]. If the binary alloy is comprised of A and B atoms, and if the flux of A atoms is larger than the flux of B atoms, then more A atoms migrate and cause the enrichment of B atoms at the sink. Hence, the local segregation that occurs at sinks as a consequence of defect migration is known as RIS [123]. Rest [63] studied the swelling in U-10Zr and other U-xPu-10Zr (0≤x≤19) fuels by assuming that the irradiation features seen in fissionable metals are analogous to the well-established theories on swelling by void formation in non-fissionable metals. Similarly, if the well-established theories on RIS in non-fissionable metals are hypothesized to be analogous to fissionable metals, then the observation of localized Zr-enrichment at cavities (see red arrows in Fig. 4.10 (c and m)) indicate that U atoms diffused from cavities at a faster rate than Zr atoms. Furthermore, out-of-pile diffusion couple experiments by Park et al. [133] on depleted U and Zr at 650°C, 680°C, and 710°C provides credence to the above-mentioned hypothesis. Park et al. [133] reported that at elevated temperatures (650°C, 680°C, and 710°C), the intrinsic diffusivity of U atoms (3.6×10^{-15} m^2/s, 3.4×10^{-15} m^2/s, and 4.7×10^{-15} m^2/s) is greater than that of Zr atoms (1.4×10^{-15} m^2/s, 1.3×10^{-15} m^2/s, and 1.9×10^{-15} m^2/s) [133]. Hence, by correlating the experimental observations reported by Park et al. [133] and the Zr-enrichment observed at cavities from the current study (see red arrows in Fig. 4.10 (c and m)), it can be hypothesized that during neutron

irradiation the flux of vacancies to a sink (grain boundary/cavity) is complemented by an equal flux of atoms (U and Zr) in the opposite direction, and since U atoms diffuse faster than Zr atoms, Zr-enrichment is observed at the cavities. In summary, it can be concluded that U diffuses faster than Zr locally near sinks such as cavities, a consequence of RIS. However, considering that only a small dataset has been analyzed, more experimental and modelling assessment which is beyond the scope of this study is required to validate the theory of RIS in fissionable metals (i.e. neutron irradiated U-10wt.%Zr fuels). Additionally, the TEM assessment also revealed the presence of Zr-enrichment along grain boundaries.

The STEM-EDS maps presented in Fig. 4.12 (i-p) revealed the presence of U-rich precipitates (see white arrows in Fig. 4.12 (i)) and FPs (see dashed white circles with red arrows in Fig. 4.12 (l-p)) in a Zr-rich grain/particle. Although the Zr-rich grain/particle appears to share a resemblance to impurity stabilized Zr particles (a common occurrence in injection cast U-Zr fuels), and possess an FCC crystal structure (see Fig. 4.12 (e-h)), a confirmed conclusion on the reasoning behind the nucleation of U-rich precipitates and presence of FPs in the Zr-rich grain/particle cannot be provided from the current study. However, the probable causes to the observed phenomena (i.e. nucleation of U-rich precipitates and presence of FPs) can be hypothesized via correlating the observations from the current study to the observations and results produced from: (1) SEM-EDS maps assessed by Harp et al. [6], and (2) out-of-pile U-Zr-Ce diffusion couple experiments by Ogata et al. [134]. The SEM-EDS maps investigations by Harp et al. [6] revealed that at the FCCI region, the Zr EDS map nearly mimics the Ce and Nd EDS maps, and as a consequence, the Zr-rich regions are also rich in FPs, while, out-of-pile U-Zr-Ce diffusion couple experiments by Ogata et al. [134] revealed that Ce migrates to regions with higher Zr content. Hence, based on the observations reported by Harp et al. [6] and Ogata et al. [134], it can be assumed that FPs possess an affinity to migrate towards the Zr-rich regions of the fuel (in this case, the Zr-rich grain), provided that the FP elements observed in the neutron irradiated fuel is considered to be analogous to Nd and Ce elements reported by Harp et al. [6] and Ogata et al. [134].

In conclusion, the TEM investigations at region C revealed the presence of: (1) grains with U-rich, U-intermediate, and U-lean localities (similar to features seen at regions A and A/B), (2) U-rich grains with Zr-rich precipitates (similar to features seen at region B), (3) probable RIS at cavities and grain boundaries, and (4) the presence of an FCC structured Zr-rich grain with U-rich

126

precipitates and FPs. The grains with U-intermediate localities were determined to be δ-UZr$_2$, while the Zr-rich grain/particle was determined to possess an FCC crystal structure.

5.1.4 Transmission Electron Microscopy of the Neutron Irradiated HT9 Cladding

SEM-EDS experiments by Harp et al. [6] on the neutron irradiated HT9 cladding revealed the following: (1) FP migration along grain boundaries, and (2) presence of FP precipitates, while the TEM investigations presented in Section 4.1.4 revealed the following: (1) matrix phase of the neutron irradiated HT9 cladding is BCC-Fe, (2) Intergranular FP migration, and (3) presence of various types of FP precipitates which were composed of Nd, Pd, Pr, Sn, Ce, and La. Even though Figs. 4.13-4.16 corroborate the findings reported by Harp et al. [6], it is interesting to note that the TEM investigation presented in the current study showed that FP migration does not occur along all the grain boundaries of the neutron irradiated HT9 cladding (i.e. there is potentially a preferred grain orientation for FP migration). The STEM-BF image presented in Fig. 4.13 (a) revealed the presence of several grains in FIB lamella-9 from the neuron irradiated HT9 cladding, while Fig. 4.13 (j) revealed the migration of Nd along a specific grain boundary. Considering that only one FIB lamella from the neutron irradiated HT9 cladding was investigated in this study, a conclusive statement on preferred grain orientation for FP migration cannot be established, and consequently, this warrants for a more comprehensive assessment to be conducted.

Even though the SEM-EDS assessments by Harp et al. [6] on the neutron irradiated HT9 revealed the presence of FP precipitates, the current study (i.e. TEM investigations) being a higher resolution assessment (see Figs. 4.14-4.16) revealed the complexity in identifying the type of precipitate (i.e. there are several types of Fe rich precipitates, and Nd-rich FP precipitates). Furthermore, the SEM-EDS assessment by Harp et al. [6] at the fuel-FCCI-HT9 contact region revealed the presence of three distinct localities (i.e. HT9 edge, HT9+fission products, and FCCI), and consequently, nano-indentation experiments (see Section 4.4 and Section 5.4) were performed at the three distinct localities to determine the effect of microstructural alterations on the local mechanical properties exhibited by the neutron irradiated HT9 cladding.

5.2 Microscale Characterization

5.2.1 Serial Sectioning of Region A, Region A/B, and Region B

As presented in Fig. 4.18 and detailed in Section 4.2.1, the serial sectioning of the FIB cuboid-1 from region A revealed the presence of: (1) a U-Zr matrix phase with U-rich precipitates, (2) FP precipitates, and (3) large spherical pores. Furthermore, correlating the TEM experiments presented in Section 4.1.1 and Section 5.1.1 indicated that the U-Zr matrix phase is δ-UZr$_2$, while the U-rich precipitates are α-U.

As shown in Fig. 4.18 (f), an Nd-Pd based FP precipitate was present in the FIB cuboid-1 from region A (at a serially sectioned depth of 8.8 µm). Interestingly, the SEM-EDS experiments by Harp et al. [6] at region A of the same fuel cross-section analyzed in this study also revealed the presence of Pd-Nd-Ce based FP precipitates. Mariani et al. [84,135,136] reported the observation of similar FP precipitates and suggested that they could be used to reduce the FCCI occurring at the fuel and cladding interface. They performed out-of-pile experiments and suggested that the addition of Pd in U-Zr fuels facilitates the binding of FP as precipitates in the fuel slug and consequently mitigate the FP migration to the FCCI region. The suggestions provided by Mariani et al. [84,135,136] were also used by Harp et al. [6] as a reference to the observation of FP precipitates at region A of the neutron irradiated U-10wt.%Zr fuel cross-section that achieved a burnup of 5.7 at.%. Furthermore, several other out-of-pile experiments have also been performed to study the stability of various FP in U-Zr fuels [137–139]. Hence, the observation of Nd-Pd based FP precipitates in the FIB cuboid-1 from region A of the neutron irradiated U-10wt.%Zr fuel cross-section in this study may provide plausible credence to the FCCI mitigation strategy proposed by Mariani et al. [84,135,136].

Figs. 4.18 (a-h) show the presence of spherical and extended porosity in the FIB cuboid-1 from region A. Hofman et al. [2], postulated the following at the fuel center: (1) large gas bubbles formed are a consequence of high plasticity and low capability to withstand shear stresses. (2) In an extreme scenario, the center may behave in a viscous manner, and the fission-gas pressure in the center would result in a biaxial loading of the peripheral shell with the radial stress component being twice the axial component [2]. Even though similar microstructural alterations (i.e. spherical and extended porosity) have been observed in the current study and the PIE performed by Hofman et al. [2], their postulations are yet to be validated. Moreover, they also postulated that the central

region of a neutron irradiated U-10wt.%Zr fuel that achieved a burnup of 6 at.% was predominantly γ-U+β-U (provided the fuel centerline temperature was greater than 662˚C) [35]; however, the TEM investigations provided in Sections 4.1.1 and 5.1.1 indicate that the central region of a neutron irradiated U-10wt.%Zr fuel that achieved a burnup of 5.7 at.% was predominantly α-U+δ-UZr₂. In conclusion, further research (both experiments and models) is required to describe the phenomena behind the formation of spherical and extended porosity at region A of the neutron irradiated U-10wt.%Zr fuel cross-section.

As shown in Fig. 4.19 and detailed in Section 4.2.1, the serial sectioning of the FIB cuboid-2 from region A/B revealed the presence of: (1) a U-Zr grain with U-rich precipitates and large spherical pores, and (2) U-rich grains with small spherical pores. Even though the correlative TEM investigations of region A/B (detailed in Section 4.1.1 and Section 5.1.1) indicated that the U-Zr grain is δ-UZr₂ and the U-rich precipitates are α-U phases, the serial sectioning experiments also revealed the presence of U-rich grains with small spherical pores. The presence of two different types of grains (i.e. U-Zr and U-rich) at region A/B is a consequence of the FIB cuboid-2 being produced at the intersection of regions A and B. More interestingly, synchrotron µ-CT experiments (see Section 5.3.1) of a FIB obelisk from region A/B, also showed similar observations (i.e. presence of large spherical pores and a large concentration of small spherical pores). A more comprehensive correlation on the classes of porosity and their effects on the localized microscopic fuel swelling at region A/B of the fuel cross-section is provided in Section 5.3.1 of the dissertation.

As shown in Fig. 4.20 and detailed in Section 4.2.1, the serial sectioning of the FIB cuboid-3 from region B revealed the presence of: (1) a U-Zr grain with U-rich precipitates and spherical pores, (2) Zr and Nd-Ce based FP precipitates in pores, (3) U-rich grains which were severely affected by radiation with extended/interconnected pores, and (4) the large concentration of small pores. Even though the crystal structures of the U-Zr grain with spherical pores at region B were not identified in this study, a correlation between the other observations and the TEM investigations detailed in Section 4.1.2 and Section 5.1.2 can be established. The TEM investigations in region B revealed the presence of: (1) α-U, β-U, and δ-UZr₂ phases, (2) FCC structured Zr FP precipitates, and (3) a variety of amorphous and crystalline FP precipitates. These observations corroborated with several observations seen in the serial sectioned FIB cuboid-3 from region B. For example, the TEM investigations at region B revealed the presence of an α-U phase (severely affected by radiation) with large quantities of Zr/Nd-Ce-Pd/Nd-Ce-Pd-La/Nd-Ce-La

based FP precipitates (see Figs. 4.5-4.8), while the serial sectioning experiment revealed the presence of U-rich grains which were severely affected by radiation with extended/interconnected pores, and Zr/Nd-Ce based FP precipitates in pores. Even though Hofman et al. [2] postulated that the anisotropic growth and grain boundary tearing of the α-U phase facilitates, the formation of extended/interconnected pores, the current study cannot validate the phenomena responsible for the formation of extended/interconnected pores. However, the correlated TEM investigations and serial sectioning experiments in region B indicate that the α-U phase is the U-rich phase that possessed extended/interconnected pores with FP precipitates. The synchrotron μ-CT experiments of a FIB obelisk from region B also showed similar microstructural observations (i.e. various types of pores), and a comprehensive correlation on the classes of porosity and their effects on the localized microscopic fuel swelling at region B is detailed in Section 5.3.1 of the dissertation.

5.2.2   Serial Sectioning of the FCCI locality

BSE micrographs presented in Fig. 4.17 were produced at a fuel cross-sectional burnup of 5.7 at.%, and the same fuel cross-section was assessed by Harp et al. [6]. As detailed in Section 2.4, the SEM-EDS maps produced by Harp et al. [6] at the FCCI locality of the MFF-3 fuel revealed the presence of Cr rich precipitates, interdiffusion of Fe into the fuel, presence of a Zr-rich barrier, presence of Ce-Nd solid FP precipitates, mixing of Ce-Nd with the Zr-rich barrier, and FP migration along the grain boundaries of the HT9 cladding. From their SEM-EDS maps, it is evident that even though the Zr-rich barrier may have assisted in preventing the initial gross interdiffusion between the fuel and cladding, the formation of cracks on the Zr-rich barrier (a consequence of fuel swelling and irradiation/thermal stresses) led to accelerated FCCI and formation of multiple binary/ternary phases [6].

As shown in Fig. 4.21 and detailed in Section 4.2.2, serial sectioning of the FIB cuboid-4 from the FCCI locality revealed the presence of: (1) spherical and aspherical cavities on the fuel side, (2) a Zr-rich barrier preventing the interdiffusion of U into the cladding, (3) Ce-Pd-Nd based FCCI layer between the fuel and cladding, and (4) Cr-rich precipitates on the cladding side. Fig. 4.21 revealed that the Zr-rich barrier may have initially impeded interdiffusion between the fuel and cladding, and with time, the barrier cracked as a consequence of various factors (such as fuel constituent re-distribution, FP migration, and fuel swelling). The cracks provided an easy path for interdiffusion between the fuel and the cladding, and consequently, FPs diffused from the fuel to

the cladding and formed FCCI layers and other compounds. Similar microstructural alterations were also seen in the SEM-EDS map produced by Harp et al. [6], and several theories detailing the formation of a Zr-rich barrier between the fuel and cladding interface, the effectiveness of a Zr-rich barrier mitigating interdiffusion between the fuel and cladding, and the cracking of the Zr-rich barrier as a consequence of thermal stresses, annealing time, and driving forces between diffusion couple elements have been reported [3–5,7–9,11]. A comprehensive description of the various theories proposed is provided in Section 2.3.4 of the dissertation. Even though the current study was unable to determine the phenomena that govern the formation of the Zr-rich barrier at the fuel and cladding interface, the serial sectioning experiment provided 3D insight on how the cracked Zr-rich barrier led to enhanced FCCI. Furthermore, the current study also revealed the formation of Cr-rich precipitates at the cladding side, a phenomenon that was not reported prior to this study.

5.3   Mesoscale Characterization[2]

5.3.1   Synchrotron µ-CT Experiments of Region A/B and Region B

5.3.1.1   Phase Transformations

The sectioned FIB obelisks from regions A/B and B analyzed in this study were produced from regions of the fuel that reached an irradiation temperature of ~671°C and ~655-671°C, respectively [1,88]. As depicted from the U-Zr phase diagram in Fig. 1.1, U-35wt.%Zr alloys under equilibrium conditions possess γ-U at 671°C, α-U+γ_2 within a temperature range of 617-662°C, and α-U+δ-UZr$_2$ below 617°C. Similarly, U-4wt.%Zr to U-10wt.%Zr alloys under equilibrium conditions possess β-U+γ_2 phases within a temperature range of 662-693°C, α-U+γ_2 phases within a temperature range of 617-662°C, and δ-UZr$_2$+α-U phases below 617°C [13]. Since regions A/B and B were cooled from an elevated irradiation temperature of ~671°C and ~655-671°C, the above-mentioned phase regions should be taken into consideration when evaluating phases post-

irradiation. Out-of-pile annealing experiments on U-10wt.%Zr alloys by Rai et al. [16] showed the following phase transformations: α-U+α'+δ-UZr$_2$ $\rightarrow$ α-U+γ_2 $\rightarrow$ β+γ_2 $\rightarrow$ γ_1+γ_2 $\rightarrow$ γ when heated at 3 K/min from a baseline temperature of 200ºC. Whereas, out-of-pile annealing experiments on U-10wt.%Zr alloys by Williams et al. [17] showed the following phase transformations: γ $\rightarrow$ α-U+γ_2 $\rightarrow$ α-U+δ-UZr$_2$ when cooled from an annealing temperature of 900˚C. In summary, the out-of-pile experiments by Rai et al. [16] and Williams et al. [17] revealed that a conclusive phase transformation route for un-irradiated U-10wt.%Zr is yet to be established, and consequently, this adds to the complexity of determining the phase transformation paths followed by U-10wt.%Zr alloys that are subjected to neutron irradiation. To further enhance the existing complexity, the prediction of the phase transformation paths followed by in-pile U-Zr fuels during neutron irradiation cannot be determined without appropriate in-pile experiments. For instance, performing short term in-pile irradiation experiments at various doses, temperatures, and U-Zr alloy compositions will assist in determining and validating the various phases transformations that occur in a neutron irradiated U-Zr alloy system. This uncertainty in predicting the phase transformation pathways is due to the in-pile non-equilibrium conditions, including radiation damage, irradiation temperature gradients, and burnup gradients that lead to fuel constituent re-distribution, and generation of FP (including Zr).

As specified in Section 2.3.2, historical work conducted by Hofman et al. [35,65] postulated that U-10wt.%Zr fuels that achieved a burnup of 6 at.% (with the fuel centerline temperature assumed to be above 662˚C) possessed three distinct regions. While U-10wt.%Zr fuels that achieved a burnup of 0.8 at.% (with the fuel centerline temperature assumed to be below 662˚C) possessed two distinct phase regions [35,65]. The U-10wt.%Zr fuels that achieved a burnup of 6 at.% comprised of a central region (γ+β-U), an intermediate region (α-U+ γ_2), and a fuel periphery region (α-U+δ-UZr$_2$), while the U-10wt.%Zr fuels that achieved a burnup of 0.8 at.% comprised of a central region (α-U+γ_2) and a fuel periphery region (α-U+δ-UZr$_2$), respectively [35,65]. In comparison, Yacout et al. [34] postulated that U-10wt.%Zr fuel that achieved a burnup of 5 at.% possessed a central region where the fuel temperature was ~693-699˚C and γ_2 was the major phase, an intermediate region where the fuel temperature was ~663-693˚C and γ_2+β-U were the major phases, and a fuel periphery region where the fuel temperature was ~636-663˚C and γ_2+α-U were the major phases.

132

The exact MFF-3 fuel cross-section used in the current study was assessed by Harp et al [6] via SEM-EDS and SEM-BSE examinations. Harp et al. [6] observed Zr migration in the neutron irradiated fuel cross-section and categorized the three concentric regions observed into the fuel-central zone or region A, the fuel-intermediate zone or region B, and the fuel-peripheral zone or region C. Harp et al. [6] stated that during irradiation; the higher Zr content (~30-35 wt.%) and a calculated irradiation temperature of 682˚C at the fuel center provided the suggestion that after removal from the reactor, the dominant equilibrium phases present at the fuel center were α-U and δ-UZr$_2$. The FIB obelisks analyzed in this study were obtained from regions A/B (i.e. at the intersection of fuel center [U~30-35wt.%Zr [6]] and intermediate zones [U~4wt.%Zr [6]]), and B (i.e. the intermediate zone [U~4wt.%Zr [6]]) of the fuel with estimated irradiation temperatures of ~671 ˚C, and ~655-671 ˚C, respectively. Consequently, the possibilities of γ$_2$, α-U, β-U, and δ-UZr$_2$ phases being present in the FIB obelisks analyzed are hence justified. Furthermore, the correlative TEM investigations at regions A/B and B (detailed in Sections 4.1.1, 4.1.2, 5.1.1, and 5.1.2) revealed the presence of α-U, β-U, δ-UZr$_2$, and several varieties of FP precipitates.

The spatial heterogeneity of chemical compositions observed via SEM-EDS assessments by Harp et al. [27] in regions A/B and B is attributed to neutron irradiation-induced fuel constituent re-distribution and non-equilibrium phase transformations. Although the SEM-EDS and SEM-BSE characterization by Harp et al. [6] at regions A/B and B revealed an average composition of U~30-35wt.%Zr/U~4wt.%Zr and U~4wt.%Zr, respectively, a closer inspection revealed the presence of differing localities in regions A/B and B possessing varying of compositions U and Zr, as well as Zr precipitates. Hence, it can be inferred that even though macroscopically, the average composition of regions A/B and B is U~30-35wt.%Zr/U~4wt.%Zr and U~4wt.%Zr, respectively, it may vary microscopically and nanoscopically. Furthermore, the evidence to variations in the chemical compositions at local levels was also identified via the TEM investigations and serial sectioning experiments performed at regions A/B and B (see Sections 5.1 and 5.2). Additionally, the SEM-EDS maps and line scans reported by Harp et al. [6] had a minimum scan step size of 4.8 µm, and as a consequence, features smaller than 4.8 µm will not be detected.

The average chemical compositions of the U-rich, U-intermediate, and U-poor regions of the sectioned FIB obelisk from region A/B was determined to be ~51.9wt.%U**,** ~40.1wt.%U, and ~29.5wt.%U, respectively. Similarly, the sectioned FIB obelisk from region B also possessed U-rich, U-intermediate, and U-poor regions with an average chemical composition of ~54.0wt.%U**,**

~41.0wt.%U, and ~28.8wt.%U, respectively. The average chemical compositions were determined by utilizing the average attenuation of the U-rich, U-intermediate, and U-poor regions (specified in Section 4.3.1) and Eq. (3.5). Even though average compositional estimates provide an approximated estimation on the chemical composition of each region, the estimates are affected by the presence of various microstructural features that are smaller than the resolution of the μ-CT technique. Correlating the observations from the current study to the observations reported by Harp et al. [6] revealed that the reduced U compositions in the U-rich, U-intermediate, and U-poor phase regions (from the absorption contrast μ-CT images) is a consequence of the sectioned FIB obelisks being produced from a locality possessing non-homogeneous, sub-micron compositions of U and Zr, and FP precipitates. Furthermore, the comprehensive TEM investigations (detailed in Sections 4.1.1, 4.1.2, 5.1.1 and 5.1.2) and serial sectioning experiments (detailed in Sections 4.2.1 and 5.2.1) of regions A/B and B, confirmed the presence various major phases (α-U, β-U, and δ-UZr$_2$) and several types of FP precipitates at different regions of the neutron irradiated U-10wt.%Zr fuel cross-section.

5.3.1.2   Pore Morphology Relationship to Phases

Fuel constituent re-distribution arising as a consequence of axial and radial temperature gradients within the fuel pin not only determines the phases present at different regions of the fuel but also influences pore morphologies [6]. As detailed in Section 2.3, the α-U and γ-U phases in neutron irradiated U-10wt.%Zr fuels were suggested to play a vital role in influencing the pore morphologies at a particular locality [6,35]. The pores in the α-U phase were found to be asymmetrical, which was attributed to grain boundary tearing, while the pores in the γ-U phase were observed to have a spherical morphology [6,35]. Although a direct correlation cannot be provided from this study, correlative TEM investigations (see Sections 5.1.1 and 5.1.2) and serial sectioning experiments (see Section 5.2.1) revealed that at region B, the U-rich (α-U) grains were more affected by radiation than the U-rich (β-U) grains with Zr-rich precipitates. More importantly, the U-rich (α-U) grains possessed a greater concentration of FP precipitates and extended/interconnected porosities, while U-rich (β-U) grains with Zr-rich precipitates possessed more spherical pores. As specified in Section 5.1.2, the Zr-rich precipitates in the U-rich (β-U) grains may act as defect sinks and absorb both vacancies and interstitials and suppress the growth of voids and dislocations. Consequently, the suppression of growth of voids and dislocations may

134

have facilitated the formation of small spherical pores or gas bubbles at region B of the fuel cross-section. Furthermore, the correlated TEM investigations and serial sectioning experiments at region A/B of the fuel cross-section also revealed the presence of large spherical pores in the δ-UZr$_2$ phase and presence of small spherical pores in U-rich grains.

As specified in Section 2.3, the PIE of U-10wt.%Zr fuels showed the presence of irregularly shaped pores and spherical pores [35]. The irregularly-shaped pores were assumed to be due to grain boundary tearing and anisotropic growth of α-U; whereas, the smaller pores were believed to be associated with either the δ-UZr$_2$ or the γ_2 phase [35]. The PIE of U-10wt.%Zr fuels also showed the presence of large interconnected globular porosity at the fuel center where the γ phase was presumed to be dominant [35]. SEM investigation of U-10wt.%Zr MFF-3 fuels by Harp et al. [6] indicated the presence of three concentric phase regions, and BSE micrographs revealed that each region in the fuel possessed different pore morphologies (i.e. dominant presence of spherical pores in region A and aspherical pores in region B). These previous 2D SEM studies provided qualitative porosity observations, and hence lack a comprehensive 3D understanding of the spatial distribution, pore morphology, and sphericity. Previously, a comprehensive analysis was complicated by high levels of heterogeneity in the pore morphologies (a consequence of various factors such as temperature gradients, phase transformations, burnup gradients, fuel constituent re-distribution, and fission product generation), and lack of 3D techniques that could characterize irradiated nuclear fuel.

Fig. 4.28, Fig. 4.30, and Fig. 4.31 revealed that a substantial number of aspherical (irregular shaped) pores were present in the sectioned FIB obelisks from regions A/B and B. The largest pore in the sectioned FIB obelisk from region A/B was irregularly shaped with a sphericity of 0.12 and occupied a volume of 25,047 μm^3. Similarly, the largest pore in the sectioned FIB obelisk from region B also possessed an irregular morphology with a sphericity of 0.1 and occupied a volume of 12,894 μm^3. More importantly, the porosity segmentation of the sectioned FIB obelisks from regions A/B and B revealed that the irregular shaped pores appeared to be surrounded by a U-poor region; while certain spherical pores appeared to be surrounded by U-rich and U-poor regions. Albeit the presence of irregularly shaped pores is dependent on the irradiation temperature of the region; it may also be dependent on the anisotropic growth of α-U grains. Hence, correlating the synchrotron μ-CT assessments, TEM investigations, and the assessment of the SEM-EDS maps by Harp et al. [6], indicated that phase regions rich in U wt.% potentially contains a large quantity

135

of α-U and/or β-U grains, while phase regions low in U wt.% contains δ-UZr$_2$, FP and Zr precipitates. The volume fraction of the U-rich phase regions (which could have contributions from α-U, β-U, γ, δ-UZr$_2$, and Zr-rich precipitates) in the sectioned FIB obelisks from regions A/B and B encompassed 26.13% and 20.2% of the total volume fractions, respectively. Theories/observations of anisotropic grain growth of α-U leading to potential grain boundary tearing have been previously proposed, and by correlating the theories/observations to the experimental observations from the current study, it can be hypothesized that the irregular shaped pores observed are due to fission gas accumulation, the interconnection of pores, and tearing at α-U grain boundaries [35,63,140,141].

Moreover, at region A/B there was: (1) 372 pores (pores in nucleation state) occupying 6.19% the total porosity volume fraction, (2) 128 pores (pores in their growth state) occupying 7.97% the total porosity volume fraction, and (3) 1 pore (extended/interconnected pore) occupying 71.77% the total porosity volume fraction of the sectioned FIB obelisk. In comparison, at region B there was: (1) 2123 pores (pores in nucleation state) occupying 17.8% the total porosity volume fraction, (2) 130 pores (pores in their growth state) occupying 24.8% the total porosity volume fraction, and (3) 1 pore (extended/interconnected pore) occupying 21.2% the total porosity volume fraction of the sectioned FIB obelisk. Hence it can be inferred that the localized microscopic fuel swelling at region A/B and region B is due to the presence of extended/interconnected pores and pores in their growth state, respectively.

In comparison to the current study, Hofman et al. [35] speculated that the central zone (region A) and intermediate zone (region B) in neutron irradiated U-10wt.%Zr (3 at % burnup) possessed β-U+γ$_2$ and α-U+γ$_2$ phases, respectively. Furthermore, Hofman et al. [35] also stated that at the intermediate zone, grain boundary tearing occurs along the α-U phase boundaries resulting in aspherical pores, and fission gas bubble growth in the lamellar γ$_2$ phase resulting in spherical pores. Although the proposed influence of crystal structure on pore type/morphology may hold precedence, the postulations provided by Hofman et al. [35] did involve any form of crystallographic assessment and were based on correlative SEM-BSE and equilibrium U-Zr phase diagram assessment. Additionally, the TEM investigations detailed in Section 4.1 and Section 5.1 of this dissertation contrasts the findings by Hofman et al. [35]. In this study, the intermediate zone or region B of the neutron irradiated U-10wt.%Zr fuel possessed α-U, β-U, δ-UZr$_2$, and several types of FP precipitates phases.

Although the confirmed mechanisms of pore nucleation and growth cannot be depicted by a standalone case study via an ex-situ examination, this was the first study that provided a detailed analysis of the 3D distribution of pores in a neutron irradiated U-10wt.%Zr fuel. To fully understand the effects of irradiation on the porosity distribution in U-10wt.%Zr fuels, it is suggested that additional specimens subjected to a range of irradiation conditions and locations within the fuel be harvested and subjected to synchrotron μ-CT experiments. Conducting these experiments will not only assist in providing localized microscopic swelling, pore volume, and morphological details but also assist in providing an early assessment of possible phase transformations in the fuel. Once a more detailed relationship between the pore volume and morphology is established at various regions of the irradiated fuel, a possible correlation of theory and mechanisms can be developed.

5.3.1.3   Fuel Swelling

Hofman et al. [35] performed PIE on U-10wt.%Zr fuel pins that were cladded with austenitic stainless steels and irradiated in the EBR-II to burnups of 15 at.%. These experiments were carried out to assist in fuel development for the Integral Fast Reactor program. Detailed information about the fuel and cladding dimensions for the EBR-II irradiated U-10wt.%Zr fuels were provided by Hofman et al. [35]. Fig. 4.31 shows the volumetric swelling in U-10wt.%Zr fuel pins that were irradiated in the EBR-II as a function of burnup at.%, and the localized microscopic swelling estimates from regions A/B and B of a U-10wt.%Zr fuel that was irradiated at the FFTF (current study). The volumetric swelling estimates of U-10wt.%Zr fuels irradiated in the EBR-II were determined by correlating the axial growth data to fuel/cladding parameters before and after irradiation [35]. The three assumptions that were taken into consideration for the swelling estimates in the EBR-II irradiated U-10wt.%Zr fuels are as follows: (1) The cladding diameter remains constant and does not change when the fuel is in contact with cladding. (2) The fuel and cladding are in contact at ~1 at.% burnup. (3) The U-Zr fuel is fully dense following fabrication.

Although the U-10wt.%Zr fuel pins used for neutron irradiation experiments in the EBR-II and the FFTF were produced via injection casting, there is no known published information detailing the density of the MFF-3 fuel pins [36,142]. The X425 series U-10wt.%Zr fuel pins that were similarly injection cast for irradiation experiments were reported to have a design density of 15.8 g/cm^3 and an as-cast density of 15.6 g/cm^3 (averaged from 15 individual diameter

137

measurements from 13 fuel pins) [36,142]. The discrepancy between the designed and as-fabricated densities was most likely a consequence of hot tearing during injection casting resulting in the formation of pores, which is commonly observed in injection casted fuels [142]. Hence, based on the mass and volume measurements reported, a difference in the volume fraction of the X425 series fuel pins was calculated to be ~6%, which was attributed to the porosity introduced from injection casting. Since the X425 series and MFF-3 series fuel pins were fabricated in a similar fashion, it is assumed that similar casting defects were also present in the MFF-3 series fuel pins. In summary, the injection cast MFF-3 series fuel pins were not completely dense following fabrication; however, they were assumed to be fully dense in this study to simplify the calculations required for estimating the macroscopic fuel swelling.

Williams et al. [74] recently reported the necessity to better understand fuel swelling in U-Zr metallic fuels in a more detailed manner. Current metallic fuel swelling models assume at ~30-36.5% fuel swelling, a bubble interconnection threshold is reached, and further gaseous swelling is eliminated as a consequence of the release of fission gas from the interconnected bubble into the plenum [79,143]. However, the 3D porosity segmentations (Figs. 4.28, 4.29 and 4.30) in the current study indicated that pores existed in all growth stages (i.e. extended/interconnected pores, interconnected pores, coalesced pores, pores in the growth phase, and pores in the nucleation phase), which all contributed to the localized microscopic fuel swelling. Moreover, it is reasonable to assume that since fission is still occurring, the opportunity to nucleate, grow, and coalesce new pores still exists within the fuel.

As specified in Section 3.4.2 and Section 4.2.3, three assumptions were taken into consideration for the determining the localized microscopic swelling in the sectioned FIB obelisks from regions A/B and B. The volume fractions used for the determination of the localized microscopic fuel swelling were based on the assessments of phase regions and porosity detailed in Section 4.2.3 and Table.4.3. Using Eq. (3.6), the localized microscopic swelling, of the sectioned FIB obelisks from regions A/B and B were estimated to be 16.8 and 7.70%, respectively.

Fig. 4.31 also showed a consistent trend of higher macroscopic swelling in the historical EBR-II fuels for multiple fuel diameters in comparison to the localized microscopic swelling estimate obtained at region B. In comparison, at region A/B, the localized microscopic swelling estimate appeared to be near the macroscopic swelling in the historical EBR-II fuels for multiple fuel diameters (see Fig. 4.31). The difference in swelling estimates calculated from this study

138

(localized microscopic swelling) versus the historical studies (macroscopic swelling) can be attributed to a few reasons: (1) The specimens selected for this study are highly localized and represents only two regions within the fuel (i.e. region A/B and region B) and not the entirety of the fuel pin. (2) FP precipitates cannot be accounted for, and consequently, the localized microscopic swelling value was underestimated. (3) A limited number of pores in the regions analyzed may result in a lower swelling value (i.e. limitations in the size of the FIB obelisks produced could prevent the sampling of large interconnected pores). (4) Different fuel cross-sections subjected to different burnups and temperature gradients possessed different swelling percentages. (5) Any features smaller than 0.84 μm^3 were below the detection limit for the μ-CT technique, therefore this would result in a slight underestimation of the localized microscopic swelling. In summary, the localized microscopic fuel swellings determined from this study revealed the singular effect of pore volumes at different regions on fuel swelling.

The volumetric swelling of 16.8% and 7.70% in the current study was specific to the regions at the intersection of the central and intermediate zones (region A/B) and the intermediate re-distribution zone (region B), respectively. The assessments detailed in this dissertation also represented the first 3D study conducted to quantify localized microscopic fuel swelling. Furthermore, since the microstructure, porosity distribution, temperature, and burnup gradients were not homogeneous in the neutron irradiated U-10wt.%Zr fuel pin, it is suggested that more FIB obelisks be harvested and analyzed from different irradiation conditions and cross-sectional regions of the fuel to provide a comprehensive localized microscopic fuel swelling comparison. Additionally, a detailed assessment and comparison of localized fuel swelling in different regions of the fuel cross-sections will also reveal the potential effects of various phases and irradiation conditions on pore morphology and evolution.

5.3.2 Synchrotron μ-CT Experiments of the Neutron Irradiated HT9 Cladding

As specified in Section 2.4 and Section 4.2.2, fuel swelling leads to contact between fuel and cladding, and consequently, facilitates the occurrence of FCCI. Historically, several studies have reported the presence of a Zr-rich barrier at the fuel and cladding interface impeding FCCI [4,5,7]. Even though the formation of the Zr-rich barrier was reported to be either a consequence of the ZrO_2 mold powder that was used on quartz to protect the mold during injection casting of metallic fuels or dissolution of the δ-UZr_2 near the fuel and cladding contact interface, they have

been reported to mitigate FCCI [4,5,7–9,11,87]. The Zr-rich barrier eventually cracks as a consequence of several effects (such as continued fuel swelling, thermal/mechanical stresses, temperature gradients, constituent migration, and fissioning) and provides pathways for FP migration between the fuel and cladding. The FP migration between the fuel and cladding was observed in the SEM-EDS maps reported by Harp et al. [6], and in Figs. 4.13, 4.21, and 4.32 of the current study. The synchrotron μ-CT assessment of the FIB obelisk from the neutron irradiated HT9 cladding (see Fig. 4.32) corroborated the suggestion that contact between fuel and cladding facilitates the formation of FCCI layers, beyond which FPs migrate intergranularly within the HT9 cladding. As presented in Figs. 4.32 (b-c), the FP migration was identified as crests in the line scan plots produced from the absorption contrast μ-CT images, while the grain boundaries were identified as troughs in the line scan plots produced from the phase contrast synchrotron μ-CT images. Furthermore, the correlative TEM investigations of the same locality (see Section 5.1.4) indicated that there may be a preferred grain orientation for FP migration along specific grain boundaries. A conclusive statement on the preferred grain orientation for FP migration was not established in this study; however, this is the first study that has observed such a phenomenon. Although, the mechanism which governs FP migration (i.e. whether they are liquid-like diffusion or not) is still of debate, the current study provides new methods to analyze FP migration in 3D in a non-destructive manner [5,84].

5.4   Nano-Mechanical Property Assessment

As shown in Fig. 4.35 (a) nano-indentation experiments on the neutron irradiated HT9 cladding were performed from the HT9 edge locality to the FCCI locality. The HT9 edge, HT9+fission products, and FCCI localities possessed an average nano-hardness of 5.18±0.40 GPa, 5.07±0.21 GPa, and 6.92±1.31 GPa, respectively. The H_0 and h^* values of the neutron irradiated HT9 cladding (detailed in Fig. 4.34 (c) and Section 4.4) were determined utilizing the Nix and Gao [101] method detailed in Section 3.5. In general, neutron irradiation is expected to decrease the h^*, and increase the H_n and H_0 behavior of materials [105,109]. Nix and Gao [101] performed indentation experiments on cold worked materials and associated the decrease in h^* value to the increased dislocation density in the material [101]. Elmustafa et al. [144] also reported similar observations. Hence, the low h^* value observed in the current study is assumed to be a consequence of a high concentration of dislocation pinning point defect densities present in the neutron

irradiated HT9 cladding. Furthermore, in the current study, a negative h^* and low R^2 value were observed, and similar values were also reported for neutron irradiated T91 and HT9 steels assessed by Krumwiede et al. [105,109]. Krumwiede [105] stated that negative h^* and low R^2 values indicate the extreme depth insensitivity to hardness, and consequently, the negative slope and derived h^* value should be considered qualitative rather than quantitative. Furthermore, Prasitthpayong et al. [103] also observed a negative h^* value for neutron irradiated T91 steels and stated the following: (1) negative h* values are a consequence of a slight increase in hardness as a function of penetration depth, and (2) if the h* value is less than -50 nm, then hardness decreases as a function of decreasing depth.

Un-irradiated HT9 was reported to possess an of nano-hardness ranging between 3.1-3.6 GPa [104,105]. In comparison, the HT9 edge locality of the neutron irradiated HT9 cladding assessed in this study showed an average nano-hardness of 5.18±0.40 GPa. The increase in nano-hardness in the HT9 edge locality is a consequence of in-pile several factors such as: (1) DBTT, (2) Formation of second phases, and precipitate phases, (3) creep (both irradiation and thermal), and (4) probable high-temperature He embrittlement. The nano-indentation experiments in the current study revealed that the nano-hardness (see Fig. 4.35 and Fig. 4.36 (b)) and calculated yield stresses (see Fig. 4.36 (b)) from the HT9 edge locality of the neutron irradiated HT9 cladding matched well with the nano-hardness and yield stresses of a neutron irradiated HT9 steel assessed by Krumwiede [105], and a substantial change in nano-hardness was observed as the nano-indentation experiments progressed to the HT9+fission products and FCCI localities. The variation in nano-hardness and calculated yield stresses in the HT9+fission products and FCCI localities is most likely a consequence of the following: (1) FP migration along grain boundaries of the neutron irradiated HT9 cladding, and (2) presence of various other microstructural alterations (such as intermetallic phases, FP precipitates, Zr-rich barrier, and pores). Furthermore, the correlated TEM investigations (detailed in Sections 4.1.4 and 5.1.4), serial sectioning experiments (detailed in Section 4.2.2 and Section 5.2.2), synchrotron μ-CT experiments (detailed in Section 4.3.2 and Section 5.3.2), and SEM-EDS assessments by Harp et al. [6] also corroborate the supposition that the large deviations in nano-hardness and calculated yield stresses observed at the HT9+fission products and FCCI localities of the neutron irradiated HT9 cladding is a consequence of the said microstructural alterations (such as intermetallic phases, FP precipitates, and Zr-rich layer).

Fig. 4.37 presents a comparison of the calculated Milot's and Busby's yield stress at the HT9 edge locality of the neutron irradiated HT9 cladding analyzed in this study and the yield stresses reported for HT9 steels that were neutron irradiated at various reactors at different irradiation temperatures and doses. The calculated Milot's and Busby's yield stress from the HT9 edge locality in Fig. 4.37 was determined by using Eqs. 3.8-3.10 on the averaged nano-indentation values ranging from ~55.55-332.75 µm in Fig. 4.35 (a). Fig. 4.37 revealed that the calculated Milot's yield stresses from the HT9 edge locality appeared to match well with few of the yield stresses that were reported for doses below 35 dpa [24,109,124–127]. More importantly, from the two calculated yield stresses (i.e. Milot's and Busby's), the Milot's yield stress at the HT9 edge locality of the neutron irradiated HT9 cladding appeared to align more closely to the yield stresses of neutron irradiated HT9 steels reported by Krumwiede et al. [109], Maloy et al. [129], and Klueh et al. [125] (see Fig. 4.37). Krumwiede et al. [109] experimented on neutron irradiated HT9 steels that were irradiated to a dose of 6.49 dpa, while Klueh et al. [125] experimented on neutron irradiated HT9 steels that were irradiated to doses of 6, 12, and 15 dpa. In comparison, Maloy et al. [129] experimented on neutron irradiated HT9 steels that were irradiated to doses of 7 and 18 dpa. Furthermore, Krumwiede et al. [109] experimented on neutron irradiated HT9 steels via tensile testing and nano-indentation and reported that the calculated Milot's yield stress value (calculated from the nano-indentation experiments) was close to the yield stress value determined by tensile testing [109].

Although similarities were observed between the calculated yield stresses from the current study and the yield stresses from the existing historical literature on neutron irradiated HT9 steels, it is difficult to obtain a true one-to-one correlation as a consequence of the following: (1) The work presented in the current study being performed on a neutron irradiated HT9 cladding was in contact with a neutron irradiated U-10wt.%Zr fuel. (2) Different fuel/cladding cross-sections were subjected to different burnup and temperature gradients. (3) The yield stresses reported in historical literature were macroscopic, while the calculated yield stresses determined via nanoindentation is highly localized. For instance, Maloy et al. [126] reported that neutron irradiated HT9 steels that were subjected to a range of doses (i.e. 35.3 dpa, 44 dpa, and 67.5 dpa) and irradiation temperatures (390 and 427 ˚C) possessed varying yield stresses (i.e. 1015.27 MPa, 745.12 MPa, and 833.60 MPa), while the HT9 edge locality of the neutron irradiated HT9 cladding (irradiated to a dose of 19.42 dpa) in the current study possessed a Milot's yield stress of

1267.71±108.6 MPa. A large deviation exists between the yield stresses due to the following reasons: (1) yield stresses of the neutron irradiated HT9 steels reported in the historical literature were determined via tensile testing and were dependent on the irradiation temperature and dose experienced in the reactor [24,109,124–127], and (2) the calculated yield stresses of the neutron irradiated HT9 cladding determined in this study were affected by several other factors. Since neutron irradiation causes metallic fuel to swell and come in contact with the cladding, the cladding is subjected to the following: (1) axial and diametrical stresses and strains, (2) thinning via FCCI, (3) FP migration, (4) formation of FP precipitates and several other phases, and (5) temperature gradients. The effects of axial and diametrical stresses and strains in neutron irradiated HT9 claddings are of utmost importance, and several studies (both experimental and modeling) have been performed to measure these values [75,145]. Diametrical strains (a consequence of fuel swelling) imposed on neutron irradiated claddings are often accompanied by irradiation creep at low temperatures and thermal creep at high temperatures [75,145]. Pahl et al. [75] reported that unbreached HT9 steels that were clad to U-10wt.%Zr fuels and neutron irradiated to a burnup of 10 at.% in the EBR-II had diametrical strains ranging between 0%-2%. The failure strains for HT9 steels were reported to be between 2%-4% and hence achieving a high diametrical strain value is detrimental for the cladding integrity [75]. Carmack et al. [1] performed linear profilometry assessment on the same neutron irradiated HT9 cladding from the MFF- 3 series fuel pin and reported a peak diametrical strain of 1.3%. It was assumed that the peak diametrical strain near the top of the fuel column is due to thermal creep, while diametrical strains at other locations were due radiation induced creep and/or void swelling [1]. Consequently, in this study, it is hypothesized that the axial and diametrical strains experienced by the neutron irradiated HT9 cladding (due to fuel swelling) were one of the major contributors responsible for the high yield stresses estimated at the HT9 edge, HT9+fission product, and FCCI localities. Furthermore, this was the first study performed to analyze the localized mechanical property of a neutron irradiated HT9 cladding, and consequently, this study warrants for a more comprehensive assessment to be performed.

In summary, the current study provided the means to comprehend the effects of microstructural alterations on the mechanical properties at various localities of a neutron irradiated HT9 cladding via synchrotron µ-CT, SEM, TEM, and nano-indentation experiments. Furthermore, the current study also provided a unique perspective of changes in yield stresses at different localities of a neutron irradiated HT9 cladding.

CHAPTER 6.   CONCLUSIONS

This study analyzed the neutron irradiation induced alterations in the microstructure and mechanical properties of a U-10wt.%Zr fuel and HT9 cladding from the MFF-3 series experiment which was irradiated in the FFTF reactor. Harp et al. [6] classified the same U-10wt.%Zr fuel cross-section assessed in this study into regions A, B, and C on basis of fuel constituent re-distribution. Regions A, B, and C were reported to have an average composition of U~30-35wt.%Zr, U~4wt.%Zr, and U~10wt.%Zr, respectively [6], and consequently, in this study, a coordinated group of experiments were assessed on a nanoscale, microscale, and mesoscale at each region. To effectively correlate and convey the findings determined via the experiments performed at various size scales, the conclusions section of the dissertation is detailed on the basis of the individual phase regions present in the microstructure of the neutron irradiated U-10wt.%Zr fuel cross-section. Furthermore, several interrelationships were identified between the microstructural observations at various size scales, and these interrelationships were correlated to the available historical literature on neutron irradiated metallic fuels and steel claddings. The findings from this study were also correlated to several in-pile and out-of-pile experiments. Several theories on phase transformation paths, formation of FCC structured Zr-rich grains, formation of U-rich and FP precipitates in Zr-rich grains, and RIS in fuels were established. The highlights of this study are described in this section.

6.1   Microstructural Characterization

6.1.1   Region A of the Neutron Irradiated U-10wt.%Zr Fuel

In this study, the FIB lamellas from region A (possessing an irradiation temperature ranging between 671-682˚C) revealed the following: (1) presence of two major phases which were determined to be α-U (U-rich locality) and δ-UZr$_2$ (U-intermediate locality), and (2) U-lean localities at grain boundaries that showed pathways along which Zr diffused from region B to A of the irradiated fuel cross-section. In comparison, a U-10wt.%Zr nuclear fuel that achieved a cross-sectional burnup of 6 at.% at the EBR-II was reported to have γ-U+β-U as the major phases

at the fuel central region (provided the fuel centerline temperature was greater than 662˚C) [35,65]. Even though Hofman et al. [35,65] used SEM imaging and the U-Zr equilibrium phase diagram to postulate that the major phases at the fuel central region were γ-U+β-U, no crystallographic assessment was performed to confirm the postulation.

In this study, TEM investigations of FIB lamellas from region A determined that the major phases in the fuel central region (i.e. region A) were α-U and δ-UZr$_2$. As depicted from the U-Zr equilibrium phase diagram by Sheldon et al. [13], U-35wt.%Zr alloys under equilibrium conditions possess γ-U at 682°C, α-U+γ$_2$ within a temperature range of 617-662°C, and α-U+δ-UZr$_2$ below 617°C. If the fuel was assumed to be cooled slowly from an elevated temperature of 682°C post reactor shutdown, then the plausible phase transformation route is γ→α-U+γ$_2$→α-U+δ-UZr$_2$. Additionally, the phases identified in the central region of the fuel (region A) in the current study were also correlated to the results reported from several out-of-pile U-Zr experiments. For instance, Basak [111] performed out-of-pile experiments on homogenized U-35wt.%Zr and revealed the presence of α-U precipitates with platelet/acicular structured morphologies in a δ-UZr$_2$ matrix phase, while Moore et al. [113] discussed the presence of acicular structured U-rich precipitates in U-Zr alloys. Hence the nanoscale assessments at region A of the fuel cross-section provided plausible reasoning on how the α-U+δ-UZr$_2$ dual-phase region evolved as a consequence of temperature gradient, kinetics of phase transformations, and fuel constituent re-distribution.

Serial sectioning of FIB cuboid-1 from region A revealed the following: (1) a U-Zr matrix phase, (2) U-rich precipitates within the U-Zr matrix phase, and at grain boundaries, (3) several FP precipitates, and (4) large spherical/extended pores. Correlative TEM investigations of region A indicated that the U-Zr matrix phase is δ-UZr$_2$, and the U-rich precipitates are α-U, respectively. In this study, an Nd-Pd based FP precipitate was observed in the FIB cuboid-1 from region A. SEM-EDS experiments by Harp et al. [6] at region A of the same fuel cross-section also revealed the presence of Pd-Nd-Ce based FP precipitates. Interestingly, Mariani et al. [84,135,136] reported the observation of similar FP precipitates and suggested that they could be used to reduce the FCCI occurring at the fuel and cladding interface. It was suggested that the addition of Pd in U-Zr fuels facilitates the binding of FP as precipitates in the fuel slug and consequently mitigate the FP migration to the FCCI region [84,135,136]. Hence, the observation of Nd-Pd based FP precipitates in this study provides plausible credence to the FCCI mitigation strategy by Mariani et al. [84,135,136]. The serial sectioning of the FIB cuboid-1 from region A also revealed the

presence of spherical and extended porosity. Hofman et al. [2], postulated the following at the fuel center: (1) Large gas bubbles are formed as a consequence of high plasticity and low capability to withstand shear stresses. (2) In an extreme scenario, the center may behave in a viscous manner, and the fission-gas pressure in the center would result in a biaxial loading of the peripheral shell with the radial stress component being twice the axial component. Even though similarities in microstructural alterations (i.e. spherical and extended porosity) exist between the current study and the PIE performed by Hofman et al. [2], their postulations are yet to be validated. In conclusion, further research (both experiments and models) is required to describe the phenomena behind the formation of spherical and extended porosity at region A of the neutron irradiated U-10wt.%Zr fuel cross-section.

6.1.2   Region A/B of the Neutron Irradiated U-10wt.%Zr Fuel

Since region A/B is at the intersection of regions A and B, it possesses phases from both regions and was determined to have an irradiation temperature of ~667°C. In this study, like region A, the FIB lamella from regions A/B revealed the presence of two major phases which were determined to be α-U (U-rich locality) and δ-UZr$_2$ (U-intermediate locality), and U-lean localities along grain boundaries that showed pathways along which Zr diffused from region B to A of the irradiated fuel cross-section. However, considering that only one FIB lamella was assessed from this region, it is highly likely that the major phases observed in region B were not captured in this region, and consequently, this study warrants the necessity to perform further TEM investigations. Like region A, if the fuel was assumed to be cooled slowly from an elevated temperature of 667°C post reactor shutdown, then the plausible phase transformation route at an alloy composition of U-35wt.%Z is $\gamma \rightarrow \alpha$-U+$\gamma_2 \rightarrow \alpha$-U+$\delta$-UZr$_2$.

Serial sectioning of FIB cuboid-2 from region A/B revealed the following: (1) a U-Zr grain with U-rich precipitates and large spherical pores, and (2) U-rich grains with spherical pores. Correlative TEM investigations of region A/B indicate that the U-Zr grain is δ-UZr$_2$ and the U-rich precipitates are α-U phases, respectively. Furthermore, regions A/B and A share similarities in microstructural alterations as a consequence of the FIB cuboid being produced at the intersection of region A and region B. Even though the crystal structure of the U-rich grains with spherical pores was not identified in this study, synchrotron μ-CT experiments of a FIB obelisk from region A/B, also showed similar microstructural observations (i.e. presence of 372 spherical pores).

146

Furthermore, currently, metallic fuel swelling models assume that at ~30-36.5% fuel swelling, a bubble interconnection threshold is reached, and further gaseous swelling is eliminated as a consequence of the release of fission gas from the interconnected bubble into the plenum [79]. The serial sectioning and synchrotron µ-CT experiments presented in the current study contrast with the fuel swelling assumptions and revealed the presence of small spherical pores. Consequently, these observations indicate the necessity to enhance the currently utilized fuel swelling models.

The synchrotron µ-CT experiments at region A/B revealed the presence of three distinct phase regions (U-rich, U-intermediate, and U-poor) and pores. The 3D image segmentation presented in this study revealed that the U-rich (~51.9wt.%U), U-intermediate (~40.1wt.%U), U-poor (~29.5wt.%U), and pores occupied a volume fraction of 6.13%, 6.92%, 52.55%, and 14.40%, respectively. More importantly, the 3D porosity segmentation at regions A/B revealed the presence of five porosity classes: (1) pores in the nucleation stage 0.84-42 μm^3, (2) pores in the growth stage 43-378 μm^3, (3) coalesced pores 379-1260 μm^3, (4) interconnected pores 1261-8400 μm^3, and (5) extended/interconnected >8401 μm^3. In this study, at region A/B, the extended/interconnected pore occupied the largest volume fraction followed by interconnected pores, pores in their growth stage, pores in their nucleation stage, and interconnected pores. Following the 3D porosity segmentation, sphericity values were assigned for each pore on the basis of pore volume and morphology. In this study, the localized microscopic fuel swelling at region A/B was estimated to be 16.8%, and the swelling estimate was compared to the localized microscopic fuel swelling in region B of the same fuel cross-section and the calculated macroscopic fuel swelling in U-10wt.%Zr fuels irradiated in the EBR-II. Even though the macroscopic swelling estimates in the historical EBR-II fuels for multiple fuel diameters appeared to be in close agreement with the localized microscopic fuel swelling estimated at region A/B, caution must be taken when comparing the swelling estimates. The following are several reasons that should be considered when comparing the localized microscopic and macroscopic fuel swelling: (1) The FIB obelisk from region A/B represents a highly localized region and not the entirety of the fuel pin. (2) FP precipitates were not be accounted for, and consequently, the localized microscopic swelling value will be underestimated. (3) A limited number of pores in the regions (i.e. limitations in the size of the FIB obelisks produced prevents the sampling of large interconnected/extended pores). (4) Different fuel cross-sections were subjected to different burnups and temperature gradients and consequently possessed different swelling percentages. In summary, the localized microscopic fuel swellings determined

147

from this study revealed the singular effect of pore volumes at region A/B on fuel swelling. Additionally, the 3D porosity segmentation and sphericity estimations revealed that the leading contributor to the localized microscopic fuel swelling at region A/B is the presence of extended/interconnected pores. Current metallic fuel swelling models assume that at ~30-36.5% fuel swelling, a bubble interconnection threshold is reached and further gaseous swelling is eliminated as a consequence of the release of fission gas from the interconnected bubble into the plenum [79]. The 3D porosity segmentations presented in the current study indicated that pores existed in all growth stages (i.e. extended/interconnected pores, interconnected pores, coalesced pores, pores in the growth phase, and pores in the nucleation phase), and consequently, all growth stages contributed to the localized microscopic fuel swelling. Hence, the current study stresses the need to further enhance the existing fuel swelling models.

Since historical works [6,35] suggested that the crystal structure of phases in neutron irradiated U-10wt.%Zr fuels play a vital role in influencing the pore morphologies at a particular locality, a correlation between the TEM investigations, serial sectioning experiments, and synchrotron μ-CT experiments was made in this study. TEM investigations and serial sectioning experiments at region A/B revealed the presence of large spherical pores in the δ-UZr$_2$ phase and the presence of small pores in U-rich grains. In comparison, the synchrotron μ-CT experiments at region A/B of the fuel cross-section revealed the presence of various classes of pores (i.e. pores in the nucleation stage, pores in the growth stage, coalesced pores, interconnected pores, and extended/interconnected pores). Consequently, these observations corroborate each other. Hence by correlating the nanoscale, microscale, and mesoscale assessments at region A/B, it can be concluded that the type of phases present at a locality influences the pore volume and morphology.

6.1.3   Region B of the Neutron Irradiated U-10wt.%Zr Fuel

Hofman et al. [35,65] postulated that a neutron irradiated U-10wt.%Zr fuel that achieved a cross-sectional burnup of 6 at.% at the EBR-II (provided the fuel centerline temperature was greater than 662˚C) possessed an intermediate region (i.e. region B) that comprised of α-U and γ_2 as the major phases. Since no crystallographic assessments were performed to validate the postulation, the assumption of an intermediate region with α-U and γ_2 as the major phases may or may not hold credence. In this study, the TEM investigations of FIB-lamellas from region B (possessing an irradiation temperature ranging between -655-671˚C) of a neutron irradiated U-

148

10wt.%Zr fuel that achieved a cross-section burnup of 5.7 at.% at the FFTF reactor revealed the presence of several microstructural alterations, which were unique to previous studies [1,6,34,35]. The microstructural alterations observed at region B are as follows: (1) an FCC structured Zr-rich grain, (2) α-U grain, (3) U-rich (β-U) grains with Zr-rich precipitates, (4) δ-UZr$_2$, and (5) solid FPs with varying chemical compositions and levels of crystallinity. Previous studies indicate that depending on the burnup at.% and temperature gradient experienced, region B was thought to possess either α-U+γ$_2$ or β-U+γ$_2$ [34,35]; however, the TEM investigations presented in the current study revealed that the situation is more complex and a multitude of phases was identified at region B of the fuel cross-section. The TEM investigations revealed that the U-rich (β-U) grain with Zr-rich precipitates was less affected by radiation than the α-U grain (i.e. the α-U grain was observed to have numerous inhomogeneities, such as several cavities and solid FP precipitates). These observations indicate that each phase behaves in an unique manner when subjected to neutron irradiation, and provides credence to the postulation that during neutron irradiation the orthorhombic crystal structure of the α-U phase undergoes anisotropic swelling, and consequently, facilitates grain boundary tearing and formation of irregular shaped cavities [2]. In this study, the U-rich (β-U) grains with Zr-rich precipitates were identified to possess fewer inhomogeneities such as cavities and solid FP precipitates, Consequently, the Zr-rich precipitates were hypothesized to act as defect sinks that absorb both vacancies and interstitials, and inherently suppress the growth of voids and dislocations. Furthermore, the suppression of the growth of voids and dislocations may have facilitated the formation of small spherical pores or gas bubbles.

At region B, an FCC structured Zr-rich grain was also observed and several probable causes that facilitated the formation of the FCC structured Zr-rich grain were provided. The probable causes that facilitated the formation of the FCC structured Zr grains are as follows: (1) oxidation of a Zr-rich grain, (2) mechanical deformation of an HCP structured α-Zr grain, (3) formation of Zr-rich solid FP, or (4) impurity stabilized Zr particles (often observed as a byproduct in injection casted fuels). Even though oxidation of the FIB lamella may facilitate the formation of FCC structured Zr-rich grains, mechanical deformation of HCP structured α-Zr grains to FCC structured Zr-rich grains may also be a potential cause. Manna et al. [130] revealed the polymorphic transformation of HCP structured α-Zr with an elemental purity >99.5 wt% to FCC structured Zr under mechanical deformation. Correlating the findings by Manna et al. [130] to the current study revealed that the FCC structured Zr-rich grain may be a consequence of mechanical deformation

of an HCP structured Zr grain via microscopic stresses (produced by cavities and the formation of solid/gaseous FP precipitates) and macroscopic stresses (produced by fuel swelling and fuel constituent re-distribution) during neutron irradiation. Additionally, Zr is also known to be a high yield FP in fuel systems that possess U^{235} atoms [146,147]. Interestingly, the high-resolution chemical composition assessment presented in this study also revealed that the FCC structured Zr-rich grain possessed concentrations of other FPs (such as Pd, La, and Ce).

Serial sectioning of FIB cuboid-3 from region B revealed the following: (1) a U-Zr grain with spherical pores, (2) Zr-rich and Pd-Nd-Ce FP precipitates in pores, (3) U-rich grains which appear to be more damaged with extended/interconnected pores, and (4) the large concentration of small pores. Even though a one-to-one correlation between the serial sectioning experiments and TEM investigations cannot be provided in this study, the TEM investigations of a locality in region B (near to the locality from where the FIB cuboid was produced for serial sectioning) revealed the presence of α-U, β-U, δ-UZr$_2$, FCC structured Zr, and a variety of amorphous and crystalline FP precipitates. At region B, the TEM investigations also revealed the presence of a heavily damaged α-U phase with large quantities of Zr/Nd-Ce-Pd/Nd-Ce-Pd-La/Nd-Ce-La based FP precipitates, while the serial sectioning experiment revealed the presence of U-rich grains which were severely damaged with extended/interconnected pores and Zr/Nd-Ce based FP precipitates. Furthermore, historical literature suggests that during irradiation, the orthorhombic crystal structure of the α-U phase undergrows anisotropic growth, and consequently, this facilitates grain boundary tearing and formation of extended/interconnected pores [2]. Even though the current study cannot validate the postulations of anisotropic growth and grain boundary tearing of the α-U phase, the correlated TEM investigations and serial sectioning experiment in region B indicate that the α-U phase possessed extended/interconnected pores with several types of FP precipitates. The synchrotron μ-CT experiments of a FIB obelisk from region B also showed similar microstructural observations (i.e. various categories/classes of pores).

The synchrotron μ-CT experiments at region B revealed the presence of three distinct phase regions (U-rich, U-intermediate, and U-poor) and pores. The 3D image segmentation revealed that the U-rich, U-intermediate, U-poor, and pores identified in this study occupied a volume fraction of 20.2%, 33.4%, 39.2%, and 7.2%, respectively. Like region A/B, the 3D porosity segmentation at regions B revealed the presence of five porosity classes: (1) pores in the nucleation stage 0.84-42 μm^3, (2) pores in the growth stage 43-378 μm^3, (3) coalesced pores 379-1260 μm^3, (4)

interconnected pores 1261-8400 μm^3, and (5) extended/interconnected >8401 μm^3. In this study, in region B, the pores in their growth stage occupied the largest volume fraction followed by extended/interconnected pores, interconnected pores, pores in their nucleation stage, and coalesced pores. Following the 3D porosity segmentation, sphericity values were calculated for each pore on basis of pore volume and morphology. In this study, the localized microscopic fuel swelling at region B was estimated to be 7.70%. The swelling estimate was compared to the localized microscopic fuel swelling at region A/B of the same fuel cross-section and the calculated macroscopic fuel swelling (~13-20 %) in U-10wt.%Zr fuels irradiated in the EBR-II. Even though the macroscopic swelling estimates in the historical EBR-II fuels for multiple fuel diameters appeared to consistently higher than the localized microscopic fuel swelling estimated at region B, caution must be taken when comparing the swelling estimates. As stated in Section 6.1.2, the difference in swelling calculated from this study (localized microscopic swelling) versus the historical studies (macroscopic swelling) was due to the following reasons: (1) The specimen from region B was highly localized and does not represent the entirety of the fuel pin. (2) FP precipitates cannot be accounted for, and consequently, the localized microscopic swelling value was underestimated. (3) Limitations in the size of the FIB obelisks produced could prevent the sampling of large interconnected pores. (4) Different fuel cross-sections subjected to different burnup and temperature gradients possessed different swelling percentages. (5) Features smaller than 0.84 μm^3 were below the detection limit for the μ-CT technique. The 3D porosity segmentation and sphericity estimations also revealed that the leading contributor to the localized microscopic fuel swelling at region B is the presence of pores in their growth stage. As specified in Section 6.1.2, current metallic fuel swelling models assume that at ~30-36.5% fuel swelling, a bubble interconnection threshold is reached beyond which gaseous swelling is eliminated as a consequence of the release of fission gas from the interconnected bubble into the plenum [79]. Like region A/B, the 3D porosity segmentations at region indicated that pores existed in all growth stages (i.e. extended/interconnected pores, interconnected pores, coalesced pores, pores in the growth phase, and pores in the nucleation phase), and consequently, all growth stages contributed to the localized microscopic fuel swelling. Consequently, the current study emphasizes the need to further enhance the existing fuel swelling models.

Historical works [6,35] suggested that the crystal structure of phases in neutron irradiated U-10wt.%Zr fuels influence the pore morphologies at a locality. TEM investigations and serial

sectioning experiments in region B indicate that the U-rich (α-U) grains were more affected by radiation than the U-rich (β-U) grains with Zr-rich precipitates. Hence, depending on the type of U-rich grains (i.e. α-U or β-U), extended/aspherical pores or small spherical pores may exist in the fuel microstructure. Furthermore, the observation of extended/aspherical and small spherical pores was also corroborated via the synchrotron μ-CT experiments at region B of the fuel cross-section. The synchrotron μ-CT experiments in region B revealed the presence of five porosity classes (i.e. pores in the nucleation stage, pores in the growth stage, coalesced pores, interconnected pores, and extended/interconnected).

The 2D PIE (using conventional SEM imaging) of U-10wt.%Zr fuels irradiated in the EBR-II to a burnup of 0.8 at.% revealed the presence of irregularly shaped pores and spherical pores at the fuel center [35]. The irregular-shaped pores were hypothesized to be due to grain boundary tearing and anisotropic growth of α-U; whereas, the smaller pores were believed to be associated with either the δ-UZr$_2$ or the γ_2 phase [35]. In contrast, the PIE of U-10wt.%Zr fuels irradiated in the EBR-II to a burnup of 3 at.% showed the presence of large interconnected spherical porosity at the fuel center where the γ phase was presumed to be dominant [35]. Recent SEM investigation of a U-10wt.%Zr MFF-3 fuel by Harp et al. [6] revealed the presence of three-phase regions with different pore morphologies. The low magnification SEM images reported by Harp et al. [6] showed region A possessing spherical pores, region B possessing extended/interconnected pores, and region C possessing a mix of spherical and extended/interconnected pores. Although the previous 2D SEM studies provided a qualitative assessment on the porosity in nuclear fuels, previously there was a lack of understanding of the spatial distribution, pore morphology/volume, and sphericity. Hence, the current study provided a comprehensive 3D analysis of porosity distribution and their effects on localized fuel swelling, an assessment that was previously unattainable due to the lack of 3D preparation and characterization techniques available for irradiated nuclear fuels.

6.1.4 Region C of the Neutron Irradiated U-10wt.%Zr Fuel

Hofman et al. [35,65] postulated that a neutron irradiated U-10wt.%Zr fuel that achieved a cross-sectional burnup of 6 at.% at the EBR-II possessed a peripheral region (i.e. region C) comprised of α-U and δ-UZr$_2$ as the major phases (provided the fuel centerline temperature was greater than 662˚C). The postulation was based on the examination of the U-Zr equilibrium phase

diagram and PIE of SEM-BSE micrographs. Furthermore, since no crystallographic assessment was performed to confirm the major phases, the postulation of α-U and δ-UZr$_2$ as the major phases in region C may or may not hold credibility [35,65]. In this study, the TEM investigations of region C (or periphery region) of a neutron irradiated U-10wt.%Zr fuel that achieved a cross-section burnup of 5.7 at.% at the FFTF reactor revealed the presence of several microstructural alterations which included: (1) U-intermediate (δ-UZr$_2$) grains with U-rich precipitates and U-lean localities. Similar microstructural features (both in the crystal structure and chemical compositions) were identified at region A (with an average composition of U~35wt.%Zr) of the fuel cross-section. (2) U-rich grains with Zr-rich precipitates. Similar microstructural alterations (chemical compositions) were identified in region B of the fuel cross-section. (3) FCC Zr-rich grain possessing U-rich precipitates and FPs. Although a clear cause for an FCC structured Zr-rich grain/particle possessing U-rich precipitates and FPs was not determined from this study, probable causes of the observed phenomena was hypothesized via correlating the observations from the current study to the observations and results produced from: (1) SEM-EDS maps assessed by Harp et al. [6], and (2) out-of-pile U-Zr-Ce diffusion couple experiments by Ogata et al. [134]. Harp et al. [6] revealed that at the FCCI region, the Zr EDS map nearly mimics the Ce and Nd EDS maps, and as a consequence, the Zr-rich regions are also rich in FPs, while, out-of-pile U-Zr-Ce diffusion couple experiments by Ogata et al. [134] revealed that Ce migrates to regions with higher Zr content. Hence, based on the reported observations, it can be assumed that FPs possess an affinity to migrate towards the Zr-rich regions of the fuel (in this case, the Zr-rich grain).

More interestingly, in this study, in region C, several U-rich grains were observed to possess Zr-enriched localities at/near cavities. Although several factors (such as temperature, stresses inside boundaries, Zr-FP, Zr-rich phase precipitation, etc.) could be responsible for Zr-enrichment at cavities, RIS was hypothesized as a probable cause. Rest [63] assessed the swelling in U-xPu-10Zr (0≤x≤19) fuels by assuming that the irradiation features seen in fissionable metals are analogous to well-established theories on swelling by void formation in non-fissionable metals. Similarly, if the microstructural alterations seen in fissionable metals are assumed to be analogous to the well-established theories on RIS in non-fissionable metals, then the Zr-enrichment at cavities show localities where RIS was prevalent. In other words, the observed Zr-enrichment at cavities indicates that U atoms diffused away from the cavities at a faster rate than Zr atoms, leaving behind Zr-enriched regions at the cavities. Additionally, Park et al. [133] performed out-of-pile diffusion

couple experiments and reported that the intrinsic diffusivity of U atoms is greater than that of Zr atoms at elevated temperature. Hence, by correlating the experimental observations reported by Park et al. [133] and the Zr-enrichment observed at cavities from the current study, it can be hypothesized that during neutron irradiation the flux of vacancies to a sink (grain boundary/cavity) is complemented by an equal flux of atoms (U and Zr) in the opposite direction, and since U atoms diffuse faster than Zr atoms, Zr-enrichment is observed at the cavities. However, considering that only a small dataset has been analyzed, more experimental and modeling assessments are required to validate the theory of RIS in fissionable metals (i.e. neutron irradiated U-10wt.%Zr fuels). Additionally, the TEM assessment also revealed the presence of Zr-enrichment along grain boundaries.

6.1.5   Neutron Irradiated HT9 Cladding and FCCI Locality

In this study, the major phase of the neutron irradiated HT9 cladding was identified to be BCC structured Fe. A comprehensive chemical compositional assessment of the FIB lamella indicated the following: (1) Intergranular FP migration, and (2) Presence of a variety of FP precipitates which were composed of Nd, Pd, Pr, Sn, Ce, and La. Even though these observations were corroborated by the SEM-EDS assessment reported by Harp et al. [6], it is interesting to note that in this study, intergranular FP migration was observed along selected grain boundaries of the neutron irradiated HT9 cladding. In this study, only one FIB lamella was assessed from the neutron irradiated HT9 cladding locality, and consequently, a more comprehensive analysis via TEM investigation of several FIB lamellas is necessary to establish a correlation between preferential intergranular FP migration and grain orientation. Even though further analysis is required to correlate preferential intergranular FP migration to grain orientation, this is the first study that observed such a phenomenon in a neutron irradiated HT9 cladding.

Serial sectioning of FIB cuboid-4 from the FCCI locality revealed the following: (1) U-rich grains on the fuel side, (2) U-Zr intermetallics on the fuel side, (3) spherical and aspherical cavities on the fuel side, (4) Zr-rich layer acting as a barrier and mitigating the interdiffusion of U into the cladding, (5) Ce-Pd-Nd FCCI layer between the fuel and cladding sides, (6) Cr-rich precipitates on the cladding side, and (7) HT9 cladding side (rich in Fe). Previously, numerous theories on the formation of a Zr-rich barrier between the fuel and cladding, the effectiveness of a Zr-rich barrier mitigating interdiffusion between the fuel and cladding, and the cracking of the Zr-

154

rich barrier as a consequence of thermal stresses, annealing time, and driving forces between diffusion couple elements were initially investigated via several out-of-pile experiments [3–5,7–9,11]. By correlating the previous studies to the several observations identified at the FCCI locality of the serial sectioned FIB cuboid, it can be stated that the Zr-rich barrier seen at the FCCI locality impeded the initial interdiffusion between the fuel and cladding. However, during in-pile exposure, the barrier cracked as a consequence of various factors (such as fuel constituent re-distribution, FP migration, and fuel swelling). The cracks provided an easy path for interdiffusion between the fuel and the cladding, and consequently, the FP diffused from the fuel to the cladding and formed FCCI layers/other compounds. Similar microstructural alterations were also observed in the SEM-EDS maps assessed by Harp et al. [6]; however, the current study provides the first 3D assessment of FCCI in a neutron irradiated U-10wt.%Zr fuel and HT9 cladding. Interestingly, the current study also revealed the formation of Cr-rich precipitates at the cladding side, an observation that was not previously reported.

The synchrotron µ-CT experiments qualitatively revealed that FPs migrate along the grain boundaries of the neutron irradiated HT9 cladding, and similar observations were also determined qualitatively and quantitatively via the SEM and TEM investigations. In this study, the FP migration was identified as crests in the line scans produced from the absorption contrast µ-CT images. While the grain boundaries were identified as troughs in the line scans produced from the phase contrast µ-CT images. In addition to temperature gradient dictating FP migration in nuclear fuels, Mariani et al. [84] reported on the possibility of FPs in the fuel migrating to the fuel edge via a liquid-like diffusion. Even though the mechanism which governs FP migration (i.e. whether they are liquid-like diffusion or not) was not established from this standalone study, the current assessment provides a new method to analyze FP migration in 3D in a non-destructive manner.

6.2   Nano-Mechanical Property Assessment

The nano-indentation experiments revealed a substantial change in mechanical properties as a function of distance from the HT9 edge (furthest point from fuel/cladding contact surface) to the FCCI (points at fuel/cladding contact and interaction) locality. In general, the nano-hardness increased as a function of distance from the HT9 edge to the FCCI locality. The increase in nano-hardness at the FCCI locality is most likely due to the presence of several microstructural alterations such as FP precipitates, FCCI layers, intermetallics, and other complex precipitates. In

this study, the HT9 edge, HT9+fission products, and FCCI locality were estimated to have an average nano-hardness of 5.18±0.40 GPa, 5.07±0.21 GPa, and 6.92±1.31 GPa, respectively. The SEM micrographs, TEM investigations, nano-indentation SEM micrographs, and nano-indentation estimates presented in this study revealed that the HT9 edge, being the furthest from point of contact with the fuel possessed fewer microstructural alterations, while the HT9+fission products locality possessed several types of FP precipitates and FP migration along the grain boundaries of the cladding. In comparison, the FCCI locality possesses several other alterations (such as intermetallics, FP precipitates, and FCCI layers), and these alterations were also reported by Harp et al. [6]. In this study, the Milot's and Busby's yield stresses were calculated for each indentation of the neutron irradiated HT9 cladding. The calculated yield stresses were compared to the historical literature of yield stresses in neutron irradiated HT9 steels that were irradiated at various doses, temperatures, and reactors.

The current study also revealed that the calculated yield stresses at the HT9 edge locality of the neutron irradiated HT9 cladding matched fairly well the historical literature of yield stresses in neutron irradiated HT9 steels. From the two calculated yield stresses, the Milot's yield stress at the HT9 edge locality of the neutron irradiated HT9 cladding appeared to align more closely to the yield stresses of neutron irradiated HT9 steels reported by Krumwiede et al. [109], Maloy et al. [129], and Klueh et al. [125]. Krumwiede et al. [109] performed tensile testing experiments and nano-indentation experiments on HT9 steels that were neutron irradiated to a dose and temperature of 6.49 dpa and 320 ˚C, respectively, while Maloy et al. [129] performed tensile testing experiments on HT9 steels that were neutron irradiated to doses of 7 dpa, 18 dpa, and 35.3 dpa and temperatures of 240˚C and 390˚C. Similarly, Klueh et al. [125] performed a tensile testing experiment on HT9 steel that was neutron irradiated to a dose and temperature of 6 dpa and 300˚C, respectively. Although similarities were observed between the yield stresses from the current study and existing historical literature on neutron irradiated HT9 steels, a one-to-one correlation cannot be made as a consequence of the following: (1) The work being presented in the current study was performed on a neutron irradiated HT9 cladding which was in contact with a neutron irradiated U-10wt.%Zr fuel (i.e. the HT9 steel analyzed was not used as a reactors structural component, but rather a reactors core component). (2) The doses and irradiation temperatures experienced by the neutron irradiated HT9 steels (i.e. existing historical literature) in the reactor were not same as the dose and irradiation temperature experience by the neutron irradiated HT9 cladding, (3) Different

fuel cross-sections were subjected to different burnup and temperature gradients, and consequently, these affect the microstructural alterations that are to be expected on the neutron irradiated HT9 cladding. Furthermore, the yield stresses of the neutron irradiated HT9 steels reported in the historical literature were determined via tensile testing experiments (i.e. they were more macroscopic) [24,109,124–127].

The calculated yield stresses determined in this study provided the first insight into changes in the local mechanical properties of a neutron irradiated HT9 cladding that was in contact with a neutron irradiated U-10wt.%Zr fuel. Since neutron irradiation causes the U-10wt.%Zr metallic fuel to swell and come in contact with HT9 cladding, the HT9 cladding is subjected to the following: (1) axial and diametrical stresses, (2) thinning via FCCI, (3) FP migration, (4) formation of FP precipitates and several other phases, and (5) temperature gradients. Furthermore, the observation of large diametrical strains in neutron irradiated HT9 claddings as a consequence of fuel swelling was previously reported by several researchers [75,145]. Diametrical strains imposed on neutron irradiated claddings are commonly accompanied by irradiation creep at low temperatures and thermal creep at high temperatures [75,145]. Pahl et al. [75] reported that unbreached HT9 steels that were clad to U-10wt.%Zr fuels and neutron irradiated to a burnup of 10 at.% in the EBR-II had diametrical strains ranging between 0%-2% and that the failure strains for HT9 steels were reported to be between 2%-4%. Hence, achieving a high diametrical strain value is detrimental for the cladding integrity, and consequently, these strains may affect the yield stress exhibited by the material [75]. Even though a conclusive reason to the observed high calculated yield stresses in the neutron irradiated HT9 cladding was not attained from this study, the probable causes were explained (i.e. formation of precipitate phases, diametrical strains, and temperature gradient). Furthermore, this was the first study performed to analyze the localized mechanical property of a neutron irradiated HT9 cladding.

6.3   Impact of this study

A comprehensive assessment of a neutron irradiated U-10wt.%Zr fuel and HT9 cladding was provided at the nanoscale, microscale, and mesoscale to assess several microstructural alterations that form as a consequence of several interdependent phenomena, including phase transformations, swelling, FCCI, and fuel constituent re-distribution. Furthermore, the current study successfully assessed the various interdependent phenomena by assessing fuel constituent

re-distribution, phase transformations, and FCCI via TEM investigations (nanoscale assessments) and serial sectioning experiments (microscale assessments), and fuel swelling via synchrotron µ-CT experiments (mesoscale assessments). The TEM investigations revealed that regions A, A/B, B, and C of the fuel cross-section possessed varying chemical compositions, and inherently, this resulted in the formation of a multitude of phases. The microstructural alterations identified in region A (α-U, δ-UZr$_2$, and Zr-enrichment at grain boundaries), region B (β-U, Zr-rich FCC grain, δ-UZr$_2$, and solid FP precipitates), and region C (Zr-rich FCC grains, δ-UZr$_2$, and features similar to region A and B) revealed that the phase transformations in neutron irradiated U-10wt.%Zr fuels are complex and dependent on several factors. Even though historical studies [34,35] assumed the probable major phases at different regions via SEM imaging, electron probe microanalysis, and the equilibrium phase diagram, the nanoscopic assessments presented in this study proved that a detailed crystallographic assessment was essential to determine the actual phases that exist.

Historically, depending on the fuel burnup and temperature gradient, the αU phase was suggested to have an anisotropic growth that facilitates grain boundary tearing, γU phase was suggested to possess large interconnected globular pores, and δ-UZr$_2$ + γ_2 dual phase regions possess smaller pores [35,63]. Although these suppositions were made, no correlative crystallographic and spectroscopy proof was provided to support the suggestions. In comparison, the correlative TEM and serial sectioning experiments performed in this study revealed the presence of several phases, and types of porosities whose morphology appeared to be influenced by the phases that surround them. For instance, at region A, U-Zr (δ-UZr$_2$) grains with U-rich precipitates (αU) were observed to have large spherical pores. While at region A/B, a U-Zr (δ-UZr$_2$) grain with U-rich (αU) precipitates possessed large spherical pores and certain U-rich grains possessed small spherical pores while others were less affected by radiation. Similarly, at region B, U-Zr grains possessed spherical pores, and U-rich grains possessed spherical and/or aspherical pores. Hence, the observations made in this study provides additional evidence to the previous assumptions that the crystal structure of phases influences the pore morphologies present at a specific locality. The serial sectioning experiments also revealed the presence of a Zr-rich barrier that appeared to halt the interdiffusion of U into the HT9 cladding at the FCCI locality.

The synchrotron µ-CT experiments presented in this study showed the effects of various types of pores (i.e. pores in their nucleation, growth, coalescence, interconnected, and extended/interconnected state) on the localized microscopic fuel swelling at regions A/B and B,

and consequently warrants for the need to improve current fuel swelling models [79,143] that assume a bubble interconnection threshold at ~30-36.5% fuel swelling. The models also assume that at the bubble interconnection threshold, further gaseous swelling is eliminated as a consequence of release of fission gas into the plenum [79,143]. Additionally, the data produced from this research can also be used to enhance existing temperature distribution models. The nano-indentation experiments presented in this study were performed at various localities on the HT9 cladding to comprehend how the mechanical properties vary in a neutron irradiated HT9 cladding from the cladding edge to the point of fuel contact (FCCI region). Each locality of the neutron irradiated HT9 cladding behaved uniquely due to the presence of various microstructural alterations, and consequently, the insights obtained from these experiments provided pivotal information for more realistic mechanical failure models.

In summary, the study presented in this dissertation established several new theories on the basis of the observations made from the nanoscale, microscale, and mesoscale assessments, and provided pivotal groundwork required for improving existing fuel performance models (such as swelling models, temperature distribution models, phase field models, and fracture models). Finally, this research also stressed the importance of understanding several interrelated effects (such as phase transformation, FP generation, fuel swelling, fuel constituent re-distribution, and FCCI) and their implications within the neutron irradiated fuel and cladding.

CHAPTER 7.   FUTURE WORK

Both computational and experimental work can be conducted to further enhance the results obtained within the study. Additional research could include the following:

a) Evaluating the major phases in various regions at different fuel cross-sectional bunups. This systematic methodology of assessment will allow for a better understanding of the various phase transformations, their effect on pore morphology and localized fuel swelling, and their relationships to different burnups and temperature gradients.

b) Establishing a database (including both chemical composition and crystal structure) for various FP precipitates identified in the neutron irradiated U-10wt.%Zr fuel and HT9 cladding.

c)   Harvesting FIB obelisks for synchrotron µ-CT experiments from other localities of the fuel cross-section to attain a more precise estimation on localized fuel swelling.

d) Performing synchrotron µ-CT experiments on FIB obelisks produced from the FCCI locality of the neutron irradiated U-10wt.%Zr fuel and HT9 cladding and segmenting the FCCI layers for correlating with the serial sectioning experiments at the same locality.

e) Stitching and re-aligning the serially sectioned FIB cuboids for performing a more comprehensive 3D assessment.

f) Performing more nano-indentation experiments to determine how fuel constituent re-distribution, phase structure, neutron irradiation, FP precipitates, and pore morphologies affect the local mechanical properties at regions A, B, and C of the neutron irradiated U-10wt.%Zr fuel.

g) Performing TEM investigations at the FCCI locality of the neutron irradiated HT9 cladding to determine the various phases that are responsible for the increased nano-hardness.

h) Utilizing the pore morphologies, swelling estimates, and phase structures identified to enhance existing fuel swelling performance codes.

i) Utilizing the nano-indentation data produced for improving the existing fuel-cladding failure models.

REFERENCES

[1] W.J. Carmack, Temperature and Burnup Correlated FCCI in U- 10Zr Metallic Fuel, Ph. D. dissertation, University of Idaho, 2012. doi:10.2172/1055966.

[2] G.L. Hofman, L.C. Walters, T.H. Bauer, Metallic Fast Reactor Fuels, Prog. Nucl. Energy. 31 (1997) 83–110. doi:10.1016/0149-1970(96)00005-4.

[3] C.T. Lee, H. Kim, T.K. Kim, C.B. Lee, Diffusion Behavior in an Interface Between U-10Zr Alloy and HT-9 Steel, J. Nucl. Mater. 395 (2009) 140–144. doi:10.1016/j.jnucmat.2009.10.044.

[4] D.D. Keiser, M.A. Dayananda, Interdiffusion between U-Zr Fuel vs Selected Cladding steels, Metall. Mater. Trans. A. 25 (1994) 1649–1653. doi:10.1007/BF02668530.

[5] C. Matthews, C. Unal, J. Galloway, D.D. Keiser jr, S.L. Hayes, Fuel-Cladding Chemical Interaction in U-Pu-Zr Metallic Fuels: A Critical Review, Nucl. Technol. 198 (2017) 231–259. doi:10.1080/00295450.2017.1323535.

[6] J.M. Harp, D.L. Porter, B.D. Miller, T.L. Trowbridge, W.J. Carmack, Scanning Electron Microscopy Examination of a Fast Flux Test Facility Irradiated U-10Zr Fuel Cross Section Clad with HT-9, J. Nucl. Mater. 494 (2017) 227–239. doi:10.1016/j.jnucmat.2017.07.040.

[7] D.D. Keiser, M.A. Dayananda, Interdiffusion between U-Zr fuel and Selected Fe-Ni-Cr Alloys, J. Nucl. Mater. 200 (1993) 229–243. doi:10.1016/0022-3115(93)90334-U.

[8] R.G. Pahl, C.E. Lahm, R. Villarreal, G.L. Hofman, W.N. Beck, Recent Irradiation Tests of Uranium-Plutonium-Zirconium Metal Fuel Elements, No. CONF-860931-9. Argonne Natl. Lab., Idaho Falls, ID (USA); Argonne Natl. Lab., (USA),. (1986).

[9] G.L. Hofman, A.G. Hins, D.L. Porter, L. Leibowitz, E.L. Wood, Chemical Interaction of Metallic Fuel with Austenitic and Ferritic Stainless Steel Cladding, Int. Conf. Reliab. Fuels Liq. Met. React. (1986).

[10] S. Ahn, Comprehensive Invsetigation of the Uranium-Zirconium Alloy System: Thermophysical Properties, Phase Characterization and Ion Implantation Effects, Texas A&M University, 2013.

[11] M. Akabori, A. Itoh, T. Ogawa, M. Ugajin, Reactions between U-Zr Alloys and Nitrogen, J. Alloys Compd. 213 (1994) 366–368. doi:10.1016/0925-8388(94)90933-4.

[12] R.G. Pahl, D.L. Porter, C.E. Lahm, G.L. Hofman, Experimental Studies of U-Pu-Zr Fast

Reactor Fuel Pins in The Experimental Breeder Reactor-ll, Metall. Trans. A. 21 (1990) 1863–1870. doi:10.1007/BF02647233.

[13] R.I. Sheldon, D.E. Peterson, The U-Zr (Uranium-Zirconium) System, Bull. Alloy Phase Diagrams. 10 (1989) 165–171. doi:10.1007/BF02881432.

[14] F.A. Rough, A.A. Bauer, Constitution of Uranium and Thorium Alloys, Battelle Memorial Institute BMI-1300, U.S. Atomic Energy Commission, 1958. doi:10.2172/4324513.

[15] A. Bauer, G. Beatty, F. Rough, R. Dickerson, The Constitution of Zirconium-Uranium Alloys Containing Oxygen or Nitrogen, Battelle Memorial Institute BMI-1187, (1957).

[16] A. Rai, R. Subramanian, R. Hajra, H. Tripathy, Calorimetric Study of Phase Stability and Phase Transformation in U-xZr (x= 2, 5, 10 wt pct) Alloys, Mater. Trans. A. 46 (2015) 4986–5001. doi:10.1007/s11661-015-3102-2.

[17] W.J. Williams, M.A. Okuniewski, S.C. Vogel, J. Zhang, An In-Situ Neutron Diffraction Study of Crystallographic Evolution and Thermal Expansion Coefficients in U-22.5at.%Zr during Annealing, JOM. (2020) 1–9. doi:10.1007/s11837-020-04086-8.

[18] C. Zheng, E.R. Reese, K.G. Field, T. Liu, E.A. Marquis, S.A. Maloy, D. Kaoumi, Microstructure Response of Ferritic/Martensitic Steel HT9 after Neutron Irradiation: Effect of Temperature, J. Nucl. Mater. 528 (2020) 151845. doi:10.1016/j.jnucmat.2019.151845.

[19] F.A. Garner, M.B. Toloczko, B.H. Sencer, Comparison of Swelling and Irradiation Creep Behavior of FCC-Austenitic and BCC-Ferritic/Martensitic Alloys at High Neutron Exposure, J. Nucl. Mater. 276 (2000) 123–142. doi:10.1016/S0022-3115(99)00225-1.

[20] S.J. Zinkle, G.S. Was, Materials Challenges in Nuclear Energy, Acta Mater. 61 (2013) 735–758. doi:10.1016/j.actamat.2012.11.004.

[21] R.L. Klueh, A.T. Nelson, Cladding and Duct Materials for Advanced Nuclear Recycle Reactors, J. Nucl. Mater. 371 (2007) 37–52. doi:10.1016/j.jnucmat.2007.05.005.

[22] T.R. Allen, J.T. Busby, R.L. Klueh, S.A. Maloy, M.B. Toloczko, Cladding and duct materials for advanced nuclear recycle reactors, JOM. 60 (2008) 15–23. doi:10.1007/s11837-008-0002-6.

[23] D.S. Gelles, Development of Martensitic Steels for High Neutron Damage Applications, J. Nucl. Mater. 239 (1996) 99–106. doi:10.1016/S0022-3115(96)00474-6.

[24] Y. Chen, Irradiation Effects of HT-9 Martensitic Steel, Nucl. Eng. Technol. 45 (2013) 311–322. doi:10.5516/NET.07.2013.706.

[25] J.L. Séran, A. Alamo, A. Maillard, H. Touron, J.C. Brachet, P. Dubuisson, O. Rabouille, Pre- and Post-Irradiation Mechanical Properties of Ferritic-Martensitic Steels for Fusion Applications: EM10 Base Metal and EM10/EM10 Welds, J. Nucl. Mater. 212–215 (1994) 588–593. doi:10.1016/0022-3115(94)90128-7.

[26] P.J. Grobner, The 885°F (475°C) Embrittlement of Ferritic Stainless Steels, Metall. Trans. 4 (1973) 251–260. doi:10.1007/BF02649625.

[27] M. Kangilaski, Radiation Effects in Structural Materials, React. Mater. 13 (1970) 124–131. doi:10.1146/annurev.ms.09.080179.002201.

[28] R.L. Klueh, Elevated Temperature Ferritic and Martensitic Steels and their Application to Future Nuclear Reactors, Int. Mater. Rev. 50 (2005) 287–310. doi:10.1179/174328005X41140.

[29] P. Dubuisson, D. Gilbon, J.L. Séran, Microstructural Evolution of Ferritic-Martensitic Steels Irradiated in the Fast Breeder Reactor Phénix, in: Int. Conf. Evol. Microstruct. Met. Dur. Irradiat., North-Holland, 1992: p. 20. doi:10.1016/0022-3115(93)90080-I.

[30] P.J. Maziasz, R.L. Klueh, J.M. Vitek, Helium Effects on Void Formation in 9Cr-1MoVNb and 12Cr-1MoVW Irradiated in HFIR, J. Nucl. Mater. 141–143 (1986) 929–937. doi:10.1016/0022-3115(86)90120-0.

[31] E.A. Little, D.A. Stow, Void-Swelling in Irons and Ferritic Steels. II. An Experimental Survey of Materials Irradiated in a Fast Reactor, J. Nucl. Mater. 87 (1979) 25–39. doi:10.1016/0022-3115(79)90123-5.

[32] J.J. Kai, R.L. Klueh, Microstructural Analysis of Neutron-Irradiated Martensitic Steels, J. Nucl. Mater. 230 (1996) 116–123. doi:10.1016/0022-3115(96)00165-1.

[33] M.H. Mathon, Y. De Carlan, G. Geoffroy, X. Averty, A. Alamo, C.H. De Novion, A SANS Investigation of the Irradiation-Enhanced α-α′ Phases Separation in 7-12 Cr Martensitic Steels, J. Nucl. Mater. 312 (2003) 236–248. doi:10.1016/S0022-3115(02)01630-6.

[34] A.M. Yacout, W.S. Yang, G.L. Hofman, Y. Orechwa, Average Irradiation Temperature for the Analysis of In-Pile Integral Measurements, Nucl. Technol. 115 (1996) 61–72. doi:10.13182/NT96-A35275.

[35] G.L. Hofman, R.G. Pahl, C.E. Lahm, D.L. Porter, Swelling Behavior of U-Pu-Zr Fuel, Metall. Trans. A. 21 (1990) 517–528. doi:10.1007/BF02671924.

[36] J. Thomas, A. Figueroa, S. Nori, R. Ren, P. Kenesei, J. Almer, J. Hunter, J. Harp, M.

Okuniewski, The Application of Synchrotron Micro-Computed Tomography to Characterize the Three-Dimensional Microstructure in Irradiated Nuclear Fuel, J. Nucl. Mater. 152161 (2020). doi:10.1016/j.jnucmat.2020.152161.

[37] T. Abram, S. Ion, Generation-IV Nuclear Power: A Review of the State of the Science, Energy Policy. 36 (2008) 4323–4330. doi:10.1016/j.enpol.2008.09.059.

[38] B.R. Seidel, G.L. Batte, C.E. Lahm, R.M. Fryer, J.F. Koenig, G.L. Hofman, Off-Normal Performance of EBR-II (Experimental Breeder Reactor) Driver Fuel, CONF-860931-10, Argonne Natl. Lab. IL. (1986).

[39] C.E. Lahm, J.F. Koenig, P.R. Betten, J.H. Bottcher, W.K. Lehto, B.R. Seidel, EBR-II Driver Fuel Qualification for Loss-of-Flow and Loss-of-Heat-Sink Tests Without Scram, Nucl. Eng. Des. 101 (1987) 25–34. doi:10.1016/0029-5493(87)90147-6.

[40] B.R. Seidel, D.L. Porter, L.C. Walters, G.L. Hofman, Experience with EBR-II [Experimental Breeder Reactor] Driver Fuel, in: CONF-860931-13, Argonne Natl. Lab. IL., 1986.

[41] H. Mikami, A. Shono, H. Hiroi, Sodium Leak at Monju (I): Cause and Consequences, in: Tech. Comm. Meet. Eval. Radioact. Mater. Release Sodium Fires Fast React. IWGFR/92, O-Arai, Ibaraki, Japan, 1996: pp. 271–2811.

[42] A. Miyakawa, H. Maeda, Y. Kani, K. Ito, Sodium Leakage Experience at the Prototype FBR Monju, in: Proc. TCM Unusual Occur. Dur. LMFR Oper. Vienna, Austria, 1998.

[43] J.H. Kittel, B.R.T. Frost, J.P. Mustelier, K.Q. Bagley, G.C. Crittenden, J. Van Dievoet, History of Fast Reactor Fuel Development, J. Nucl. Mater. 204 (1993) 1–13. doi:10.1016/0022-3115(93)90193-3.

[44] T. Ogawa, M. Akabori, F. Kobayashi, R.G. Haire, Thermochemical Modeling of Actinide Alloys Related to Advanced Fuel Cycles, J. Nucl. Mater. 247 (1997) 215–221. doi:10.1016/S0022-3115(97)00047-0.

[45] T.C. Totemeier, R.D. Mariani, Morphologies of Uranium and Uranium-Zirconium Electrodeposits, J. Nucl. Mater. 250 (1997) 131–146. doi:10.1016/S0022-3115(97)00288-2.

[46] T. Inoue, Actinide Recycling by Pyro-process with Metal Fuel FBR for Future Nuclear Fuel Cycle Dystem, in: Prog. Nucl. Energy, 2002: pp. 547–554. doi:10.1016/S0149-1970(02)00049-5.

[47] L.C. Walters, Thirty Years of Fuels and Materials Information from EBR-II, J. Nucl. Mater. 270 (1999) 39–48. doi:10.1016/S0022-3115(98)00760-0.

[48] L.R. Chapman, C.E. Holcombe, Revision of the Uranium-Iron Phase Diagram, J. Nucl. Mater. 126 (1984) 323–326. doi:10.1016/0022-3115(84)90046-1.

[49] M. Kurata, T. Ogata, K. Nakamura, T. Ogawa, Thermodynamic Assessment of the Fe-U, U-Zr and Fe-U-Zr Systems, J. Alloys Compd. 271–273 (1998) 636–640. doi:10.1016/S0925-8388(98)00176-5.

[50] S. Kaity, J. Banerjee, M.R. Nair, K. Ravi, S. Dash, T.R.G. Kutty, A. Kumar, R.P. Singh, Microstructural and thermophysical properties of U-6 wt.%Zr alloy for fast reactor application, J. Nucl. Mater. 427 (2012) 1–11. doi:10.1016/j.jnucmat.2012.03.045.

[51] C.M. Walter, G.H. Golden, N.J. Olson, U-Pu-Zr Metal Alloy: A Potential Fuel for LMFBR's, ANL-76-28, Argonne Natl. Lab. (1975). doi:10.2172/7138403.

[52] K. Nakamura, T. Ogata, M. Kurata, T. Yokoo, M.A. Mignanelli, Phase Relations in the Quaternary Fe-Pu-U-Zr System, J. Nucl. Mater. 304 (2002) 63–72. doi:10.1016/S0022-3115(02)00855-3.

[53] S. Kaity, T.R.G. Kutty, R. Agarwal, A. Laik, A. Kumar, Chemical Compatibility of Uranium based Metallic Fuels with T91 Cladding, Nucl. Eng. Des. 250 (2012) 267–276. doi:10.1016/j.nucengdes.2012.04.028.

[54] T.R.G. Kutty, S.K. Rakshit, A. Laik, A. Kumar, H.S. Kamath, C.B. Basak, Studies of the Reaction between Metal Fuels and T91 Cladding, J. Nucl. Mater. 412 (2011) 53–61. doi:10.1016/j.jnucmat.2011.02.016.

[55] D.L. Porter, G.L. Hofman, B.R. Seidel, L.C. Walters, Factors Controlling Metal Fuel Lifetime, in: CONF-860931-16, Argonne Natl. Lab. IL., 1986.

[56] M. V. Nevitt, Fast Reactor Fuel Alloys: Retrospective and Prospective Views, J. Nucl. Mater. 165 (1989) 1–8. doi:10.1016/0022-3115(89)90501-1.

[57] H.A. Tsai B Cohen M C Billone, L.A. Neimark, by H. Tsai, A.B. Cohen M C Billone, Irradiation Performance of U-Pu-Zr Metal Fuels for Liquid-Metal-Cooled Reactors, in: CONF-950426-6, Argonne Natl. Lab. IL., 1994.

[58] D.E. Burkes, R.S. Fielding, D.L. Porter, D.C. Crawford, M.K. Meyer, A US perspective on Fast Reactor Fuel Fabrication Technology and Experience Part I: Metal Fuels and Assembly Design, J. Nucl. Mater. 389 (2009) 458–469. doi:10.1016/j.jnucmat.2009.02.035.

[59] D.E. Janney, S.L. Hayes, Experimentally Known Properties of U-10Zr Alloys: A Critical Review, Nucl. Technol. 203 (2018) 109–128. doi:10.1080/00295450.2018.1435137.

[60] B.G. Carlson, ANL Memo to M. Vaughn, July 1989, Argonne National Laboratory Intralab Memo. Unpublished work, (n.d.).

[61] J.E. Sanecki, ANL Memo to Hofman and Tsai, Jan 1991, Argonne National Laboratory Intralab Memo. Unpublished work, (n.d.).

[62] A.L. Pitner, R.B. Baker, Metal Fuel Test Program in the FFTF, J. Nucl. Mater. 204 (1993) 124–130. doi:10.1016/0022-3115(93)90208-G.

[63] J. Rest, Kinetics of Fission-Gas-Bubble-Nucleated Void Swelling of the Alpha-Uranium Phase of Irradiated U-Zr and U-Pu-Zr Fuel, J. Nucl. Mater. 207 (1993) 192–204. doi:10.1016/0022-3115(93)90261-V.

[64] M. Ishida, T. Ogata, M. Kinoshita, Constituent Migration Model for U-Pu-Zr Metallic Fast Reactor Fuel, Nucl. Technol. 104 (1993) 37–51. doi:10.13182/NT93-A34868.

[65] G.L. Hofman, S.L. Hayes, M.C. Petri, Temperature Gradient Driven Constituent Redistribution in U- Zr Alloys, J. Nucl. Mater. 227 (1996) 277–286. doi:10.1016/0022-3115(95)00129-8.

[66] W. Murphy, W. Beck, F. Brown, B. Koprowski, Postirradiation Examination of U-Pu-Zr Fuel Elements Irradiated in EBR-II to 4.5 Atomic Percent Burnup, No. ANL-7602. Argonne Natl. Lab., Ill. (1969). doi:10.2172/4169781.

[67] G.W. Greenwood, The Effects of Neutron Irradiation on γ-Uranium and some Fissile Alloys of Cubic Crystal Structure, J. Nucl. Mater. 6 (1962) 26–34. doi:10.1016/0022-3115(62)90213-1.

[68] D. Yun, A.M. Yacout, M. Stan, T.H. Bauer, A.E. Wright, Simulation of the Impact of 3-D Porosity Distribution in Metallic U-10Zr Fuels, J. Nucl. Mater. 448 (2014) 129–138. doi:10.1016/j.jnucmat.2014.02.002.

[69] J.G. Huber, P.H. Ansari, The Superconductivity of BCC UZr Alloys, Phys. B+C. 135 (1985) 441–444. doi:10.1016/0378-4363(85)90527-3.

[70] M. Akabori, T. Ogawa, A. Itoh, Y. Morii, The Lattice Stability and Structure of delta -UZr2 at Elevated Temperatures, J. Phys. Condens. Matter. 7 (1995) 8249. doi:10.1088/0953-8984/7/43/005.

[71] M. Akabori, A. Itoh, T. Ogawa, F. Kobayashi, Y. Suzuki, Stability and Structure of the δ

Phase of the U-Zr Alloys, J. Nucl. Mater. 188 (1992) 249–254. doi:10.1016/0022-3115(92)90480-9.

[72]   A.C. Lawson, C.E. Olsen, J.W. Richardson, M.H. Mueller, G.H. Lander, Structure of β-Uranium, Acta Crystallogr. Sect. B Struct. Sci. 44 (1988) 89–96. doi:10.1107/S0108768187009406.

[73]   G. Ondracek, B. Schulz, The Porosity Dependence of the Thermal Conductivity for Nuclear Fuels, J. Nucl. Mater. 46 (1973) 253–258. doi:10.1016/0022-3115(73)90039-1.

[74]   W.J. Williams, D.M. Wachs, M.A. Okuniewski, S. van den Berghe, Assessment of Swelling and Constituent Redistribution in Uranium-Zirconium Fuel Using Phenomena Identification and Ranking Tables (PIRT), Ann. Nucl. Energy. 136 (2020) 107016. doi:10.1016/j.anucene.2019.107016.

[75]   R.G. Pahl, C.E. Lahm, S.L. Hayes, Performance of HT9 Clad Metallic Fuel at High Temperature, J. Nucl. Mater. 204 (1993) 141–147. doi:10.1016/0022-3115(93)90210-P.

[76]   T. Ogata, T. Yokoo, Development and Validation of ALFUS: An Irradiation Behavior Analysis Code for Metallic Fast Reactor Fuels, Nucl. Technol. 128 (1999) 113–123. doi:10.13182/NT99-A3018.

[77]   A. Karahan, N.C. Andrews, Extended Fuel Swelling Models and Ultra High Burn-up Fuel Behavior of U-Pu-Zr Metallic Fuel using FEAST-METAL, Nucl. Eng. Des. 258 (2013) 26–34. doi:10.1016/j.nucengdes.2013.02.004.

[78]   B. Ehrenberg, S. Amiel, Independent Yields of Krypton and Xenon Isotopes in Thermal-Neutron Fission of U235. Observation of an Odd-Even Effect in the Element Yield Distribution, Phys. Rev. C. 6 (1972) 618–628. doi:10.1103/PhysRevC.6.618.

[79]   Y. Miao, N. Stauff, A. Oaks, A.M. Yacout, T.K. Kim, Fuel Performance Evaluation of Annular Metallic Fuels for an Advanced Fast Reactor Concept, Nucl. Eng. Des. 352 (2019). doi:10.1016/j.nucengdes.2019.110157.

[80]   S. Kaity, J. Banerjee, S.C. Parida, A. Laik, C.B. Basak, V. Bhasin, Studies on Fuel-Cladding Chemical Interaction between U−10wt%Zr Alloy and T91 Steel, J. Nucl. Mater. 513 (2019) 16–32. doi:10.1016/j.jnucmat.2018.10.041.

[81]   K. Nakamura, T. Ogata, M. Kurata, A. Itoh, Reactions of U–Zr alloy with Fe and Fe–Cr Alloy, J. Nucl. 275 (1999) 246–254. doi:10.1016/S0022-3115(99)00227-5.

[82]   T. Ogata, K. Nakamura, A. Itoh, M. Akabori, Reactions between U–Zr Alloys and Fe at

1003K, J. Nucl. Mater. 441 (2013) 579–582. doi:10.1016/j.jnucmat.2012.09.038.

[83] T. Ogata, M. Kurata, K. Nakamura, A. Itoh, Reactions between U–Zr Alloys and Fe at 923 K, J. Nucl. 250 (1997) 171–175. doi:10.1016/S0022-3115(97)00262-6.

[84] R. Mariani, D. Porter, T. O'Holleran, S. Hayes, J.R. Kennedy, Lanthanides in Metallic Nuclear Fuels: Their Behavior and Methods for their Control, J. Nucl. 419 (2011) 263–271. doi:10.1016/j.jnucmat.2011.08.036.

[85] C.W. Arnold, J. Galloway, C. Unal, Modeling Lanthanide Transport in Metal Fuels with BISON, in: Proc. Glob., 2015: pp. 20–24.

[86] C.W. Arnold, J. Galloway, N. Carlson, C. Unal, Improvements to Coding of Lanthanide Behaviors in Metal Fuel, ANS Trans. 113 (2015) 538–542.

[87] M. Akabori, A. Itoh, T. Ogawa, T. Ogata, Interdiffusion in the U–Zr system at δ-phase compositions, J. Alloys Compd. (1998).

[88] W.J. Carmack, H.M. Chichester, D.L. Porter, D.W. Wootan, Metallography and Fuel Cladding Chemical Interaction in Fast Flux Test Facility Irradiated Metallic U-10Zr MFF-3 and MFF-5 Fuel Pins, J. Nucl. Mater. 473 (2016) 167–177. doi:10.1016/j.jnucmat.2016.02.019.

[89] O. Betz, U. Wegst, D. Weide, M. Heethoff, L. Helfen, W.-K. Lee, P. Cloetens, Imaging Applications of Synchrotron X-ray Phase-Contrast Microtomography in Biological Morphology and Biomaterials Science. I. General Aspects of the Technique and its Advantages in the Analysis of Millimetre-Sized Arthropod Structure, J. Microsc. 227 (2007) 51–71. doi:10.1111/j.1365-2818.2007.01785.x.

[90] J. Hunter, D.W. Brown, M. Okuniewski, Evaluation of Computed Tomography of Mock Uranium Fuel Rods at the Advanced Photon Source, CINDE J. 36 (2015).

[91] J. Hunter, T. Ickes, B. Lattimore, Overview of Tomography Developments at LANL, 2011.

[92] J. Schindelin, I. Arganda-Carreras, E. Frise, V. Kaynig, M. Longair, T. Pietzsch, S. Preibisch, C. Rueden, S. Saalfeld, B. Schmid, J.-Y.J.-Y. Tinevez, D.J. White, V. Hartenstein, K. Eliceiri, P. Tomancak, A. Cardona, K. Liceiri, P. Tomancak, C. A., Fiji: An Open Source Platform for Biological Image Analysis., Nat. Methods. 9 (2012) 676–682. doi:10.1038/nmeth.2019.

[93] M. Doube, M.M. Klosowski, I. Arganda-Carreras, F.P. Cordelières, R.P. Dougherty, J.S. Jackson, B. Schmid, J.R. Hutchinson, S.J. Shefelbine, BoneJ: Free and Extensible Bone

Image Analysis in ImageJ, Bone. 47 (2010) 1076–1079. doi:10.1016/j.bone.2010.08.023.

[94] A. McNaughton, Image J Thresholding - Measuring Area Using Thresholds, 256 (2010) 8–10.

[95] S. Bolte, F.P. Cordelières, A Guided Tour into Subcellular Colocalization Analysis in Light Microscopy, J. Microsc. 224 (2006) 213–232. doi:10.1111/j.1365-2818.2006.01706.x.

[96] H. Wadell, Sphericity and Roundness of Rock Particles, J. Geol. 41 (1933) 310–331. doi:10.1086/624040.

[97] C. Chuang, D. Singh, P. Kenesei, J. Almer, J. Hryn, R. Huff, 3D Quantitative Analysis of Graphite Morphology in High Strength Cast Iron by High-Energy X-ray Tomography, Scr. Mater. 106 (2015) 5–8. doi:10.1016/j.scriptamat.2015.03.017.

[98] B.R.S. Rogne, N. Kheradmand, Y. Deng, A. Barnoush, In situ micromechanical testing in environmental scanning electron microscope: A new insight into hydrogen-assisted cracking, Acta Mater. 144 (2018) 257–268. doi:10.1016/j.actamat.2017.10.037.

[99] L. Gao, J. Song, Z. Jiao, W. Liao, J. Luan, J.U. Surjadi, J. Li, H. Zhang, D. Sun, C.T. Liu, Y. Lu, High-Entropy Alloy (HEA)-Coated Nanolattice Structures and Their Mechanical Properties, Adv. Eng. Mater. 20 (2018) 1700625. doi:10.1002/adem.201700625.

[100] G.M. Pharr, An Improved Technique for Determining Hardness and Elastic Modulus using Load and Displacement Sensing Indentation Experiments, J. Mater. Res. 7 (1992) 1564–1583. doi:10.1557/JMR.1992.1564.

[101] W.D. Nix, H. Gao, Indentation Size Effects in Crystalline Materials: A Law for Strain Gradient Plasticity, J. Mech. Phys. Solids. 46 (1998) 411–425. doi:10.1016/S0022-5096(97)00086-0.

[102] A. Prasitthipayong, S.J. Vachhani, S.J. Tumey, A.M. Minor, P. Hosemann, Indentation Size Effect in Unirradiated and Ion-irradiated 800H Steel at High Temperatures, Acta Mater. 144 (2018) 896–904. doi:10.1016/j.actamat.2017.11.001.

[103] A. Prasitthipayong, D. Frazer, A. Kareer, M.D. Abad, A. Garner, B. Joni, T. Ungar, G. Ribarik, M. Preuss, L. Balogh, S.J. Tumey, A.M. Minor, P. Hosemann, Micro Mechanical Testing of Candidate Structural Alloys for Gen-IV Nuclear Reactors, Nucl. Mater. Energy. 16 (2018) 34–45. doi:10.1016/j.nme.2018.05.018.

[104] P. Hosemann, J.G. Swadener, D. Kiener, G.S. Was, S.A. Maloy, N. Li, An Exploratory Study to determine Applicability of Nano-hardness and Micro-compression Measurements

for Yield Stress Estimation, J. Nucl. Mater. 375 (2008) 135–143. doi:10.1016/j.jnucmat.2007.11.004.

[105] D.L. Krumwiede, Correlation of Nanohardness to Bulk Mechanical Tensile and Shear Properties through Direct Characterization and Comparison of Neutron-Irradiated Steels, University of California, Berkeley, 2018. https://escholarship.org/uc/item/1qv0h8fk.

[106] T. Milot, Establishing Correlations for Predicting Tensile Properties Based on the Shear Punch Test and Vickers Microhardness Data, University of California, Santa Barbara, 2013.

[107] J.T. Busby, M.C. Hash, G.S. Was, The Relationship between Hardness and Yield Stress in Irradiated Austenitic and Ferritic Steels, J. Nucl. Mater. 336 (2005) 267–278. doi:10.1016/j.jnucmat.2004.09.024.

[108] A.C. Fischer-Cripps, Contact Mechanics, in: 2004: pp. 1–20. doi:10.1007/978-1-4757-5943-3_1.

[109] D.L. Krumwiede, T. Yamamoto, T.A. Saleh, S.A. Maloy, G.R. Odette, P. Hosemann, Direct comparison of nanoindentation and tensile test results on reactor-irradiated materials, J. Nucl. Mater. 504 (2018) 135–143. doi:10.1016/j.jnucmat.2018.03.021.

[110] C.B. Basak, N. Prabhu, M. Krishan, On the Formation Mechanism of UZr2 Phase, Intermetallics. 18 (2010) 1707–1712. doi:10.1016/J.INTERMET.2010.05.006.

[111] C.B. Basak, Microstructural Evaluation of U-rich U-Zr Alloys under Near-Equilibrium Condition, J. Nucl. Mater. 416 (2011) 280–287. doi:10.1016/j.jnucmat.2011.06.011.

[112] C.B. Basak, S. Neogy, D. Srivastava, G.K. Dey, S. Banerjee, Disordered BCC γ-phase to δ-phase Transformation in Zr-rich U-Zr Alloy, Philos. Mag. 91 (2011) 3290–3306. doi:10.1080/14786435.2011.577756.

[113] A.P. Moore, C. Deo, M.I. Baskes, M.A. Okuniewski, Atomistic Mechanisms of Morphological Evolution and Segregation in U-Zr alloys, Acta Mater. 115 (2016) 178–188. doi:10.1016/j.actamat.2016.05.052.

[114] J.T. McKeown, S. Irukuvarghula, S. Ahn, M.A. Wall, L.L. Hsiung, S. McDeavitt, P.E.. Turchi, Coexistence of the α and δ phases in an As-Cast Uranium-rich U–Zr Alloy, J. Nucl. Mater. 436 (2013) 100–104.

[115] J. Lindon, G. Tranter, D. Koppenaal, Encyclopedia of Spectroscopy and Spectrometry, 3rd ed., Academic Press, Elsevier, 2016.

[116] S.S. Singh, C. Schwartzstein, J.J. Williams, X. Xiao, F. De Carlo, N. Chawla, 3D

Microstructural Characterization and Mechanical Properties of Constituent Particles in Al 7075 Alloys using X-ray Synchrotron Tomography and Nanoindentation, J. Alloys Compd. 602 (2014) 163–174. doi:10.1016/j.jallcom.2014.03.010.

[117] R. Lewis, Medical Phase Contrast X-ray Imaging: Current Status and Future Prospects, Phys. Med. Biol. 49 (2004) 3573. doi:10.1088/0031-9155/49/16/005.

[118] J.Y. Buffiere, E. Ferrie, H. Proudhon, W. Ludwig, Three-Dimensional Visualisation of Fatigue Cracks in Metals Using High Resolution Synchrotron X-ray Micro-Tomography, Mater. Sci. Technol. 22 (2006) 1019–1024. doi:10.1179/174328406X114135.

[119] J.H. Hubbell, S.M. Seltzer, Tables of X-Ray Mass Attenuation Coefficients and Mass Energy-Absorption Coefficients from 1 keV to 20 MeV for Elements Z = 1 to 92 and 48 Additional Substances of Dosimetric Interest*, (n.d.). doi:https://dx.doi.org/10.18434/T4D01F.

[120] E. Maire, P.J. Withers, Quantitative X-ray Tomography, Int. Mater. Rev. 59 (2014) 1–43. doi:10.1179/1743280413Y.0000000023.

[121] D.C. Crawford, D.L. Porter, S.L. Hayes, Fuels for Sodium-Cooled Fast Reactors: US Perspective, J. Nucl. Mater. 371 (2007) 202–231. doi:10.1016/J.JNUCMAT.2007.05.010.

[122] L.R. Greenwood, Neutron Interactions and Atomic Recoil Spectra, J. Nucl. Mater. 216 (1994) 29–44. doi:10.1016/0022-3115(94)90004-3.

[123] G.S. Was, Fundamentals of Radiation Materials Science: Metals and Alloys, Springer, 2016.

[124] A. Sarkar, A.H. Alsabbagh, K.L. Murty, Investigation of Microstructure and Mechanical Properties of Low Dose Neutron Irradiated HT-9 Steel, Ann. Nucl. Energy. 65 (2014) 91–96. doi:10.1016/j.anucene.2013.11.008.

[125] R.L. Klueh, N. Hashimoto, M.A. Sokolov, K. Shiba, S. Jitsukawa, Mechanical Properties of Neutron-Irradiated Nickel-containing Martensitic Steels: I. Experimental Study, J. Nucl. Mater. 357 (2006) 156–168. doi:10.1016/j.jnucmat.2006.05.048.

[126] S.A. Maloy, M.B. Toloczko, K.J. McClellan, T. Romero, Y. Kohno, F.A. Garner, R.J. Kurtz, A. Kimura, The Effects of Fast Reactor Irradiation Conditions on the Tensile Properties of Two Ferritic/Martensitic Steels, J. Nucl. Mater. 356 (2006) 62–69. doi:10.1016/j.jnucmat.2006.05.024.

[127] A. Almazouzi, E. Lucon, Mechanical Behavior of Neutron Irradiated High Cr Ferritic-Martensitic Steels, TMS Lett. 2 (2005).

[128] A.F. Rowcliffe, J.P. Robertson, R.L. Klueh, K. Shiba, D.J. Alexander, M.L. Grossbeck, S. Jitsukawa, Fracture Toughness and Tensile Behavior of Ferritic–Martensitic Steels Irradiated at Low Temperatures, J. Nucl. Mater. 258 (1998) 1275–1279. doi:10.1016/S0022-3115(98)00163-9.

[129] S.A. Maloy, T. Romero, M.R. James, Y. Dai, Tensile testing of EP-823 and HT-9 after irradiation in STIP II, J. Nucl. Mater. 356 (2006) 56–61. doi:10.1016/j.jnucmat.2006.05.003.

[130] I. Manna, P.P. Chattopadhyay, F. Banhart, H.-J. Fecht, Formation of Face-Centered-Cubic Zirconium by Mechanical Attrition, Appl. Phys. Lett. 81 (2002) 4136–4138. doi:10.1063/1.1519942.

[131] D.E. Janney, J.R. Kennedy, J.W. Madden, T.P. O'Holleran, Crystal Structure of High-Zr Inclusions in an Alloy Containing U, Pu, Np, Am, Zr and Rare-Earth Elements, J. Nucl. Mater. 448 (2014) 109–112. doi:10.1016/j.jnucmat.2014.01.044.

[132] A. Aitkaliyeva, J.W. Madden, B.D. Miller, C.A. Papesch, J.I. Cole, TEM Examination of Phases formed between U–Pu–Zr Fuel and Fe, J. Nucl. Mater. 467 (2015) 717–723. doi:10.1016/S0022-3115(01)00426-3.

[133] Y. Park, R. Newell, A. Mehta, D.K. Jr, Y.H. Sohn, Interdiffusion and Reaction between U and Zr, J. Nucl. Mater. 502 (2018) 42–50. doi:10.1016/j.jnucmat.2018.01.063.

[134] T. Ogata, M. Akabori, A. Itoh, Diffusion of Cerium in Uranium-Zirconium Solid Solutions, Mater. Trans. 44 (2003) 47–52. doi:10.2320/matertrans.44.47.

[135] G.W. Egeland, R.D. Mariani, T. Hartmann, D.L. Porter, S.L. Hayes, J.R. Kennedy, Reducing Fuel-Cladding Chemical Interaction: The Effect of Palladium on the Reactivity of Neodymium on Iron in Diffusion Couples, J. Nucl. Mater. 432 (2013) 539–544. doi:10.1016/j.jnucmat.2012.07.028.

[136] G.W. Egeland, R.D. Mariani, T. Hartmann, D.L. Porter, S.L. Hayes, J.R. Kennedy, Reduction of FCCI Effects in Lanthanide-Iron Diffusion Couples by Doping with Palladium, J. Nucl. Mater. 440 (2013) 178–192. doi:10.1016/j.jnucmat.2013.04.060.

[137] Y. Xie, M.T. Benson, J.A. King, R.D. Mariani, J. Zhang, Characterization of U-Zr Fuel with Alloying Additive Sb for Immobilizing Fission Product Lanthanides, J. Nucl. Mater. 498 (2018) 332–340. doi:10.1016/j.jnucmat.2017.10.039.

[138] Y. Xie, M.T. Benson, L. He, J.A. King, R.D. Mariani, D.J. Murray, Diffusion Behaviors between Metallic Fuel Alloys with Pd Addition and Fe, J. Nucl. Mater. 525 (2019) 111–

124. doi:10.1016/j.jnucmat.2019.07.028.

[139] Y. Xie, J. Zhang, X. Li, J.P. Isler, M.T. Benson, R.D. Mariani, C. Unal, Lanthanide Migration and Immobilization in Metallic Fuels, Prog. Nucl. Energy. 109 (2018) 233–238. doi:10.1016/j.pnucene.2018.08.019.

[140] B. Hudson, K.H. Westmacott, M.J. Makin, Dislocation Loops and Irradiation Growth in Alpha Uranium, Philos. Mag. 7 (1962) 377–392. doi:10.1080/14786436208212172.

[141] S. Pugh, Swelling in Alpha Uranium due to Irradiation, J. Nucl. Mater. 4 (1961) 177–199. doi:10.1016/0022-3115(61)90126-X.

[142] C.W. Wilkes, G.L. Batte`, D.B. Tracy, V. Griffiths, EBR-II Fuel Slug Casting Experience, ANL-IFR-73, Argonne, IL (United States), 1987. doi:10.2172/713795.

[143] W.N. Beck, R.J. Fousek, J.H. Kittel, Irradiation Behavior of High-Burnup Uranium-Plutonium Alloy Prototype Fuel Elements, III (1968). doi:10.2172/4793507.

[144] A.A. Elmustafa, D.S. Stone, Indentation Size Effect in Polycrystalline F.C.C. Metals, Acta Mater. 50 (2002) 3641–3650. doi:10.1016/S1359-6454(02)00175-1.

[145] M. Hackett, S. Miller, R. Latta, C. Xu, HT9 Strain Modeling for Fuel Pin Deformation, in: Int. Conf. Nucl. Eng. Proceedings, ICONE, American Society of Mechanical Engineers (ASME), 2014. doi:10.1115/ICONE22-30414.

[146] H. Farrar, H.R. Fickel, R.H. Tomlinson, Cumulative Yields of Light Fragments in UZ35 Thermal Neutron Fission, 1062. doi:10.1139/p62-107.

[147] W.E. Grummitt, G. Wilkinson, Fission products of U235, Nature. 158 (1946) 163. doi:10.1038/158163a0.